



Institut für Erd- und Umweltwissenschaften  
Mathematisch-Naturwissenschaftliche Fakultät  
Universität Potsdam



# **3-D modeling of shallow-water carbonate systems:**

A scale-dependent approach based on  
quantitative outcrop studies

Frédéric Amour

Kumulative Dissertation zur Erlangung des akademischen Grades  
Doktor der Naturwissenschaften (Dr. rer. Nat.)

Eingereicht an der  
Mathematisch-Naturwissenschaftlichen Fakultät der Universität Potsdam

Potsdam, March 2013



Published online at the  
Institutional Repository of the University of Potsdam:  
URL <http://opus.kobv.de/ubp/volltexte/2013/6662/>  
URN <urn:nbn:de:kobv:517-opus-66621>  
<http://nbn-resolving.de/urn:nbn:de:kobv:517-opus-66621>

*To my mother, my father, my sister, my brother, and to my lovely Gweni,  
Who supported me in my choices and believed in me over the years!*

---



# Content

---

<b>Content</b>	<b>iii</b>
<b>Abstract</b>	<b>vii</b>
<b>Zusammenfassung</b>	<b>viii</b>
<b>List of figures</b>	<b>ix</b>
<b>List of tables</b>	<b>xi</b>
<b>Acknowledgements</b>	<b>xii</b>
<b>1. Introduction</b>	<b>1</b>
1.1. Context and challenges	1
1.2. (FC) <sup>2</sup> Alliance	3
1.3. Organization of the thesis	3
<b>2. Capturing and modeling metre-scale spatial facies heterogeneity in a Jurassic ramp setting (Central High Atlas, Morocco)</b>	<b>5</b>
<i>Abstract</i>	5
<b>2.1. Introduction</b>	<b>5</b>
<b>2.2. Regional geological setting</b>	<b>7</b>
<b>2.3. Study area</b>	<b>9</b>
<b>2.4. Materials and methods</b>	<b>11</b>
2.4.1. Field data collection	11
2.4.2. Kinematic d-GPS mapping	12
2.4.3. 3-D stochastic modeling	12
<b>2.5. Lithofacies types</b>	<b>13</b>
<b>2.6. Depositional environments</b>	<b>18</b>
<b>2.7. Depositional cycles and sequences</b>	<b>20</b>
2.7.1. Medium-scale sequences	20
2.7.2. Small-scale cycles	21
<b>2.8. 3-D stochastic models using PETRELT<sup>M</sup></b>	<b>24</b>
2.8.1. Key surfaces	24
2.8.2. Geocellular model	25

2.8.3. Integradation of sedimentological data into PETREL™	25
2.8.4. 3-D facies modeling	26
2.8.5. Quality control	28
<b>2.9. Models comparisons</b>	<b>28</b>
<b>2.10. Discussion</b>	<b>33</b>
2.10.1. Geological uncertainties about stochastic simulation	33
2.10.2. Impact of the algorithm choices on the facies distribution	34
<b>2.11. Conclusion</b>	<b>37</b>
<b>3. Outcrop analogue for an oolitic carbonate ramp reservoir: A scale-dependent geological modeling approach based on stratigraphic hierarchy</b>	<b>39</b>
<i>Abstract</i>	<i>39</i>
<b>3.1. Introduction</b>	<b>39</b>
<b>3.2. Geological setting</b>	<b>41</b>
<b>3.3. Characterization of the study area</b>	<b>42</b>
<b>3.4. Methods applied and terminology</b>	<b>43</b>
3.4.1. Field methods	43
3.4.2. Statistical analysis	44
3.4.3. 3-D Outcrop Modeling	44
<b>3.5. Lithofacies classification and depositional setting</b>	<b>45</b>
3.5.1. Distal middle to outer ramp	45
3.5.2. Proximal middle ramp	48
3.5.3. Inner ramp	48
3.5.3.1. Foreshoal	48
3.5.3.2. Shoal complex	50
3.5.3.3. Inter- to backshoal	51
<b>3.6. Depositional sequences</b>	<b>51</b>
<b>3.7. Scale-dependent geological heterogeneity</b>	<b>52</b>
<b>3.8. Scale-dependent modeling approach</b>	<b>55</b>
3.8.1. Modeling the high-frequency depositional sequences	55
3.8.2. Modeling the facies association	56
3.8.3. Modeling the lithofacies	57
<b>3.9. Discussion</b>	<b>60</b>
3.9.1. Scale-dependent geological heterogeneity and their controlling factors	60
3.9.2. Scale-dependent geological modeling	62
3.9.3. Geological heterogeneity and modeling strategy: Recommendations	62
<b>3.10. Conclusion</b>	<b>64</b>

<b>4. Lateral variability of cycle across the Latemar platform top: A spatially-dependent cyclicality record (Dolomites, northern Italy)</b>	<b>67</b>
<i>Abstract</i>	<i>67</i>
<b>4.1. Introduction</b>	<b>67</b>
<b>4.2. Geological setting</b>	<b>70</b>
<b>4.3. Latemar isolated platform</b>	<b>71</b>
4.3.1. Stratigraphic succession	71
4.3.2. Platform top cyclicality	71
4.3.3. Depositional profile	72
4.3.3.1. <i>Slope</i>	72
4.3.3.2. <i>Margin</i>	72
4.3.3.3. <i>Interior platform</i>	72
<b>4.4. Study window and methodological approach</b>	<b>74</b>
<b>4.5. Lithofacies types and depositional conditions</b>	<b>75</b>
4.5.1. Subtidal deposits	75
4.5.2. Intertidal deposits	77
4.5.3. Intertidal to supratidal deposits	78
<b>4.6. Vertical stacking pattern and lateral variability of Latemar carbonate cycles</b>	<b>82</b>
4.6.1. Classification of carbonate cycles	82
4.6.2. Lateral variability of cycle types	83
<b>4.7. Hierarchical cyclicality of the Latemar platform top</b>	<b>88</b>
<b>4.8. Depositional profile and cyclicality</b>	<b>90</b>
4.8.1. Margin to lagoon palaeotopographic relief	90
4.8.2. Cycle variability along the depositional profile	91
<b>4.9. Discussion</b>	<b>93</b>
4.9.1. Controlling factors on lateral cycle variability	93
4.9.2. Consequences on the Latemar controversy	94
4.9.3. Platform top aggradation	95
<b>4.10. Conclusion</b>	<b>96</b>
<b>5. 3-D modeling of the margin-to-lagoon depositional profile of the Latemar isolated platform (Middle Triassic, Dolomites)</b>	<b>99</b>
<i>Abstract</i>	<i>99</i>
<b>5.1. Introduction</b>	<b>99</b>
<b>5.2. Geological and stratigraphic setting</b>	<b>100</b>
5.2.1. The Latemar platform	100

5.2.2. The study area: Cima del Forcellone	102
<b>5.3. Methodology</b>	<b>103</b>
5.3.1. Field work	103
5.3.2. GPS mapping	103
5.3.3. Constrains on facies modeling	105
<b>5.4. Lithofacies and facies association</b>	<b>106</b>
5.4.1. The lagoon	106
5.4.2. The backmargin to tepee belt	107
5.4.3. The backreef	108
<b>5.5. Scale-dependent geological modeling</b>	<b>108</b>
5.5.1. Skeleton framework of the 3-D model	108
5.5.2. Evolution of the margin-to-lagoon depositional profile	109
<b>5.6. Discussion</b>	<b>113</b>
5.6.1. Depositional profile of the platform top	113
5.6.2. Stratigraphic architecture of the platform top	114
5.6.3. Evolution of the Latemar isolated platform	114
<b>5.7. Conclusion</b>	<b>116</b>
<b>6. Discussion</b>	<b>119</b>
<b>6.1. Intrinsic properties of carbonate systems</b>	<b>119</b>
6.1.1. Morphological profile and depositional environment	119
6.1.2. Lithofacies mosaic and depositional sequence	120
<b>6.2. 3-D modeling of shallow-water carbonate systems</b>	<b>124</b>
6.2.1. A compromise between deterministic and stochastic approaches	124
6.2.2. A nested arrangement of carbonate bodies	125
6.2.3. Scale-dependent modeling approach	127
<b>7. Conclusion</b>	<b>131</b>
<b>8. References</b>	<b>133</b>
<b>9. Appendix</b>	<b>143</b>
<b>A1. Interpretation of the lateral variability of small-scale sequences from the inner to proximal middle ramp</b>	<b>143</b>
<b>A2. Correlation panel across Cima del Forcellone</b>	<b>145</b>
<b>A3. Summary of the vertical and NE-SW dimensions of depositional environments and lithofacies types using semi-variogram analysis</b>	<b>147</b>
<b>A4. Mathematical concepts applied during stochastic simulation</b>	<b>148</b>

# Abstract

---

The study of outcrop modeling is located at the interface between two fields of expertise, Sedimentology and Computing Geoscience, which respectively investigates and simulates geological heterogeneity observed in the sedimentary record. During the last past years, modeling tools and techniques were constantly improved. In parallel, the study of Phanerozoic carbonate deposits emphasized the common occurrence of a random facies distribution along single depositional domain. Although both fields of expertise are intrinsically linked during outcrop simulation, their respective advances have not been combined in literature to enhance carbonate modeling studies. The present study re-examines the modeling strategy adapted to the simulation of shallow-water carbonate systems, based on a close relationship between field sedimentology and modeling capabilities.

In the present study, the evaluation of three commonly used algorithms Truncated Gaussian Simulation (TGSim), Sequential Indicator Simulation (SISim), and Indicator Kriging (IK), were performed for the first time using visual and quantitative comparisons on an ideally suited carbonate outcrop. The results show that the heterogeneity of carbonate rocks cannot be fully simulated using one single algorithm. The operating mode of each algorithm involves capabilities as well as drawbacks that are not capable to match all field observations carried out across the modeling area.

Two end members in the spectrum of carbonate depositional settings, a low-angle Jurassic ramp (High Atlas, Morocco) and a Triassic isolated platform (Dolomites, Italy), were investigated to obtain a complete overview of the geological heterogeneity in shallow-water carbonate systems. Field sedimentology and statistical analysis performed on the type, morphology, distribution, and association of carbonate bodies and combined with palaeodepositional reconstructions, emphasize similar results. At the basin scale ( $\times 1$  km), facies association, composed of facies recording similar depositional conditions, displays linear and ordered transitions between depositional domains. Contrarily, at the bedding scale ( $\times 0.1$  km), individual lithofacies type shows a mosaic-like distribution consisting of an arrangement of spatially independent lithofacies bodies along the depositional profile. The increase of spatial disorder from the basin to bedding scale results from the influence of autocyclic factors on the transport and deposition of carbonate sediments.

Scale-dependent types of carbonate heterogeneity are linked with the evaluation of algorithms in order to establish a modeling strategy that considers both the sedimentary characteristics of the outcrop and the modeling capabilities. A surface-based modeling approach was used to model depositional sequences. Facies associations were populated using TGSim to preserve ordered trends between depositional domains. At the lithofacies scale, a fully stochastic approach with SISim was applied to simulate a mosaic-like lithofacies distribution. This new workflow is designed to improve the simulation of carbonate rocks, based on the modeling of each scale of heterogeneity individually.

Contrarily to simulation methods applied in literature, the present study considers that the use of one single simulation technique is unlikely to correctly model the natural patterns and variability of carbonate rocks. The implementation of different techniques customized for each level of the stratigraphic hierarchy provides the essential computing flexibility to model carbonate systems. Closer feedback between advances carried out in the field of Sedimentology and Computing Geoscience should be promoted during future outcrop simulations for the enhancement of 3-D geological models.

# Zusammenfassung

---

Das Modellieren von geologischen Aufschlüssen liegt der Schnittstelle zwischen zwei geo-logischen Teildisziplinen, der Sedimentologie und der geologischen Modellierung. Hierbei werden geologische Heterogenitäten untersucht und simuliert, welche im Aufschluss beobachtet wurden. Während der letzten Jahre haben sich die Werkzeuge und die Technik der Modellierung stetig weiter-entwickelt. Parallel dazu hat die Untersuchung der phanerozoischen Karbonatablagerungen ihren Fokus auf gemeinsamen Vorkommen von zufälligen Faziesverteilungen in beiden Ablagerungs-gebieten. Obwohl beide Teildisziplinen durch die Aufschlussmodellierung eigentlich verbunden sind, wurden ihre jeweiligen Vorteile in der Literatur nicht miteinander verbunden, um so eine Verbesserung ähnlicher Studien zu erreichen. Die vorliegende Studie überprüft erneut die Modellierungsstrategie, angepasst an die Simulation von Flachwasser-Karbonat-Systemen und basierend auf einer engen Beziehung zwischen Sedimentologie und Modellierung.

Die vorliegende Arbeit behandelt erstmals die Evaluierung der drei am häufigsten verwendeten Algorithmen „Truncated Gaussian Simulation (TGSim)“, „Sequential Indicator Simulation (SISim)“ und „Indicator Kriging (IK)“, um sie visuell und quantitativ mit dem entsprechenden Aufschluss zu vergleichen. Die Ergebnisse zeigen, dass die Heterogenität von Karbonatgesteinen nicht komplett mit nur einem Algorithmus simuliert werden kann. Die Eigenschaften jedes einzelnen Algorithmus beinhalten Vor- und Nachteile, sodass kein Algorithmus alle Beobachtungen aus dem Aufschluss widerspiegelt.

Die zwei Endglieder im Spektrum der Ablagerungsbedingungen von Karbonaten, eine flachwinklige, jurassische Karbonat-Rampe (Hoher Atlas, Marokko) und eine isolierte, triassische Plattform (Dolomiten, Italien), wurden untersucht, um einen kompletten Überblick über die verschiedenen Heterogenitäten in Flachwasser-Karbonat-Systemen zu erhalten. Sedimentologische und statistische Analysen wurden für die verschiedenen Typen, Morphologien, Verteilungen und Assoziationen von Karbonatablagerungen durchgeführt und mit paläogeografischen Rekonstruktionen kombiniert und zeigen ähnliche Ergebnisse. Im Beckenmaßstab zeigen die Faziesassoziationen, bestehend aus Fazieszonen mit ähnlichen Ablagerungsbedingungen, einen linearen und kontinuierlichen Übergang zwischen den einzelnen Ablagerungsbereichen. Im Gegensatz dazu zeigt für einzelne Lithofaziestypen im Maßstab einzelner Schichten eine mosaikartige Verteilung, bestehend aus einer Anordnung räumlich unabhängiger Lithofazieszonen entlang des Ablagerungsprofils. Das Ansteigen der räumlichen Unordnung von der beckenweiten Ablagerung zur Ablagerung einzelner Schichten resultiert aus dem Einfluss autozyklischer Faktoren bei der Ablagerung von Karbonaten.

Die Skalenabhängigkeit von Karbonat-Heterogenität ist mit der Auswertung der Algorithmen verknüpft um eine Modellierungsstrategie zu etablieren, welche sowohl die sedimentären Charakteristiken des Aufschlusses als auch die Modellierfähigkeit berücksichtigt. Für die Modellierung der Ablagerungssequenzen wurde ein flächenbasierter Ansatz verwendet. Die Faziesassoziationen wurden durch die Benutzung des TGSim-Algorithmus simuliert, um die regulären Trends zwischen den einzelnen Ablagerungsgebieten zu erhalten. Im Bereich der verschiedenen Lithofazies wurde mit dem SISim-Algorithmus, ein voll stochastischer Ansatz angewendet, um die mosaikartige Verteilung der Lithofazies-Typen zu simulieren. Dieser neue Arbeitsablauf wurde konzipiert, um die Simulation von Karbonaten auf Basis der einzelnen Heterogenitäten in verschiedenen Größenordnungen zu verbessern.

Im Gegensatz zu den in der Literatur angewendeten Simulationsmethoden berücksichtigt diese Studie, dass eine einzelne Modellierungstechnik die natürlichen Ablagerungsmuster und Variabilität von Karbonaten wahrscheinlich nicht korrekt abbildet. Die Einführung verschiedener Techniken, angepasst auf die verschiedenen Ebenen der stratigrafischen Hierarchie, liefert die notwendige Flexibilität um Karbonatsysteme korrekt zu modellieren. Eine enge Verknüpfung zwischen den Fortschritten auf dem Gebieten der Sedimentologie und dem Gebiet der modellierenden Geowissenschaften sollte weiterhin bestehen, um auch zukünftig bei der Simulation von geologischen Gelände-Aufschlüssen eine Verbesserung der 3-D-Modellierung zu erreichen.

# List of figures

---

2.1.	Geological setting of the study area	8
2.2.	Stratigraphic setting of the study area	9
2.3.	Panoramic view of the study window	10
2.4.	Workflow of the digital outcrop modeling process	11
2.5.	Outcrop photos and photo micrographs of the lithofacies types	15
2.6.	Field pictures showing examples of dimension, morphology, and facies association observed in the field	19
2.7A.	Stratigraphic correlation of the study window showing small- and medium-scale depositional packages	22
2.7B.	Legend of Figure 2.7A	23
2.8.	Tentative of palaeoenvironmental reconstruction of the Bajocian carbonate ramp	24
2.9.	Major steps for building the four 3-D facies models	26
2.10.	Panels showing the four facies models (model A, model B, model C, and model D)	27
2.11.	Three quality tests made in the the 3-D facies model A	29
2.12.	Comparisons of the vertical lithofacies distribution observed in the field and simulated during modeling process	32
2.13.	Comparisons of the horizontal lithofacies distribution built by the four facies models	33
3.1.	Geological and stratigraphic setting of the study area	42
3.2.	Overview of outcrop conditions within the study window	43
3.3.	Comparisons between both georeferencing methods DGPS survey and LIDAR data	45
3.4.	West-East cross section showing the facies distribution and sequence stratigraphy in the study area	47
3.5.	Palaeodepositional reconstruction of the Bajocian carbonate ramp	49
3.6.	Micro- and macroscopic characterization of inner ramp lithofacies	50
3.7.	Palaeocurrent features observed in oolitic grainstones	51
3.8.	Transect of the east face of the outcrop showing lithofacies distribution	53
3.9.	Theoretical exponential and sampled cumulative frequency distribution of thicknesses of the oolitic grainstone and the peloidal grainstone	54
3.10.	Input of geological data and building of the model framework	56
3.11.	Summary of the major, minor, and vertical dimensions of inner ramp shoals and inner ramp lithofacies using semi-variograms analysis	58
3.12.	3-D view of the facies association model and lithofacies model	59
3.13.	SW-NE cross sections of the scale-dependent model located within the inner ramp and lithofacies maps	61
3.14.	Summary of scale-dependent geological features based on section SEF-1 from the large-scale stacking pattern of high-frequency depositional sequences (level 1) to the intermediate-scale facies association (level 2) and to the finest-scale lithofacies types (level 3)	63
4.1.	Summarize of interpretations of the Latemar cyclicity based on cyclostratigraphic studies and spectral analysis	69
4.2.	Geological and stratigraphic setting of the Latemar isolated platform	70
4.3.	Depositional profile of the asymmetric Latemar platform top from the lagoon to foreslope with the location of the study area	73
4.4.	Legend for Figures 4.3, 4.8, 4.9, 4.10, 4.11, and 4.14	73
4.5.	Schematic map view of Latemar platform morphology with the location of the study window	74
4.6.	Micro- and macroscopic photographs showing the main characteristics of each lithofacies type	79
4.7.	Field pictures of inter- to supratidal features observed in the field	81
4.8.	Schematic summary of cycle types observed in the study area	82
4.9.	Transect A showing lateral cycle variability at the top of the LCF and base of the MTF	84

4.10.	Transect B displaying lateral cycle variability at the middle part of the MTF,	86
4.11.	Transect C showing lateral variability of cycles at the top part of the MTF	87
4.12.	Composite section of the Cima del Forcellone from top of the LCF to top of the MTF and displaying locations of marker horizons and transects	89
4.13.	Graphic displaying DGPS data point collected in the field during the mapping of Marker Horizon E	91
4.14.	Schematic view of the depositional profile of the Latemar platform top from the lagoon to backreef showing the lateral variability of small cycle sets	92
5.1.	Geological and stratigraphic setting of the study area	101
5.2.	Depositional profile of Latemar platform top from the foreslope to the lagoon	102
5.3.	Latemar isolated platform in map view with location of the study area in Cima del Forcellone outcrop	103
5.4.	Composite section from the uppermost LCF and the MTF	104
5.5.	GPS mapping survey of Cima del Forcellone outcrop and its geological features	105
5.6.	Lithofacies proportion within the backreef, the tepee belt to backmargin and the lagoon	106
5.7.	Data input of the 15 sections (L1 to L15), the digital elevation model and the five marker horizons in the PETRELTm modeling software	109
5.8.	3-D view of the scale-dependent outcrop model of Cima del Forcellone displaying the distribution of the facies association (A) and the lithofacies types (B)	109
5.9.	SW-NE transect of Cima del Forcellone showing the distribution of the backreef, tepee belt to backmargin, and lagoon based on field observations and on the 3-D outcrop model (B)	110
5.10.	Vertical variation of lithofacies proportion through the MTF extracted from the 3-D outcrop model and showing the rhythmic occurrence of tepee structures controlled by intermediate and medium cycle set cyclicity	112
5.11.	Compilation of the major geological features at the transition between the platform top and the slope, based on the present data and previous studies (Harris, 1993, 1994; Emmerich et al.,2005; Preto et al., 2011)	115
6.1.	Examples of ancient and modern carbonate systems showing the morphology, distribution, and association of carbonate bodies from large to small scale.	123
6.2.	Summary of the hierarchical arrangement of shallow-water carbonate patterns and their associated modeling approaches based on the Jurassic ramp case study.	129
A1.	Interpretation of the lateral variability of small-scale depositional sequence from the inner to proximal middle ramp	143
A2.	Correlation panel across Cima del Forcellone	145
A3.	Semi-variogram analysis of carbonate bodies from the depositional environments to the lithofacies types	147
A4.1	Example of conditioning cumulative distribution function of a categorical random variable such as facies types	148
A4.2	Schematic explanation of the probability estimation of a facies F1 using IK	150
A4.3	Schematic explanation of the probability estimation of a facies F1 using SISim	151
A4.4	Four examples of the probability density function of a Gaussian random variable	152
A4.5	Example of truncation of a standard ( $\mu=0$ , $\sigma^2=1$ ) Gaussian random function $Y(u)$ by five facies types F1, F2, F3, F4, and F5.	153



# List of tables

---

2.1.	Lithofacies descriptions and depositional environment interpretations	17
2.2.	Summary table of the percentage deviation and associated standard deviation between the final model and data input	30
3.1.	Lithofacies classification and interpretation	46
4.1.	Summarize of the lithofacies classification and the interpretation of depositional conditions with their color codes	76
4.2.	Summary of each hierarchical cyclicity interpreted from the MTF of Cima del Forcellone and comparisons with previous spectral analysis (Zühlke et al., 2003)	95
5.1.	Summarize of lithofacies classification and interpretation of depositional conditions	107
5.2.	Vertical and NE-SW dimensions of the facies associations and lithofacies types	108

# Acknowledgements

---

First of all, I would like to thank my supervisor Maria Mutti for all her advice and help during the different stages of my PhD project. I also acknowledge the team of sedimentologists at the University of Potsdam especially Sara Tomás, Gianluca Frijia, Matteo Di Lucia, Ursula Hammes, and Michael Szurlies for their fruitful comments and discussions.

The project was part of a joint industry-academy initiative financially supported by ExxonMobil Corporation and known as the (FC)<sup>2</sup> Alliance, in which several European Universities participated. I would like to thank the director of the (FC)<sup>2</sup> Alliance, Susan M. Agar, who has supported me and stimulated this large consortium of universities over the years. Gregory S. Benson was my mentor during my internship in ExxonMobil Corporation and has kindly taught me the rudiments as well as the “dark side” of Petrel<sup>TM</sup> software. Gregory has been decisive for the achievement of this PhD and I am particularly indebted to him. I have also benefited from the help and field experience of Robert Alway, Kul Karcz, Ravi Shekhar, Lyndon Yose, Stephen Kaczmarek, and John Bova from ExxonMobil Corporation.

During my PhD project, I have been fortunate enough to meet and collaborate with geoscientists from numerous universities. I have closely worked with Adrian Immenhauser and Nicolas Christ from the University of Bochum, which have provided much help during collection of data in the field and have contributed to this PhD project via fruitful discussions and comments. I have strongly appreciated casual as well as constructive discussions with Fiona Withaker and Graham Felce from the University of Bristol, Giovanni Bertotti and Herman Boro from the Vrije University, and Enrique Gomez-Rivas and Juan Diego Martin from the Universitat autònoma de Barcelona.

I also acknowledge Lahcen Kabiri from the University of Moulay Ismail for his logistic support during our field excursions in Morocco. The data collection in the field has been performed with the much appreciated help and companionship of Martin Homann, Max Zitzmann, Fadi Semmo, Dennis Bunke, and Falko Kraul (University of Potsdam) in Morocco and Mike Curtis and Rosalind Preston (University of Bristol) as well as Kenneth Ewonde, Jeroen van der Vaart, and Jop Klaver (Vrije University) in Italy.

I am grateful to my colleagues and friends from the Institute für Erd- und Umweltwissenschaften at the University of Potsdam for their support and companionship over the years. I also would like to thank Tanja Klaka-Tauscher and Steffi Zarnack for their continuous help to deal with the German administration as well as Michael Krause, Urs Böniger, and Max Zitzmann for translating the abstract of this thesis into German! Ines Muench and René Muschkorgel have provided technical software support and Christine Fischer has produced the thin-sections. I also thank the “Ingenieurbüro” GILAN (Berlin) for the collection and processing of the LiDAR data and Simon Buckley (CIPR, Bergen) for access to the LIME software. Thanks to Schlumberger for providing the 3-D geological modeling software Petrel<sup>TM</sup>.

I warmly thank Assou, Moha, and all the Agouzil Family for their friendship and hospitality in the Kasbah Amellago during my field excursions in Morocco as well as all the Gabrielli Family, the owners of the “Torre di Pisa” hut for the logistic help and initiation to a long list of tasteful grappas during cold evenings at Mount Latemar in Italy.

Finally, I am profoundly grateful to my family and to Gweni for their continuous support and confidence in my choices.

# Chapter 1

---

## Introduction

### 1.1. Context and challenges

The study of outcrop modeling provides the opportunity to investigate and quantify the geometry and the distribution of sedimentary bodies along a depositional profile. Field-based, 2-D and 3-D geological data play an essential role for the characterization of sub-surface reservoir properties, which cannot be accessed using geophysical imaging tools and wells (Kerans et al., 1994; Grammer et al., 2004; Jones et al., 2008). Whereas outcrop modeling studies have been intensely performed on clastic sediments (e.g. Miall and Tyler, 1991; Bryant and Flint, 1993), the scientific interest on the 3-D modeling of ancient carbonate systems, which currently account for 60% of the world's oil and 40% of world's gas reserves, has drastically increased during the last ten years (Blendinger et al., 2004; Verwer et al., 2004; Adams et al., 2005; Aigner et al., 2007; Qi et al., 2007; Borgomano et al., 2008; Kenter et al., 2008; Phelps et al., 2008; Pöppelreiter et al., 2008; Verwer et al., 2009; Koehrer et al., 2010; Palermo et al., 2010; Tomás et al., 2010).

Various simulation techniques and strategies have been generated (e.g. Matheron et al., 1987; Gómez-Hermández and Srivastava, 1990; Caers and Zhang, 2004; Adams et al., 2005; Sech et al., 2009) and constantly improved (Gringarten and Deutsch, 2001; Coburn et al., 2006; Zappa et al., 2006; Jones et al., 2008, 2009; Kenter et al., 2008; Tolosana-Delgado et al., 2008; Koehrer et al., 2010) in order to capture geological heterogeneity observed in the sedimentary record into an outcrop model. The prevalent modeling technique is called stochastic facies modeling, which applies simulation algorithms to populate facies between data points (Kjongsvik et al., 1994; White et al., 2003; Aigner et al., 2007; Falivene et al., 2007; Pöppelreiter et al., 2008; Koehrer et al., 2010). The flexibility to match data input, the relatively short time required for each simulation, and the opportunity to establish an fully automated modeling workflow make stochastic modeling the privileged technique for outcrop and sub-surface case studies. Despite considerable effort devoted to the improvement of stochastic simulation (e.g. Coburn et al., 2006), the experience and knowledge of the modeler still play a crucial role in the quality of the final model (Journel et al., 1998; Falivene et al., 2007). The establishment of a suitable modeling strategy designed to capture the geological heterogeneity observed in the sedimentary record remains challenging for the building of a realistic 3-D geological model for carbonate deposits.

Due to lack of a prevalent modeling methodology in literature, previous studies carried out in clastic rocks (Gotway and Rutherford, 1994; Journel et al., 1998; Falivene et al., 2006a, 2007; Bastante et al., 2008) built facies models using different stochastic algorithms and based on the same data input. Comparisons between outcrop and facies models then enable to evaluate the impact of each algorithm on the simulated facies distribution and provide basic modeling rules to assist modeler decisions. The latter studies emphasized an essential link between the sedimentological characteristics of an outcrop and the capabilities and drawbacks of simulation techniques. The choice of an algorithm must be based on the objective and scale of the modeling target as well as the spatial relationship between sedimentary bodies. The building of a realistic, 3-D outcrop model then relies on advanced

knowledge of geological heterogeneity and conceptual depositional model, interpreted from field observations and facies analysis. Only few studies (Zappa et al., 2006; Koehrer et al., 2010) quantitatively documented in details the geological features of an outcrop prior to modeling. Sedimentological investigation is yet of primary interest to justify the use of one peculiar simulation technique compared to another and ensure the quality of the 3-D facies model.

Within ancient shallow-water carbonate systems, the concept of sequence stratigraphy assumes that the geological heterogeneity consists of a cyclic stacking pattern of sedimentary bodies, stratal thickness, and discontinuity surfaces (Goldhammer et al., 1990; Lehrmann and Goldhammer, 1999). The hierarchical arrangement of sequences or cycles allows the establishment of a chronostratigraphic framework, based on the identification of short- and long-term Milankovitch-driven sea level oscillations (allocyclic model). Such cyclic and hierarchical interpretation of the sedimentary record involves the implicit assumption of a more or less predictable distribution of facies, displaying ordered and repetitive deepening- and shallowing-upward trend. The predictable nature of facies heterogeneity was questioned by field observations and statistical analysis carried out on shallow-water carbonate rocks (Ginsburg, 1971; Hardie and Shinn, 1986; Pratt and James, 1986; Read, 1995; Drummond and Wilkinson, 1993; Wilkinson et al., 1997, 1999). The latter studies showed the common occurrence of a random distribution of facies in the sedimentary record, caused by the predominance of internal factors (autocyclic model) on sedimentation such as tidal-flat progradation, variability of carbonate production and transport, unfilled accommodation, clastic input, and storms. In the effort of integration, recent studies (Wright and Burgess, 2005; Burgess, 2008; Strasser and Védrine, 2009) have highlighted that the predictable or random nature of carbonate heterogeneity is dependent of the scale of observation considered. Whereas at the basin scale, the association of facies exhibits gradational and ordered trends along a proximal-distal depositional profile, facies distribution, at the bedding scale, lacks clear trends in facies-to-facies transitions, leading to an unpredictable spatial arrangement. These recent advances on the field of carbonate sedimentology modified previous conceptions on carbonate heterogeneity and brought new viewpoints, which need to be considered for the improvement carbonate outcrop modeling.

The present study re-examines the modeling strategy adapted to the simulation of shallow-water carbonate systems, based on a close relationship between field sedimentology and modeling capabilities. In this purposes, two outcrops were investigated, a Jurassic carbonate ramp (Central High Atlas, Morocco) and a Triassic isolated platform (Dolomites, Italy). The selection of two opposed morphologies allow for a complete overview of the geological heterogeneity within shallow-water carbonate settings. Within both platforms, a 1 kilometer long study area were selected in order to investigate the evolution of the platform as well as access the facies heterogeneity at the bedding scale. The understanding of both depositional systems and the building of digital outcrop models were carried out by using several approaches such as i) field data collection, ii) microfacies analysis and interpretation, iii) palaeodepositional reconstruction, iv) sequence stratigraphy, v) DGPS mapping, vi) LIDAR data post-processing and analysis, vii) geostatistical analysis on facies geometry and distribution, and viii) facies modeling with Petrel<sup>TM</sup> software.

## 1.2. The (FC)<sup>2</sup> Alliance

This Ph.D. project was financially supported by the Exxonmobil (FC)<sup>2</sup> Alliance, an Industry-Academic community designed to understand fluid flow in carbonates. The (FC)<sup>2</sup> Alliance is composed of several research groups, including the university of Bochum, Barcelona, Bristol, Amsterdam, Edinburgh, Pierre et Marie Curie Paris, Aix-Marseille, Kansas, Calgary, Leoben, and Imperial College London. This large community consists of a thematic research framework spanning from sedimentology, diagenesis, geochemistry, structural geology, to fluid flow simulation and including static, forward, and mechanical modeling studies. In the (FC)<sup>2</sup> Alliance, this Ph.D. project was designed to collect, quantify, and interpret data from ancient shallow-water carbonate systems as well as provide 3-D geological models to be used for fluid flow simulation.

This Ph.D. thesis contributed to three papers (Agada et al., in review in Soc. Petrol. Eng.; Shekhar et al., submitted to Petrol. Geosc.; Whitaker et al., submitted to Petrol. Geosc.). Whitaker et al. investigates the reservoir properties of isolated carbonate platforms by comparing process-based forward models and field observations carried out in the present study (Chapters 4, 5). Agada et al. and Shekhar et al. perform a series of fluid flow simulations using the 3-D outcrop model of a Jurassic carbonate ramp built during this Ph.D. thesis (Chapter 3).

## 1.3. Organization of the thesis

The present study is divided into 7 chapters, in which chapters 2 and 3 focus on a Jurassic carbonate ramp in Morocco, whereas a Triassic isolated platform is presented in chapters 4 and 5. A similar approach was applied to both study areas: a detailed description and interpretation of the depositional system and its geological modeling. The chapter 6 discusses the intrinsic capabilities of a scale-dependent simulation approach to honor the natural patterns and variability of ancient and modern carbonate systems.

Chapter 2 is also devoted to the evaluation of three simulation algorithms, Truncated Gaussian Simulation, Sequential Indicator Simulation, and Indicator Kriging, which are commonly used in literature. Visual and quantitative comparisons between outcrop and facies models inform on the operating mode of each algorithm by emphasizing its capabilities and drawbacks. These findings highlight that the choice of a simulation algorithm requires a detailed investigation of the geometry and connectivity of sedimentary bodies in order to build a realistic geological model. Chapter 2 provides first basic rules adapted to the modeling of ancient shallow-water carbonate systems and enlightens challenges associated to stochastic simulation.

In chapter 3, the palaeodepositional reconstruction of the Jurassic carbonate ramp is carried out and supported by field-based and statistical analysis of the geometry, distribution, and association of carbonate bodies. The study area shows a scale-dependent geological heterogeneity from facies at the bedding scale to facies association at the basin scale. Each hierarchical level of the sedimentary record involves specific geometry and association of carbonate bodies. The present study proposes a new workflow designed to improve the stochastic simulation of shallow-water carbonate rocks and based on the modeling of each scale of heterogeneity individually. A rethought on current simulation techniques suggested here, provides new perspectives on modeling strategies applied to carbonate rocks.

Chapter 4 documents and interprets the palaeodepositional profile of the Latemar platform top, based on a detailed investigation of a margin-to-lagoon transect. Providing the first documentation on lateral cycle variability, a new cyclostratigraphic framework is introduced here, that links field observations and spectral analysis carried out in the Latemar platform during the last two decades, and known as the Latemar Controversy. These findings have impacts on the application of Milankovitch-driven sequence stratigraphy concepts within shallow-water carbonate systems during the Phanerozoic.

Chapter 5 focuses on the modeling of the Latemar platform top. Field observations and statistical analysis carried out on the geometry and distribution of sedimentary bodies indicate a scale-dependent heterogeneity from facies to facies association such as observed in the Jurassic carbonate ramp. The simulation strategy developed in Chapter 3 is therefore also applied to this study area in order to visualize and interpret the evolution of the platform top through time. Providing first evidence for repetitive flooding periods and progradational trends of the margin, these findings question current concepts thought to control the architecture of the Latemar platform.

Chapter 2 is published in *Sedimentology* journal (Amour et al., 2012) and chapter 3 is in press in *American Association of Petroleum Geologists Bulletin* (Amour et al., in press). Chapter 4 will be soon submitted to *Journal of Sedimentary Research* and Chapter 5 is in preparation. This Ph.D. thesis contributed to three other papers (Tomás et al., in review; Christ et al., 2012a, 2012b). Whereas Tomás et al. (in review) is focused on the palaeoecology of bioconstructions observed in the carbonate ramp of Morocco, Christ et al. (2012a, 2012b) investigate the diagenetic history of both the carbonate ramp in Morocco and the isolated Latemar platform in the Dolomites.

## Chapter 2

---

# Capturing and modeling metre-scale spatial facies heterogeneity in a Jurassic ramp setting (Central High Atlas, Morocco)

### *Abstract*

Each simulation algorithm, including Truncated Gaussian Simulation, Sequential Indicator Simulation and Indicator Kriging is characterized by different operating modes, which variably influence the facies proportion, distribution and association of digital outcrop models, as shown in clastic sediments. A detailed study of carbonate heterogeneity is then crucial to understanding these differences and providing rules for carbonate modeling. Through a continuous exposure of Bajocian carbonate strata, a study window (320 m long, 190 m width and 30 m thick) was investigated and metre-scale lithofacies heterogeneity was captured and modeled using closely-spaced sections. Ten lithofacies, deposited in a shallow-water carbonate-dominated ramp, were recognized and their dimensions and associations were documented. Field data including height sections were georeferenced and input into the model. Four models were built in the present study. The model A used all sections and Truncated Gaussian Simulation during the stochastic simulation. For the three other models, model B was generated using Truncated Gaussian Simulation as model A, Model C using Sequential Indicator Simulation and Model D using Indicator Kriging. These three additional models were built by removing two out of eight sections from data input. The removal of sections allows direct insights on geological uncertainties at inter-well spacings by comparing modeled and described sections. Other quantitative and qualitative comparisons were carried out between models to understand advantages/disadvantages of each algorithm. The model A is used as base case. Indicator Kriging (model D) simplifies the facies distribution by assigning continuous geological bodies of the most abundant lithofacies to each zone. Sequential Indicator Simulation (model C) is confident to conserve facies proportion when geological heterogeneity is complex. The use of trend with Truncated Gaussian Simulation is a power tool for modeling well-defined spatial facies relationships. However, in shallow-water carbonate, facies can coexist and their association can change through time and space. The present study shows that the scale of modeling (depositional environment or lithofacies) involves specific simulation constraints on shallow-water carbonate modeling methods.

## 2.1. Introduction

Outcrop analogue studies are a powerful tool to characterize and model geological heterogeneity at different spatial scales. Quantitative data on dimension, distribution, relative proportion of geological bodies and their spatial and temporal variability are indispensable for building subsurface models and are accessible from outcrop analogue (Immenhauser et al., 2004; Mikes and Geel, 2006).

In carbonate settings, Kjensvik et al. (1994) and Kerans et al. (1994) show that at inter-well scale, typically from metre to few hundred metres scale, the stacking pattern of high-frequency carbonate cycles called parasequences as well as the rock fabric (sedimentary structures, porosity/permeability values) of facies are the two critical factors to be incorporated into models. In order to provide quantitative and qualitative geological data on both factors, digital outcrop modeling (DOM) studies have been carried out from few kilometres scale (Adams et al., 2005; Phelps et al.,

2008; Palermo et al., 2010; Tomás et al., 2010) down to the inter-well scale (Kjongsvik et al., 1994; Qi et al., 2007; Aigner et al., 2007; Verwer et al., 2009). The application of inter-well scale geological data to real reservoir case studies and therefore the necessity to capture metre-scale facies heterogeneity into 3-D models remains controversial. Whereas Falivene et al. (2006b) and Løseth et al. (2004) suggest a decrease of the quality of reservoir modeling by taking into account small scale features, Kjongsvik et al. (1994) and Willis and White (2000) highlight the necessity to capture such type of detail in order to properly understand their impact on flow prediction. On the other hand, it is widely believed that fluid flow patterns are controlled by heterogeneities on a range of scales, from sub-millimetre (porosity) to tens-of-kilometres scale (basin evolution) (Eaton, 2006).

The modeling methodology used to capture and simulate facies heterogeneity at the inter-well scale varies from one study to the other. Four main categories of DOM methodology can be defined from deterministic to stochastic approaches. First, interactive facies modeling tools that draw facies on to the 3-D model, have been applied to several outcrop studies (Willis and White, 2000; Aigner et al., 2007; Koehrer et al., 2010) in order to ideally match field observations and the model. However, this time consuming method cannot be included in an automated modeling workflow and is ultimately fully deterministic. The second approach called surface-based modeling, focuses on GPS mapping of key stratigraphic surfaces (Verwer et al., 2009) and facies transitions (Adams et al., 2005; Sech, et al., 2009) to build the model framework. Morphological changes of carbonate platform types (Phelps et al., 2008) can also be easily modeled. Such a method avoids any stochastic simulation and then reduces geological uncertainties. However, the accessibility for GPS mapping or the quality of LIDAR data of the modeled outcrop is a crucial factor and partially or poorly exposed areas cannot be studied. The third and more commonly used category focuses on stochastic simulations based on among others, the Truncated Gaussian Simulation algorithm (TGSim) (White et al., 2003), Sequential Indicator Simulation algorithm (SISim) (Kjongsvik et al., 1994; Zappa et al., 2006; Aigner et al., 2007; Koehrer et al., 2010) or Indicator Kriging algorithm (IK) (Falivene et al., 2007; Tolosana-Delgado et al., 2008). The flexibility to honour data input and the relatively short time required for simulation are two powerful advantages for this method. The last category mixes several modeling methodologies in their simulation workflow (Tomás et al., 2010; Palermo et al., 2010). The aim is to improve the quality of the DOM by taking advantage of each modeling tool. The choice of the most suitable modeling strategy involves numerous decisions of the modeller. Facies modeling tests are needed in order to understand and assist these decisions. Simulation algorithms are characterized by their specific operating modes, which will generate different final models even if the database used for the simulations is the same (Gotway and Rutherford, 1994; Bastante et al., 2008). Differences of facies proportion, spatial facies distribution and facies connectivity/association between models have been shown on clastic sediments (Journel et al., 1998; Falivene et al., 2006a; Falivene et al., 2007). Each algorithm can then be appropriated for the simulation of a specific modeling target (Journel, 1983; Matheron et al., 1987; Gómez-Hermández and Srivastava, 1990). These results demonstrate that stochastic modeling methodology changes significantly from one study to another depending on the outcrop modeled (depositional model, dimension and data available), the objective of the model and the modeling tools available. A unique modeling workflow cannot be applied to all DOMs studies. The experience and knowledge of the modeller play a crucial role in the quality of the final model.



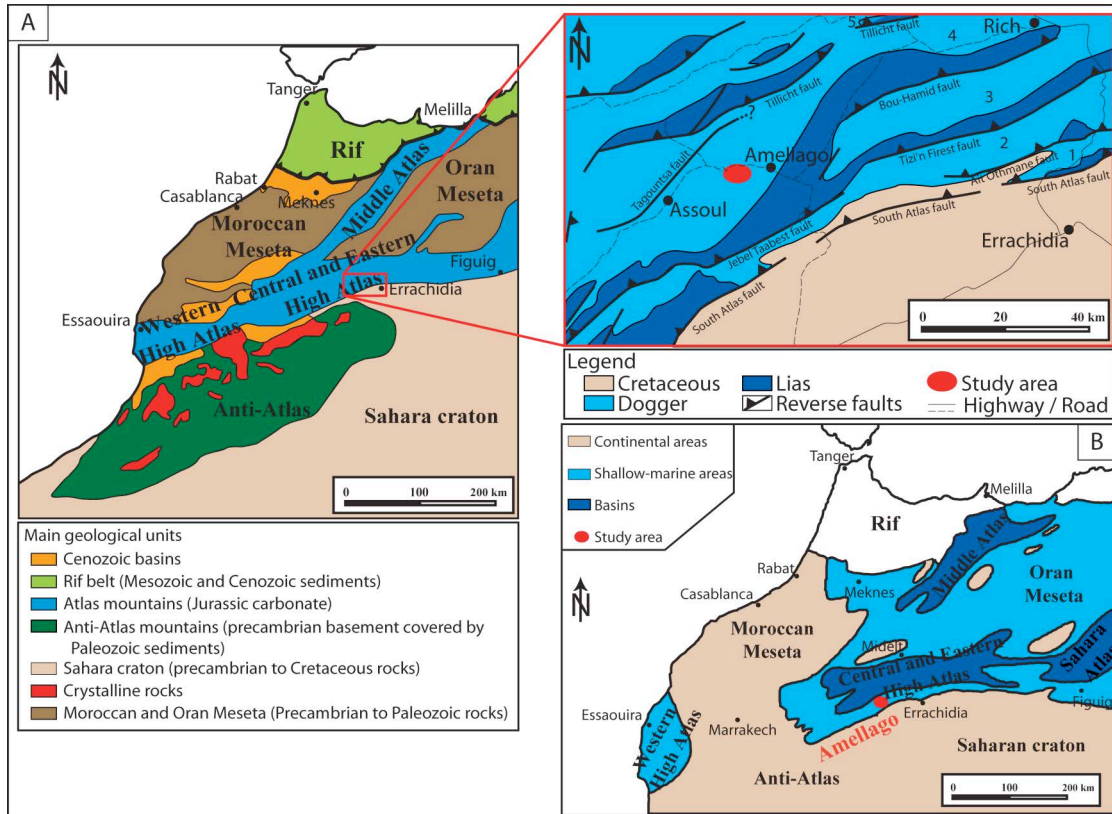
In this context, the present paper tried to provide insights and basic rules on the effect of pixel-based methods (Journel et al., 1998) on stochastic simulation of carbonate rocks by documenting metre-scale geological heterogeneity. Four models were built in the present study. Model A used all measured sections and TGSim during the stochastic simulation. For the three other models, model B was generated using TGSim as model A, model C using SISim and model D using IK. These three additional models were built by removing two out of 8 sections from data input. The removal of two out of eight sections allows a vertical lithofacies comparison between sections described in the field and built by stochastic simulation. This type of comparison (described/simulated sections) provides insight to geological uncertainties associated with stochastic modeling at inter-well spacings. Such studies can be useful for subsurface reservoir characterization where wells are the only direct access to the rock. The main objective of this study was to test facies modeling approaches and to discuss the impact of algorithm choice on spatial (vertical and horizontal) facies distribution and observed uncertainties at the inter-well scale. This objective can only be reached by documenting and understanding spatial facies distribution and association, and stratigraphic hierarchy within the study area. Three algorithms TGSim, SISim and IK were tested because they are the most commonly used for facies modeling in PETREL™ (Trademark of Schlumberger) (Journel et al., 1998; Hu and Le Ravelec-Dupin, 2004; Falivene et al., 2006a).

## 2.2. Regional geological setting

The High Atlas mountain range of Morocco is an ENE-WSW trending structure, which developed by inversion of the Triassic-Jurassic rifting system during the Cenozoic collision of the African and European plate (Choubert and Faure-Muret, 1962; Jacobshagen et al., 1988; Warne, 1988; Dewey et al., 1989; Beauchamp et al., 1996). During the Late Triassic to the Early Jurassic, the dislocation of Pangaea resulted in the opening of the North Atlantic Ocean. In this post-convergent extensive context, the High Atlas rift system developed, consisting of a seaway open to the northeast and connected with the Tethys Ocean (Figure 2.1). The tectonic evolution of the High Atlas basin rifting is still under debate. Warne (1988) proposed a unique continuous rifting step, which spanned from Upper Triassic to Bathonian. An alternative interpretation by Laville et al. (2004) suggested the occurrence of two individual crustal extension events, which took place during the Carnian and the Early Toarcian.

The Jurassic carbonate succession, outcropping in the High Atlas, rests unconformably over the Hercynian basement and is composed of two distinct carbonate platforms, referred to as the Lower Carbonate Platform Complex and the Upper Carbonate Platform Complex, Lias and Dogger in age respectively (Figure 2.2). The two platforms are separated by a 100 m thick Toarcian hemipelagic marl succession deposited in deeper water (Dresnay, 1979; Warne, 1988). The drowning of the Lower Carbonate Platform Complex is probably the result of a combination of both a sea level rise and the ecological changes related to the Early Toarcian oceanic anoxic event (Jenkyns, 1988; Blomeier and Reijmer, 1999; Bailey et al., 2003). Moreover, this drowning event may correspond to a renewed crustal extension characterized by a rapid subsidence (Laville et al., 2004). Most of the studies carried out in the High Atlas region focussed on the Lower Carbonate Platform Complex (Kenter and Campbell, 1991; Crevello, 1992; Blomeier and Reijmer, 1999; Kaoukaya et al., 2001; Mehdi et al., 2003; Merino-Tomé et al., 2007;

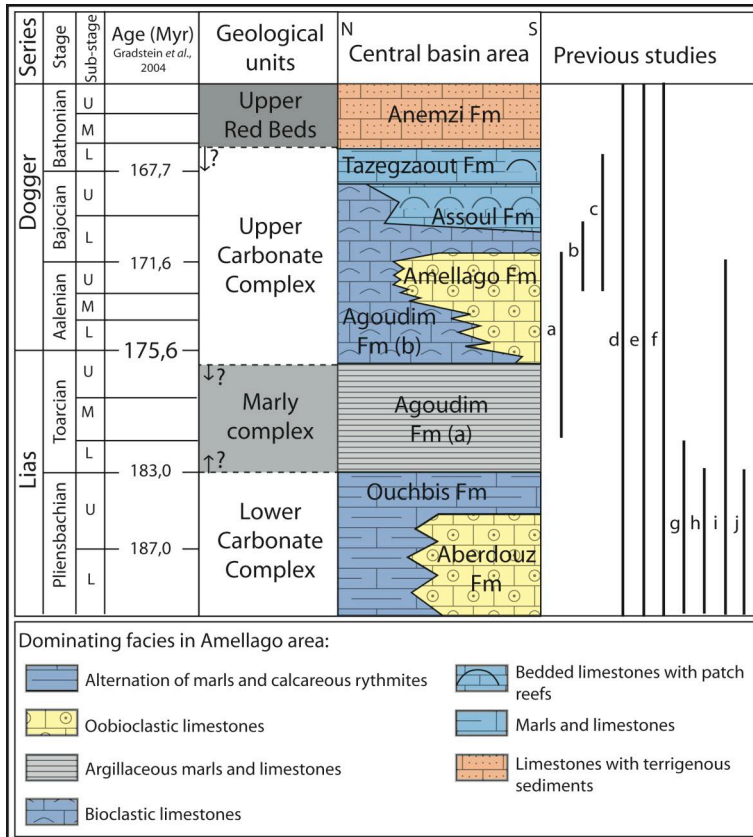
Wilmsen and Neuweiler, 2007; Verwer et al., 2009; Lachkar et al., 2009). In comparison, relatively few studies have investigated the Upper Carbonate Platform Complex (Poisson et al., 1998; Milhi et al., 2002; Ait Addi, 1998, 2006; Sadki, 1992; Pierre, 2006) (Figure 2.2).



**Figure 2.1: Geological setting of the study area. A. Geological map of Morocco with a close-up view of the study area. The south margin of the High Atlas mountain is composed of 5 tilted blocks, 1: Boutazart block, 2: Ait Othmane block, 3: Seddour block, 4: Rich block and 5: Tillich block. B. Palaeogeographic reconstruction of northwest Africa during the Middle Lias (modified after Bloemeier and Reijmer, 1999).**

Within the southern margin of the basin, decreasing accommodation during the Dogger (Middle Jurassic) favoured the progradation of the shallow-water Upper Carbonate Platform Complex into the basin towards the northeast (Stanley, 1981). However, a transtensional tectonic regime operating from the Toarcian to the Bathonian (second crustal extensive event), led to the dislocation of this carbonate platform. Consequently, the Upper Carbonate Complex recorded the development of numerous rhomb-shaped sub-basins bounded by syndepositional ridges (Studer and Du Dresnay, 1980; Laville et al., 2004). Stanley (1981) proposed that these topographic highs, which were characterized by shallow-water deposits, represented the crests of tilted blocks. During the Aalenian-Lower Bajocian, the second crustal extensive event associated with a relatively high sedimentary supply triggered a change of the platform geometry from a rimmed platform into a ramp platform observed toward the east of Rich city (Stanley, 1981; Aid addi, 2006). At the same period, toward the west of Rich city, the south margin of the High Atlas rifting basin remained stable and recorded two progradations of a carbonate ramp, the Amellago and Assoul

formations, toward the basin (Hadri, 1993; Pierre et al., 2010). The infilling of the rifting basin is dated as Middle Bathonian by fossil terrestrial reptiles (Monbaron, 1979; Jenny et al., 1981). From palaeontological and palynological studies and palaeoclimate simulations, it is inferred that the Jurassic climate along the Tethys Ocean margins was characterized by seasons with alternate arid and humid conditions related to monsoonal effects (Moore et al., 1992; Hallam, 1993).



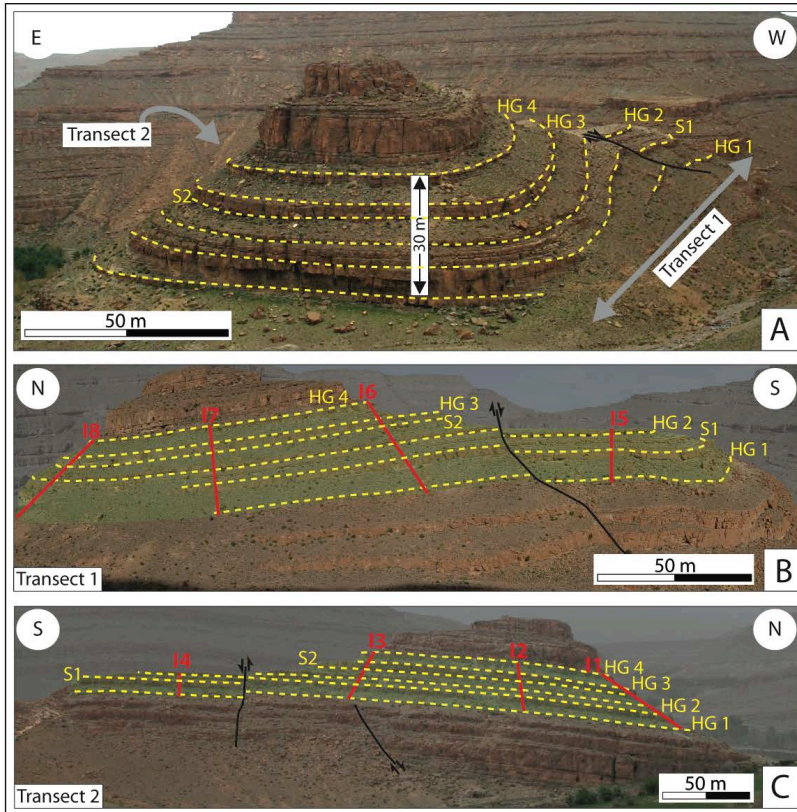
**Figure 2.2: Stratigraphic setting of the study area (south margin of the High Atlas mountains) during the Lias and Dogger (Milhi et al., 2002; Pierre, 2006). Compilation of previous studies in the region: ‘a’ Pierre, 2006; ‘b’ Addi, 1998; ‘c’ Addi, 2006; ‘d’ Poisson et al., 1998; ‘e’ Milhi et al., 2002; ‘f’ Crevello, 1992; ‘g’ Wilmsen and Neuweiler, 2007; ‘h’ Kaoukalaya et al., 2001; ‘i’ Blomeier and Reijmer, 1999; and ‘j’ Verwer et al., 2009.**

### 2.3. Study area

The area investigated in this study is located in the Amellago canyon, approximately 50 km southwest of the city of Rich in the High Atlas mountain range of Morocco (Figure 2.1). The outcrop consists of an isolated relief carved by fluvial erosion into a continuous exposure, 320 m long and 190 m wide, which has been nicknamed the “Island” (Figure 2.3). This configuration is ideal for description of the spatial distribution of metre-scale vertical and horizontal facies heterogeneity (Figure 2.3).

The “Island” outcrop is part of the Assoul Formation, which belongs to the Upper Carbonate Complex (Figure 2.2). The Assoul Formation is 300 m thick and comprises shallow-water deposits that prograded toward the northeastern sub-basin (Poisson et al., 1998). According to Pierre et al. (2010) and Christ et al. (2012a), the depositional profile is composed of two carbonate ramps, an ooid-free muddy ramp and an oolitic ramp, which alternate during the early transgressive and late transgressive to highstand phase of fourth-order depositional

sequences, respectively. For both ramp types, the depositional profile is composed of bioclastic and peloidal wackstone-packstone to floatstone from the inner to proximal middle ramp with the occurrence of coral-dominated bioconstructions. The biota is dominated by cyanobacteria, gastropods, corals debris, bivalves, echinoids and green algae. The distal middle to outer ramp shows alternating marl-mud with echinoids, ostracods, bivalves, brachiopods and bryozoans deposited in water depths up to -50 m (Pierre et al., 2010). In this setting, metre to hundreds of metres long bioconstructions dominated by oysters, corals, and sponges develop (Stanley, 1981; Warne, 1988; Christ et al., 2012a). The oolitic shoals develop in the shoreline and prograde toward the basin, which leads to the formation of a kilometre long lagoonal environment. Shoals form then a discontinuous barrier disconnected from the shoreline (Pierre et al., 2010). These shoal bodies are composed of cross-bedded ooid grainstone and peloidal grainstone. Oncoid rudstone is deposited within the fore-shoal and composed of micritic intraclasts, which preserve filaments of cyanobacteria (cayeuxia), ooids and peloids. Marls alternating with oolitic intraclast floatstone-rudstone occur within the back-shoal.



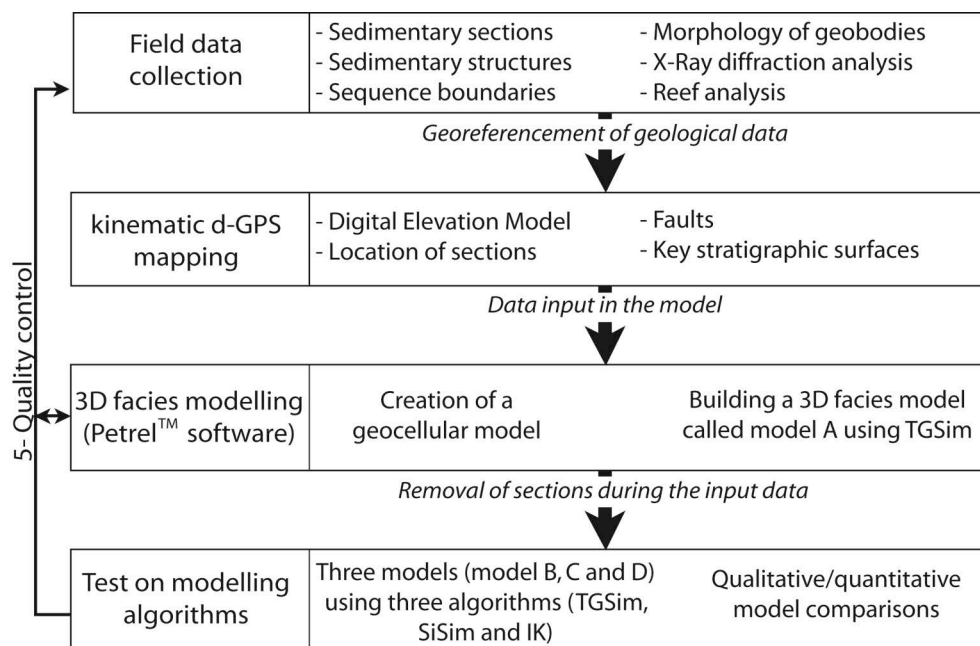
**Figure 2.3: Panoramic view of the “Island” outcrop setting, with the location of the two transects in the west (transect 1) and east (transect 2) sides of the study area. The location of the stratigraphic sections (in red), faults (in black) and small-scale cycle boundaries (dashed lines) is also illustrated. HG = hardground and S = surface.**

## 2.4. Materials and methods

The methodology used in this work combines 1) classical field data collection, 2) DPGS location of sedimentary sections, key stratigraphic surfaces and faults by using a Leica DPGS 1200 and 3) 3-D stochastic modeling by using PETREL™ software (Figure 2.4).

### 2.4.1. Field data collection

The description of the metre-scale facies heterogeneity (dimension, distribution and association) of the Assoul Formation is not well documented in previous studies (Stanley, 1981; Warne, 1988; Poisson et al., 1998; Pierre et al., 2010; Christ et al., 2012a). These data being crucial to testing algorithms, 8 densely-spaced sections (I1 to I8) were logged with an average of 3 to 4 samplings per meter. In the laboratory, 68 thin-sections were analysed in order to further characterize the sedimentary facies. The inter-well space ranges from 40 to 120 m (Figure 2.3). The study of the lateral continuity of geological bodies was carried out by using closely-spaced sections and tracing lithofacies continuity in the field. In addition, key stratigraphic surfaces (referred to as HG 1 to HG 4, S1 and S2) were recognized as small-scale cycle boundaries and were traced across the study area. The semi-quantitative analysis of grains was performed by using visual comparison charts of Flügel (2004). X-ray diffraction (XRD) was used to determine the type and proportion of clay minerals in marls.



**Figure 2.4: Workflow of the digital outcrop modeling process, from the field data to the four final 3-D facies models using three different algorithms.**



### ***2.4.2. Kinematic DPGS mapping***

The key stratigraphic surfaces, faults and locations of sedimentary sections were accurately mapped using a Leica System 1200 Differential Global Positioning System (DPGS) (Leica Geosystems AG, Heerburgg, Switzerland). Georeferenced data points acquired in the field were post-processed using recorded satellite ephemeris data, rather than real-time kinematic differential global positioning corrections which would have required radio transmission of the ephemeris data. The DPGS consisted of two single-frequency receivers GX 1210, which worked simultaneously. The first one, called “rover” was used in two different modes to collect data points. The “moving point” acquisition mode (one point per second) allowed the quick mapping of a large area with a resolution of about 0.7 m. The “static point” acquisition mode, for which the unit must remain stationary at a location for a period of time, was used to measure specific high-resolution (< 0.5 m) DPGS points, such as the top and the base of described sections. In order to map surfaces and faults, a static point was measured every 2 to 3 m and moving points were collected as the DPGS rover was carried between consecutive static points. The second DPGS receiver, called “static base station”, was mounted on a tripod at a distance of 8 km from the study window. The base station collects second-by-second satellite data corrections relative to a known reference point location, which was used for the post-processing of the data points acquired with the rover.

After the acquisition of georeferenced data, a Digital Elevation Model (DEM) was integrated in order to build the DOM. The acquisition of a high-resolution (below 1 m) DEM can be carried out using various methods such as LIDAR technology or aerial and ground-based digital photogrammetric methods (McCaffrey et al., 2005; Pringle et al., 2006). However, the combination of different GPS data sets, collected at different times or with different acquisition methods, may show an offset (vertical and/or horizontal) between one data set and another (Verwer et al., 2007; Tomás et al., 2010). In order to avoid this problem, the DEM was built using the same acquisition mode as used for the mapping of geological data. Finally, a robust and detailed DEM was created including all georeferenced data points (19838 points). It is important to highlight that the use of the same methodology for the DPGS mapping of the geological data and the DEM, allowed the creation of a coherent GPS point cloud in the whole study area and a homogeneous resolution for the GPS points.

### ***2.4.3. 3-D stochastic modeling***

All the georeferenced geological data (faults, key surfaces, sections and DEM) were input in PETREL™ to build the deterministic skeleton of the 450 m long, 350 m wide and 30 m thick 3-D geocellular model. Subsequently, the identified lithofacies are digitized for each section. The inter-well lithofacies distribution was simulated by means of a stochastic approach. The spatial lithofacies trends observed in the stratigraphic interval, the semi-variograms, the proportion of each lithofacies and the palaeocurrent measurements were used to constrain the lithofacies distribution and morphology during the modeling process. From all these data a model called “model A” was built using Truncated Gaussian Simulation (TGSim).

The quality and exposure of the outcrop allows rules to be inferred regarding the effects of modeling algorithms on the lithofacies distribution at the inter-well scale. The test consists of the removal of two out of eight sections (sections I2 and I6) during the modeling process. From the new dataset, three models model B, model C and model

D were built using three algorithms, TGSim as model A, SIS and IK respectively. Beyond the use of different algorithms, all geostatistical parameters used to constrain the spatial lithofacies distribution (vertical facies proportion and semi-variograms) remains the same. Three quantitative and qualitative comparisons were carried out between the four models. First, the estimation of the quality of each model by calculating the percentage deviation of lithofacies proportion between model and data input. Second, the comparison of vertical lithofacies distribution simulated (model B, model C and model D) and described in the field (sections I2 and I6). This type of comparison (described/simulated sections) provides insights on geological uncertainties associated with stochastic modeling at inter-well spacings. This comparison can be useful for subsurface reservoir studies where wells are the only direct access to the rock. The third one is based on a comparison of the horizontal lithofacies association between the four models. Located in two specific layers, this comparison highlights the operating mode of each algorithm in the way lithofacies are populated at inter-well spacings.

## 2.5. Lithofacies types

Ten different lithofacies (Lf) types are differentiated according to the expanded Dunham classification (Dunham, 1962; Embry and Klovan, 1971), rock composition (mainly skeletal and non-skeletal components), sedimentary structures and strata dimensions (Table 2.1). The lithofacies associations and morphologies are investigated because of their importance in modeling the geological heterogeneity (Figures 2.5, 2.6).

### ***Lithofacies 1: Greenish to Greyish Marl***

This lithofacies is characterized by thick (up to 1 m) discontinuous beds of greenish to greyish marl (Figure 2.6 D). The bioclasts are composed of centimetre-sized brachiopods and bivalve shells. Subangular to subrounded micritic intraclasts are present. Terrigenous sediments occur (up to 25% of marl) and are composed of illite, smectite and quartz.

### ***Lithofacies 2: Bioclastic Mudstone to Wackestone with interbedded Marly Limestone***

This lithofacies consists of decimetre tabular bioclastic peloidal mudstone to wackestone beds alternating rhythmically with greenish to greyish marls (Figure 2.5; A1). Marl beds vary in thickness from 0.1 m to 0.5 m (Table 2.1). The greenish marly sediment is composed of 15 to 20% of terrigenous sediments (illite, smectite, and quartz) and contains micritic intraclasts, black pebbles and peloids (Figure 2.5; A2). Mudstone to wackestone beds show bioclasts of ostracods, echinoderms and rare thin-shell bivalves (Figure 2.5; A3). On the top of each bed, a soft to firmground with abundant *Thalassinoides* burrows is recognized. No other sedimentary structures are observed.

### ***Lithofacies 3: Bioclastic Ferruginous Peloidal Wackestone-Packstone***

Lf 3 consists of decimetre-scale tabular and irregular beds, which are interbedded with thin marly beds (Figure 2.6A). The biota association (up to 40% of the components) is mainly composed of echinoid spines, bryozoans, brachiopods, oysters, bivalves and crinoids (Figure 2.5; A6). Gastropods, coral debris and cyanobacteria are rare. The reddish peloids (20 to 40% of the components), characterized by the presence of iron oxides, are sub-angular to sub-rounded. No sedimentary structures are recognized.

***Lithofacies 4: Bioclastic Peloidal Wackestone to Wackestone-Packstone***

Bioclastic peloidal wackestone to wackestone-packstone occur in medium to highly bioturbated tabular beds ranging in thickness from 0.2 up to 3 m. The bioclasts (up to 30% of the components) are sometimes micritized and mainly composed of gastropods, bivalves, brachiopods, textulariid foraminifera and cyanobacteria products (*Cayeuxia* and *Rivularia*). Echinoderms, coral debris, green algae and calcareous sponge spicules also occur. Sub-rounded peloids (up to 15% of the components) and oncoids are present. No sedimentary structures are recognized.

***Lithofacies 5: Peloidal Bioclastic Wackestone-Packstone to Packstone***

Forming beds of 0.3 to 3.5 m thick (Figure 2.6B), medium to highly bioturbated, Lf 5 contains sub-rounded to rounded peloids and micritic intraclasts (up to 60%) (Figure 2.5; B3). Millimetre- to centimetre-sized, sometimes micritized, bioclasts (up to 15%) also occur and are mainly composed of cyanobacteria, gastropods, bivalves and echinoderms. Green algae, bryozoans and textulariid foraminifera are also present and oncoids are frequent. Bioclasts are encrusted by microbialites, bryozoans and cyanobacteria (Figure 2.5; B4). No sedimentary structures are recognized.

***Lithofacies 6: Bioclastic Floatstone***

From 5 to 70 cm thick (Figure 2.5; B1), the bioclastic floatstone is composed of centimetre-sized skeletal components (around 30%) of gastropods, coral debris, bivalves and brachiopods, which are partially micritized (Figure 2.5; B2). Large cyanobacteria (up to 3.6 mm) also occur. Bioclasts are encrusted by microbialite and bryozoan. Except for the occurrence of centimetre-sized bioclasts, Lf 6 has a similar composition to Lf 4. No sedimentary structures are recognized.

***Lithofacies 7: Peloidal Oolitic Packstone-Grainstone***

0.2 to 3 m thick, well-sorted peloidal oolitic packstone-grainstone (Figures 2.6C, 2.6E) is mainly observed in the middle portion of the studied sections. The peloid size (0.2 to 0.5mm) and uniform shape (rounded to sub-rounded) suggest a faecal origin (Figure 2.5; C2, C5). Ooids displaying few fine radial laminae are present in variable proportions (up to 35%) whereas radial ooids are rare. The nuclei of the ooids are mainly peloids and textulariid foraminifera. No sedimentary structures are recognized, probably due to bioturbation shown by *Thalassinoides* burrows.

***Lithofacies 8: Oolitic Skeletal Grainstone***

Lf 8 shows bed thicknesses from 0.1 to 1.4 m (Figures 2.6C, 2.6D, 2.6E). The facies comprises ooids with a cortex formed by fibrous radial laminae and lesser amounts by laminated fine-radial crystals with a low nucleus-to-cortex ratio (Figure 2.5; C4). Ooids characterized by coarse radial cortices are also present. The nuclei of the ooids are mainly peloids and textulariid foraminifera. Micritized and composite ooids are also observed. Occasionally, oolitic intraclasts (up to 1 cm) and rip-up clasts are recognized. Bioclasts also occur and are composed of gastropods and bivalve debris. Toward the top of the study window, the lithofacies becomes locally poorly sorted with an increase in micrite and oolitic intraclasts (up to 20%). Cross-bedding with 2-D and 3-D bidirectional ripples oriented 45°N are observed and measured in the southern part of the outcrop.



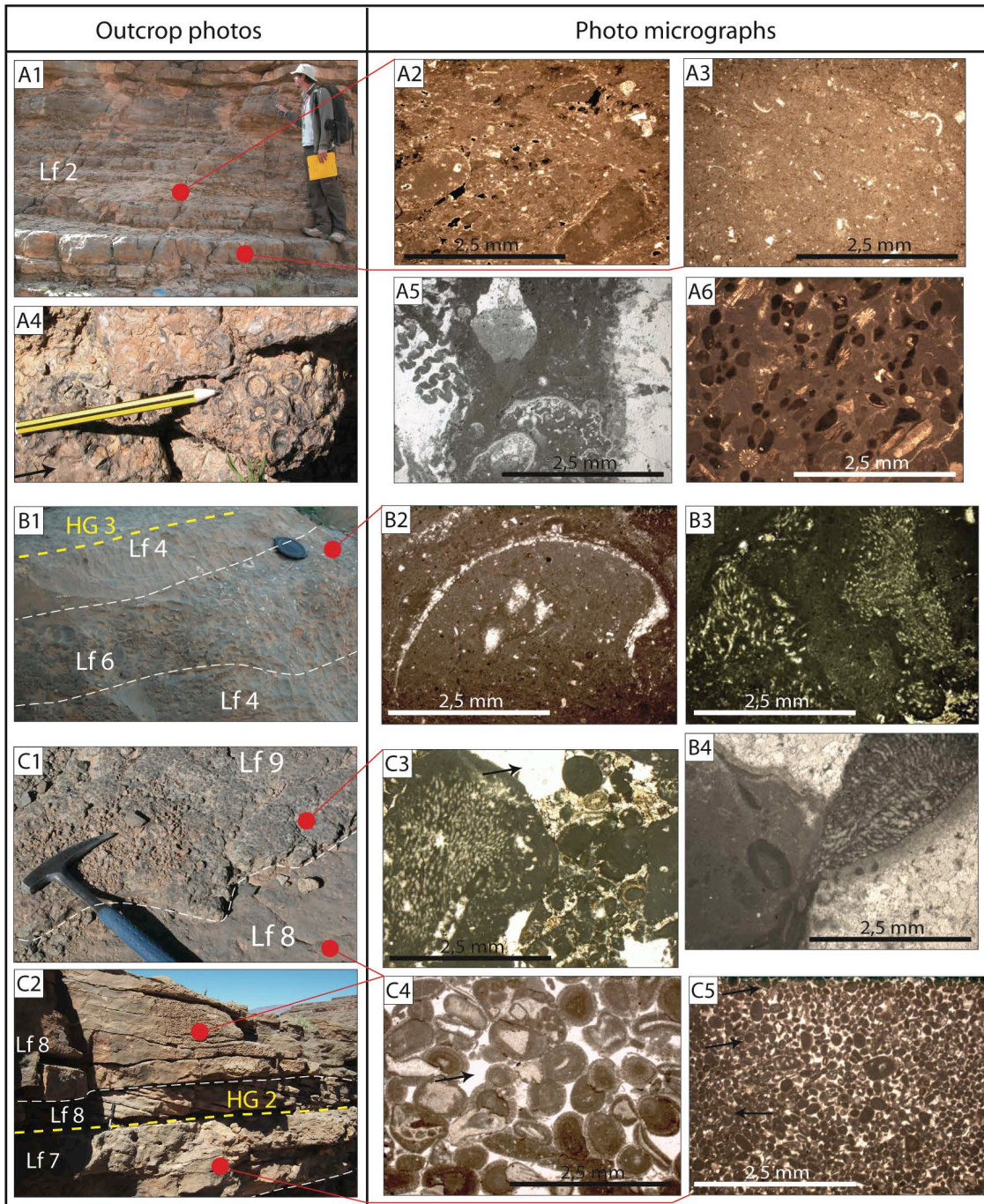


Figure 2.5: Outcrop photos and photo micrographs of the main lithofacies types of the distal middle to outer ramp (A), proximal middle ramp (B) and inner ramp (C). Note the morphological contrasts between geological bodies. A1. Outcrop photo of mud-marl alternations of Lf 2 located at 3 m in section I1. A2. Photo micrograph of marl with micritic intraclasts located at 4 m in section I1. A3. Photo micrograph of bioclastic mudstone to wackestone with ostracod shells located at 2.3 m in section I1. A4. Outcrop photo of the oyster-dominated bioconstruction showing *in situ* oysters located at 23 m in section I2. Note the occurrence of platy scleractinian corals (black arrow) (12 cm long pencil for scale). A5. The two other components of the bioconstruction (Lf 10), scleractinian corals and sponges located at 20.2 m in section I3. A6: Photo micrograph of lithofacies Lf 3 with ferruginous peloids and echinoid debris located at 19.9 m in section I3. B1. Outcrop photo of lithofacies Lf 6 located at 19.6 m in section I2 (5.1 cm lens cap for scale). B2: Photo

micrograph of lithofacies Lf 6 showing bioerosion of bioclasts and located at 20.9 m in section I6. B3. Photo micrograph of peloidal bioclastic packstone (Lf 5) with cyanobacteria located at 8.1 m in section I1. B4. Photo micrograph of the three main encruster features (bryozoan, cyanobacteria and microbialite) located at 26 m in section I8 and observed across the entire study window. C1 and C2. Outcrop photo of the three main lithofacies of the inner ramp located around 11 m in section I4 (33 cm long hammer for scale). C3. Photo micrograph of microbial rudstone (Lf 9) with millimetre- to centimetre-sized cyanobacteria intraclasts and located at 7.2 m in section I4. Note the infilling of porosity by blocky calcite (black arrow) and the occurrence of ooids. C4. Photo micrograph of oolitic grainstone (Lf 8) with blocky cement (black arrow) located at 11.2 m in section I4. Note the thin cortical fabric compared to the nuclei (superficial ooids). C5. Photo micrograph of peloidal packstone-grainstone (Lf 7) showing the homogeneous size of peloids and located at 10.5 m in section I4. The porosity is filled by blocky cement. Note the occurrence of small superficial ooids (black arrows). Lf = Lithofacies.

### ***Lithofacies 9: Microbial Rudstone***

This lithofacies is composed of rounded to ovoid 2 to 9 mm long micritic intraclasts (up to 60% of the components), which often preserve filaments of cyanobacteria (*Cayeuxia*, *Rivularia*, *Garwoodia*) (Figure 2.5; C1 and C3) and occurs in 60 cm thick beds. Lf 9 is also composed of peloids, ooids, gastropods, textulariids foraminifera, undetermined molluscs and echinoderms. Bivalves and bryozoans are rare. Large lituolinid foraminifera (Flügel, 2004) are also observed. No sedimentary structures are recognized.

### ***Lithofacies 10: Reefal Facies***

Located in the upper part of the section, a biostrome, 2 to 3 m thick and 150 m long (Figure 2.6A), consists of a heterozoan-photozoan association of oysters-brachiopods-corals-sponges growing above a hardground (Figure 2.5; A5). Oysters occur in growth position and are the main framebuilders; the oyster shells (2 to 4 cm long) are found cemented to each other (Figure 2.5; A4). Scleractinian corals (*Complexastrea*, *Dendrorea*, *Cladophyllia* and *Stylosmilia*), which are locally abundant correspond to the typical composition of Lower Bajocian reef communities (Lathuilière, 2000a, b). Calcareous and siliceous sponges are also observed. Oyster shells and corals are encrusted by microbialites, bryozoans and cyanobacteria. The inter-reefal facies vary from centimetre-size bioclastic floatstone-rudstone to bioclastic peloidal wackestone-packstone. The bioclasts are similar to those observed within the reefal facies. The local deposition of silty marl sediments is observed throughout the biostrome.

Locally, smaller-size patch reefs (1 m long and 0.6 m high) are also found in association with the oolitic shoals (Lf 5) (Figure 2.6D). In this particular setting, the reefal facies is mainly composed of branching corals (*Cladophyllia* and *Stylosmilia*) and only a low percentage of oysters is observed.

**Table 2.1: Descriptions and depositional environment interpretations of the ten lithofacies observed within the Assoul Formation, High Atlas, Morocco.**

Lf code	Lithofacies (Lf)	Texture	Skeletal and non-skeletal components	Dimensions used for modeling (m)	Sedimentary features	Depositional environment
Lf1	Greenish to greyish marl	m	Brachiopods, bivalves Subrounded micritic intraclasts Up to 25% of clastic sediments	Thickness: 0.3 to 1 Length: 100	Interbedded with oolitic grainstone (Lf8)	Inner Ramp
Lf2	Limestone and interbedded marl	m/Ms	Ostracods, echinoderms, bivalves. Subrounded micritic intraclasts. From 15 to 20% of clastic sediments	Thickness: 0.1 to 0.5 Length: 150	Low to medium bioturbation. Rhythmic clastic input. 1 to 2 m long bioconstructions (Lf10)	Distal middle to outer ramp
Lf3	Limestone and interbedded marl	m/Ps	Echinoids, brachiopods, crinoids. Ferruginous peloids	Thickness: 0.1 to 1 Length: 150	Low to medium bioturbation. Rhythmic clastic input Hundreds of metre long bioconstructions (Lf10)	Distal middle to outer ramp
Lf4	Bioclastic limestones	Ws/ Ws-Ps	Bivalves, cyanobacteria, gastropods, corals, green algae, sponge spicules Oncoids, peloids	Thickness: 1.1 to 3.5 Length: 150	Low to high bioturbation	Proximal middle ramp
Lf5	Peloidal limestones	Ws-Ps	Cyanobacteria, gastropods, bivalves, echinoderms, bryozoans, green algae Peloids	Thickness: 0.3 to 3.5 Length: 150	Medium bioturbation	Proximal middle ramp
Lf6	Bioclastic limestones	Fs	Gastropods, corals, bivalves, brachiopods, cyanobacteria. Oncoids, peloids.	Thickness: 0.05 to 0.7 Length: 70	Micritization Encrustation of bioclasts	Proximal middle ramp
Lf7	Peloidal oolitic limestones	Ps-Gs	Peloids, ooids. Peloids, foraminifera as nucleus	Thickness: 0.2 to 3 Length: 150	Cement: crystals of sparite	Inner ramp
Lf8	Oolitic limestones	Gs	Bivalves, gastropods, foraminifera Ooids, composite ooids, intraclasts Peloids, foraminifera as nucleus	Thickness: 0.1 to 1.4 Length: 150	Cross-bedding, ripples Sutured contact, brittle deformation. Cement: crystals of sparite	Inner ramp
Lf9	Micritic nodule limestones	Fs-Rs	Cyanobacteria, gastropods, echinoderms Peloids, ooids, intraclasts	Thickness: 0.1 to 1 length: 90	Cement: crystals of sparite	Inner ramp
Lf10	Molluscan-coral-sponge limestones	Bs	Oysters, brachiopods, bivalves, corals, calcareous and siliceous sponges Local marl deposits	Thickness: 0.7 to 3 Length: 150	Encrustation by microbialite, bryozoans, cyanobacteria	Distal to outer ramp

## 2.6. Depositional environments

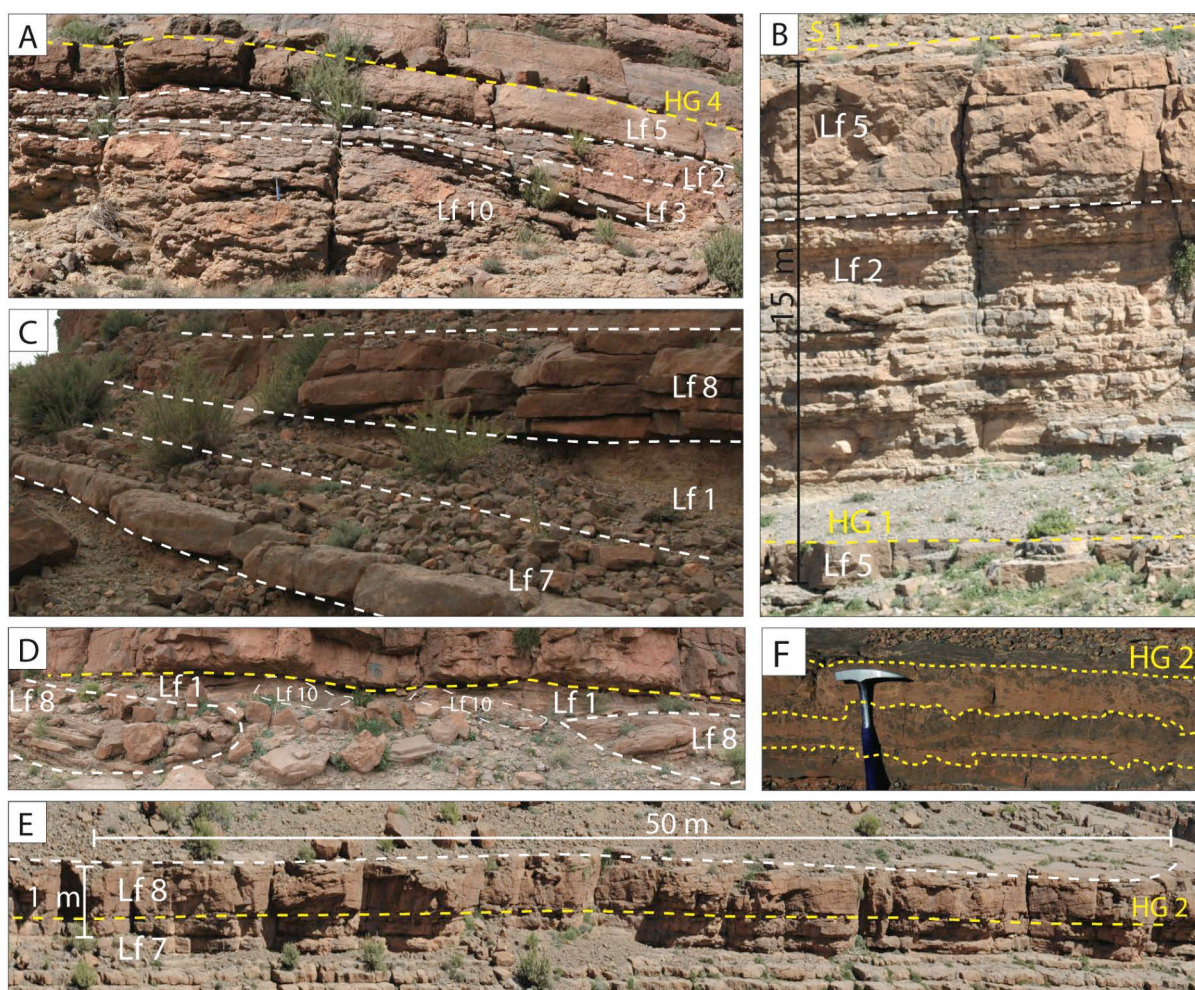
The lithofacies data collected in the present study (texture, organic and inorganic components, bioturbation, sedimentary structures and numerous condensed surfaces) indicate a shallow-water depositional environment mainly dominated by low energy conditions. The overall low hydrodynamic level is indicated by the common lack of sedimentary structures, the occurrence of several mud-dominated lithofacies and the predominance of radial cortical fabric within ooids. By analysing the microfacies and spatial distribution of the 10 lithofacies described above, three main depositional environments are identified: an inner ramp setting located above the Fair Weather Wave Base (FWWB) and mainly characterized by high energy grain-supported lithofacies, a proximal middle ramp environment composed of mud-supported lithofacies with semi-restricted and open marine mixed biota association and a distal middle ramp to outer ramp setting with mud-marl alternations (Figures 2.7A, 2.7B). A palaeoenvironmental reconstruction of the carbonate ramp is carried out in Figure 2.8. The description of the cycles and sequences identified in Figures 2.7A and 2.7B is given in Section 7.

The mud-marl alternations of Lf 2 and Lf 3 are composed of debris of echinoderms, bryozoans, ostracods and brachiopods that suggest low energy and marine conditions during the time of deposition. Lf 2 and Lf 3 were likely deposited in a distal middle ramp to outer ramp setting. Three lines of evidence suggest transport of clastic sediments from continental to marine areas. First, XRD analysis on Lf 2 and Lf 3 highlight the deposition of quartz, illite and smectite derived from the continent. Second, the presence of ferruginous peloids within Lf 3 could be explained either as a result of the erosion and transport of Fe-rich soil from continental areas (Germann et al., 1994) to the carbonate system or as the result of *in situ* iron precipitation (Young, 1989; Burkhalter, 1995). The absence of iron oxides within the micritic matrix of Lf 3 (Figure 2.5; A6) suggests an allochthonous origin for the ferruginous peloids. Third, the occurrence of 1 to 100 m wide oyster-dominated build-ups (Lf 10) within the mud-marl alternations indicates turbidity in the water column (Johnson et al., 2007) likely associated with the influx of terrigenous sediments as shown by the occurrence of local marly deposits within the bioconstruction. The distal middle to outer ramp environment also records periodic high energy conditions shown by the presence of reworked sediments (micritic intraclasts) in Lf 2 and probably due to storm or high tide events. The occurrence of bioclastic floatstone-rudstone (bioclasts up to 8 cm) in the inter-reef areas reflecting short and energetic events is in agreement with this interpretation.

Within mud-dominated lithofacies (Lf 4, Lf 5 and Lf 6), the mix between cyanobacteria, gastropods, green algae, oncoids and echinoderms, coral debris, sponge spicules and brachiopods suggests semi-restricted conditions with an open marine influence. The mix between both biota assemblages is explained by the palaeogeography of the margin at the time of deposition. During the Middle Jurassic, the south margin of the High Atlas rifting basin is composed of rhomb-shaped sub-basins bounded by syndepositional ridges (Poisson et al., 1998; Laville et al., 2004). In this context, sub-basins are characterized by a decrease in water circulation and oxygenation compared to the topographic highs (Stanley, 1981; Ait Addi, 2006). Bioclastic floatstones (Lf 6) occur at the top of depositional packages, probably as the result of winnowing during period of low accommodation (Wilmsen et al., 2010; Christ et al., 2012a). The occurrence of condensed surfaces above Lf 6 and the intense bioerosion of bioclasts (micritization



and encrustation features) are in agreement with this interpretation. The three lithofacies (Lf 4, Lf 5, and Lf 6) are likely deposited in a proximal middle ramp setting.



**Figure 2.6:** Field pictures showing examples of dimension, morphology and lithofacies association observed in the field. A. Morphology of the oyster-dominated bioconstruction (Lf 10) located around section I1 and overlain by a condensed surface (HG 4). Note the lateral continuity of Lf 2 and Lf 5 whereas Lf 3 shows thickness variability (33 cm long hammer for scale). B. Located in section I8, significant thickness variability between thick Lf 5 beds and alternating thin beds of Lf 2 occurring in cycle 1. C, D (located between sections I2 and I3) and E (located in section I6). Lithofacies association and morphological features of the inner ramp (33 cm long hammer for scale). Note the well-bedded and continuous Lf 7 (C and E) whereas Lf 8 shows various morphologies from discontinuous and curved (C and D) to tens to hundreds of metres long beds (E). F. Erosive features on condensed surfaces (HG 2) showing reworked micritic clasts and located in section I4. Note the occurrence of multi-generation erosive surfaces (dashed line) (33 cm long hammer for scale).

The grain-supported lithofacies (Lf 7, Lf 8 and Lf 9) showing sedimentary structures (ripples and cross-beddings) indicate an active shoal belt located above and around the FWFB and are then deposited in an inner ramp setting. However, three lines of evidences suggest generally moderate energy conditions prevailed with only periodic high energy pulses. First, the predominance of radially structured ooid cortices with a general low nucleus-

to-cortex ratio within Lf 7 and Lf 8, suggests moderate energy conditions (Figure 2.5; Strasser, 1986). Second, the local micritization of ooids suggests early lithified and stabilized shoal areas. Third, Lf 7 characterized by the predominance of peloids and superficial ooids, is likely deposited under moderate to high energy conditions depending on the proportion of ooids/peloids. The Lf 9 is composed of rounded millimetre-sized micritic intraclasts (up to 8 mm), which often preserve filaments of cyanobacteria, ooids and peloids (Figure 2.5; C3). The absence of micrite in Lf 9 and the rounded shape of micritic intraclasts suggest that cyanobacteria has been transported from a mud-dominated environment, probably the proximal middle ramp. In addition, the texture of Lf 9 and the presence of centimetre-sized micritic intraclasts and ooids indicate shallow-water and relatively high energy conditions during deposition (Mancinelli and Ferrandes, 2001). This evidence suggests that Lf 9 is deposited within a fore-shoal environment at the transition between the middle and inner ramp. The location of Lf 9 (Figure 2.7A) suggests also the influence of both, the proximal middle ramp (Lf 4, Lf 5 and Lf 6) and the inner ramp (Lf 7 and Lf 8). Locally, discontinuous greenish to greyish marl (Lf 1) deposits are interbedded with oolitic grainstone (Lf 8), which shows an increase in oolitic intraclasts and micrite content. The marl deposits contain the higher amount of continental sediments compared to other lithofacies (25% of illite, smectite and quartz) indicating significant influence of the land. Alternating high and low energy lithofacies within an oolitic inner ramp is characteristic of an inter-shoal to back-shoal environment.

## 2.7. Depositional cycles and sequences

The environmental interpretation based on lithologies and bedding patterns provides the basis for the identification of stacking patterns of facies and depositional cycles and their hierarchy. The cycles were correlated between sections by walking along key facies boundaries in the field (Figures 2.7A, 2.7B). The stacking pattern displays small and medium-scale depositional events. The small-scale cycles (few metres) are the building blocks of larger, medium-scale sequences (few metres to tens of metres). The medium-scale sequences described in this paper and part of the Assoul Formation coincide in terms of sequence thickness with those identified by Pierre et al. (2010) in their regional study on the Amellago Formation and referred to as small-scale sequences.

### 2.7.1. *Medium-scale sequences*

Two medium-scale sequences, one complete (sequence A) and one incomplete (sequence B), are recognized in the “Island” stratigraphic window and are discussed in this paper (Figures 2.7A, 2.7B). These sequence boundaries correspond to the most significant turning point in facies and depositional environment, recording the change from inner to distal middle ramp. These surfaces are abrupt and characterized by marine cementation, multi-generation borings, microencrustations and are interpreted as hardgrounds. These surfaces do not show any evidence of subaerial-exposure related features (vadose or phreatic meteoric diagenesis) in the field and thin-section (Christ et al., 2012a). Erosional features such as reworked mudclasts and erosive depressions (Figure 2.6F) are frequent at the top of the depositional sequences. This evidence suggests that the sequence boundaries are explained by periods of relative sea level fall. During the relative sea level fall, the sea floor was exposed to wave and current action.

However, the amplitude of relative sea level fluctuation does not allow for sub-aerial exposure of the sea floor. For a more detailed description please refer to Christ et al. (2012a).

The medium-scale sequence A is from 17 m (section I3) to 21 m (section I8) thick. Its lower sequence boundary coincides with a continuous hardground (HG 1) characterized by iron-staining, bore holes, organism encrustation (corals, oysters, and bivalves) and erosional features. The transgressive phase is characterized by the deposition of mud-marl alternation (Lf 2) with 0.5 to 2 m long oyster-dominated bioconstructions (Lf 10). Because of the lack of evidence of a maximum flooding surface, a maximum flooding interval is assigned to the thicker marl interval. The highstand phase is characterized by two distinct phases. First, a thickening-upward trend of beds is observed by the occurrence of 2 to 3.5 m thick wackestone to packstone (Lf 5) beds. The second phase is the deposition of microbial rudstone and peloidal packstone-grainstone (Lf 9 and Lf 7) overlain by cross-bedded oolitic grainstone (Lf 8). The sequence A records a progressive transition from the distal to proximal middle ramp and to the inner ramp. At the top of sequence A, a hardground HG 3 delimits an abrupt environmental change from inner to outer ramp. This surface displays encrustation features of bivalves, oysters and corals, erosional features (reworked mudclasts, erosional depressions), iron precipitation, abundant bioclasts of gastropods, bivalves, coral debris and multi-generation bore-holes. This line of evidence suggests that HG 3 represents a significant stratigraphic boundary and a long-term omission period and is then interpreted as a medium-scale sequence boundary. Similar to the sequence A, the sequence B is incomplete and only the onset of the deepening-upward trend is observed by the growth of oyster-dominated bioconstruction (Lf 10) on surface HG 3 and overlain by mud-marl alternations (Lf 2 and Lf 3). The occurrence of iron from Lf 3 is likely the result of the erosion and transport of Fe-rich soil from continental areas (see above) during the transgressive phase.

### ***2.7.2. Small-scale cycles***

Five small-scale cycles, 1 to 5, are defined. The sequence A comprises four small-scale cycles (cycle 1, 2, 3 and 4) whereas the incomplete sequence B comprises one small-scale cycle (cycle 5). Except for the surface S2 (Figure 2.7A), the small-scale cycle boundaries show similar features (reworked clasts and erosive depressions) as medium-scale sequence boundaries (Figure 2.6F). However, small-scale cycle boundaries toward the base of the sequence A are less expressed due to periods of high accommodation, which tend to reduce the erosive effect of the wave and current action on the sea floor (Christ et al., 2012a). Cycle 1, ranging in thickness from 5.9 m (section I4) to 7.5 m (section I1), has a lower boundary coinciding with the medium-scale sequence boundary (HG 1). A 1 m thick deepening-upward trend is recorded by a thickening-upward of marl beds. The shallowing-upward unit is expressed by the transition from Lf 2 to Lf 5, which shows an upward increase in encrustation and micritization features as well as oncoids and cyanobacteria (*Cayeuxia* type) and culminates with grain-supported lithofacies (Lf 9). This vertical trend records a transition from distal to proximal middle ramp. The upper cycle boundary (S1) is a poorly expressed firmground showing few reworked micritic clasts and bioclasts.



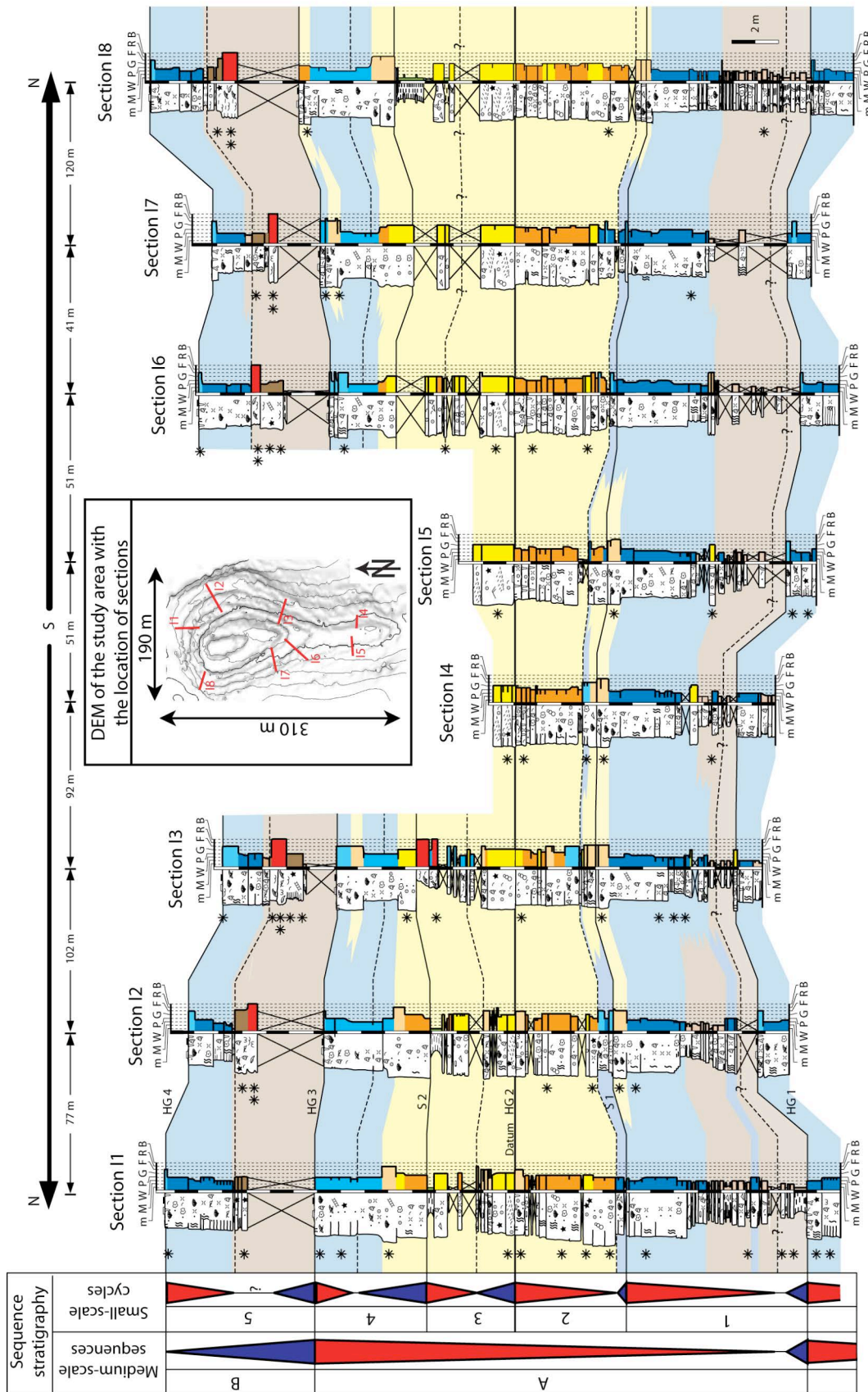



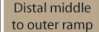








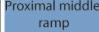




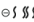


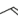
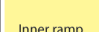


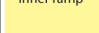



Figure 2.7A: Stratigraphic correlation of the study window based on physical tracing of the beds in the field showing vertical stacking of small- and medium-scale depositional packages.



Lithofacies types and environmental interpretations		Key to Symbols	
Distal middle to outer ramp	 Biocalstic Ws with interbedded marls (Lf.2)	 Intraclasts	 Coral, coral debris
	 Biocalstic ferruginous peloidal Ws to Ps with interbedded marls (Lf.3)	 Sponges, sponge debris	 Echinoderms
	 Oyster-coral Bs (Lf.10)	 Foraminifera	 Ostracods
Proximal middle ramp	 Biocalstic peloidal Ws to Ps (Lf.4)	 Brachiopods	 Green algae
	 Peloidal biocalstic Ps (Lf.5)	 Burrows	 <i>Thalassinoides</i>
	 Biocalstic Fs (Lf.6)	 Bioturbation (undiff.)	 Cross-bedding
Inner ramp	 Greenish to greyish marl (Lf.1)	 Sequence boundary	 Ripples
	 Peloidal ooidal Ps to Gs (Lf.7)	 mfs/mfi (maximum flooding surface/interval)	 Thin-section analysis
	 Ooidal Gs (Lf.8)		
	 Oncoidal Fs-Rs (Lf.9)		

**Figure 2.7B: Legend of Figure 2.7A showing the lithofacies, associated depositional environments and symbols used.**

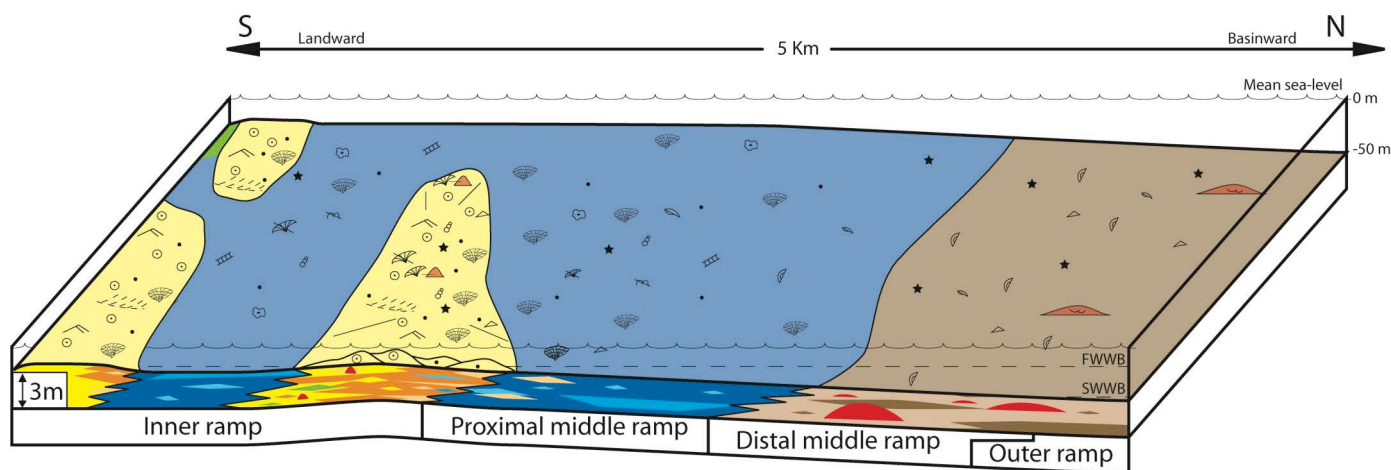
Cycle 2 ranges in thickness from 3.4 m (section I3) to 5.5 m (section I8). The deepening-upward trend is recorded by a vertical transition from grain-supported (Lf 7 and Lf 9) to mud-dominated lithofacies (Lf 5 and Lf 6). In section I5, I6 and I7, the maximum flooding surface is shown by the occurrence of 5 to 20 cm thick discontinuous marly beds. The upper part of the cycle consists of Lf 7 interbedded with thin beds of Lf 8, which sometimes show cross-bedding. The shallowing-upward trend is expressed by a clear increase in the proportion of ooids (up to 35% at the top) from the base to the top of the cycle. The cycle 2 shows the progradation of grain-supported lithofacies of the inner ramp setting. The upper cycle boundary (HG 2) is a hardground, which displays numerous *Thalassinoides* burrows with sharp borders, abundance bioclasts of gastropods, coral debris and bivalves and rare and located iron precipitation.

Cycle 3, ranging in thickness from 3.7 m (section I1) to 5.1 m (section I8), has a lower boundary coinciding with a hardground (HG 2), overlain by an oolitic shoal (Lf 8). At the top of the cycle, the shoal (Lf 8) is interbedded with Lf 1 beds (up to 1 m). Locally, the Lf 8 shows the occurrence of oolitic intraclasts. This alternation indicates an inter-shoal or back-shoal environment. The upper cycle boundary (S2) is a transgressive surface characterized by a sharp transition from marly sediments (Lf 1) of back-shoal environment to grain-supported lithofacies (from Lf 7 to Lf 9) deposited within the shoal complex.

Cycle 4 ranges in thickness from 2.9 m (section I6) to 4.6 m (section I1). The deepening trend is recorded by a transition from Lf 7, Lf 8 and Lf 9 (inner ramp) to Lf 4 (proximal middle ramp). The maximum flooding surface is shown by a progressive decrease in bioclasts up to a 0.5 m thick interval composed of millimetre-sized undetermined bioclasts and gastropods debris at the middle of the cliff. The shallowing-upward unit is characterized by the occurrence of centimetre coral and gastropod debris as well as oncoids (Lf 4 and Lf 6) and overlain by a medium-scale sequence boundary (HG 3).

Cycle 5, ranging in thickness from 4.5 m (section I3) to 6.3 m (section I8), has a lower boundary coinciding with a hardground (HG 3). This condensed surface is overlain by a 2 to 3 m thick oyster-dominated bioconstruction (Lf 10), which grows on the top of a hard substrate. Due to the absence of clear evidence, the maximum flooding surface is assigned to the occurrence of Lf 2. The shallowing-upward unit shows a vertical change from Lf 10 and Lf 3

(distal middle to outer ramp) to Lf 5 and Lf 6 (proximal middle ramp) as recorded in cycle 1. The cycle 5 is bounded at the top by a hardground (HG 4), which displays numerous bioclasts of gastropods, coral debris, bivalves and oysters, bore holes and local iron precipitation.



**Figure 2.8:** Tentative of palaeoenvironmental reconstruction of the Bajocian carbonate ramp. A five kilometres long plan view represents the depositional environments and distribution of the main organic and inorganic lithofacies components. A 3 m thick vertical transect shows the spatial lithofacies heterogeneity observed in the field and modeled in this study. (for legend of Lf colours and symbols see Figure 2.7B).

## 2.8. 3-D stochastic models using PETREL™

The second aspect of this study is building four metre-scale 3-D facies models that are model A, model B, model C and model D. A specific modeling methodology was used to generate these four different models and is explained below. The detailed sedimentological study described above provided an understanding of the spatial lithofacies relationships and therefore provided a reference against which to judge the results of the various stochastic modeling algorithms. The dual aim of these 3-D models was to 1) test the effect of different algorithms on spatial facies distribution between control points and 2) provide rules for modeling shallow-water carbonates rocks. Each step of the workflow leading to the building of the digital outcrop model is described below.

### 2.8.1. Key surfaces

In order to create a DOM that was as reliable as possible, the six horizons used for the generation of zone boundaries were the six small-scale cycle boundaries (see above) (Figures 2.7A, 2.9B). These key surfaces were physically traced and mapped by using a DPGS system and located on the digitized stratigraphic sections as well. This methodology allowed the modeling of each small-scale cycle (cycle 1 to cycle 5) separately. Two types of surfaces were used to generate the deterministic skeleton framework of the 3-D models. The first surface type was the DEM, which used all of the GPS points collected in the field (19838 points). The minimum curvature algorithm with a grid node spacing of 1.5 x 1.5 m was used to construct the DEM. The second type of surface included stratigraphic horizon grids representing the elevations of the small-scale cycle boundaries. Also, two post-

depositional normal faults were described in the south part of the outcrop but only one occurred in the modeled area (Figures 2.3, 2.9A). This fault, a 3 m vertical displacement, was mapped in the field and input as gridded surfaces into PETREL™ using “Pillar gridding” process.

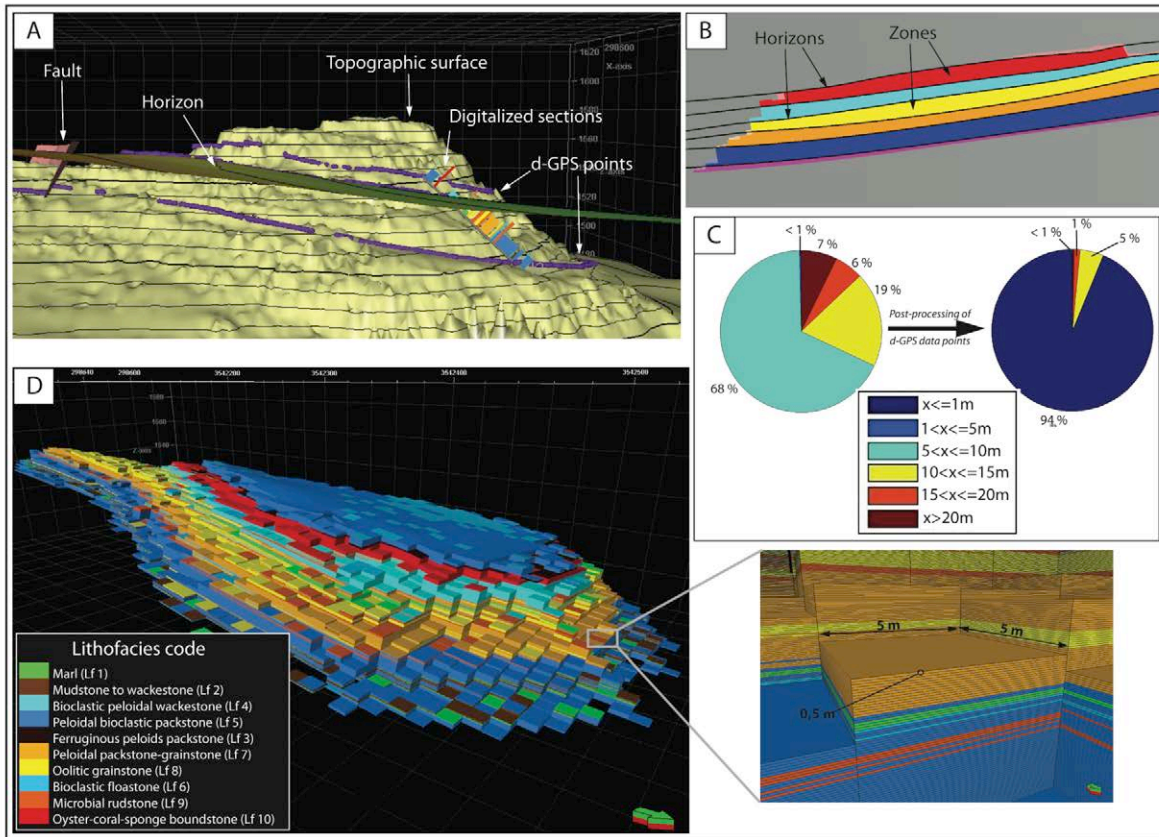
### ***2.8.2. Geocellular model***

In order to correctly model distribution and morphology of geological bodies, the modeled area was slightly extended outside the studied area. The dimensions of the geocellular model are 450 m long, 350 m wide and 30 m thick. To define the size of the cells forming the model, the first consideration was the size of the smallest geological features, which needed to be resolved in the final model. The cell plan-view dimensions need to be small enough to reflect the horizontal facies variation observed in the study window and the cell vertical-view dimension must be small enough to preserve the observed vertical facies variability. In order to properly capture the horizontal and vertical facies distribution, cells should be no larger than half the dimensions of these smallest resolvable geological features observed in the field (Fabuel-Perez, 2008). For this work, the smaller horizontal variations in dimensions are observed in the microbial rudstone (Lf 9), which are about 10 m. Then, the final horizontal dimensions chosen for each cell are 5x5 m. The vertical dimensions (Z) of the cells are defined by the thinnest modeled geological bodies, which are the mudstone and marl beds included in the Lf 2 with a thickness of approximately 0.1 m. Thus, to preserve these features the average thickness for the cells needs to be 0.05 m. The model contains a total of 30844836 3-D cells whose average dimensions are 5 x 5 x 0.05 m (X, Y, Z) (Figure 2.9D).

### ***2.8.3. Integration of sedimentological data into PETREL™***

Before creating a facies model, six cycle boundaries, one fault and height georeferenced sections (Figures 2.7A, 2.9) were input into model A to serve as initialized control points for the next stochastic modeling steps. During later processes, the building of three additional models, model B, model C and model D was carried out by removing sections I2 and I6 from data input. In other words, these three additional models were built using the same input data from only six of the eight sections (sections I1, I3, I4, I5, I7 and I8). Despite the removal of two sections as initial conditioning for the facies modeling, there was still a fairly homogeneous spatial distribution of the sections across the model area. The removal of sections I2 and I6 allowed a vertical lithofacies comparison between sections described in the field and built by stochastic simulation. This test provided a direct access to document geological uncertainties associated with stochastic simulation at inter-well spacings.

The lithofacies code input into models was identical to the lithofacies classification (see above) except for greenish to greyish marls (Lf 1) and bioclastic mudstone to wackestone with interbedded marly limestone (Lf 2). For the purpose of the present DOM study, all marly beds from the greenish to greyish marl and from the bioclastic mudstone to wackestone with interbedded marly limestone were grouped into Lf 1. Then, Lf 2 represents bioclastic mudstone to wackestone beds and all other lithofacies codes remained the same during simulation (Figure 2.9D).

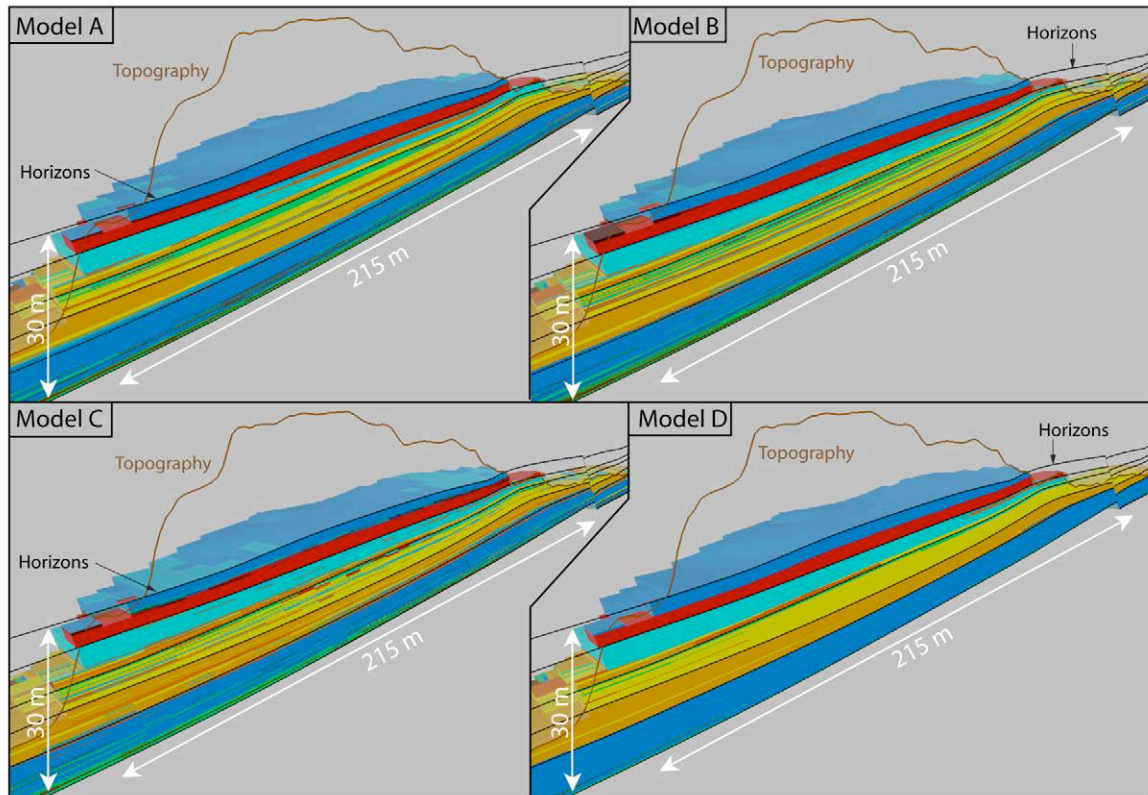


**Figure 2.9:** Major steps for building the 3-D facies model. **A.** Compilation of the three types of georeferenced data (horizons, fault and digitalized stratigraphic sections) used to build the deterministic skeleton of the model. The DPGS points (in purple) represent the points acquired during the mapping of the key stratigraphic surfaces. **B.** 2-D intersection plane of the study outcrop showing the five created zones delimited by the horizons. Each zone corresponds to a small-scale depositional cycle. **C.** Post-processing of the acquired DPGS points. Note the improvement of the accuracy of DPGS points <1 m from 68% before (left) to 94% after (right) the processing of the data. **D.** 3-D view of the geocellular facies model called model A, generated using the TGSim algorithm. Close-up view of the cell dimensions chosen to best represent the morphology of the modeled geological bodies (5x5x0.5 m - x, y, z).

#### 2.8.4. 3-D facies modeling

After importing sections in PETREL™, the next step was to distribute the lithofacies into the unpopulated cells between the "pseudo-logs" (inter-well space). The stochastic algorithm TGSim was used for model A because its assumptions reflect the rules of Walther's law (Matheron et al., 1987). Model B, model C and model D, which contain the same input data (sections I1, I3, I4, I5, I7 and I8), was built using three different algorithms. Model B was generated using TGSim as model A, model C using SISim and model D using IK. These algorithms are chosen because they are the most commonly used for facies modeling in PETREL™ (Journel et al., 1998; Hu and Le Ravelec-Dupin, 2004; Falivene et al., 2006a). During the modeling process, each zone, which was defined earlier as small-scale cycle (Figure 2.9), was simulated individually.





**Figure 2.10: Panels showing the four models (model A, model B, model C and model D) built during the present study. Note the significant spatial variability of the modeled lithofacies distribution resulting from differences of data input and algorithm choice. Model C (SISim) displays significant vertical lithofacies heterogeneity compared to model A and model B (TGSim) whereas the horizontal lithofacies continuity seems similar between the three models. Model D (IK) builds a layer-cake model (for legend of Lf colours see Figure 2.9).**

In order to describe the complexity of the spatial relationship between lithofacies and geometrical characteristics of each lithofacies, two geostatistical parameters must be provided to the stochastic algorithm. The first parameter is the vertical proportion trend of the lithofacies along the sections for each lithofacies for each zone. The vertical proportion section (1D controlling parameter) represents the evolution of the percentage of each lithofacies along the stratigraphic sections. Because of a homogeneous spatial distribution of the sections within the study window, the vertical proportion of the lithofacies captured in the sections is considered to reflect the real vertical proportion of lithofacies within the whole of the studied area. The second geostatistical parameter is the semi-variogram, which describes the vertical and horizontal continuity of the geological bodies being modeled (Table 2.1; Dimensions column). The semi-variogram approximates the dimensions of each geological body of each lithofacies (3-D controlling parameter). According to the palaeocurrent direction of the shoals measured in the field ( $45^{\circ}\text{N}$ ), the orientation of all lithofacies modeled is considered to be  $135^{\circ}\text{N}$ . The dimensions of the potential reservoir rocks (Lf 7 and Lf 8), a few metres thick and tens to hundreds of metres long, are similar to those measured in other DOM studies (Kostic and Aigner, 2004; Borkhataria et al., 2005).

The resulting 3-D facies models (A, B, C and D) (Figure 2.10) can then be compared. Recall that all inputs remain identical between models. Only the algorithm and the number of "pseudo-logs" are being varied. Model A

takes into account all available sections (eight sections) during modeling steps. Consequently, model A is considered as the base case for qualitative and quantitative comparisons between models. In order to validate the later model comparisons, quality control points are carried out in model A.

### ***2.8.5. Quality control***

Quality control is an essential part of the geomodeling workflow during which qualitative and quantitative assessments can be made of the validity of the 3-D lithofacies distributions built during the modeling process. Three different tests were applied in model A, which will be used as base case for model comparisons (Figure 2.11). The first test validates the quality of the geological data input in PETREL™ and the two other tests check the reasonableness of the 3-D stochastic simulation.

The first quality control test consists of a visual comparison between the original sedimentary section II measured in the field and the associated modeled section called “pseudo-logs”. This test demonstrates that the geological data collected in the field are not strongly modified during their input into the model. The input data and the modeled data are similar regardless of the thickness of the modeled beds (Figure 2.11A). For example, marly intervals from Lf 2, which are thin especially at the base of the sections, are correctly modeled in the cells, as are the thick beds of wackestones (Lf 4 or Lf 5). The initialized cell data do not display any significant departures between the sections and “pseudo-logs” due to the suitable choice of cell size.

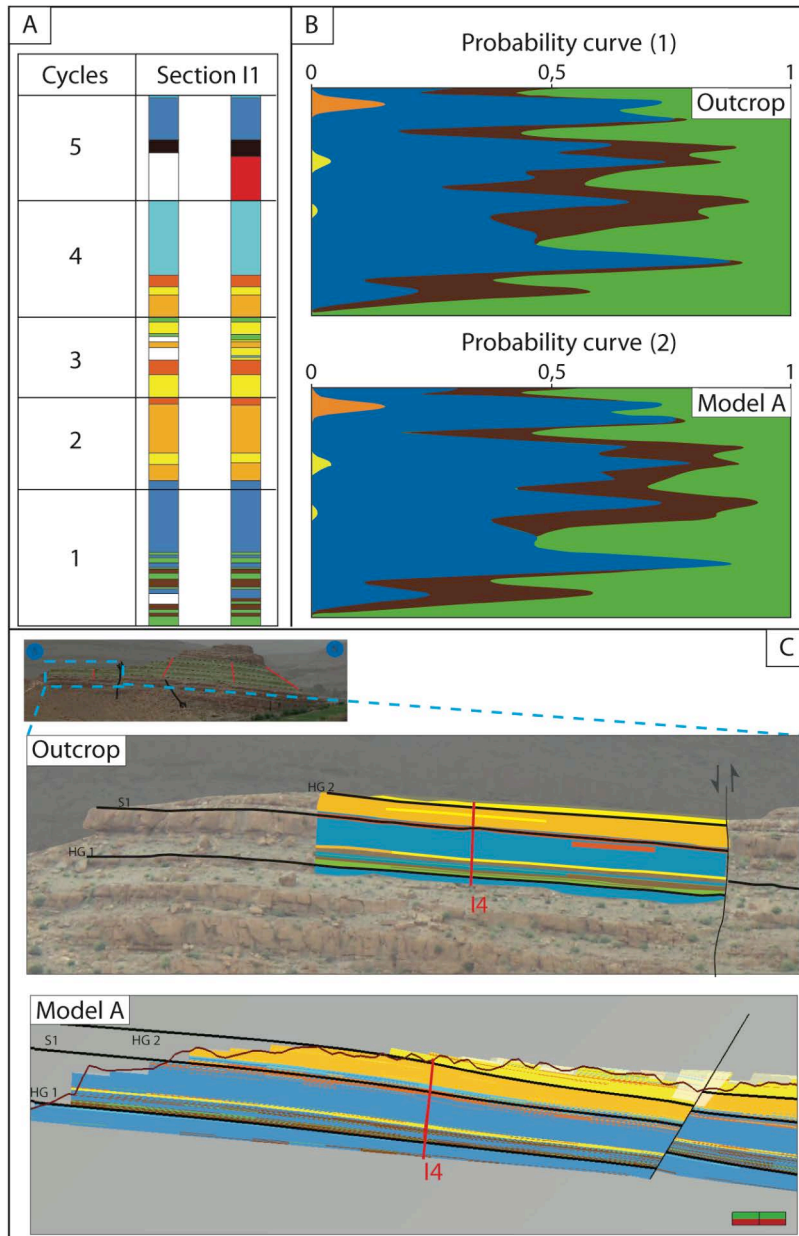
A second test evaluates the modeling of the large-scale vertical lithofacies evolution. It focuses on a quantitative comparison between the vertical proportion of the lithofacies curves from the original sections and those from the generated stochastic model. As shown in Figure 2.11B (B1, B2), the vertical trend of the lithofacies distribution from the model (B2) is very similar to the original described sections (B1). This quality control step provides a first approximation of the quality of the final model.

The third quality control test is a visual comparison of the lithofacies distribution within a 2-D window described in the field and the same region generated by the model. This test is essential to check if the continuity or discontinuity of the geological bodies is correctly modeled. As depicted in Figure 2.11C, the vertical and lateral facies distribution compare favourably between the “real” and modeled outcrop. The various geometrical changes of thickness and horizontal continuity of lithofacies are properly modeled. Some errors are observed in the “inter-well” regions far from the described section control points, especially for the thinner layers of Lf 9 or Lf 2.

## **2.9. Models comparisons**

In modeling projects of subsurface reservoirs, the uncertainties of the inter-well details in facies distribution are a crucial factor in trusting the performance of the reservoir model in flow simulation. The study of outcrop analogues provides a powerful tool to constrain these uncertainties in geobody morphology and connectivity of the reservoirs. The collection of numerous sections on well-exposed outcrops is ideal for testing facies modeling tools and methods. The comparison between model A and model B highlights the impact of the degrees of resolution of the modeling targets (numbers of sections) on quality of the final model. The comparisons of model B, model C and model D allow the impact of each algorithm on the modeled facies distribution to be tested at the inter-well scale. To

this end, two methods of comparison are carried out in the present study: quantitative comparison of lithofacies percentages between models and data input and qualitative comparison by visualising the final lithofacies distribution between models.



**Figure 2.11: Three different quality tests made in the 3-D facies model A. A. Comparison between the original sedimentary section I1 measured in the field (left column) and the pseudo-logs created during the modeling process (right column). Note the population of the non-outcropping intervals (in white) during the facies modeling. B. Comparison of vertical facies proportions between all of the original section (1) and the final model A (2). The transgressive interval of cycle 1 is selected for this test because of its high level of lithofacies heterogeneity. C. Comparison of the 2-D facies distribution between the outcrop and the 3-D model A. Observe the significant similarity of spatial facies distribution between outcrop and model (for legend of Lf colours see Figure 2.9).**

**Table 2.2: Summary table of the percentage deviation and associated standard deviation between final model and data input. Comparisons are carried out for the entire model as well as within each cycle.**

Domain of comparison	Model A (TGSim)	Model B (TGSim)	Model C (SISim)	Model D (IK)
Entire model	28,9% (Std: 12,6)	35,2% (Std: 17,5)	41,7% (Std: 21,3)	60,8% (Std: 35,6)
Cycle 1	13,4% (Std: 14,4)	17,4% (Std: 16,2)	15,3% (Std: 8,9)	78% (Std: 24,2)
Cycle 2	13% (Std: 8,0)	12,6% (Std: 6,8)	15,2% (Std: 11,7)	66,4% (Std: 19,7)
Cycle 3	14% (Std: 13,4)	28% (Std: 28,2)	40% (Std: 58,0)	69,7% (Std: 35,0)
Cycle 4	9% (Std: 7,5)	10% (Std: 6,0)	18,1% (Std: 13,2)	63,3% (Std: 15,4)
Cycle 5	27% (Std: 28,0)	28,8% (Std: 25,4)	25,4% (Std: 16,8)	72,2% (Std: 38,0)

A comparison of the percentage deviation and standard deviation of lithofacies percentage between model and input data is carried out in the entire model as well as in individual cycles (Table 2.2). Percentage deviation values indicate the degrees of match of the lithofacies percentages between data input and final models. Standard deviation values quantify the variability or dispersion of these percentage deviation values. Within the entire model, the model A (base case) and model B have a better data fit than the two other models (model C and model D). This result indicates the reliability of the TGSim technique in conserving the initial lithofacies proportion given by the data input. Moreover, data resolution is influenced by the number of "pseudo-logs", with the quality of the final model changing from 35.2% deviation for model B to 28.9% deviation for model A. For the entire model, model C (SISim) and model D (IK) show higher percentage deviation values, especially model D (60.8%). Standard deviation values show the same trends as the percentage deviation. However, the detailed investigation of percentage deviation and standard deviation variability in each cycle highlights other significant trends. The cycles 1, 2 and 5 display significant ranges on the morphology of geological bodies (vertical and horizontal dimensions) (Figure 2.7A, Table 2.1; dimensions column). For example, 0.1 m thick alternating mudstone and marl beds contrast with 3 m thick packstone beds in cycle 1. In these cycles, percentage deviation and standard deviation values of model C using SISim tend to be equal or even smaller than those generated by model B using TGSim. The cycle 3 showing significant morphological contrasts between bodies, is also characterized by a high proportion of no-outcropping areas. This feature influences the final model and TGSim (model B) seems to better handle such types of low resolution data input compared to SISim (model C). In contrast, cycle 4 displays geological bodies with similar dimensions (Figure 2.7A, Table 2.1; dimension column). In this case, model B using TGSim has a better data fit (10%) compared to model C using SISim (18.1%). Model D using IK shows high and similar percentage deviation and standard deviation values for all cycles (up to 78% deviation in cycle 1). The differences between model D and data input seem to be independent of geological heterogeneity modeled.



The percentage deviation variability between models and data input shows that the degree of geological heterogeneity influences the quality of the model when TGSim and SISim are used. Comparisons of the spatial lithofacies distribution are now carried out between models. This visual approach allows the effect of each algorithm on lithofacies distribution to be understood and then, the observed percentage deviation variability can be explained.

The investigation of these differences focuses on comparisons of vertical (Figures 2.12A, 2.12B) and horizontal (Figure 2.13) lithofacies distribution built by the three algorithms. For the first comparison, the model A (base case) is used as a reference to appreciate the quality of the three other models (model B, model C and model D). This test shows that all three models capture the general vertical lithofacies evolution observed in the described sections I2 (Figure 2.12A) and I6 (Figure 2.12B). However, significant differences in terms of heterogeneity and proportion occur between these four models within each zone. An increase of the vertical facies heterogeneities called spatial disorder (Journel and Deutsch, 1993) can be observed from model B (TGSim) to model C (SISim). This observation is particularly true when the vertical facies distribution becomes complex with a succession of thin lithofacies beds. Such a scenario is seen at the base of the cycles 1 and 2 and throughout cycles 3 and 5 (Figures 2.12A, 2.12B). At these localities, TGSim (model B) builds vertically homogeneous lithofacies beds whereas SISim (model C) produces a more complex vertical lithofacies interfingering, which is not always observed on the outcrop. IK (model D) tends to strongly underestimate the lithofacies that are composed of thin beds (Lf 2, Lf 3, Lf 6 and Lf 9), whereas an overestimation characterized lithofacies composed of thick beds, especially Lf 4, Lf 5, Lf 7 and Lf 8 (though IK overestimates by the largest margin) (Figures 2.10, 2.12A, 2.12B). In addition to the dimension of geological bodies modeled, the proportion of lithofacies influences the quality of the model D (IK). Whereas low percentage lithofacies are underestimated, high percentage lithofacies are overestimated as shown in most of the cycles. The results of both, lithofacies dimension and proportion are a simplification of each cycle (or zone) to the most common lithofacies. Consequently, the lithofacies interfingering and heterogeneity at the inter-well space are not captured.

Cycles 1 and 2 are characterized by significant contrasts in the morphology of geological bodies. The later features playing a major role affecting the quality of final models in terms of facies proportion and distribution (see above), both cycles are chosen for further tests. Two layers (layers A and B) are selected at the base of cycles 1 and 2 (Figures 2.12A, 2.12B). The significant increase of spatial disorder between model A, model B (TGSim) and model C (SISim) observed in section I2 and I6 is not observed in plan view (Figure 2.13). The horizontal dimensions of each lithofacies are relatively constant between the three models. However, differences in of the way lithofacies are populated between control points can be observed between model A, model B (TGSim), model C (SISim) and model D (IK). Whereas TGSim (model A and model B) tries to assign a trend from marl to mudstone and to wackestone (layer A) or from wackestone to floatstone to rudstone (layer B), SISim (model C) builds individual lithofacies bodies according to their corresponding semi-variograms. IK (model D) generates continuous geological bodies during the stochastic simulation. If a lithofacies is underrepresented in term of lithofacies percentage in a modeled zone, the data input are even not taken into account during the simulation (Figure 2.13).

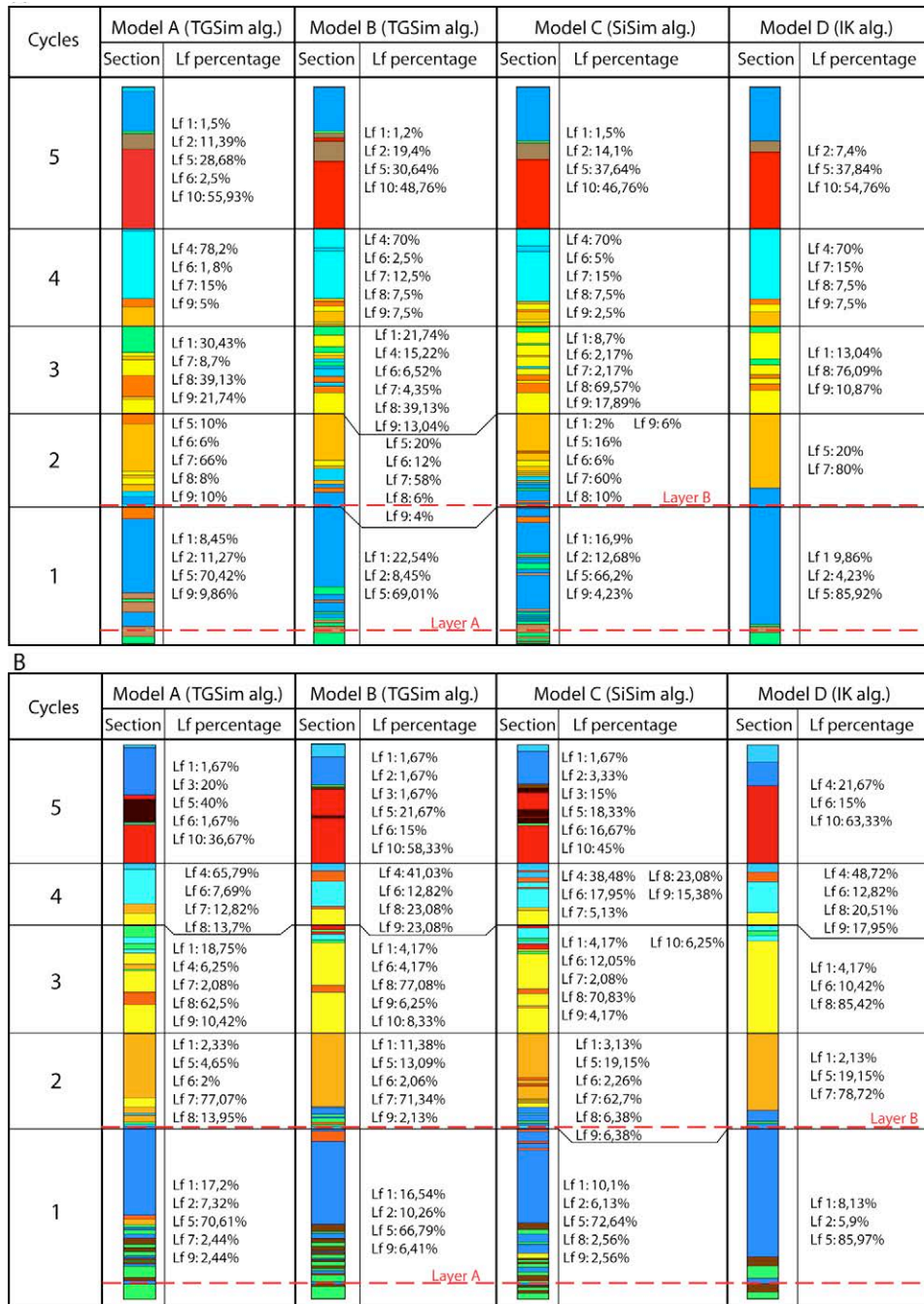
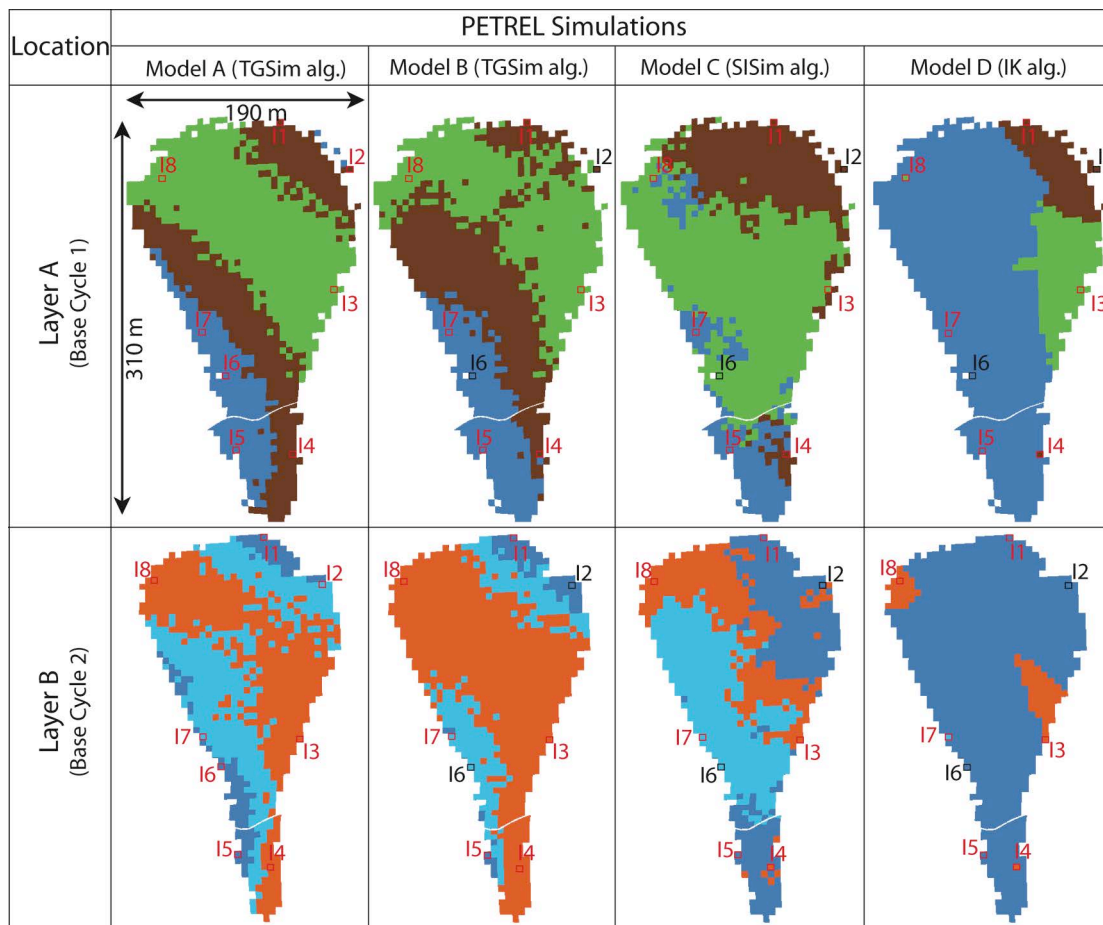


Figure 2.12: A. Comparison of the vertical lithofacies distribution located in section I2 between model A where non-outcropping area of the described section I2 has been filled during simulation, model B (TGSim), model C (SiSim) and model D (IK). Lithofacies percentage and distribution are displayed for each small-scale cycle. Note the high degrees of lithofacies heterogeneity for model C and the layer-cake model built in model D. B. Comparison of the vertical lithofacies distribution between the measured section I6 where non-outcropping area has been filled during simulation, model B (TGSim), model C (SiSim) and model D (IK). Lithofacies percentage and distribution are displayed for each small-scale cycle (for legend of Lf colours see Figure 2.9).



**Figure 2.13: Comparisons of the spatial facies distribution built by TGSim (model A and model B), SISim (model C) and IK (model D) located at the base of cycles 1 and 2. For each cycle, the four facies maps come from the same layer. The "pseudo-logs" are displayed in each layer (red square). For model B, model C and model D, section I2 and section I6 are not used during the stochastic modeling (black square). Despite the use of the same database and the equivalent facies proportion, the four final models show significant differences in term of spatial lithofacies distribution. TGSim tends to assign a trend between lithofacies whereas SISim and IK generate individual geological bodies without any correlation or trend (for legend of Lf colours see Figure 2.9).**

## 2.10. Discussion

### 2.10.1. Geological uncertainty about stochastic simulation

Stochastic simulation involves three categories of spatial and statistical uncertainties, i) conditioning data (density, distribution and geological hypothesis), ii) facies simulation due to the stochastic nature of the algorithm and iii) algorithm choice (Gotway and Rutherford, 1994). Each category can influence the quality of the final model and their review is crucial to understand which factor is responsible for the differences observed between models. For the first category, the conditioning data used to build models are different between model A (eight sections) and model B, model C and model D (six sections). Therefore, comparisons between model A and model B need to take into account the influence of data conditioning. For the second category, the stochastic nature of facies modeling

involves the use of random numbers (random number seed; Boisvert et al., 2010) during the simulation, which provide equiprobable realizations of the same modeling target. The geological uncertainty resulting from these equiprobable realizations is called ergodic fluctuations (Caers and Zhang, 2004) and is well known for building training images. The ergodicity induces statistical errors (percentage deviation and facies proportion) and tends to decrease the continuity of geological bodies (spatial disorder) in the final model. Two methods allow geological uncertainties to be reduced in relation to ergodic fluctuation during stochastic modeling. First, the ratio between the size of modeling parameters (semi-variogram) and the size of the modeled area should be lower than 1/2 (Caers and Zhang, 2004). In the present study, some lithofacies such as Lf 8 in cycle 3 or Lf 4 in cycle 1 occur locally across the entire modeled area (Figure 2.7A). Despite the significant continuity of these geological bodies, the lithofacies dimensions considered for modeling are not longer than 150 m, which is less than the half distance of the modeled area. In addition, ergodic fluctuation for the present study is reduced due to the extension of the modeled area outside the study window. Second, a minimum of 10 equiprobable realizations allows the ergodic effect to be reduced significantly (Goovaerts, 1999) for a single modeling target. This method has been applied to clastic sediments (Falivene et al., 2007) with a modeling scale similar to the present study. The reduction of ergodic effect shows that SISim is characterized by a significant vertical lithofacies disorder compared TGSim whereas the horizontal lithofacies continuity simulated is similar between both algorithms. These observations, which illustrate the impact of algorithm choice on facies distribution for clastic sediments, are similar to those observed in the present study on carbonate rocks (Figures 2.10, 2.12A, 2.12B, 2.13). The ergodicity does not seem to modify the effect of algorithm choice in the present study. The results of statistical and spatial comparisons between models are likely data conditioning (model A and model B) and algorithm related (model B, model C and model D).

### ***2.10.2. Impact of the algorithm choices on the facies distribution***

The choice of the pixel-based algorithms (among others TGSim, SISim and IK), which are commonly used for facies modeling, plays a crucial role in the way the facies distribution is populated between sections (Journel et al., 1998; Falivene et al., 2006a; Bastante et al., 2008). Their main advantages are their flexibility in honouring the conditioning field or well data and their quantitative measurements. However, one disadvantage is that their methods of populating the facies distributions between control wells are not necessarily constrained by geological reasoning. A second disadvantage is that the simulated geometries of individual bodies are not necessarily continuous (Journel and Deutsch, 1993; Hu and Le Ravalec-Dupin, 2004). The tests carried out in the present study, have shown that at the inter-well scale (x10 to x100m), TGSim (model A and B) and SISim (model C) provide a reasonable approximation of the lithofacies proportion, distribution and heterogeneity (Table 2.2, Figures 2.12A, 2.12B). In contrast, IK (model D) produces significant errors in the lithofacies distributions and proportions. Its operating mode transforms lithofacies types into indicators, which correspond to the probability of lithofacies occurrence for each zone modeled. In this study, using the IK leads to a simplification of the facies heterogeneity by assigning the most common facies to each zone and to underestimating or even eliminating the occurrence of underrepresented lithofacies. This result diverges from previous conclusions by Bastante et al. (2008), who suggested an overestimation of facies types present in a low proportion. The major drawback of IK is the unrealistic estimation of

the probability of a specific facies type in an unsampled area (Tolosana-Delgado et al., 2008). These unrealistic probability values induce significant errors in the facies proportion (underestimation or overestimation of the facies type proportion) during the simulation, which seem to be inconsistent from one study to another.

Based on the present work, TGSim (model A and B) seems to be the best approach for honouring conditioning field data at the inter-well scale compared to SISim (model C). However, there are two main issues, one concerning the emphasis placed on initial facies percentage (Table 2.2) and another the modeled spatial facies distribution (Figures 2.12A, 2.12B, 2.13) shown in the present study. For the first issue, the degree of lithofacies heterogeneity seems to play a major role on the quality of models. Using TGSim (model A and B), the simulation is controlled by the probability distribution and one semi-variogram assigned to all lithofacies types within each zone. On the contrary, SISim (model C) applies one semi-variogram for each of the facies types (Journel et al., 1998). Due to this major difference of operating mode between both algorithms, SISim is more flexible than TGSim for modeling numerous lithofacies characterized by various size and morphology. Consequently, the operating mode of the SISim is likely to produce higher quality models compared to TGSim during the modeling of complex geological heterogeneity and geometry, as shown in cycles 1, 2 and 5 (Table 2.2; Dimension column). The second issue focuses on the way facies distribution is simulated at inter-well spacings for both algorithms. In order to understand the effect of TGSim on the spatial facies distribution, its mode of operation will be briefly reviewed. The TGSim function (Matheron et al., 1987) transforms the facies codes into a continuous model property. This continuous property is then partitioned into facies codes using several numerical thresholds or cutoffs, which produces transitions between facies according to a trend (e.g. it will always create an intermediate energy domain between a high energy domain and a low energy domain; or always transition from proximal through medial to distal). This application of trending is a powerful tool that allows adherence to both, geological concepts (e.g. Walther's Law) and interpretations/descriptions based on field observation, which cannot be handled by either the IK or SISim algorithms. TGSim is well suited to modeling at the scale of the depositional environment (x100 to x1000m) because of the well-defined spatial relationships of environments along a depositional profile. However, at the much finer facies scale (x1 to x100m), it is questionable if such trends are useful and necessary for modeling shallow-water carbonate rocks. Within shallow platforms, various autocyclic (rainfall, storm or current) and allocyclic (regional and local subsidence, eustasy) factors influence the depositional records at different amplitudes and frequencies. In these systems, different facies types can coexist and their association can change through time and space (Strasser et al., 1999). Then, it can be problematic to assign a trend when facies-to-facies relationships are complex and do not always display standardized transitions through intermediate facies codes. For example in this study, the field observations (Figure 2.7A; base cycle 2) indicate that Lf 5 can either laterally change to Lf 9 or Lf 6 as well as Lf 9 to Lf 5 or Lf 6. Consequently, a modeller who wishes to use TGSim must compromise and choose which one of these facies transitions will be the most important to represent in the final model. Instead, SISim (model C) assigns a facies code pixel by pixel by using local probability distribution. As shown in Table 2.2, this operating mode independent of any trends or associations is more flexible to honour the complex facies distribution characteristic of shallow-water carbonate rocks at the metre to tens of metre scale (Aigner et al., 2007).

The above discussion on the use of TGSim, SISim and IK algorithms illustrates how complex is the choice of a specific modeling algorithm and its impact on the model. The use of outcrop analogues is then crucial to provide

rules for modeling shallow-water carbonate rocks. During stochastic simulation, vertical and horizontal variograms are investigated in order to constrain the morphology of geological bodies (Gringarten and Deutsch, 2001). The present study suggests first that the level of spatial complexity of geological bodies (heterogeneity and geometry) influences the quality of the model. Before building the model, every dimension of the geological bodies should be compared to each other and modeling decisions need to be taken if one variogram is sufficient to reflect the geological heterogeneity of the modeling target. This first rule could avoid devoting an excessive amount of time during data processing and stochastic simulation. Second, the present study shows that the conceptual depositional model (facies association and trend) needs to be carefully considered for lithofacies modeling methodology as shown by Falivene *et al.*, (2007) for clastic-dominated sediments. In carbonate system, the modeling strategy of depositional environments (lagoon, back-barrier, fore-barrier and basin) is also based on the understanding of factors (geological trends and association) controlling the depositional mode. In this specific case, the present study suggests that TGSim should be used during simulation to conserve fundamental geological concepts involved in the interpretation of depositional environments. Contrarily, lithofacies modeling methodology in shallow-water carbonate environments needs to take into account complex lateral lithofacies associations and distributions (Strasser *et al.*, 1999). At the finer scale, the present study and previous studies (Wilkinson *et al.*, 1997, 1999) focused on geological outcrops, show the common occurrence of complex lateral lithofacies arrangement and significant spatial variability of lithofacies size, connectivity and association involving stochastic process during the deposition (Wright and Burgess, 2005) or record (Sadler, 1981; Rankey, 2002) of shallow-water carbonate sediments. This stochastic process has been demonstrated by the analysis of lithofacies thickness within numerous Phanerozoic and Proterozoic carbonate successions (Wilkinson *et al.*, 1999; Burgess, 2008). Each lithofacies is characterized by an exponential distribution of their thickness from thin to thick units. This observation indicates stochastic Poisson process occurring in the stratigraphic succession and then, explains the complex lithofacies arrangement observed. During time of deposition of carbonate deposits, the unpredictability aspect of lithofacies mosaic (Wilkinson *et al.*, 1999) reflects the predominant influence of autocyclic factors (lateral migration, accumulation rate, clastic input) compared to allocyclic factors on sedimentary record (Burgess, 2006). The character random of geological heterogeneity at the lithofacies scale suggests the need of flexible modeling algorithm as SISim, where geological association and trend are not required. However, stochastic distribution of carbonate deposits is not applied to all stratigraphic succession and more deterministic lithofacies heterogeneity is also observed, especially during low amplitude eustatic oscillations (Lehrmann and Goldhammer, 1999; Strasser *et al.*, 1999). Nevertheless, the above discussion and previous studies (Wilkinson *et al.*, 1997, 1999; Burgess, 2008) point out that the level of order in the geological record depends on the scale of observation. The latter studies indicate an increase of spatial disorder at scale of metre to hundreds of metre, whereas at a lower scale (kilometre to tens of kilometre), the lateral and vertical geological heterogeneity shows more predictable patterns. These observations are in agreement with the present study, which suggests a pure stochastic modeling approach at the lithofacies scale (metre to few hundreds of metre) using SISim. The use of deterministic modeling tools as geological trend and association using TGSim is required for depositional environment modeling (hundreds of metre to tens of kilometre).

## 2.11. Conclusion

A sedimentological study was carried out within the carbonated-dominated Assoul Formation in the High Atlas mountain range (Morocco). Data from this field work was used in tests of three stochastic 3-D modeling algorithms to investigate the metre-scale facies variability on a carbonate ramp. Ten lithofacies were recognized and grouped into three different depositional environments: i) an inner ramp, ii) a proximal middle ramp and iii) a distal middle to outer ramp. The stacking pattern is composed of five small-scale cycles (cycles 1 to 5) and two medium-scale depositional sequences called sequence A and an incomplete sequence B. The vertical lithofacies evolution expressed in one of the two medium-scale depositional sequences indicates a transition from distal to proximal middle ramp. Prograding oolitic shoal bodies are recorded during the highstand deposit of medium-scale depositional sequences. A 3-D facies Digital Outcrop Model (model A) was created by using the TGSim stochastic algorithm, which allows the use of a trend from low (Lf 2) to high (Lf 8) energy lithofacies. Three quality controls based on visual and quantitative comparisons between the model and the “real” outcrop confirm the realistic representation of the observed geology. Finally, the model clearly exhibits a significant amount of grainy lithofacies, which represent almost 50% of the entire area.

The continuous exposure of the study area also allowed the effect of three different algorithms on the facies distribution to be investigated at the inter-well scale. Three additional facies models, model B using TGSim, model C using SISim and model D using IK were created. Visual and quantitative comparisons between the four models A, B, C and D illustrate the favourable or unfavourable results of those three algorithms. The IK algorithm is observed to simplify the facies distribution, largely assigning the majority lithofacies to the whole zone even when the geological described section data are close enough that such simplifications seem unfounded. Of the two last algorithms, the TGSim seems to do the best job of modeling the facies distribution at the inter-well space when there is a high density of described section data. However, when the TGSim algorithm (used in many studies) is compared in detail to SISim algorithm, significant differences are observed. The operating mode of the TGSim produces lower quality models compared to SISim during the modeling of complex geological heterogeneity and geometry, especially in cycles 1, 2 and 5. In addition, the use of TGSim can introduce problems, especially when the geological data are numerous as in the present study. TGSim requires that facies be arranged into a vertical and lateral trend. However, such facies trends are not necessarily present when modeling shallow-water carbonate rocks (e.g. lateral relationships between lithofacies do not display a predictable pattern). Then, the scale of modeling (from depositional environment to lithofacies) involves specific simulation constraints on shallow-water carbonate modeling methods. Whereas deterministic simulation tools as trend using TGSim should be used for the modeling of depositional environment (kilometre to tens of kilometre), a pure stochastic approach using SISim need to be applied to model lithofacies heterogeneity (metre to few hundreds of metre). These results show that the geometry and spatial arrangement of the geological control data points is just as important as the nature and distribution of the geological features that have to be modeled.





# Outcrop analogue for an oolitic carbonate ramp reservoir: a scale-dependent geological modeling approach based on stratigraphic hierarchy

### *Abstract*

Considerable effort has been devoted to the development of simulation algorithms for facies modeling, whereas there has not been a discussion of how to combine those techniques. The integration of multiple geological data into a 3-D model that requires the combination of simulation techniques, is yet a current challenge for reservoir modeling. This paper presents a thought process that guides the acquisition and modeling of geological data at various scales. Our work is based on outcrop data collected from a Jurassic carbonate ramp located in the High Atlas mountain range of Morocco. The study window is 1 km wide and 100 m thick. We describe and model the spatial and hierarchical arrangement of carbonate bodies spanning from largest to smallest: (1) stacking pattern of high-frequency depositional sequences, (2) facies association, and (3) lithofacies. Five sequence boundaries were modeled using DGPS mapping and LIDAR data. The surface-based model shows a low-angle profile with modest palaeotopographic relief at the inner-to-middle ramp transition. Facies associations were populated using Truncated Gaussian Simulation to preserve ordered trends between the inner, middle and outer ramp. At the lithofacies scale, field observations and statistical analysis show a mosaic-like distribution that was simulated using a fully stochastic approach with Sequential Indicator Simulation.

The present study observes that the use of one single simulation technique is unlikely to correctly model the natural patterns and variability of carbonate rocks. The selection and implementation of different techniques customized for each level of the stratigraphic hierarchy will provide the essential computing flexibility to model carbonate settings. This study demonstrates that a scale-dependent modeling approach should be a common procedure when building sub-surface and outcrop models.

### **3.1. Introduction**

The investigation of outcrop analogues is a key research tool for the improvement of carbonate reservoir characterization and modeling of sub-surface hydrocarbon fields. Outcrop studies provide insights into the distribution and morphology of geological bodies across a broad range of scales from tens of kilometers down to micrometer-scale features (Kjongsvik et al., 1994; Kerans et al., 1994; Eaton, 2006; Mikes and Geel, 2006; Jones et al., 2008). One of the current challenges is the integration of various scales of geological data and concepts into a single 3-D model (Jones et al., 2009).

Within carbonate systems, facies associations across carbonate platforms and ramps (1 to 10 km) display gradational and ordered trends between neighboring depositional domains. In contrast, the spatial arrangement of lithofacies (1 to 100 m) shows a mosaic-like distribution pattern lacking clear and regular trends in facies-to-facies transitions (Wright and Burgess, 2005). A lithofacies mosaic appears to result from somewhat random processes during the deposition and preservation of carbonate sediments (Burgess, 2008). Each level of the stratigraphic

hierarchy displays different distribution patterns, which requires a specific modeling technique designed to reproduce its unique characteristics (Falivene et al., 2006a, 2007). Accordingly, the modeling of carbonate outcrop should involve the combination of various techniques to accommodate the scale-dependent nature of geological heterogeneity.

Most of the previous modeling studies applied one single simulation method to model carbonate rocks. These methods span from surface-based modeling (Adams et al, 2005; Sech et al., 2009; Verwer et al., 2009) to interactive facies modeling (Willis and White, 2000; Aigner et al., 2007; Palermo et al., 2010) and to algorithm-based modeling approaches (Kjongsvik et al., 1994; Aigner et al., 2007; Kenter et al., 2008; Tomás et al., 2010). Only a few studies Zappa et al. (2006) on alluvial deposits and Koehrer et al. (2010) on dolomite bodies tried to implement multiple simulation methods during facies modeling. We will demonstrate in this paper that the building of a realistic 3-D geological model must systematically combine various simulation techniques into the same modeling workflow to capture and model scale-dependent carbonate heterogeneities.

Previous outcrop modeling studies focused on carbonate systems have provided information about the morphology and dimension of shoals (Qi et al., 2007; Aigner et al., 2007; Palermo et al., 2010). These studies encompass areal dimensions on the order of 1 to 10 km in length and up to 100 m in thickness. Shoal body dimensions can vary significantly from 37 km in length and 4.2 m in thickness (Palermo et al., 2010) down to 1 km in length and 9 m in thickness (Qi et al., 2007). Other outcrop studies, such as those shown by Borkhataria et al. (2005) for a carbonate ramp and by Barnaby and Ward (2007) for a carbonate shelf, cover smaller areal dimensions (less than 1.5 km in length). Shoal complexes display lower lateral continuity ranging from 200 m to 1.3 km in length. Modern analogues also show similar variability of shoal morphology and dimensions (Harris, 2010). Significantly, all of these studies suggest that the large range of dimensional scatter depends on the scale of observation. The scale-dependent approach applied in this study has the advantage to simultaneously capture and model the large range of shoal complexity.

The aim of this study is the investigation and modeling of scale-dependent heterogeneities ranging from the stacking patterns of depositional sequences to the facies associations down to the individual lithofacies. Accordingly, this study documents a workflow designed to extract, for each of these spatial scales, geostatistical data on geobody morphology, dimensions, and association. We apply this approach to a 1 km long and 100 m thick, well-exposed study window within a Jurassic carbonate ramp in the High Atlas mountain range of Morocco. Previous studies in this area (Pierre et al., 2010; Amour et al., 2012; Christ et al., 2012a) provide the necessary basis for an in-depth analysis of the oolitic shoal complex observed in the inner ramp. Our work has the potential to provide new insights on modeling capabilities that are of general use to improve simulation strategy of shallow-water carbonate systems.

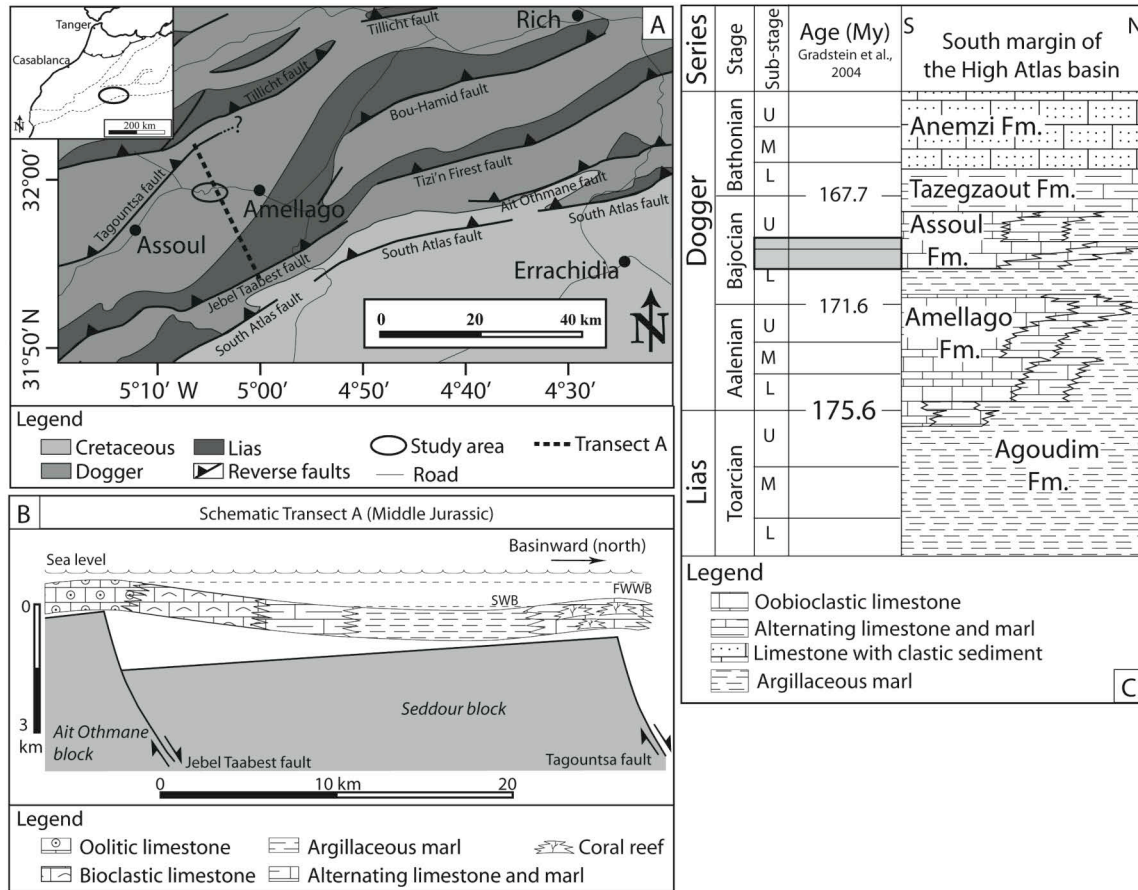
## 3.2. Geological setting

The High Atlas mountain range of Morocco (Figure 3.1A) is a southwest-northeast orogen developed by the tectonic inversion of a Triassic-Jurassic rifting system during the Cenozoic Alpine collision (Jacobshagen et al., 1988). The Triassic-Jurassic rifting phase that initiated the aborted High Atlas rift basin (Manspeizer et al., 1978), is associated to the opening of the North Atlantic Ocean (Ziegler, 1994), leading to the break-up of Pangaea. During the Early to Middle Jurassic, the High Atlas rift basin consisted of a seaway open to the northeast connected to the Tethys Ocean (Bassoullet et al., 1993). Shallow-water carbonates were deposited within the platform margin, whereas the subsiding central part of the basin recorded rhythmic marls and limestones (Jacobshagen et al., 1988; Warne et al., 1988).

Within the southern margin of the central High Atlas rift basin, an Early Toarcian crustal extension event (Laville et al., 2004) led to the dislocation of the carbonate platform into numerous rhomb-shaped sub-basins bounded by syndepositional ridges, which represented the crests of tilted blocks (Studer and du Dresnay, 1980; Poisson et al., 1998) (Figure 3.1B). These topographic highs were characterized by shallow-water carbonate with episodic emersions, whereas hemipelagic marls were deposited within the troughs of sub-basins (Stanley, 1981; Poisson et al., 1998). During Aalenian to Bajocian, carbonate platforms nucleated on the margins of the rhomb-shaped sub-basins (Ait Addi, 1998).

The study area is located in one of these sub-basins, bounded by two synsedimentary faults, the Tagountsa fault to the north and the Jebel Taabest fault to the south (Figures 3.1A, 3.1B). In this sub-basin, the Aalenian to Bajocian stratigraphic succession records two basinward progradation phases of a low-angle carbonate ramp from southwest to northeast, controlled by a second-order sea level fluctuation (Pierre et al., 2010). The two progradation phases were recorded by the Amellago Formation (Aalenian to Early Bajocian) (Poisson et al., 1998; Durllet et al., 2001; Pierre et al., 2010) and the Assoul Formation (Middle? to Late Bajocian) (Christ et al., 2012a; Amour et al., 2012). During Bathonian and Callovian times, decreasing subsidence rate (Ellouz et al., 2003) favored the infilling of the central High Atlas rift basin by deltaic and continental deposits from Anemzi Formation (Figure 3.1C).

The 220 m thick Assoul Formation consists on a carbonate ramp (Christ et al., 2012a; Amour et al., 2012) that displays stacking patterns and facies associations similar to the Amellago Formation (Durllet et al., 2001; Pierre et al., 2010). The Assoul Formation has been divided into three intervals; a lower grainy interval, a middle muddy interval, and an upper grainy interval (Christ et al., 2012a). Grainy intervals represent the inner ramp with abundant oolitic and peloidal shoals. Alternating marls and limestones from the distal middle ramp characterize the middle muddy interval. The basal and top parts of the Assoul Formation record two progradation phases of the carbonate ramp (lower and upper grainy interval) toward the northeastern sub-basin. Controlling factors on the evolution of the carbonate ramp of the Assoul Formation, such as sea level fluctuation, tectonic, climate, continental weathering and runoff, are still under debate (Pierre et al., 2010; Christ et al., 2012a).

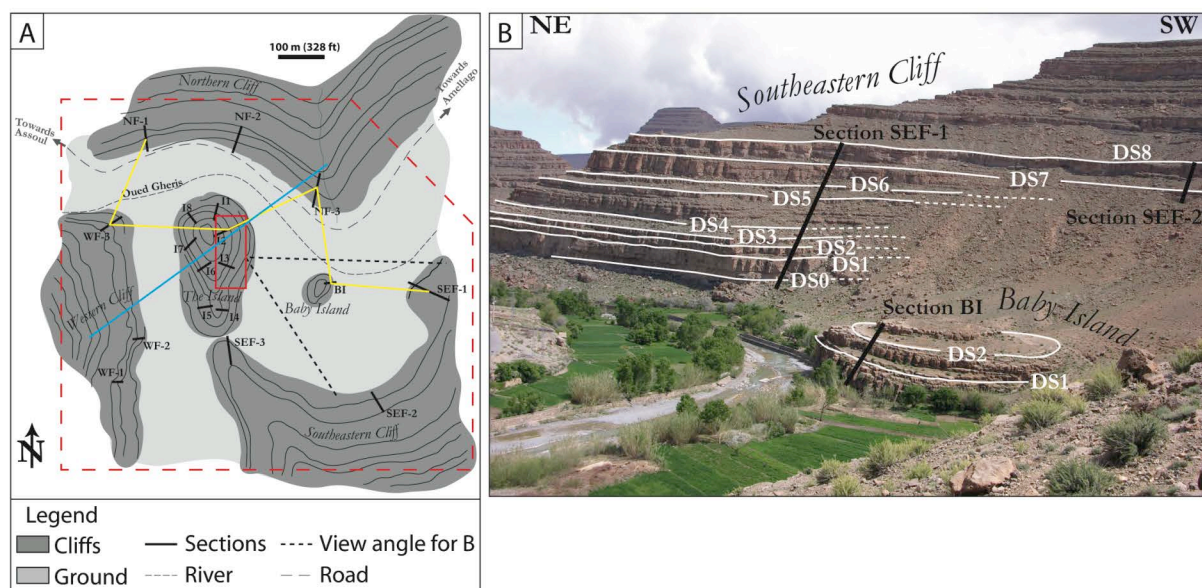


**Figure 3.1: Geological setting and location of the study area in the High Atlas mountain range (Morocco). A: Geological map of the southern margin of the Central High Atlas mountain range (Wilmsen and Neuweiler, 2008; Pierre et al., 2010). B: Schematic transect of the carbonate ramp during the Middle Jurassic (Poisson et al., 1998, Ait Addi, 2006). C: Stratigraphic column of the Jurassic in the south margin of the High Atlas basin (Pierre et al., 2006; Amour et al., 2012) with the study area shaded in grey. FWWB = fair weather wave base; SWB = storm-wave base.**

### 3.3. Characterization of the study area

The study window (Figures 3.1, 3.2) is located within a 100 m thick lower grainy interval of the Assoul Formation (Figure 3.1C). This interval corresponds to the first progradational pulse of the ramp system within the Assoul Formation. During the Bajocian, the inner ramp is composed of kilometer long oolitic and peloidal shoals with marly backshoal deposits. The foreshoal deposit is composed of intraclastic rudstones. The proximal middle ramp comprises wackestone to packstone lithofacies including bioclasts of gastropods, corals, bivalves, cyanobacteria, and brachiopods. Toward the distal middle ramp, alternating limestone and marl facies is deposited and associated with molluscan-coral bioconstructions (Amour et al., 2012). The inner, middle, and outer ramp terminology is determined by the position of the fair weather wave base and storm-wave base (Burchette and Wright, 1992; Immenhauser, 2009). The stacking pattern of the Assoul Formation consists of high-frequency depositional sequences bounded by hardground surfaces. Isotopic measurements and catholuminescence analysis

carried out on sequence boundaries (Christ et al., 2012a) reveal the absence of subaerial exposure features. These condensed surfaces are characterized by iron-staining, borings, reworked mudclasts, and erosional depressions (Appendix A1). The surfaces are interpreted to be related to maximum-regression but non-emergent conditions (Christ et al., 2012a).



**Figure 3.2: Overview of outcrop conditions within the study window. A: Plan view of the outcrop with the location of described sections. Red box corresponds to Figure 3.8 and cross sections shown in Figure 3.4 (yellow) and in Figure 3.13 (blue) are located. Domain of modeling (dashed red) shown in Figures 3.10 and 3.12 is also displayed. B: Pictures of the southeastern cliff and Baby Island outcrop. The view angle of the picture is shown in red on A. Five medium-scale (DS 0, 3, 5, 7, and 8) and four small-scale sequence boundaries (DS 1, 2, 4, and 6) were mapped. Three sections (black lines) are located in the photo. DS = discontinuity surface.**

## 3.4. Methods applied and terminology

### 3.4.1. Field methods

The well-exposed outcrop allowed the acquisition of 19 stratigraphic sections (Figure 3.2) with a section spacing ranging between 40 and 250 m. Lateral tracing of beds and facies transitions were carried out between the sections. The aim was to investigate dimensions and lateral variability of lithofacies and their associations. In the field, each section was logged, with an average of 3 to 4 samplings per meter to identify lithofacies. In addition, a total of 150 thin-sections were analyzed in the laboratory to confirm the field-based lithofacies classifications. Palaeocurrent features were measured in the field and X-ray diffraction was used to determine the type and proportion of clay minerals in marly deposits.

### ***3.4.2. Statistical analysis***

In addition to field observations, the Kolmogorov-Smirnov (Press et al., 1992) test and semi-variogram analysis (Gringarten and Deutsch, 2001) were performed to assess statistically the geological heterogeneity.

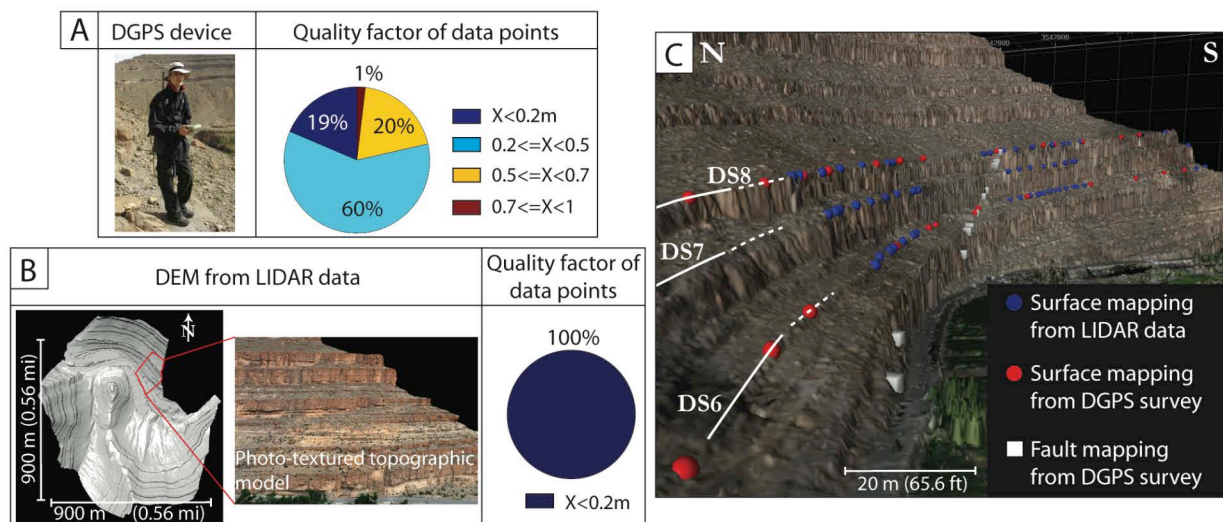
The Kolmogorov-Smirnov test estimates the degree of fit between two datasets. In the present study, the Kolmogorov-Smirnov is used to compare a lithofacies thickness distribution based on sampled data against a theoretical thickness distribution characterized by an exponential growth equation. If the two distribution functions compare favorably, the outcrop-sampled thickness distribution can be assumed to exhibit an exponential growth. An exponential lithofacies distribution can indicate the occurrence of random (or stochastic) phenomena known as a Poisson process influencing the sedimentary record (Wilkinson et al., 1997, 1999; Burgess, 2008). A Poisson process implies that the thickness of a lithofacies type at one particular stratigraphic interval is independent of what has been previously preserved in the sedimentary record. A stratigraphic succession recording a Poisson process lacks trend on vertical changes in lithofacies thickness, leading to a random accumulation (or stochastic distribution) of lithologies. Conversely, the absence of a Poisson process implies a predictable component (or deterministic distribution) on the stacking pattern of lithofacies thickness. The Kolmogorov-Smirnov test is therefore an independent statistical tool that can be used to document the degrees of complexity of geological heterogeneity.

Semi-variograms (Gringarten and Deutsch, 2001) approximate geobody dimensions with major and minor directions of elongation, and includes the azimuth of preferred orientation of the features. The minor direction semi-variogram is calculated at a right angle to the major orientation. Variogram behavior such as hole effect (Gringarten and Deutsch, 2001) can provide further information on geobody morphology. The hole effect, characterized by a variogram that oscillates periodically, indicates (sub-)parallel, regularly spaced geobodies (en-echelon arrangement) over a large distance.

### ***3.4.3. 3-D Outcrop Modeling***

A georeferencing survey of geological data was performed using DGPS mapping and LIDAR scanning (Figure 3.3). For a more detailed description of the DGPS mapping method, please refer to Amour et al. (2012). LIDAR data was used to i) obtain an accurate digital elevation model and ii) map geological features in inaccessible outcrop areas by picking surfaces and faults on the photo-textured topographic model. The LIDAR data were interpreted using LIME, a viewing and interpretation software developed by Dr. Simon Buckley (Centre for Integrated Petroleum Research, Bergen). Discrepancies between the two datasets (DGPS points and LIDAR) are not noticeable thanks to location accuracies better than 0.5 m in both mapping techniques (Figure 3.3). Each geological feature observed in the stratigraphic succession studied (Figure 3.4) is described using field observations and statistical analysis in order to establish a suitable modeling strategy. Then, each simulation methodology is combined in a single scale-dependent 3-D outcrop model.





**Figure 3.3:** Comparisons between both georeferencing methods DGPS survey (A) and LIDAR data (B) applied to map key stratigraphic surfaces, sections, and faults. **A:** DGPS mapping device in the field and pie chart, which compiles quality factors of each data points. **B:** LIDAR dataset used to obtain a high-resolution Digital Elevation Model (DEM) with a 0.2 m quality factor. Note similar quality factor of DGPS points (few tens of centimeters) between both mapping methods. **C:** DEM grided from LIDAR data demonstrating good fit between both LIDAR and DGPS georeferencing methods. DS = discontinuity surface.

### 3.5. Lithofacies classification and depositional setting

Previous investigations in this field area (Amour et al., 2012; Christ et al., 2012a) have identified 10 lithofacies. We integrate previous datasets with new sedimentological data collected here to cover a larger area and present an expanded lithofacies classification comprising a total of 14 lithofacies (Table 3.1). They were grouped into three facies associations: 1) an outer to distal middle ramp with alternating limestone and marl deposits, 2) a proximal middle ramp composed of wackestone to packstone lithofacies, and 3) an inner ramp dominated by grainstone lithofacies (Figure 3.4).

#### 3.5.1. Distal middle to outer ramp

Five lithofacies types were recognized in this association. Greyish to bluish marls of Lithofacies 1 are observed at the transition between basal deposits of the Agoudim Formation and initial shallow-water deposits of the basal Assoul Formation (Figure 3.5D). Bioclasts are rare and composed of well-preserved brachiopod shells. Horizontal laminations were also observed in the field. These two observations suggest a quiet, open-marine environment below the storm-wave base and likely deposited in an outer ramp. Numerous coral-microbial bioherms (Lithofacies 2) (Figure 3.5D) are present. These include platy to branching scleractinian corals, bryozoans, sponges, and microproblematic algae (*thaumatoporella*). The intra-reef deposits are mainly composed of microbialites, commonly thrombolites (included with Lithofacies 2). Alternating mudstone and marls and alternating packstone and marls (Lithofacies 3 and 4) are also observed (Figure 3.5C). The biota of Lithofacies 3 and 4 includes mainly bioclasts of echinoid spines, crinoids, bivalve, and ostracods. The lithology and the biota association for both Lithofacies 3 and 4

indicate a low-energy, open-marine environment below the fair weather wave base and interpreted as a distal middle ramp. Molluscan-coral lithosomes (Lithofacies 5) hundreds of meters long, mainly composed of oysters and brachiopods, developed in association with alternating ferruginous peloid packstone and marl deposits (Lithofacies 4).

Lithofacies nomenclature	Nomenclature <sup>a</sup>	Lithofacies (Lf)	Texture	Main skeletal and non skeletal components	Dimensions used for modelling	Main sedimentary features	Facies associations
Lf 1		Greyish to bluish marl	m	- Well-preserved brachiopods	- Thickness: 12 m - Length: 400 m - Width: 400 m	- 15% of Illite and quartz - Horizontal laminations	Outer ramp
Lf 2		Coral-microbial-sponge reef	B	- Scleractinian corals, microbialites, calcareous, and siliceous sponges	- Thickness: 12 m - Length: 5 to 10 m - Width: 5 to 10 m	- Domal shape	Distal middle to outer ramp
Lf 3	2	Limestone beds with interbedded marl	m, M to W	- Thin shelled ostracods, echinoderms, and molluscs - Subrounded micritic intraclasts in marl - From 15% to 20% of clastic sediments	- Thickness: 2 m - Length: 400 m - Width: 400 m	- Low to medium bioturbation - Rhythmic input of clastic sediments - Associated with meter scale mollusc-dominated bioconstructions (Lf 5)	Distal middle ramp
Lf 4	3	Limestone beds with interbedded marl	m, W to P	- Echinoderms, oysters, brachiopods, bryozoans, and coral debris. - Ferruginous peloids and subrounded micritic intraclasts	- Thickness: 3.4 m - Length: 400 m - Width: 400 m	- Low to medium bioturbation - Rhythmic input of clastic sediments - Associated with molluscs-dominated bioconstruction (Lf 5)	Distal middle ramp
Lf 5	10	Molluscan-coral-sponge reef	B	- Oysters, brachiopods, bivalves, scleractinian corals, calcareous sponges, and demosponges - Local deposition of marl	- Thickness: up to 6 m - Length: 1 to 300 m - Width: 1 to 230	- Microencrustation by microbialites, bryozoans, and cyanobacteria - Geopetal fabric - Local accumulation of shell fragments	Distal middle ramp
Lf 6	4	Bioclastic peloidal limestones	W,W-P	- Bivalves, cyanobacteria, gastropods, coral debris, green algae, and sponge spicules - Rare echinoderms and agglutinated foraminifera - Peloids and oncoids	- Thickness: 2.6 m - Length: 400 m - Width: 400 m	- Low to high bioturbation	Proximal middle ramp
Lf 7	5	Peloidal bioclastic limestones	W-P,P	- Peloids with irregular shape - Cyanobacteria, echinoderms, bryozoans, molluscs, and bivalves	- Thickness: 1.3 m - Length: 170 m - Width: 130 m	- Medium bioturbation	Proximal middle ramp
Lf 8	6	Bioclastic limestones	F	- Centimetre-sized gastropods, well-preserved coral debris, bivalves, brachiopods, and cyanobacteria - Oncoids and peloids	- Thickness: 0.8 m - Length: 390 m - Width: 360 m	- Micritization - Microencrustation by bryozoans, microbialite, and benthic foraminifera	Proximal middle ramp
Lf 9		Oncoidal limestones	F	- Pluri-centimetric oncoids and peloids - Cyanobacteria, gastropods, well-preserved coral debris, and bivalves	- Thickness: 1.8 m - Length: 400 m - Width: 370 m	- Micritization - Microencrustation by bryozoans, microbialites, cyanobacteria, and benthic foraminifera	Proximal middle ramp
Lf 10	9	Oncoidal limestones	R	- Oncoids, peloids, ooids, and intraclasts - Peloids and echinoderms as nucleus - Cyanobacteria, gastropods, and molluscs	- Thickness: 1 m - Length: 210 m - Width: 190 m	- Brittle deformation - Cement: crystal of sparite	Inner ramp
Lf 11	7	Peloidal limestones	G	- Peloids and ooids - Peloids and echinoderms as nucleus - Echinoderms, agglutinated foraminifera, and gastropods	- Thickness: 3.1 m - Length: 260 m - Width: 145 m	- Cement: crystals of sparite - No sedimentary structure	Inner ramp
Lf 12	8	Oolitic limestones	G	- Ooids, composite ooids, and intraclasts - Peloids and echinoderms as nucleus - Bivalves, gastropods, and benthic foraminifera	- Thickness: 2 m - Length: 200 m - Width: 140 m	- Cross-bedding, bidirectional ripples and asymmetric ripples - Bivalve encrustations on top of beds - Sutured contact and brittle deformation - Cement: crystal of sparite	Inner ramp
Lf 13	1	Greyish to greenish marl	m	- Well-preserved brachiopods and bivalves - Subrounded micritic intraclasts - Up to 25% of clastic sediments	- Thickness: 1 m - Length: 170 m - Width: 100 m	- Interbedded with oolitic G (Lf 12)	Inner ramp
Lf 14		Microbial mound	B	- Microbialites and sponges - Ooids within growth cavities	- Thickness: up to 2 m - Length: up to 0.3 to 4 m - Width: 0.3 to 4 m	- Locally associated with oolitic G (Lf 12)	Inner ramp

**Table 3.1: Lithofacies classification and interpretation. <sup>a</sup>: Lithofacies type from Amour et al., 2012. M = mudstone; W = wackestone; P = packstone; G = grainstone; F = floatstone; R = rudstone; B = boundstone.**



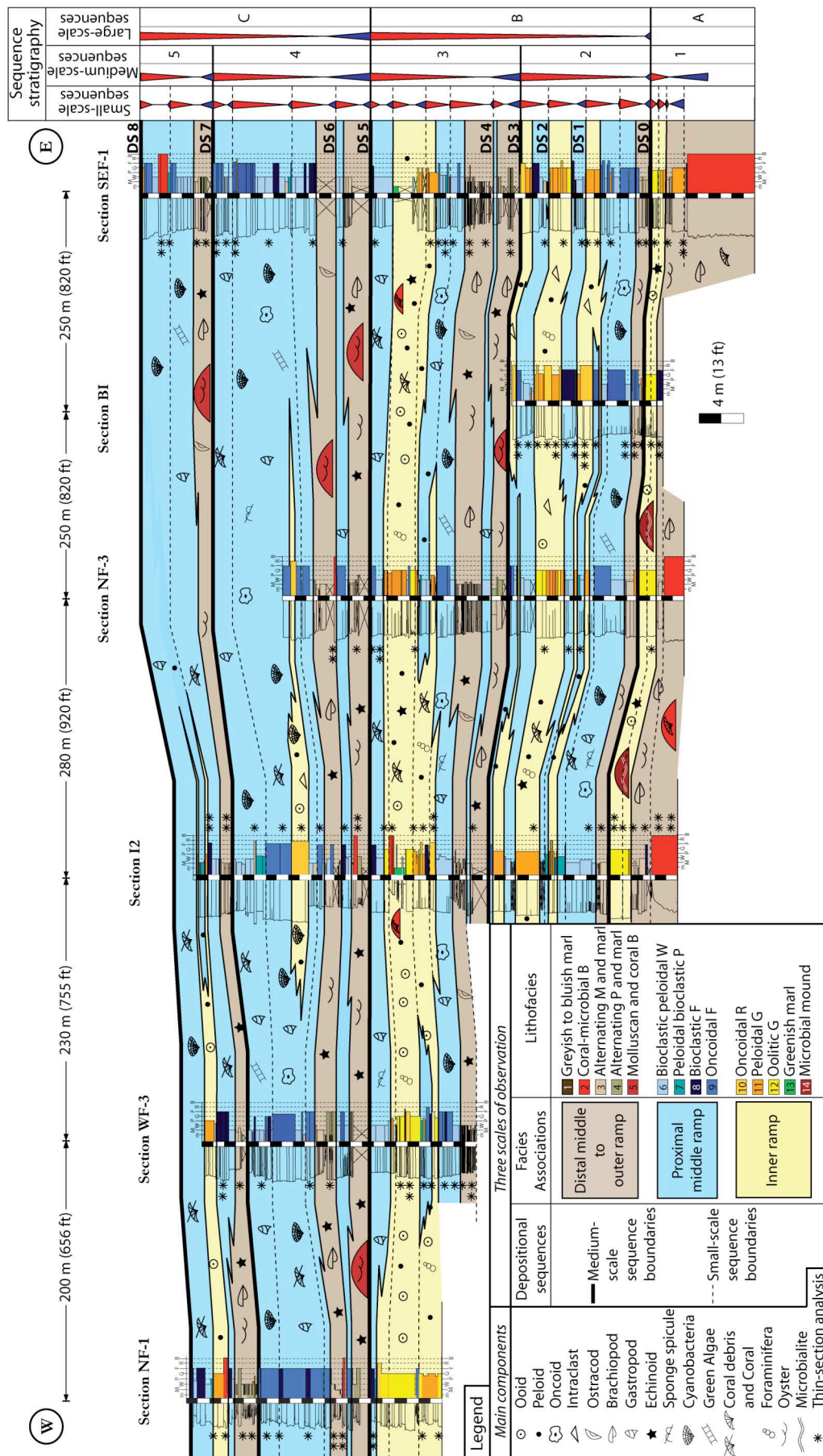


Figure 3.4: West-East cross section showing the facies distribution and sequence stratigraphy in the study area. Note the hierarchical relationship between three scales of observation from depositional sequence to facies association, and to lithofacies. Refer to Figure 3.2 for the location of the sections. DS = discontinuity surface; M = mudstone; W = wackestone; P = packstone; G = grainstone; F = floatstone; R = rudstone; B = boundstone.

### **3.5.2. Proximal middle ramp**

This association of facies contains thick bioclastic peloidal wackestone beds (Lithofacies 6) (Figure 3.5C) with micritized debris of bivalves, coral debris, gastropods, brachiopods, green algae, and textulariid foraminifera. Bioturbation is localized to pervasive and abundant *Thalassinoides* burrows are recognized. Locally, peloids become dominant and represent up to 60% of grains (Lithofacies 7). Some ooids occur with increasing peloidal abundances, suggesting nearby shoal bodies. Oncoids forming floatstone bodies (Lithofacies 9) up to 4 m thick are abundant in the study window (Figure 3.4). The subrounded to rounded oncoids show filaments of cyanobacteria (*Cayeuxia*, *Rivularia*, *Garwoodia*) in thin section. The occurrence of oncoids along with a relatively diverse biota and matrix-rich lithofacies association (Table 3.1) indicates an open-marine, shallow-water environment below the fair weather wave base and is interpreted as proximal middle ramp. Bioclastic floatstones (Lithofacies 8) composed of centimeter-sized skeletal debris of gastropods, coral debris, bivalves, and brachiopods are observed at the top and base of depositional packages. Lithofacies 8 shows abundant micritization and microencrustation of bioclasts by bryozoans, microbialites, and cyanobacteria. Often associated with condensed surfaces, the bioclastic floatstone is interpreted to be the result of storm winnowing on the middle ramp during periods of low sedimentation rates.

### **3.5.3. Inner ramp**

The inner ramp is composed of three grainstone lithofacies, plus greyish to greenish marls, and occasional microbial mounds (Table 3.1). This facies association was subdivided into three sub-associations, which record changes of depositional conditions across the inner ramp.

#### **3.5.3.1. Foreshoal**

Rudstone bodies (Lithofacies 10) composed of oncoids, which preserve filaments of cyanobacteria (*Cayeuxia*, *Rivularia*, *Garwoodia*), were recognized in the field and thin-section (right column Figure 3.6). Peloids and ooids are abundant and bioclasts of gastropods, textulariid foraminifera, unspecified molluscs, echinoderms, and large lituolinid foraminifera are present to frequent in abundance. The inorganic and organic components suggest the influence of both 1) the proximal middle ramp indicated by the occurrence of cyanobacteria and 2) the inner ramp characterized by the abundance of ooids. The texture of Lithofacies 10 suggests a foreshoal located around the fair weather wave base. The foreshoal exhibits isolated, hundreds of meters long rudstone bodies with thickness ranging from few decimeters to 2 meters (Figures 3.4, 3.5).

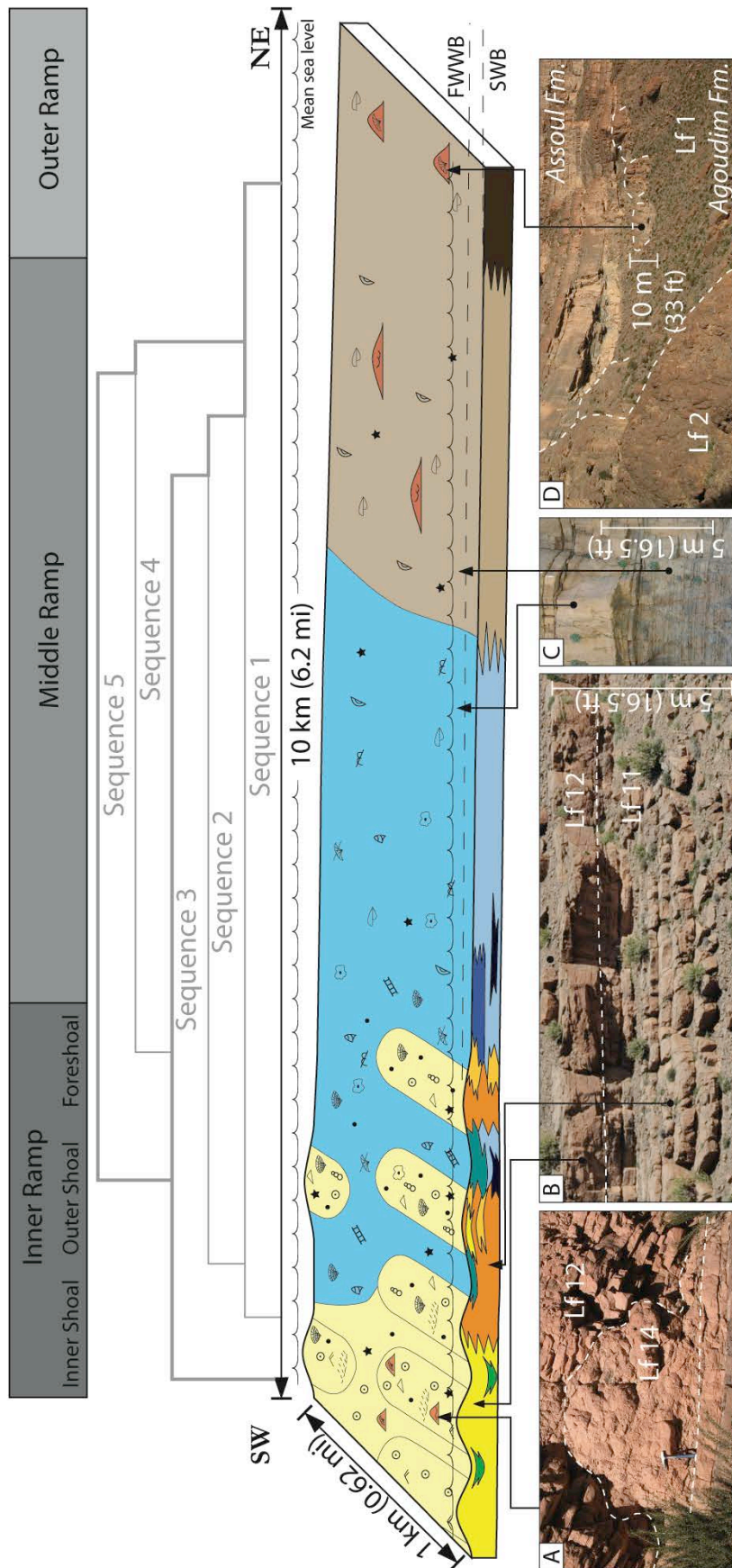


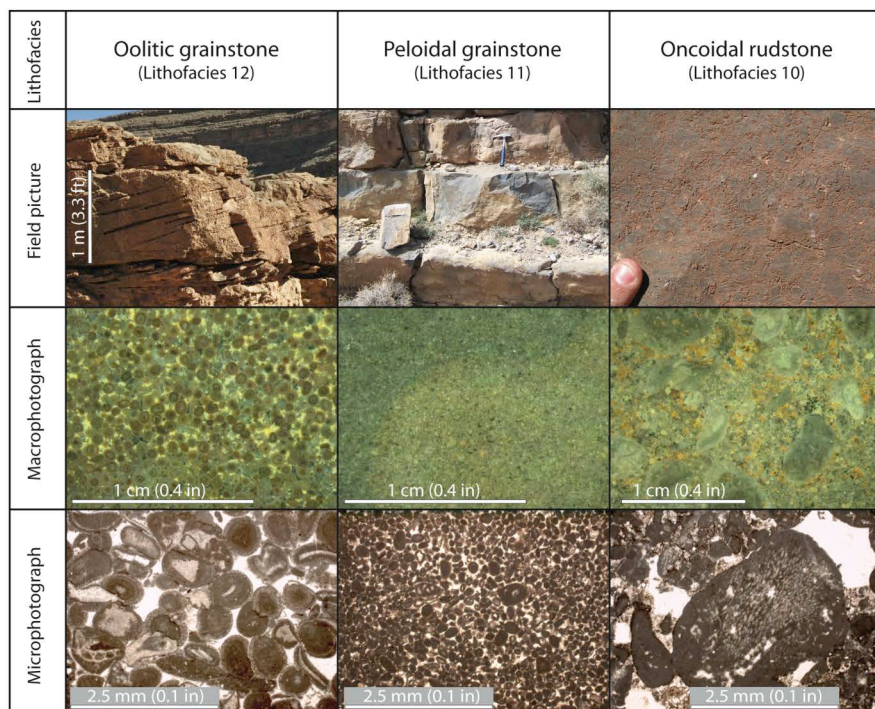
Figure 3.5: Palaeodepositional reconstruction of the Bajocian carbonate ramp profile with field pictures showing changes of lithofacies types and bedding stacking pattern between depositional domains. Approximate medium-scale depositional sequence locations (grey line) showing the two main progradation phases (bold grey line) of the carbonate ramp in the study window. A. Mud mound (Lithofacies 14) surrounding by cross-bedded oolitic grainstone. Field picture A is located at 10 m in Section I2. B and C. Bedding contrasts within the inner ramp (B), proximal middle ramp and distal middle to outer ramp (C). Field pictures B and C are located at 13 m in Section I7 and at 6 m in Section I8, respectively. D. Occurrence of coral-microbial bioconstructions (Lithofacies 2) within the distal middle to outer ramp. Field picture D is located at the base of Section NF-3. Within the inner ramp, note the transition from inner ooid grainstone shoals (yellow) to outer peloid grainstone shoals (orange). Refer to Figure 3.4 for lithofacies colors. FWWB = fair weather wave base; SWB = storm-wave base.



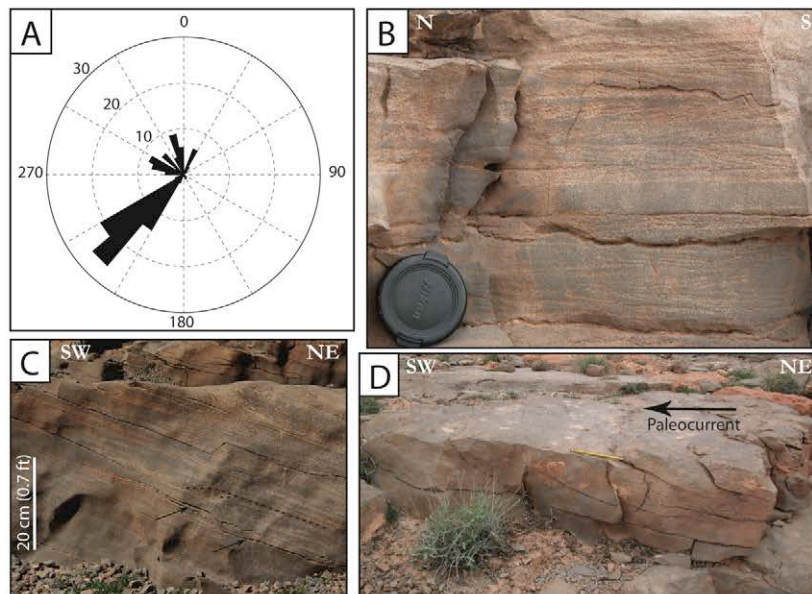
### 3.5.3.2. Shoal complex

The shoal complex is composed of peloidal grainstones (Lithofacies 11) in the outer shoal and oolitic grainstones (Lithofacies 12) deposited in the inner shoal (Figure 3.5B). A few meters thick and a kilometer long, the outer shoal (Figure 3.4) consists of well-sorted peloidal grainstone (Figure 3.6). Superficial ooids are frequent, but radial ooids are rare. The ooid nuclei are mainly peloids. No sedimentary structures have been recognized. The texture, sorting, and abundance of superficial ooids indicate moderate-energy conditions located above the fair weather wave base.

The inner shoal consists of several meters thick shoals that can be traced laterally across the study area (Figure 3.4). The inner shoal is composed of superficial and radial ooids (left column Figure 3.6) with lesser amounts of laminated, fine-radial ooids. Their nuclei are peloids, echinoderms, and unspecified mollusk clasts. The dominance of superficial and radial ooids suggests moderate-energy conditions (Strasser, 1986). Sedimentary structures such as cross-bedding, symmetric and asymmetric ripples, climbing ripples, and bidirectional ripples were measured in the field (Figure 3.7). The major palaeoflow direction is 225°N. The record of symmetric and asymmetric ripples and cross-beddings indicates the presence of unidirectional and bidirectional currents, probably due to tide and wave action. Microbial mounds (Lithofacies 14) were observed at the base of the study window interbedded with oolitic grainstone (Figures 3.4, 3.5A). The fabric is microbial thrombolite with a few recrystallized platy and branching corals, calcareous sponges, and demosponges.



**Figure 3.6: Micro- and macroscopic characterization of inner ramp lithofacies. Field picture of lithofacies 12 is located at 14 m in Section I5. Thin-section of lithofacies 12 is located at 11.2 m in Section I4. Field pictures and thin sections of lithofacies 11 and lithofacies 10 are located at 10.5 m and 7.2 m in Section I4.**



**Figure 3.7: Palaeocurrent features observed in oolitic grainstones. A. Compilation of palaeocurrent measurements showing a 225°N palaeoflow direction. B. Bidirectional ripples suggesting alternating palaeocurrent direction. C. Internal structures of cross-beddings showing the presence of climbing ripples (dashed) and mud drapes (arrow). D. Asymmetric ripples showing landward unidirectional current. Field pictures are located at 11.5 m in Section I4.**

### 3.5.3.3. Inter- to backshoal

Deposited between the oolitic shoal bodies are greyish to greenish marls (Lithofacies 13) composed of 20-25% non-carbonate minerals, mostly illite and quartz. Oolitic grainstone bodies a few decimeters thick (Lithofacies 12) were observed interbedded with the marls and show a medium- to poorly-sorted fabric with micritic and oolitic intraclasts. The occurrence of oolitic grainstones interbedded with marls suggests an inter- to backshoal with wash-over fan deposits from storms and high tides.

## 3.6. Depositional sequences

The hierarchical stacking pattern displays cyclical changes of palaeoenvironmental conditions (Figure 3.4). Due to lack of biostratigraphic or radiometric data from the study area, the present study chooses to apply a purely descriptive and time-independent nomenclature as defined by Strasser et al. (1999). Thus, the finest elementary sequences are called generically “small-scale” depositional sequences (Appendix A1), and progressively larger medium- and large-scale depositional sequences are also recognized. The stratigraphic succession contains three large-scale sequences (A, B, and C) within which we identified five medium-scale sequences (1, 2, 3, 4, and 5). These sequences show a thickening trend toward the northeastern sub-basin depocenter. Each sequence exhibits a thin deepening-upward trend at its base followed by a thick shallowing-upward trend marked at the top by a marine hardground.

Sequence boundaries are characterized by abrupt water depth changes from inner ramp below to distal middle ramp lithofacies above. Both the medium- and large-scale sequences exhibit deepening-upward trends at their bases. At the base, the interval is characterized by an open-marine biota association composed of debris of echinoid spines, crinoids, bryozoans, and brachiopods from alternating bioclastic packstone and marls (Lithofacies 4). The

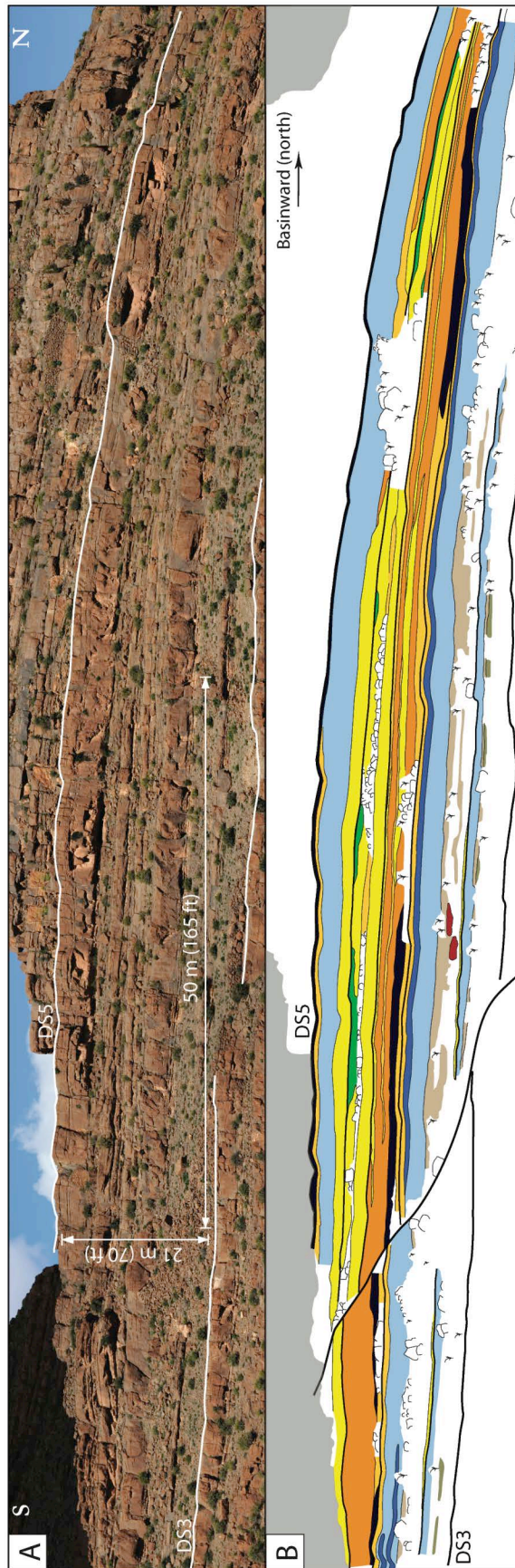
occurrence of terrigenous sediments (illite and quartz) within the interbedded marls, ferruginous peloids, and oyster-dominated lithosomes (Lithofacies 5) suggests the contributions of continental hinterland. The clastic input is related to the lowstand and early transgressive phase and reflects clastic sediment supply and basinward transport during low relative sea level. During the transgressive phase, a deepening-upward trend is interpreted from the progressive decrease of bioclast content upward and from the upward increase of alternating mudstone and marl (Lithofacies 3). Evidence of a maximum flooding surface is lacking, so the maximum flooding timeline is approximated at the top of the thicker marl interval.

The expression of the shallowing-upward trend changes according to its position in the stratigraphic succession. The incomplete Sequence A located at the top of the Agoudim Formation and base of the Assoul Formation reflects the onset of prograding shallow-water deposits into the sub-basin. The highstand deposits are characterized by the occurrence of microbial mounds interbedded with cross-bedded oolitic grainstone (Figure 3.5A). During the deposition of the large-scale Sequence B, the highstand deposit is recorded by the occurrence of peloid-dominated shoals interbedded with foreshoal rudstone deposits within medium-scale Sequence 2. Next, medium-scale Sequence 3 records the occurrence of oolitic shoals associated with marly backshoal deposits. The latter facies association suggests that Sequence 3 records the maximum progradation of the carbonate ramp in the study window (Figure 3.5). In addition, the upper sequence boundary DS 5 of medium-scale Sequence 3 (Figure 3.4) is characterized by up to five generations of *Gastrochaenolites* borings. This feature is interpreted to record a long and complex omission history and provides evidence that DS 5 is a major discontinuity surface. At the top of the stratigraphic interval, the incomplete large-scale Sequence C records an increase of accommodation as shown by the dominance of wackestone to packstone lithofacies from the middle ramp and by the increase in thickness of small-scale depositional sequences. The medium-scale Sequence 4 records the deposition of proximal middle ramp deposits associated with isolated rudstone bodies. The medium-scale Sequence 5 shows an increase of grainy lithofacies deposited in the outer and inner shoals suggesting another prograding shoal phase recorded in the large-scale Sequence C (Figure 3.5).

### 3.7. Scale-dependent geological heterogeneity

The choice of a suitable simulation methodology needs to be based on the intended scale of modeling, with considerations for the morphologies and spatial relationships between geological bodies (Falivene et al., 2007). This study provides field observations and a statistical analysis of carbonate heterogeneity (Figures 3.8, 3.9) to i) implement an adequate simulation methodology and then ii) justify our scale-dependent modeling strategy.

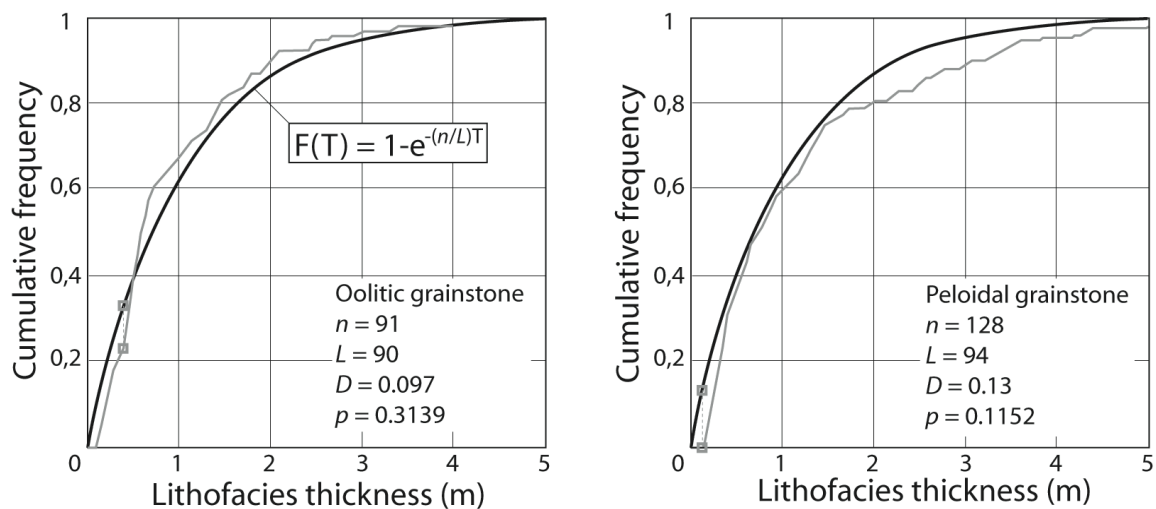




**Figure 3.8:** Transect of the east face of “Island” outcrop showing lithofacies distribution within medium-scale Sequence 3. A. Field photo displays continuous and low-angle stratal pattern. B. 2-D lithofacies distribution observed in the field. Note the lateral and vertical lithofacies variability. At the larger scale of the facies association, a layer-cake stratal pattern is observed. Refer to Figure 3.4 for lithofacies colors and Figure 3.2 for the location of the transect. DS = discontinuity surface.

At the lithofacies scale, shoal bodies show a general shoaling upward distal-to-proximal trend from oncoidal rudstone to peloidal grainstone to oolitic grainstone. This trend occurs in concert with a change of bedding pattern from massive in the proximal to few decimeters thick beds in the distal (Figures 3.5B, 3.6). This conceptual approach of shoal distribution is acceptable at the basin scale but does not fully integrate field observations. For example, oncoidal rudstone shows vertical and lateral transition to oolitic and peloidal grainstone in the inner ramp, but also displays transitions with lithofacies deposited in the middle ramp (Figures 3.4, 3.8). The complexity of lithofacies distribution and association suggests a mosaic-like arrangement through the carbonate ramp, especially from the inner to proximal middle ramp.

The Kolmogorov-Smirnov statistical test was applied to lithofacies thickness distributions to assess statistically the geological heterogeneity (Burgess, 2008). The test compares a sampled cumulative thickness distribution function with a theoretical exponential distribution function (Figure 3.9). The comparison estimates the difference  $D$  between both curves at each thickness. Then, a significance probability,  $p$ , is calculated to determine whether the maximum value of  $D$  occurs randomly or not in the present dataset. If  $p > 0.1$ , the candidate exponential distribution can be considered a good approximation to model the sampled lithofacies thickness curve. If  $p < 0.1$ , the exponential interpretation cannot be reasonably accepted. The test was carried out for oolitic grainstone ( $p = 0.3139$ ) and peloidal grainstone ( $p = 0.1152$ ) (Figure 3.9). Both lithofacies match the exponential function within tolerance suggesting a stochastic distribution pattern at the lithofacies scale. The Kolmogorov-Smirnov test supports the interpretation of a mosaic-like arrangement as observed in the field.



**Figure 3.9: Theoretical exponential (black) and sampled (grey) cumulative frequency distribution of thicknesses of the oolitic grainstone (left) and the peloidal grainstone (right). The formula of the theoretical exponential distribution is outlined in black, where  $T$  is the thickness,  $n$  is the number of lithofacies units, and  $L$  the stratigraphic thickness studied. The maximum difference between both curves is called  $D$  (grey square).**

The carbonate heterogeneity is less complex at the facies association scale than at the lithofacies scale. Despite the occurrence of interfingering at the transitions between facies associations (Figures 3.4, 3.8), the spatial relationships between the outer to distal middle ramp, proximal middle ramp, and inner ramp are known to be



laterally ordered, indicating the existence of a deterministic component in their distribution. We conclude that geological heterogeneity is more stochastically driven at the lithofacies scale than at the larger facies association scale. Consequently, the modeling methodology needs to take into account the characteristics of each level of observation by adjusting the relative strengths of stochastic and deterministic methods during simulation.

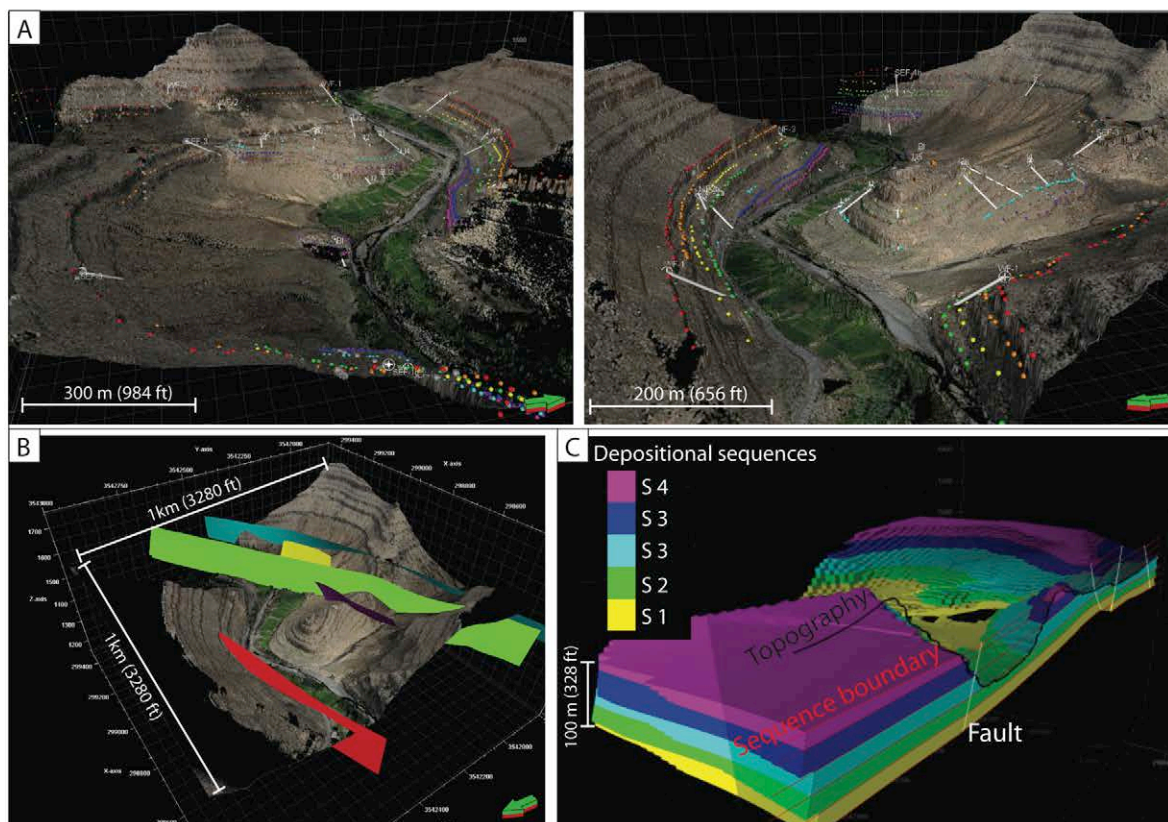
### 3.8. Scale-dependent modeling approach

The methodology consists of three steps, 1) building of the largest scale model based on the of stacking patterns of medium-scale sequences (Figure 3.10), 2) the modeling of facies association within the medium-scale sequences, and 3) the simulation of lithofacies distribution (Figures 3.11, 3.12, 3.13) within the facies association. Each step, which corresponds to one level of the stratigraphic hierarchy, follows a specific modeling methodology adapted to its sedimentary features. Care was taken to capture the dimension and morphology of carbonate bodies during variogram analysis (Figure 3.11) and to properly model their distribution by comparing field-based (Figure 3.4) and stochastically simulated (Figure 3.13) geological heterogeneity. The degree of concordance between input and output data were also used as a quality control factor. Within the geocellular model, the choice of cell dimensions is made by considering the size of the smallest geological features that need to be simulated. Significant lithofacies such as peloidal grainstone and oncoidal floatstone are locally as thin as 0.2 m (Figure 3.4). Accordingly, the geocellular model was constructed with grid cells 0.1 m thick, considering that two cells are needed to adequately resolve a feature. A horizontal cell dimension finer than 15 m would have allowed the model to capture further lateral variations, but computing limitations dictated a larger cell dimension no less than 15 m. Therefore, sedimentological features below 15x15 m, such as coral-microbial-dominated bioherms (Lithofacies 2) and microbial mounds (Lithofacies 14) cannot be explicitly captured in the model. The model contains 909 conformable layers and 5.7 million cells.

#### 3.8.1. Modeling the high-frequency depositional sequences

The first and largest scale of modeling is the construction of purely deterministic sequence stratigraphic surfaces. Five medium-scale sequence boundaries (DS 0, 3, 5, 7, and 8), four small-scale sequence boundaries (DS 1, 2, 4, and 6), five post-depositional faults, and 19 stratigraphic sections (Figure 3.10) were input to the model as grided elevation surfaces. A total of 5001 DGPS and LIDAR points were used to georeference these geological data (Figure 3.3). Sequence boundary surfaces were created using the minimum curvature algorithm with a 10 m grid node spacing. The five zones built in the model correspond to the five medium-scale depositional sequences described above (Figures 3.4, 3.10C). Despite the high density of DGPS and LIDAR points, additional user-defined control points were necessary in order to extrapolate as realistically as possible sequence boundaries across valleys and to avoid edge effects. The additional control points were carefully created to be consistent with sequence thicknesses and fault offsets measured in the field.

The mapping of medium-scale sequence boundaries reveals a general continuous and low-angle (from  $0.03^\circ$  to  $0.25^\circ$ ) dipping depositional profile toward northeast. The depositional profile becomes steeper toward the land and exhibits a 4 m palaeotopographic relief at the transition between the outer and inner shoal complexes (Figure 3.13).



**Figure 3.10: Input of geological data and building of the model framework. A: Two 3-D views of the input data, including the DEM built from LIDAR data, and the field mapping DGPS points of sequence boundaries (points) and faults (squares). Stratigraphic sections are located at the white lines in images. B: Dimensions of the digital outcrop model and location of the five major post-depositional faults modeled. C: Construction of the depositional sequence model used as a framework for stochastic simulation. Refer to Figure 3.2 for the location of the 3-D pictures. S = depositional sequence.**

### 3.8.2. Modeling the facies association

The second modeling step populates facies associations that characterize the inner, middle, and outer ramp within each medium-scale sequence. This step uses the stochastic algorithm Truncated Gaussian Simulation (TGSim) because it preserves the ordered transitions between depositional domains of the ramp (Figure 3.5) while allowing the use of conditioning tools, such as probability trends, during stochastic simulation. Particular attention was focused on the semi-variogram analysis of the shoal bodies' morphology (see above), which is a key interpretive input to the TGSim algorithm. Vertical and horizontal semi-variograms are plots of the semi-variance  $\gamma$  against sample-pair separation distance called "lag" distance (Figure 3.11). To calculate the vertical semi-variogram,

a 0.1 m “lag” distance was chosen to match the resolution of described sections. The “lag” distance for the horizontal semi-variogram was 50 m [164 ft], approximately the smallest between-section spacing.

The inner ramp represents 25% of the study area and contains inter-connected, 350 m long, 190 m width, and 5 m thick shoal bodies (Figure 3.11). The preferred orientation of elongation is 125°N, which is in agreement with palaeocurrent measurements (Figure 3.7). Three different types of shoal morphology were recognized (Figures 3.12, 3.13) in field observations (Figure 3.4). The most distal shoals are found at the transition between the proximal middle ramp and the inner ramp and consist of isolated, approximately 300 m long and up to 2 m thick rudstones. The landward increase of horizontal and vertical connectivity between shoal bodies leads to more complex morphologies. The outer shoal to foreshoal are characterized by planar, kilometer long, and up to 4 m thick shoals (Figures 3.4, 3.13). The stacking pattern of small-scale sequences displays a significant vertical compartmentalization of shoals separated by matrix-rich middle ramp bodies. Therefore, vertical shoal connectivity observed in the model (and in the field) is low. Toward the most proximal part of the ramp, the vertical connectivity across the small-scale sequence boundaries leads to more complex shoal body morphologies (Figure 3.13). The inner shoal is planar-to-domal, kilometer long, and up to 8 m thick.

### ***3.8.3. modeling the lithofacies***

For the final step, the three depositional domains of the carbonate ramp (Figure 3.12A) are filled by their unique association of lithofacies (Figure 3.12B). This modeling step captures the degrees of geological differentiation within the three types of shoal bodies (Figure 3.13). Both the mosaic-like lithofacies distribution (Figures 3.8, 3.9) and the morphological contrasts between lithofacies bodies (Figure 3.11, Table 3.1) can be simulated using Sequential Indicator Simulation (SISim). SISim is used because i) its method of populating lithofacies between data points can be independent of any geological trend and does not enforce lateral associations, and ii) a unique semi-variogram can be assigned to each lithofacies type. The operating mode of SISim is flexible enough to honor the observed variations in heterogeneity with one exception: the molluscan-coral bioherms (Lithofacies 5) were modeled using object-based modeling in order to create a scattered population of domal bioconstructions.

Semi-variogram analysis shows that each lithofacies is characterized by its own dimensions and preferred orientation. In the inner ramp, the hole effect (Gringarten and Deutsch, 2001; see above) is observed within the minor axis lithofacies semi-variograms (central column Figure 3.11) indicating the occurrence of sub-parallel, regularly spaced lithofacies bodies with average interbody spacing approximately 349 m. Oolitic grainstones constitute 32.8% of the inner ramp and average 200 m in length, 140 m in width, and 2 m in thickness with spacing of approximately 300 m [984 ft]. These bodies have a preferred elongation orientation of 114°N. Peloidal grainstones (56.9% of the inner ramp) are 260 m long, 145 m wide, and 3.1 m thick and are oriented 97°N with sub-parallel spacing of approximately 300 m. The oncoidal rudstone (10.3% of the inner ramp) shows significant anisotropy in vertical and horizontal dimensions. The 210 m long, 190 m wide, and 1 m thick rudstone bodies exhibit a nearly isotropic morphology.

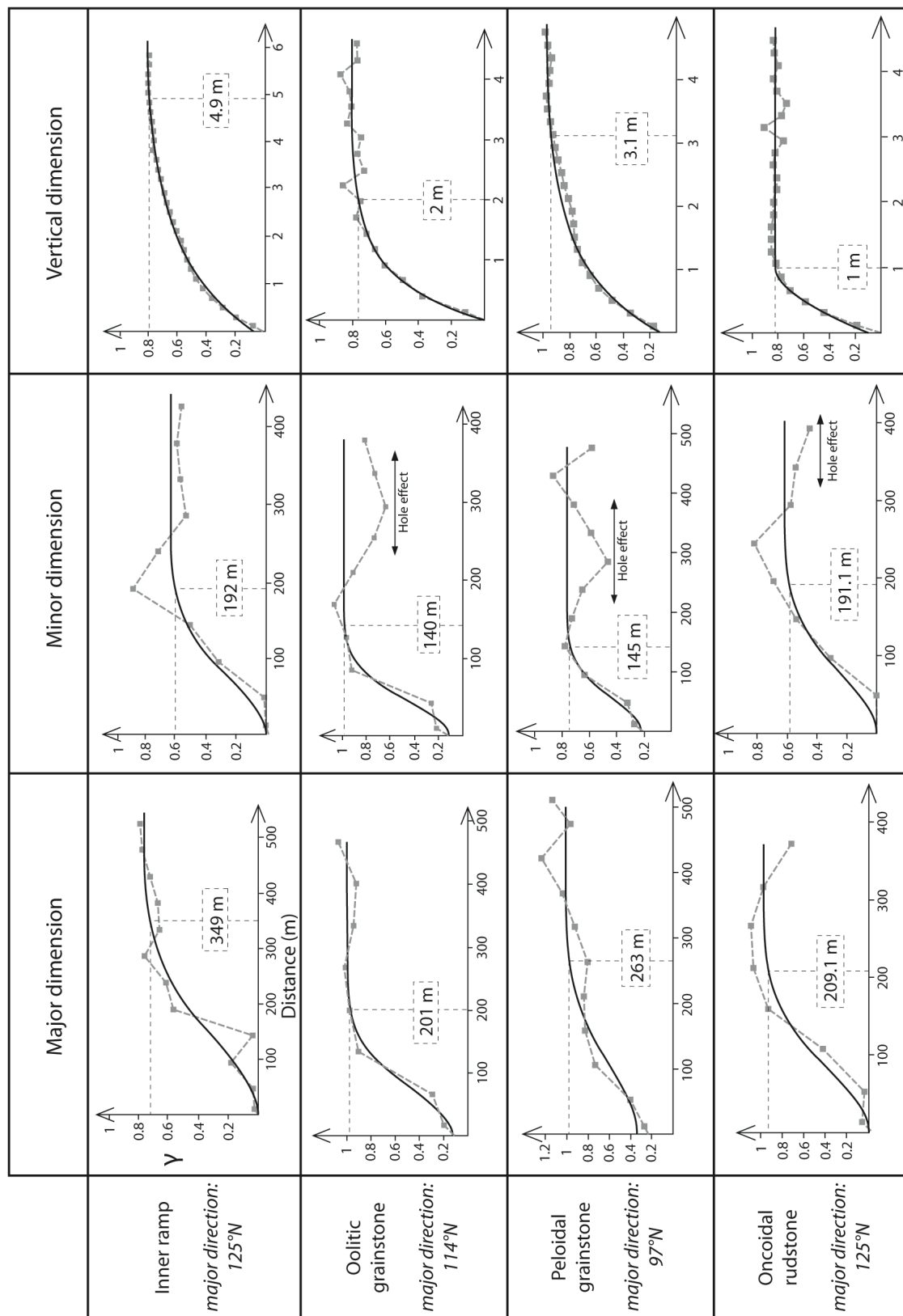
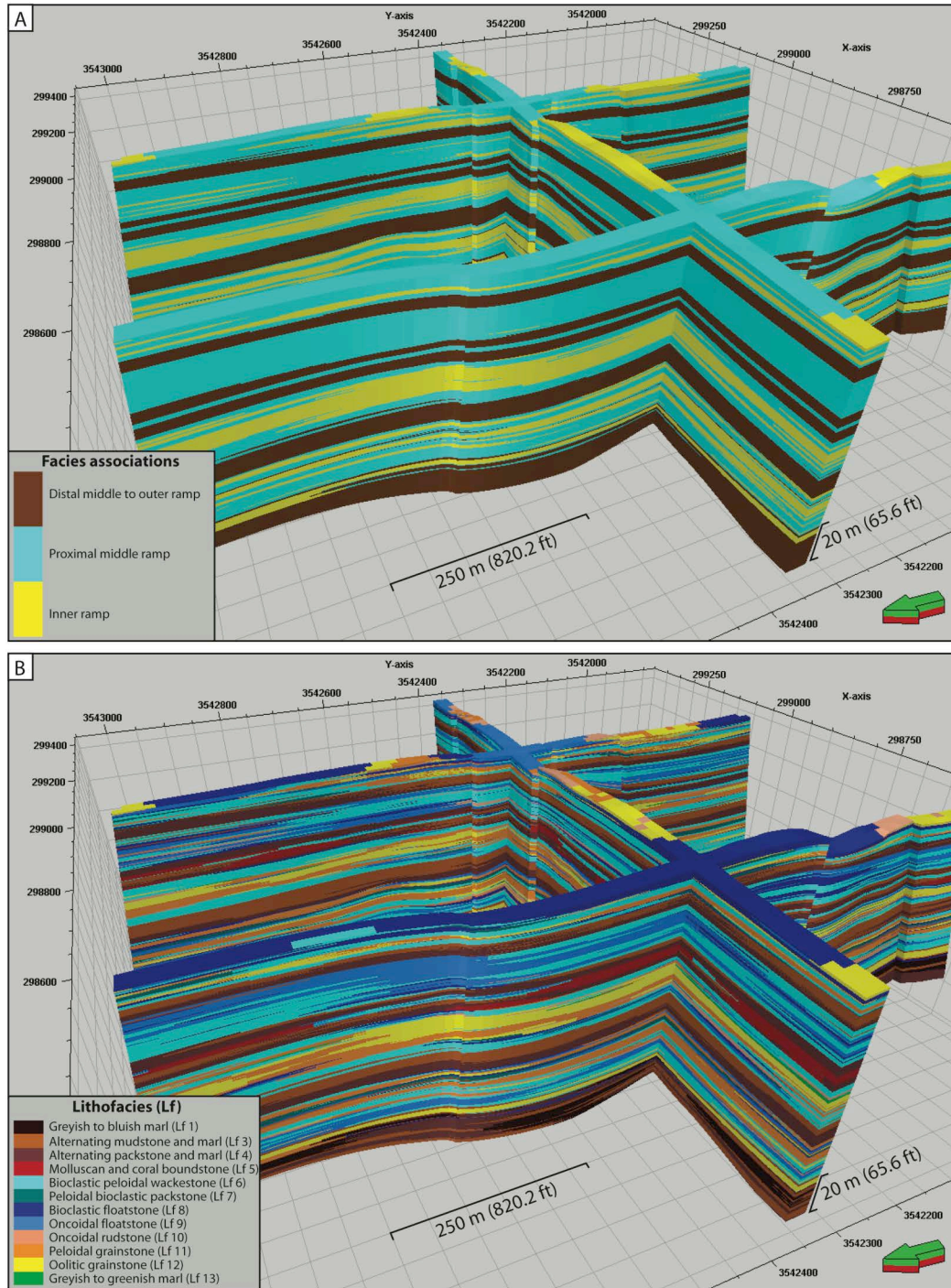


Figure 3.11: Summary of the major, minor, and vertical dimensions of inner ramp shoals and inner ramp lithofacies using semi-variograms, which are plots of the semi-variance  $\gamma$  against the distance. Note the fitting of experimental variograms (dashed grey curve) with idealized type semi-variograms (black curve). Oscillations in the experimental variograms (“hole effect”) indicate regularly spaced periodicity of features. The hole effect observed in the minor variograms of oolitic grainstone, peloidal grainstone, and oncoidal rudstone, suggests an echelon arrangement of the geobodies.





**Figure 3.12: 3-D view of the facies association model (A) and lithofacies model (B) (vertical exaggeration 3x). Note the constraints of lithofacies occurrence and distribution within each facies association. Refer to Figure 3.2 for the location of the 3-D pictures.**

The three types of shoal bodies observed within the inner ramp display significant changes in their facies associations (Figures 3.4, 3.13). Within the proximal middle ramp, isolated shoal bodies comprise mainly oncoidal rudstone and a lesser fraction of peloidal grainstone. Oolitic grainstone is absent. Within the outer shoal to foreshoal,

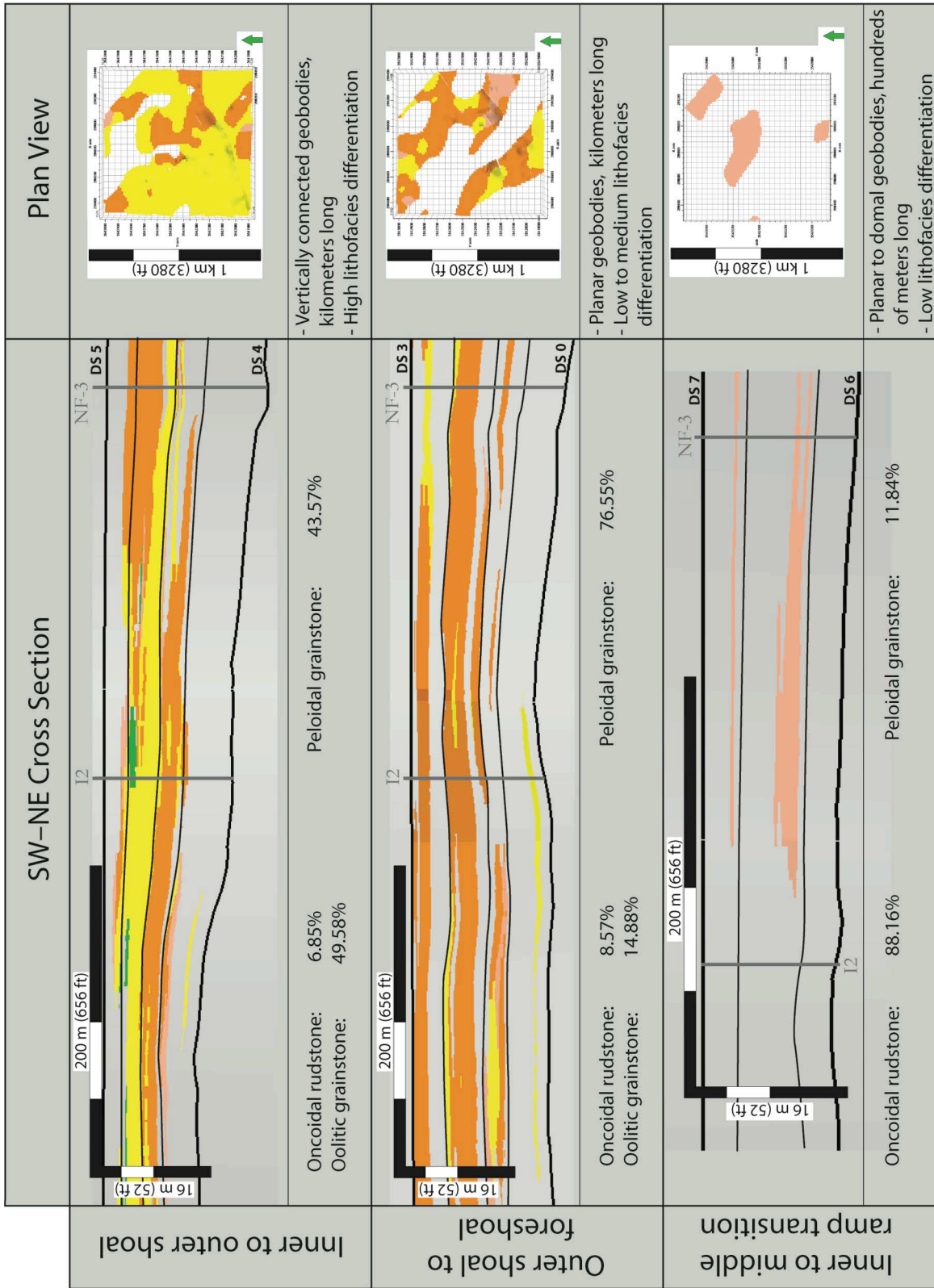
we find kilometers long planar shoal bodies composed of peloidal grainstones with frequent and locally deposited oolitic grainstones and oncoidal rudstones (Figure 3.13). In the most proximal part of the inner ramp, shoal bodies show a high degree of heterogeneity, characterized by vertical stacking and lateral transition between peloidal and oolitic grainstones (Figure 3.13). A low fraction of oncoidal rudstone occurs as thin and discontinuous layers.

## 3.9. Discussion

### *3.9.1. Scale-dependent geological heterogeneity and their controlling factors*

Along the depositional profile of the Bajocian carbonate ramp of the Assoul Formation, a clear proximal-distal linear trend between facies associations (Figure 3.5) is evidenced by lateral lithofacies variability (Figures 3.4, 3.13) and the distribution of organic and inorganic components (Figure 3.6, Table 3.1). The kilometer long shoal complex of the inner ramp can be divided into three distinct shoal bodies with different morphologies from proximal to distal, 1) planar-to-domal, kilometer long, up to 8 m thick, 2) planar, kilometer long, up to 4 m thick, and 3) isolated, hundreds of meters long shoals at the transition between the inner and proximal middle ramp (Figure 3.13). The carbonate ramp displays two episodes of basinward progradation through the stratigraphic succession (Figures 3.4, 3.5) that are likely controlled by change of accommodation. This assumption is consistent with field observations that display a clear relationship between lithofacies types and the thickness of depositional sequences (Figures 3.4, 3.5, 3.13). The abundance of grainstone lithofacies increases within thin depositional sequences, whereas wackestone to packstone lithofacies association dominates in thicker sequences. In addition, vertical variability of both lithofacies type and thickness of depositional sequences shows repetitive deepening- and shallowing-upward trends, suggesting relative sea level fluctuation and associated change in accommodation as a major controlling factor on the studied stratigraphic succession. For comparison, the Amellago Formation underlying the Assoul Formation shows a similar carbonate ramp profile and a comparable stacking pattern of lithofacies and depositional sequences. A tens-of-kilometers long study of Amellago Formation (Pierre et al., 2010) also suggested that the carbonate ramp was primarily controlled by accommodation changes.

At the bedding scale, the lithofacies heterogeneity cannot be fully explained by accommodation changes. A lithofacies mosaic (Figures 3.8, 3.9) implies local changes of environmental conditions (clastic input, turbidity, hydrodynamic level, storm frequency, water geochemistry, or nutrient availability), which affect carbonate precipitation and transport at similar water depth (Rankey, 2004; Wright and Burgess, 2005; Strasser and Védrine, 2009). In the present study, the oolitic-dominated inner shoal and peloidal-dominated outer shoal consisted of a mosaic of grainstone lithofacies, marls, and microbial mounds (Figures 3.4, 3.13), suggesting that intrinsic parameters such as hydrodynamic level, storm events, tidal parameters or differential fluvial input add to the inherent lithofacies disorder. The occurrence of both linear and mosaic arrangements of carbonate bodies within the Assoul Formation are mainly controlled by external and internal factors, respectively.



**Figure 3.13: SW-NE cross sections (left) of the scale-dependent model located within the inner ramp and representative model layer plan view maps (right). In the maps, note the strongly oriented and relatively well-connected distributions of the facies association tracts (all but the subject facies association are filtered out and appear grey), and the comparatively patchy mosaic of lithofacies (yellow, orange, and tan). Note the topographic relief at the transition between inner and outer shoals. Refer to Figure 3.12 for lithofacies colors and Figure 3.2 for the location of the cross sections. DS = discontinuity surface.**

### ***3.9.2. Scale-dependent geological modeling***

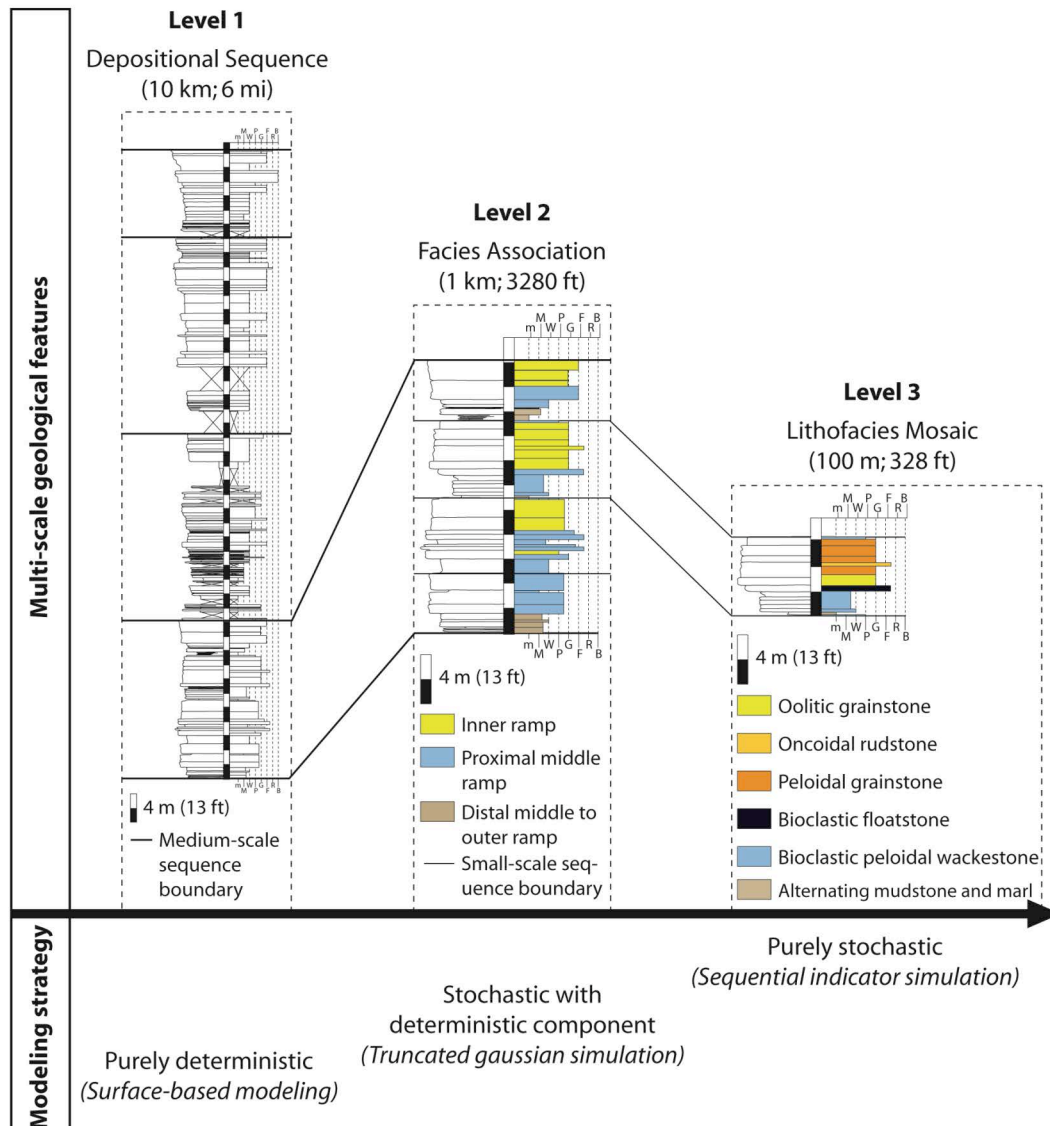
The study window displays scale-dependent geological heterogeneity, where each stratigraphic level displays specific sedimentary features (Figure 3.14). The present study establishes a different simulation method designed to reproduce the unique characteristics of each of those levels (Figure 3.14). The modeling techniques extend from a deterministic approach at the largest stratigraphic architecture scale to an environment-specific stochastic approach at the smallest lithofacies scale (Figure 3.14). On the one hand, a purely stochastic algorithm like SISim, which were used to simulate mosaic-like lithofacies patterns, should not be used to model the entire study window. If we had chosen to apply only the SISim algorithm, the ordered transitions between facies association across the depositional profile would not have been captured, and the final model would have included significant errors in terms of geobody placement and association. On the other hand, TGSim can only use a single variogram for all facies, which is clearly an oversimplification of the geological reality (Figure 3.11) and its operating mode produces a poor approximation of the observed lithofacies mosaic (Amour et al., 2012). The above examples highlight the difficulty of modeling carbonate rocks by applying one single method. Each algorithm has unique capabilities and drawbacks (Journel et al., 1998; Falivene et al., 2006a, 2007) that, in one location or another, would incorrectly render the field observations.

### ***3.9.3. Geological heterogeneity and modeling strategy: Recommendations***

During the last two decades, advances in the field of statistical analysis and field-based observations of geological heterogeneity within modern (Wilkinson and Drummond, 2004) and ancient shallow-water carbonate systems (Wilkinson et al., 1997, 1999; Burgess, 2008; Strasser and Védrine, 2009), have emphasized the common abundance of a mosaic-like distribution of lithofacies, the finest scale of our modeling strategy. At the coarser basin scale, the association of lithofacies, characterizing similar depositional conditions, tends to exhibit less spatial disorder in the sedimentary record. Facies associations display then a more gradational and linear arrangement between carbonate bodies along a proximal-distal depositional profile (Wright and Burgess, 2005), as shown here and in previous studies (Gischler and Lomando, 1999; Aurell and Bádenas, 2004; Bádenas and Aurell, 2010; Pierre et al., 2010).

During the same two decades, outcrop and sub-surface modeling has known remarkable enhancements of the simulation tools used (Coburn et al., 2006). These improvements were resulted from the large number of simulation techniques that were being constantly refined (Gringarten and Deutsch, 2001; Coburn et al., 2006; Jones et al., 2008, 2009; Kenter et al., 2008; Tolosana-Delgado et al., 2008) and successfully applied to model carbonate systems. These simulation techniques include a deterministic approach with surface-based modeling to capture the architecture of carbonate platforms (Sech et al., 2009) and an algorithm-based method to stochastically populate carbonate bodies (Aigner et al., 2007; Pöppelreiter et al., 2008; Tomás et al., 2010). Each method has been compared and contrasted in outcrop facies models in order to assess their major advantages and drawbacks (Falivene et al., 2006a, 2007; Aigner et al., 2007; Amour et al., 2012). Considerable effort has been devoted to the generation and improvement of simulation tools and techniques, whereas a reflection on how to best combine them into a single 3-D model has been lacking (Zappa et al., 2006; Koehrer et al., 2010).





**Figure 3.14: Summary of scale-dependent geological features based on section SEF-1 from the large-scale stacking pattern of high-frequency depositional sequences (level 1) to the intermediate-scale facies association (level 2) and to the finest-scale lithofacies types (level 3). The modeling strategy that was used for each level is noted across the bottom. Note the alignment between the observed spatial arrangement of geological features and the capabilities of simulation techniques chosen for each set of features. Refer to Figure 3.2 for the location of section SEF-1.**

The inability for a single simulation method to correctly render all sedimentary features is illustrated by the need to resort to interactive facies correction (pixel painting to correct facies distribution) during simulations (Willis and White, 2000; Aigner et al., 2007; Palermo et al., 2010). A scale-dependent modeling approach takes advantage of each technique's abilities, while its drawbacks can be offset by the use of other simulation tools and thus provide essential computing flexibility to model carbonate rocks. The selection of an appropriate combination of simulation tools involves a full knowledge of carbonate heterogeneity at each level of the stratigraphic hierarchy. In addition,

the implementation of multiple techniques into the same workflow requires the development of innovative modeling methodologies. Better understanding of modern and ancient carbonate systems (e.g., Lehrmann and Godlhammer, 1999; Wilkinson et al., 1999; Wright and Burgess, 2005; Strasser and Védérine, 2009) should guide the design of simulation strategies. A scale-dependent modeling approach promises to be a valuable method to build outcrop and sub-surface models.

### 3.10. Conclusion

The investigation of a study area 1 km by wide and 100 m thick within a Bajocian carbonate ramp has demonstrated the need for a scale-dependent modeling approach ranging from the large-scale stacking pattern of depositional sequences down to the facies associations at the intermediate scale, and ultimately down to lithofacies types at the finest scale. An individual simulation method has been customized for each hierarchical level of heterogeneity based on the characteristics needing to be integrated into the 3-D outcrop model. Field observations and statistical analysis have documented the variability of shoal morphologies, dimensions, distributions, and associations and provides new perspectives on modeling strategies that take advantage of algorithm strengths and capabilities.

- 14 shallow-marine lithofacies were identified and grouped into three main facies associations; an inner ramp, a proximal middle ramp, and a distal middle to outer ramp. The inner ramp was further subdivided into sub-association, an inter- to backshoal with marly deposits, an oolitic inner shoal, a peloidal outer shoal, and a foreshoal with oncoidal rudstones. The stratigraphic architecture shows five medium-scale sequences composed of four to five small-scale sequences.
- Scale-dependent geological heterogeneity within Assoul Formation requires the combination of both a deterministic and stochastic approach to realistically capture and model the spatial geobody arrangement. The largest scale model, comprising the structural and stratigraphic framework and stacking pattern of depositional sequences (1) was built using a deterministic surface-based modeling approach. The next scale model, the facies association (2) was modeled using Truncated Gaussian Simulation to portray the ordered trends observed between facies associations. Finally, the finest scale features, individual lithofacies (3) were modeled using Sequential Indicator Simulation because of its tendency to produce spatially independent lithofacies elements. Additionally, object based modeling was used to insert discrete bioherm objects into the facies model.
- The first modeling step focused on sequence boundary morphologies. The depositional profile is a low-angle (from  $0.03^\circ$  to  $0.25^\circ$ ) ramp with a 4 m topographic high at the transition between the inner and outer shoals. At the facies association scale, the kilometers long shoal complex of the Assoul Formation is composed of 1) planar-to-domal, kilometer long, and up to 8 m thick shoals in the proximal part of the inner ramp, 2) planar, kilometer long, and 3 to 4 m thick shoals within the outer shoal and foreshoal, and 3) isolated, hundreds of meters long, and 1 to 2 m thick foreshoal bodies at the transition between the proximal middle ramp and the inner ramp (3). At the finest scale of modeling, each grainstone lithofacies characterized by its own unique

dimensions, occurs in different proportions within the three types of shoal bodies. The linear and gradational trend between facies associations is influenced by changes in accommodation, whereas intrinsic parameters such as hydrodynamic level, storm events and differential fluvial input controlled the lithofacies mosaic.

- The use of one single simulation technique across all scales is unlikely to produce a realistic 3-D model of shallow-water carbonate systems. The implementation of several techniques adapted to each level of the stratigraphic hierarchy will i) provide essential computing flexibility for simulation and ii) lead to better integration of the geological heterogeneity in a 3-D model. If further efforts are devoted to the methods to combine several simulation techniques into a modeling workflow, we will produce better geologic models and thus improve sub-surface reservoir simulations at the inter-well spacing.



# Lateral variability of cycle across the Latemar platform top: A spatially-dependent cyclicity record (Dolomites, northern Italy)

### *Abstract*

Previous studies on the Latemar isolated platform have assumed that the expression and duration of each carbonate cycle was unvarying across the platform top. The recognition of margin-to-lagoon increase in the number of carbonate cycles (up to 25%), indicating the record of cycles with different duration, has provided a new viewpoint on this topic. Cyclostratigraphic interpretations need to be re-investigated in order to take into account lateral cycle variability, which was previously assumed to be insignificant.

The study area investigated a 125 m thick and 800 m long, backreef-to-lagoon transect spanning from the LCF to MTF. The data set was built on the collection 15 sections correlated by using five marker horizons and located within Cima del Forcellone outcrop. Three types of cycles were identified i) meter-thick, subtidal-dominated Type A cycles deposited in the lagoon, ii) decimeter-thick, peritidal-dominated Type B cycles recorded in the backmargin, and iii) supratidal-dominated Type C cycles located in the tepee belt. Lateral tracing of cycles indicated that Type A cycle, recorded in the lagoon, grades to a bundle of two to three Type B cycles in the backmargin, leading to an increasing of 40% (locally 66%) of cycle number.

The establishment of a new stratigraphic nomenclature was performed in order to take into account such lateral variability. Field-based observations identified six orders of cyclicity, from high to low order: elementary cycle corresponding to Type B cycles, elementary cycle set defining Type A cycle and small cycle set, which corresponds to megacycle *sensu* Goldhammer et al. (1989). Intermediate cycle sets, medium cycle sets, and large cycle sets were also recognized. At a larger scale, the aggradation stacking pattern of the Latemar platform top alternated between periods of strong aggradation associated with differential carbonate accumulation along the depositional profile and periods of tepee growth within the margin that come along with the infilling of the interior platform.

The expression of the Latemar cyclicity is highly dependent of the location of the study area along the depositional profile or across the stratigraphic record. The field-based investigation of lateral cycle variability is the only method that allows to distinguish each order of the Latemar cyclicity record.

## 4.1. Introduction

The stacking patterns of lithofacies and cycles are of primary importance for the reconstruction of the evolution of ancient shallow-water carbonate systems (Hardie and Shinn, 1986; Read, 1995; Lehrmann and Goldhammer, 1999). Cyclostratigraphic analysis investigates the hierarchical arrangement of cyclic depositional packages, which is commonly explained by oscillations of the relative sea level controlled by Milankovitch forcing (Lehrmann and Goldhammer, 1999; Hillgärtner and Strasser, 2003). Milankovitch theory relies on the recognizance in the sedimentary record of quasi-periodic perturbations in the Earth's tilt and orbit, which influence the incoming solar radiation at different latitudes (e.g. Gradstein et al., 2004; Schlager, 2005). These perturbations induce changes in climate leading to waxing and waning of ice caps and thermal expansion and contraction of oceans, which in turn

control periodic oscillations of the global sea level. There are three orbital parameters: i) changes in eccentricity with periodicities of 95, 123, and 413 kyr, ii) obliquity variation with a 41 kyr cyclicity, and iii) changes in precession with periodicities of 19 and 23 kyr. The multiple orders of global sea level oscillation controlled by Milankovitch forcing were identified in Proterozoic to Phanerozoic sedimentary record and used as a high-resolution chronostratigraphic tool (Lehrmann and Goldhammer, 1999; Strasser et al., 2000; Hillgärtner and Strasser, 2003). In combination with sedimentation rate and subsidence rate, global sea level fluctuations (allocyclic model) are commonly postulated as the main controlling factors on the stacking pattern of lithofacies and cycles in ancient carbonate systems. A number of authors (Drummond and Wilkinson, 1993; Wilkinson et al., 1997; Wilkinson and Drummond, 2004; Burgess, 2008) challenged the implicit assumption of a more or less deterministic distribution of lithofacies and cycles across the sedimentary record, as assumed by the allocyclic model. The latter studies documented the common occurrence of a random distribution of lithofacies in ancient and modern carbonate settings, which was thought to result from the predominance of internal factors. Cycles controlled by internal factors such as tidal-flat progradation (Ginsburg, 1971; Pratt and James, 1986), spatial variability of carbonate production and transport (Wright and Burgess, 2005), irregular infilling of accommodation (Eberli et al., 2008), are considered autocyclic.

The establishment of a reliable cyclostratigraphic framework within carbonate successions requires the implementation of various dating methods (cyclo-, bio-, chemo-, magnetostratigraphy, and radiometric dating), spectral analysis, and physical tracing of stratigraphic surfaces in order to insure model-independent analyses. Nevertheless, very few studies have reported such integrated stratigraphic dataset within shallow-water carbonate systems (Zühlke, 2004). The Latemar isolated platform represents an ideal location to investigate the stacking pattern of shallow-water carbonate cycles, their controlling factors and duration. Cyclostratigraphic (Hardie et al., 1986; Goldhammer and Harris, 1989; Goldhammer et al., 1990), biostratigraphic (Brack and Rieber 1993; De Zanche et al., 1995; Brack et al., 1996), and magnetostratigraphic (Kent et al., 2004) investigations as well as radiometric dating of ash layers (Mundil et al., 1996, 2003) and spectral analyses (Hinnov and Goldhammer, 1991; Preto et al., 2001, 2004; Zühlke et al., 2003), were performed on the stratigraphic succession of the Latemar platform.

The stratigraphic succession of the Latemar platform top consists of few decimeters to meter thick, subtidal to peritidal carbonate cycles, which can be grouped into shallowing- and thinning-upward bundles. Previous authors have called these bundles either 1) megacycle or pentacycle *sensu* Goldhammer and Harris (1989) or 2) macrocycle *sensu* Zühlke et al. (2003). The majority of previous studies analyzed and interpreted the cyclic stacking pattern, based on the assumption that each cycle is laterally continuous along the depositional profile (Goldhammer and Harris, 1989; Goldhammer et al., 1990; Mundil et al., 2003; Zühlke et al., 2003; Kent et al., 2004; Zühlke, 2004; Emmerich et al., 2005b) (Figure 4.1). Each carbonate cycle was therefore interpreted as time-equivalent, representing the elementary depositional package of the cyclicity record. This assumption was independently of either its location within the platform top or its stratigraphic position. Lateral continuity of cycles was one criterion to infer an autocyclic model to the platform growth, which was controlled by either Milankovitch (Goldhammer et al., 1990; Hinnov and Goldhammer, 1991) or sub-Milankovitch forcing (Zühlke et al., 2003; Zühlke, 2004). The

recognition that some carbonate cycles are discontinuous from the margin to the lagoon has provided a new viewpoint on this topic (Peterhänsel and Egenhoff, 2008). Such observation implies that what in on location appears as a bundle of carbonate cycles laterally corresponds to a single cycle. Hence, the stacking pattern and temporal duration of each cycle vary along the platform top as well as across the stratigraphic succession. Changes of the expression of the cyclicity record are of primary interest and need to be considered for the establishment of a reliable sequence stratigraphic framework.

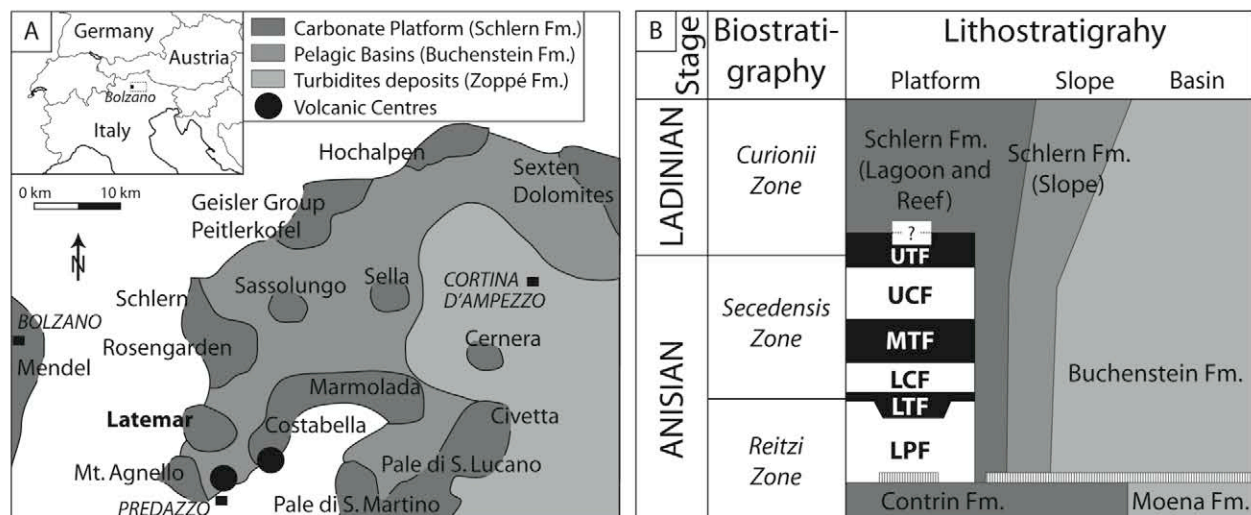
The aim of the present study is the investigation and quantification of lithofacies and cycle variability along the Latemar platform top. For this purpose, a detailed, field-based study of a 800 m long margin-to-lagoon transect was carried out across a 125 m thick stratigraphic interval. The evaluation of lateral cycle variability is required to emphasize its importance in the sedimentary record and estimate its impact during the establishment of a cyclostratigraphic framework.

	<b>Goldhammer and Harris (1989); Goldhammer et al. (1990)</b>	<b>Preto et al. (2001, 2004)</b>	<b>Zühlke et al., 2003; Zühlke, 2004</b>	<b>Egenhoff et al., 1999; Peterhänsel and Egenhoff, 2008</b>	<b>This study</b>
<b>Working hypothesis</b>	- No lateral variability of cycle	- Milankovitch model-dependant calibration for spectral analysis - No lateral variability of cycle	- No lateral variability of cycle	- No lateral variability of cycle (Egenhoff et al., 1999) - Cycles are laterally variable (Peterhänsel and Egenhoff, 2008)	- Cycles are laterally variable
<b>Cyclicity nomenclature (From high to low order)</b>	(1) Cycle (precession) (2) 1:5 bundled megacycle called pentacycle (eccentricity) (3) Long-term third-order depositional sequence or cycle	(1) Short precession peak at 1/(17.6 ky) (2) Sedimentary cycle: long precession peak at 1/(21.7 ky) (3) Weak obliquity peak at 1/(35.6 ky) (4) Eccentricity peak at 1/(95 ky) (E2), 1/(125 ky) (E3), and 1/(400 ky) (E1)	(1) Microcycle (sub-Milankovitch) (2) 1:3.61 (sub-Milankovitch or condensed precession) bundled macrocycle (3) 1:4.72 (precession) bundled macrocycle (4) Cycle bundles: stacking of 1:9.94 (obliquity), 1:23.95, 1:105.65 (short and long eccentricity) microcycles	(1) Small-scale cycle (sub-Milankovitch) (2) Meter-scale cycle (sub-Milankovitch?) (3) Pentacycle (precession or eccentricity) (4) Third-order facies change	(1) Elementary cycle (2) Elementary cycle set: stacking of 2 to 3 elementary cycles (3) Small cycle set: stacking of 4 to 5 elementary cycles (4) Intermediate, medium, and large cycle sets
<b>Vertical cycle and facies variability</b>	- Amalgamed/condensed megacycle controlled by large-scale (third-order) accommodation changes	- Periodic variation of cycle and facies thickness	- Periodic variation of cycle thickness - Amalgamation/condensation referring to Goldhammer et al., 1990	- Cycle and facies variation according to large-scale accommodation changes	- Cycle and facies variation according to large-scale accommodation changes
<b>Lateral cycle and facies variability</b>	- Not investigated but assumed to be laterally continuous	- Facies variation referred to Egenhoff et al., 1999 - No cycle variation based on a semi-automatic analysis	- < +/- 3% variation of cyclic number - 90% of all macrocycle tops continuous - A "layer-cake" geometry of the platform top	- Facies variation between marginal and lagoonal deposits - Up to 25% increase of cycle number from the lagoon to margin in the UCF	- Facies variation between backreef, tepee belt, and lagoonal deposits - Up to 40% increase of cycle number from the lagoon to margin from the LCF to the MTF
<b>Factor driving Latemar cyclicity</b>	- 100 kyr eccentricity superimposed on 20 kyr precession	- Milankovitch control with dominant forcing from the climatic precession	- Eccentricity (100 kyr) and precession (19.3 kyr) superimposed on sub-Milankovitch (4.2 kyr and 15.15kyr) forcing	- High-frequency low-amplitude sea-level fluctuation affecting solely the elevated tepee belt - Minor influence of sediment redistribution as a shallowing-upward contributing factor	- Milankovitch and sub-Milankovitch forcing influenced by the palaeotopographic profile - Minor influence of sediment redistribution and unfilled accommodation

**Figure 4.1: Summarize of interpretations of the Latemar cyclicity based on cyclostratigraphic studies (Goldhammer et al., 1987, 1990; Egenhoff et al., 1999; Peterhänsel and Egenhoff, 2008) and spectral analysis (Preto et al., 2001, 2004; Zühlke et al., 2003; Zühlke, 2004). Most of the studies were based on the working hypothesis that lateral variability is insignificant and therefore each elementary depositional package is time-equivalent, representing the same order of cyclicity across the platform top.**

## 4.2. Geological setting

The Dolomites, located in northeastern Italy, comprise outstanding exposures of Triassic shallow-water carbonate platforms, which developed within the northwestern Tethyan passive continental margin (Figure 4.2A), later uplifted during the Alpine collision. During the Early Anisian (Early Middle Triassic), the region was characterized by a widely spread, carbonate-clastic mixed ramp (Werfen and Contrin Formations) (Massetti and Neri, 1980; De Zanche and Farabegoli, 1988) situated at low latitudes (15-20°N; Dercourt et al., 2000). A Middle to Late Anisian transpressive-transpressive tectonic event led to the fragmentation of the ramp into graben and horst structures (Gaetani et al., 1981; Doglioni, 1987; Castellarin et al., 1988; Bertotti et al., 1993). During the Late Anisian to Early Ladinian, the topographic highs played the role of nuclei for the development of numerous isolated carbonate platforms such as the Latemar platform (Schlern Formation) (Gaetani et al., 1981; Bosellini, 1984; Doglioni, 1987).



**Figure 4.2:** A. Schematic palaeogeographic map of the Dolomites during the Late Anisian to Early Ladinian (after De Zanche and Farabegoli, 1988 and Emmerich et al., 2005a). The Latemar platform is part of a large complex of Triassic carbonate platforms located in a passive continental margin at the northwest end of the Tethys Ocean. B. Stratigraphic column of the Latemar platform (after Brandner et al., 1991). Biostratigraphy based on ammonoid faunas after Brack and Rieber (1993), Brack et al. (1996), and Emmerich et al. (2005a). Lithostratigraphic subdivision after Egenhoff et al. (1999). LPF = Lower Platform Facies; LTF = Lower Tepee Facies; LCF = Lower Cyclic Facies; MTF = Middle Tepee Facies; UCF = Upper Cyclic Facies; UTF = Upper Tepee Facies.

The Latemar isolated platform is located in the southwestern part of the Dolomites, forming a small mountain range southeast of Bolzano with its longest extension from southeast to northwest of approximately 5 km (Figure 4.2A). The Latemar platform formed a submarine relief of around 800 m (Figures 4.2A, 4.2B), characterized by a flat subtidal to peritidal platform top (Schlern Formation; Figures 4.2A, 4.2B) (Gaetani et al., 1981; Bosellini, 1984) with 25° to 35° dipping slope deposits, and surrounded by partly anoxic basins (Buchenstein or Livinallongo Formations) (Bosellini and Rossi, 1974; Bosellini, 1991). At the margin-to-slope transition, localized collapses of lagoonal blocks, overlain by prograding deposits, were observed and thought to be caused by syn-sedimentary



tectonic activity (proximity of volcanic centers and a major strike-slip fault, the Stava Line) (Doglioni, 1987; Emmerich et al., 2005a; Preto et al., 2011). During the Late Ladinian to Early Carnian, a regional tectono-magmatic event (Viel, 1979) buried some of the carbonate platforms such as the Latemar platform under hundreds of metres thick volcanic products of the Wengen Group.

### 4.3. Latemar isolated platform

#### 4.3.1 *Stratigraphic succession*

The platform top comprises a 720 m thick, subtidal to peritidal succession, which has been divided into six major stratigraphic units (Figure 4.2B; Goldhammer and Harris, 1989; Egenhoff, et al., 1999). At the base, the Lower Edifice (Gaetani et al., 1981) represents the earliest stage in the evolution of the platform, characterized by a strong aggradational stacking pattern. This early phase comprises the Lower Platform Facies (LPF) and the Lower Tepee Facies (LTF) (Figure 4.2B). The LPF consists of subtidal deposits with abundant submarine hardground surfaces and rare subaerial exposure surfaces (Goldhammer and Harris, 1989). The LTF is composed of subtidal deposits with short-lived subaerial exposure stages about every 10 m and expressed by tepee structures (Goldhammer and Harris, 1989; Egenhoff et al., 1999). The overlying four stratigraphic units (Figure 4.2B) comprise a repetitive succession of subtidal- to intertidal-dominated deposits (Lower Cyclic Facies and Upper Cyclic Facies) alternating with intervals (Middle Tepee Facies and Upper Tepee Facies) dominated by supratidal features such as tepee structures and caliche surfaces (Dunn, 1991). Transition between these major units has been interpreted as reflecting either 3<sup>rd</sup> order sea level fluctuations (1-10 m.y.) (Goldhammer et al., 1990; Egenhoff et al., 1999) or eccentricity forcing (Zühlke et al., 2003; Zühlke, 2004). The tepee-rich intervals are interpreted to record lowstand phases in all mentioned studies.

#### 4.3.2 *Platform top cyclicity*

The Latemar isolated platform has been object of extensive investigations and intense debate during the past twenty years, revolving on estimating the duration of each of the 700-800 decimeter- to meter-scale, carbonate cycles observed in the platform top succession (Hardie et al., 1986; Goldhammer et al., 1990; Hinnov and Goldhammer, 1991; Brack et al., 1996; Mundil et al., 1996; Preto et al., 2001; Zühlke et al., 2003). Each cycle displays a shallowing-upward trend from subtidal, to intertidal, and to supratidal deposits (Goldhammer et al., 1987; Goldhammer and Harris, 1989), which were sketched into an “idealized cycle” (Egenhoff et al., 1999). The numerous interpretations and forcing models on the Latemar cyclicity are summarized in Figure 4.1.

Cyclostratigraphic investigations, based on field observations, Fischer diagrams, and time-series analysis (Goldhammer et al., 1987, 90; Goldhammer and Harris, 1989; Hinnov and Goldhammer, 1991; Preto et al., 2001, 2004), grouped the carbonate cycles into 1:5 bundling megacycle and suggested a 100 kyr eccentricity superimposed on 20 kyr precession forcing. A Milankovitch forcing model leads to a time interval of 11-12 My for the 720 m thick stratigraphic interval. Cyclostratigraphic interpretations have been challenged by other time calibration methods such as biostratigraphy (Brack and Rieber 1993; De Zanche et al., 1995; Brack et al., 1996), magnetostratigraphy

(Kent et al., 2004), radiometric age dating (Mundil et al., 1996; Mundil et al., 2003), which suggested a  $\leq 4.9$  Myr time interval for the LCF to UCF stratigraphic succession of Latemar. Hence, each carbonate cycle represents a  $\leq 6.7$  kyr duration, significantly below the 20 kyr precession cyclicity. In this context, a model-independent spectral analysis carried out from the LCF to UTF (Zühlke et al., 2003; Zühlke, 2004) and integrating multidisciplinary dataset (cyclo-, bio-, magneto- and chronostratigraphic evidences) strongly supported a Milankovitch-driven cyclicity superimposed on sub-Milankovitch forcing (Figure 4.1).

### ***4.3.3. Depositional profile***

The depositional profile of the Latemar platform can be summarized into three depositional settings i) from basin to platform top i) a grainstone to breccia slope, ii) a margin composed of a tepee belt and a reef, and iii) an interior platform consisting of a lagoon and a backmargin (Figure 4.3).

#### ***4.3.3.1. Slope***

The slope consists of a 25°-35° dipping foreslope that grades into a 5°-10° inclined toe-of-slope beds. The foreslope is composed of breccia and megabreccia sheet and lenses with marginal-derived blocks up to several meters in diameter. Grainstone beds are intercalated between breccia bodies and display platform-derived organic and inorganic components. Foreslope deposits pinch out into turbiditic grainstones toward the toe-of-slope (Goldhammer and Harris, 1989; Harris et al., 1994). The main feature of the slope is the occurrence of hundreds of meters long slump scars, which record major collapses of the margin (Emmerich et al., 2005a; Preto et al., 2011).

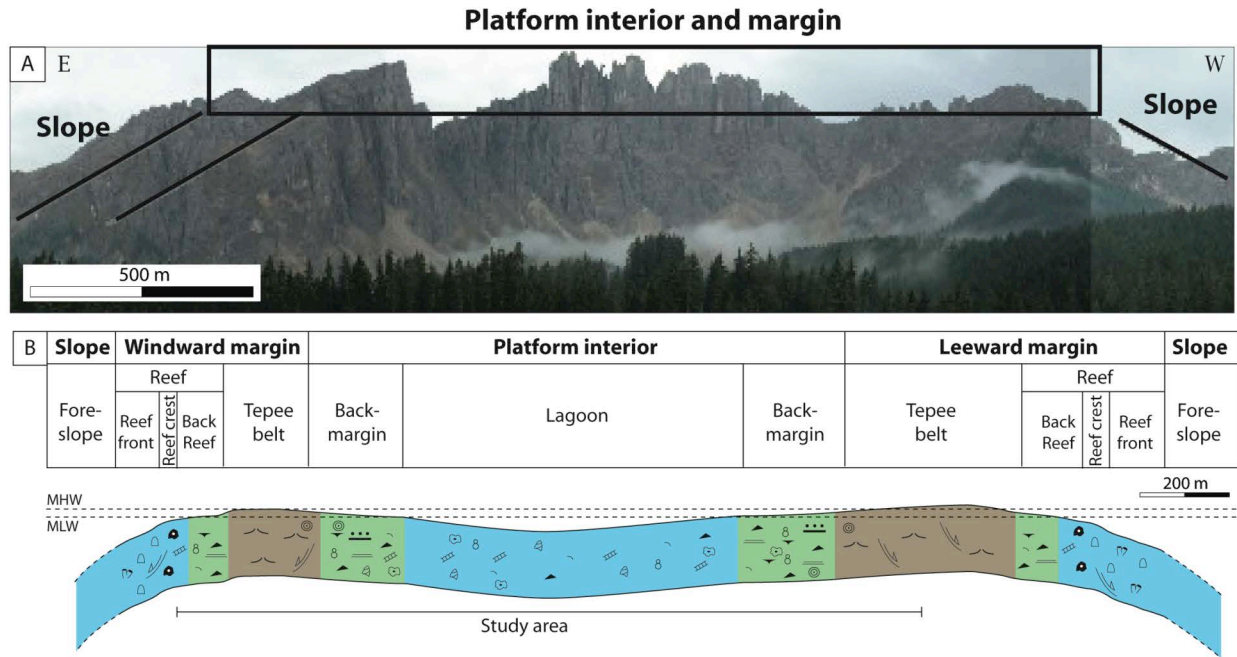
#### ***4.3.3.2. Margin***

The tepee belt represents the highest palaeotopographic relief of the platform, surrounding the lagoon. Up to 4 m thick, polygonal tepee structures (Assereto and Kendall, 1977) result from multiphase, prolonged exposures of the sea floor (Christ et al., 2012b). Repetitive exposures stages are recorded by the stacking of numerous reddish surfaces so-called “terra rossa” that suggest the development of a palaeosol (Gaetani et al., 1981). Tepee structures show a significant amount of radiaxial cement precipitation that contributes to tepee development. During sea level lowstand, marine and lagoon waters percolated from both sides of the margin to the exposed tepee belt, leading to cement precipitation (Egenhoff et al., 1999). Toward the slope, the backreef displays similar subtidal deposits and a comparable cyclic stacking pattern as in the lagoon. A reef belt is located at the transition between the foreslope and the backreef, forming several tens of meter wide bioconstructions (Goldhammer and Harris, 1989). The reefal facies comprises microbial crusts such as *Tubiphytes*, encrusting sponges, corals, and microproblematica (Harris, 1993; Emmerich et al., 2005a). The reef belt does not show any emersion feature (Harris, 1993).

#### ***4.3.3.3. Interior platform***

The interior platform displays a low-energy, subtidal-dominated lagoon that represents the deepest area of the platform top. The lagoon consists of bioclastic and peloidal wackestone to packstone with debris of dasycladacean algae, foraminifera, molluscs, gastropods, and ostracods (Goldhammer and Harris, 1989; Egenhoff et al., 1999). In addition, peloids, aggregate grains, and oncoids are present to abundant. Variation of the biota diversity was observed in the interior platform and interpreted as changes of restriction conditions (Preto et al., 2004). Toward the

margin, the platform interior grades into an intertidal-dominated backmargin. Locally inversely grading, packstone to grainstone texture associated with fenestral fabrics, horizontal laminations, oncoids and pisoids are dominant (Goldhammer and Harris, 1989). Caliche crusts and pendant and meniscus cements were observed, indicating periods of subaerial exposure (Christ et al., 2012b). The interior platform displays an asymmetric morphology with a northeastern tepee belt broader and a dipping slope angle higher than toward the southwestern side of the platform (Figure 4.3). Windward-leeward effect (Egenhoff et al., 1999) and different subsidence rates across the platform (Emmerich et al., 2005a) have been suggested as controlling factors on platform morphology.



**Figure 4.3:** A. Field picture showing the overall morphology of the Latemar isolated platform. B. Depositional profile from the lagoon to foreslope (after Egenhoff et al., 1999; Emmerich et al., 2005a) with the location of the study area. Note the asymmetric morphology of the platform top and the occurrence of collapses in the margin (Emmerich et al., 2005a; Preto et al., 2011). MHW: mean high water and MLW: mean low water. For legend, please refer to Figure 4.4.

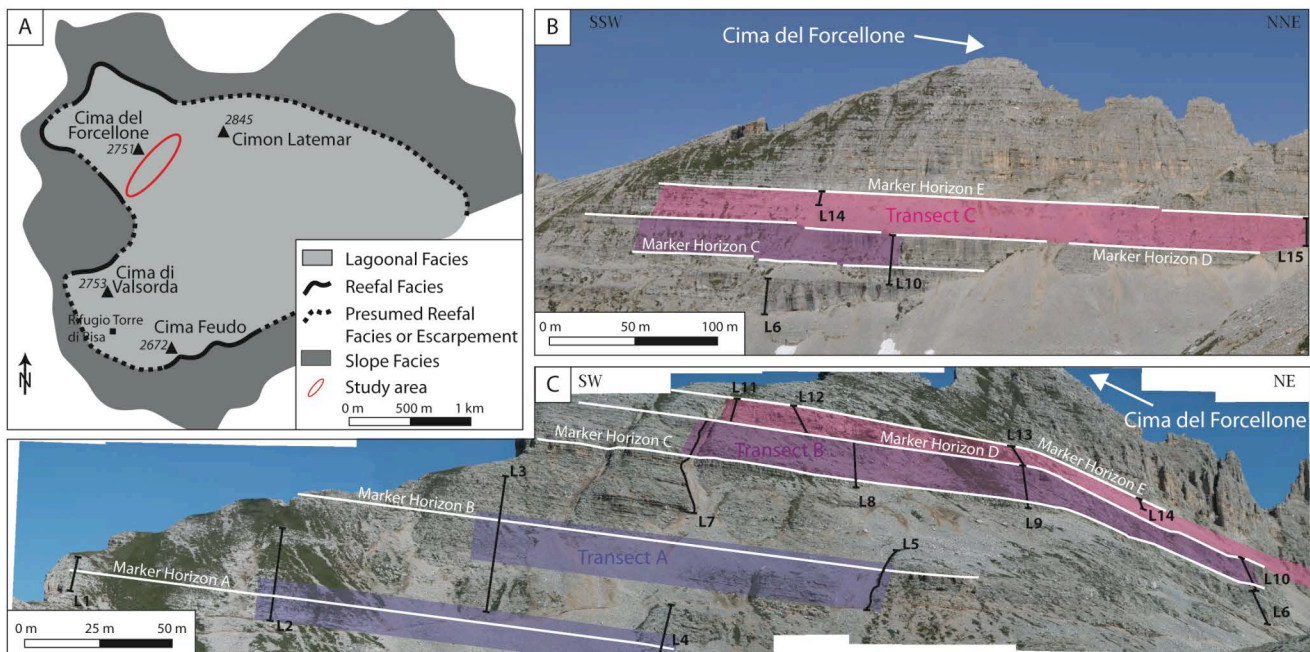
Symbols	Depositional conditions	Lithofacies types	Cycle types	
<ul style="list-style-type: none"> <li>~ Tepee structure</li> <li>— Lamination</li> <li>∇ Fenestrae porosity</li> <li>⊙ Pisoid</li> <li>⊙ Oncoid</li> <li>⊙ Lump/aggregate</li> <li>• Peloid</li> <li>▲ Intraclast</li> <li>~ Bivalve</li> <li>⊘ Dasycladalean algae</li> <li>⊘ Gastropod</li> <li>× Undetermined bioclast</li> </ul>	<ul style="list-style-type: none"> <li>⋮ Inverse grading</li> <li>⊙ Tubiphyte</li> <li>⊘ Calcsponge</li> <li>⊘ Scleractinian coral</li> <li>↘ Potential escarpment</li> </ul>	<ul style="list-style-type: none"> <li>Subtidal</li> <li>Intertidal</li> <li>Inter- to supratidal</li> </ul>	<ul style="list-style-type: none"> <li>Peloidal W to P (Lf1)</li> <li>Bioclastic P to F (Lf 2)</li> <li>Intraclastic P-G to B (Lf 3)</li> <li>Peloidal P to G (Lf 4)</li> <li>Intraclastic G (Lf 5)</li> <li>Dolostone (Lf 6)</li> <li>Terra rossa clay (Lf 7)</li> <li>Tepee structure (Lf 8)</li> </ul>	<ul style="list-style-type: none"> <li>Type A cycle</li> <li>Type B cycle</li> <li>Type C cycle</li> </ul>

**Figure 4.4:** Legend for Figures 4.3, 4.8, 4.9, 4.10, 4.11, and 4.14. Lf = Lithofacies; W = Wackestone; P = Packstone; G = Grainstone; F = Floatstone; R = Rudstone; B = Boundstone.

## 4.4. Study window and methodological approach

A 125 m thick stratigraphic interval (4.5 m no cropping out) from the top of the LCF to the boundary between the MTF and the UCF was investigated here (Figure 4.2B, Appendix A2). The study area, located in Cima del Forcellone, encompasses a 800 m long transect from the backreef to the lagoon (Figures 4.3B, 4.5A). In addition, the northeastern margin of the platform was also captured in the middle part of the MTF. This location offers the best configuration to investigate the lateral cycle variability and to reconstruct the evolution of the platform top through time. Three transects located at the base, middle, and top of the MTF were investigated (Figures 4.5B, 4.5C). The data set built on the collection and correlation of 15 stratigraphic sections. Correlations between sections were performed by physically tracing in the field five marker horizons. Each section was logged in detail bed by bed, with samples taken with an average of 3 to 4 per meter and a total of 89 thin-sections were analyzed to further characterize lithofacies types. The inter-section spacing ranges between 35 m and 235 m (Figure 4.5).

A DGPS mapping survey was carried out in order to capture and quantify the palaeotopographic profile of the platform top. The mapping survey was carried out using a Leica DGPS 1200. The quality factor of DGPS data point is around 0.5 m. The reader is referred to Amour et al. (2012) (Chapter 2, page 11) for a more detailed description of the DGPS mapping method.



**Figure 4.5:** A. Schematic map view of the Latemar platform with the location of the study area (after Emmerich et al., 2005a). Note that the studied area is perpendicular to the depositional profile of the platform top and spans from the backreef to the lagoon. B and C. Panorama of the SSW-NNE cliff (B) and the SW-NE cliff (C) of Cima del Forcellone showing the location of sections (black line) and marker horizons (white line). Transect A (blue), Transect B (purple), and Transect C (pink) respectively located at the base, middle, and top of the MTF are displayed here.

## 4.5. Lithofacies types and depositional conditions

Height different lithofacies (Table 4.1) were recognized according to texture, sedimentary structures and composition of skeletal and non-skeletal components. Each lithofacies type can be attributed to one of these three depositional conditions i) subtidal deposits showing a semi-restricted to open marine biotic association ii) intertidal deposits with fenestral and laminar fabric, and iii) intertidal to supratidal deposits displaying evidences of periodic, more or less prolonged subaerial exposure stages.

### 4.5.1. Subtidal deposits

#### *Lithofacies 1: Peloidal wackestone to packstone*

This lithofacies around 0.5 m thick (up to 1.2 m) is the more abundant type of lithofacies observed in the study area. It contains mainly subangular to rounded peloids and few subrounded to subangular millimeter sized micritic intraclasts (Figure 4.6A). Bioclasts of benthic foraminifera and thin-shelled bivalves are present in abundance whereas dasycladacean algae, echinoderms, and gastropods debris are rare.

#### *Interpretation:*

The matrix-rich fabric and low biota diversity suggest semi-restricted, low-energy depositional conditions. In addition, the absence of intertidal or emersion features indicates that Lithofacies 1 was deposited under a stable subtidal environment. The occurrence of few micritic intraclasts indicates local reworking on the sea floor.








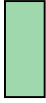








#### *Lithofacies 2: Bioclastic packstone to floatstone*

Occurring within decimeters thick beds, this lithofacies is mainly composed of abundant, often micritized dasycladacean algae debris. Bioclasts of gastropods, foraminifera, echinoderms, and thin-shelled bivalves are rare to frequent. Peloids are frequent to abundant and millimeter sized micritic intraclasts and oncoids were also observed. Lithofacies 2 is characterized by frequent and local decrease of micrite content, leading to a packstone-grainstone textures (Figure 4.6B).

#### *Interpretation:*

The abundance of dasycladacean algae and the absence of emersion feature indicate subtidal depositional conditions located in the photic zone. In addition, the relatively high biotic diversity and the decrease of mud content in comparison to Lithofacies 1, indicate an subtidal environment characterized by an increase of open marine and hydrodynamic conditions associated with the deposition of Lithofacies 2.

**Table 4.1: Summarize of the lithofacies classification and the interpretation of depositional conditions with their color codes. Lf = Lithofacies; W = Wackestone; P = Packstone; G = Grainstone; F = Floatstone; R = Rudstone; B = Boundstone.**

Lithofacies code	Color code for lithofacies	Lithofacies	Skeletal/non-skeletal components	Sedimentological features	Depositional conditions	Color code for depositional conditions
Lf 1		Peloidal W to P	Few dasycladacean algae, foraminifera, bivalves Peloids, micritic intraclasts		Subtidal	
Lf 2		Bioclastic P to F	Dasycladacean algae, gastropods few foraminifera, echinoderms Peloids, micritic intraclasts, oncoids		Subtidal	
Lf 3		Intraclastic P-G to B	Dasycladacean algae, gastropods, foraminifera, echinoderms, bivalves, <i>in situ</i> cyanobacteria Peloids, micritic intraclasts, aggregate grains, oncoids, lumps	Local inverse grading, local clotted fabrics	Subtidal	
Lf 4		Peloidal P to G	Dasycladacean algae, bivalves, gastropods, cyanobacteria Few foraminifera, echinoderms Peloids, micritic intraclasts, oncoids	Laminations, fenestral fabrics, inverse gradings, microbial encrustations	Intertidal	
Lf 5		Intraclastic G	Dasycladacean algae, gastropods, foraminifera, echinoderms, bivalves, cyanobacteria, bryozoans Peloids, micritic intraclasts, aggregate grains, oncoids, lumps, pisoids	Laminations, fenestral fabrics, inverse gradings	Intertidal	
Lf 6		Dolostone	Mainly texture-replacive with visible dasycladacean algae, gastropods, foraminifera, echinoderms, bivalves, cyanobacteria Peloids, intraclasts, pisoids, oncoids	Laminations, fenestral fabrics	Intertidal to supratidal	
Lf 7		Terra Rossa F to R	Dasycladacean algae, gastropods Intraclasts, oncoids, pisoids, Aggregate grains, lumps, clastic sediments, and breccia	Laminations, fenestral fabrics, caliches	Supratidal	
Lf 8		Tepee	See components of all others lithofacies, up to 80% of cement	Tepee structures Caliches, laminations, fenestral fabric, inverse grading	Supratidal	

***Lithofacies 3: Peloidal intraclastic packstone-grainstone to bindstone***

Up to 70 cm thick, Lithofacies 3 occurs locally interbedded with Lithofacies 1 and Lithofacies 2. Subangular to subrounded peloids are dominant in association with angular to rounded micritic intraclasts and aggregate grains. Intraclasts display filaments of cyanobacteria, clotted micrite, dark dense micrite, and dasycladacean debris (Figure 4.6D). Lumps and oncoids were also observed. Bioclasts are often micritized and consist of dasycladacean algae, benthic foraminifera, and thin-shelled bivalves. Echinoderm and gastropod debris are present. Locally, inverse grading and LF-BII type fenestral porosity were observed. The matrix of Lithofacies 3 is locally composed of a clotted micrite with dense dark micrite suggesting microbial activity. In addition, *in situ* filamentous fabrics (*Garwoodia* and *Girvanella?* type) were frequently observed (Figure 4.6C).

***Interpretation:***

The diversity of bioclast debris (dasycladacean algae, gastropods, foraminifera, echinoderms, and bivalves) and the abundance of intraclasts associated with a packstone to grainstone texture suggest an overall higher and more constant hydrodynamic level compared to Lithofacies 1 and Lithofacies 2. The Lithofacies 3 reflects open marine, relatively high-energy, subtidal conditions. In addition, the local occurrence of clotted micrite, *in situ* cyanobacteria, and rare fenestral fabric suggests either the proximity of intertidal conditions or favorable conditions for microbial activities.

**4.5.2. Intertidal deposits*****Lithofacies 4: Peloidal packstone to grainstone with fenestral porosity***

Few decimeters thick in average, Lithofacies 4 is laterally continuous and shows a textural range from packstone to grainstone. Different types of fenestral fabrics and horizontal laminations are specific to Lithofacies 4. Laminations consist of alternating dense dark micritic laminae and light laminae with peloids and dasycladacean algae debris (Figure 4.6F). Both laminae show a clotted fabric. Three types of laminoid-fenestral fabric were recognized, LF-A, LF-B I, and few LF-B II according to the shape and distribution of spar-filled voids. The LF-A I type (Figure 4.6E) is a common fenestral fabric that consists of laminated and horizontally elongated voids. The LF-B I fabric is also common and is formed of a complex network of interconnected voids. Within grain-supported Lithofacies 4, LF-B II fabric is observed and shows irregular and elongated voids. Filamentous fabric is locally preserved (Figure 4.6E). Often micritized, bioclasts consist of dasycladacean algae, bivalves, and gastropods. Foraminifera and echinoderm debris can be observed. Peloids are abundant and micritic intraclasts and oncoids are frequent. Inverse grading was locally observed.

***Interpretation:***

The abundance of various types of fenestral fabrics and horizontal laminations indicates intertidal depositional conditions during the time of deposition (Tebbutt et al., 1965; Shinn, 1983). Lithofacies 4 caps carbonate cycles and is classified as Type I surface after Christ et al. (2012b).



***Lithofacies 5: Microbially incrustated intraclastic grainstone***

Few decimeters thick and laterally continuous, Lithofacies 5 is characterized by centimeter sized micritic intraclasts, oncoids, peloids, and pisoids, displaying a very poorly to moderate sorting. Lumps and aggregate grains are frequent to abundant. Biota association is composed of often micritized, bioclasts of dasycladacean algae, foraminifera, echinoderms, gastropods, thin-shelled bivalves, and cyanobacteria. Bryozoan debris is rare to present (Figure 4.6H). The matrix of Lithofacies 5 often consists of a clotted-fabric indicating microbial activity. The microbial fabric that preserves sometimes filaments is also shown by the occurrence of meniscus-like bridges binding clasts (Figure 4.6G). Laminations, fenestral fabrics, and inverse grading are present. Pendant and meniscus cement are rare to present. Locally, a pale-red matrix can be observed in the matrix.

***Interpretation:***

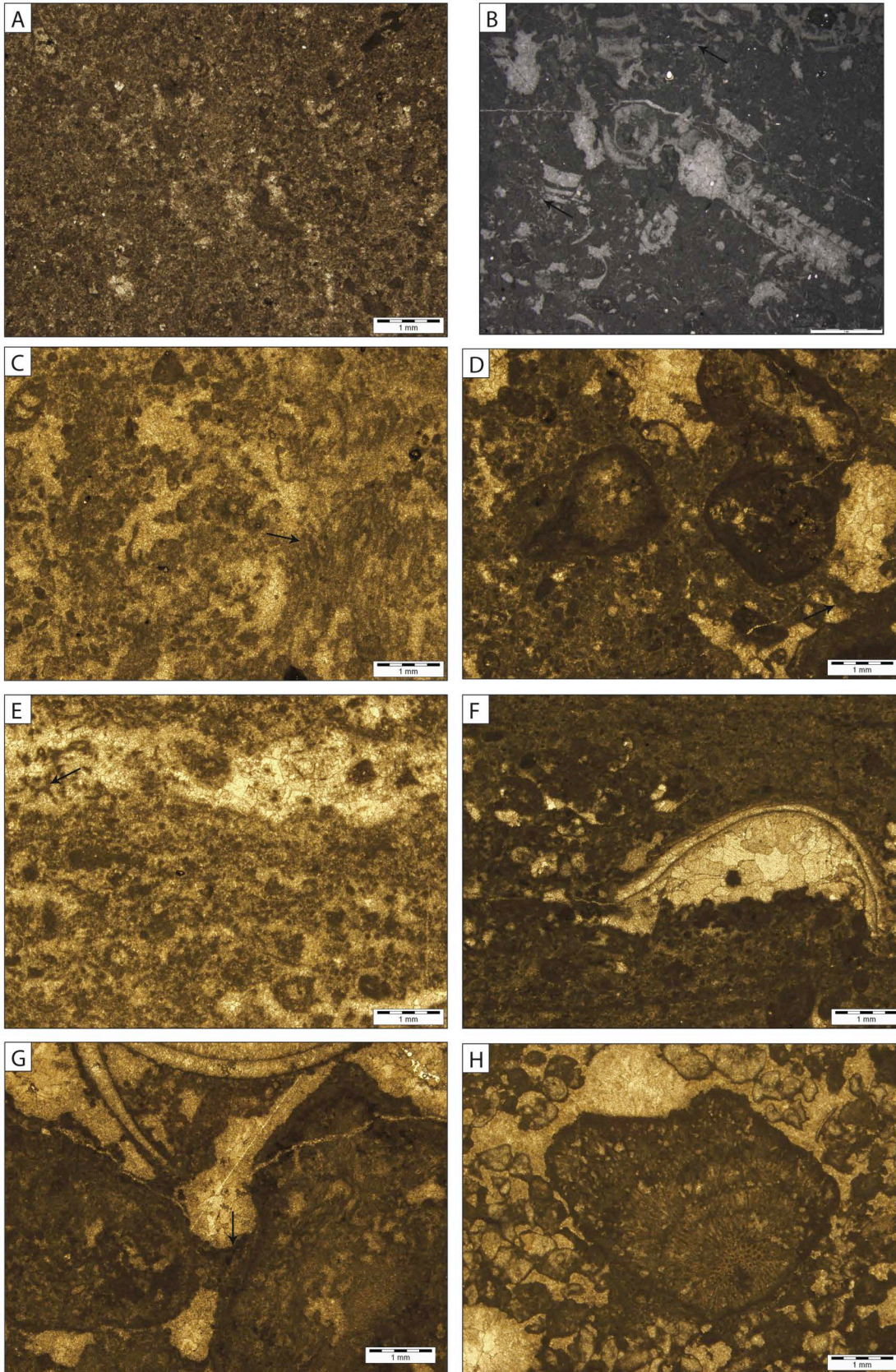
The abundance of meniscus-like bridges between grains composed of clotted and filamentous fabric similar to Lithofacies 4 as well as laminations and fenestral fabrics suggest intertidal depositional conditions. Furthermore, the local occurrence of pendant and meniscus cements indicates short-lived subaerial exposure events. Periods of emersion of the sea floor are also shown by the occurrence of pale-red matrix associated to palaeosol formation (Mutti, 1994). Lithofacies 5 caps the majority of carbonate cycles and likely reflect intertidal with short-lived emersion conditions. Lithofacies 5 is classified as Type I cycle top after Christ et al. (2012b).

**4.5.3. Intertidal to supratidal deposits*****Lithofacies 6: Dolomitized packstone-grainstone to grainstone***

Lithofacies 6 occurs mainly as a few centimeters to few decimeters thick, yellowish to brownish layer capping the top of cycles (Figure 4.7A). Crypto- to microcrystalline dolomite crystals are dominant, with rare isolated euhedral rhombs occurring. Lithofacies 6 displays mainly a grain-supported fabric with micritic intraclasts, peloids, oncoids, aggregate grains, and pisoids similar to Lithofacies 5. Horizontal laminations and fenestral fabrics were also observed.

***Interpretation:***

The rock fabric and sedimentary structures similar to lithofacies 4 and lithofacies 5 indicates intertidal conditions during the time of deposition. Accordingly to the present data and previous studies, Lithofacies 6 reflects intertidal depositional conditions, in which the dolomitization process is associated to syn-sedimentary tidal pumping (Shinn, 1983; Carballo et al., 1987; Goldhammer et al., 1987, 1990; Wilson et al., 1990). Furthermore, isotopic measurements, cathodoluminescence analysis, and the occurrence of clastic sediments (Christ et al., 2012b) cannot rule out short-lived exposure stage. Lithofacies 6 is observed at the top of carbonate cycle and reflects intertidal to perhaps supratidal environment. Lithofacies 6 is classified as Type II cycle top after Christ et al. (2012b).



**Figure 4.6: Micro- and macroscopic photographs showing the main characteristics of each lithofacies type. A. Microphotograph of Lithofacies 1 showing peloids, millimeter sized intraclasts and rare bioclasts and located at 2.2 m in section L6. B. Microphotograph of Lithofacies 2 displaying centimeter sized bioclasts of dasycladacean algae and few subangular to subrounded micritic intraclasts. The thin-section is located at 1.1 m in section L13. Note local decrease of mud content (arrow). C and D. Microphotographs of Lithofacies 3. The packstone to grainstone texture (D) with abundant micritic intraclasts and aggregates clasts shows locally the preservation of a filamentous fabric (C and D; black arrows) (*Garwoodia* Type). The thin-sections C and D are located at 2.5 m in section L2 and at 1.4 m in section L13, respectively. E and F. Microphotographs of Lithofacies 4 displaying horizontal laminations (F) associated with fenestral fabrics (E). A filamentous fabric is locally preserved (E; arrow). Discontinuous storm layers indicating by a bioclastic packstone to grainstone texture are also observed (F). The thin-sections E and F are located at 4.8 m in section L2 and at 0.4 m in section L1, respectively. G and H. Microphotographs showing the grainstone texture of Lithofacies 5. Note the occurrence of a clotted fabric and locally preserved, micritic filaments forming meniscus-like bridges between inorganic and organic components (G; black arrow). Note also the presence of a micritized bryozoan bioclasts transported from the reef front (H). The thin-sections G and H are located at 3.9 in section L15 and at 20.9 in section L3, respectively. Please, refer to Appendix A2 for the location of thin-sections.**

#### ***Lithofacies 7: Terra rossa clay***

Lithofacies 7 is 10 to 20 cm thick and is characterized by reddish horizons (Figure 4.7B). Lithofacies 7 consists of float- to rudstones with reworked bioclasts and intraclasts, oncoids, pisoids, aggregates, lumps. Caliche crusts are frequent to abundant. Locally, these surfaces appear brecciated. Cemented fenestral fabrics and horizontal laminations are abundant (Figure 4.7B). The “terra rossa” is either laterally continuous across the platform top or grades laterally into intertidal and subtidal deposits.

#### ***Interpretation:***

The abundance of laminations and fenestral fabrics suggests the influence of tidal conditions, whereas caliche crusts indicate supratidal stages during the time of deposition. Previous studies interpreted reddish carbonate matrix as a palaeosol so-called “terra rossa”, associated with solution residues after the dissolution of the host sediment (Klappa, 1980; Mutti, 1994). Lithofacies 7 was mainly deposited under supratidal depositional conditions and experienced at least temporarily intertidal conditions. “Terra rossa” clay surfaces are the more rare cycle tops and are classified as Type III cycle top after Christ et al. (2012b). The discontinuity/continuity of Lithofacies 7 indicates that exposure conditions affected either the entire or a part of the platform top.

#### ***Lithofacies 8: Tepee structures***

Resulting from syndepositional, mechanical deformation of early-lithified sediments, tepee structures can affect and comprise all types of lithofacies described above and are listed as a separate lithofacies. A major characteristic of this lithofacies is the syndepositional brecciation and diagenetic overprinting. Radial calcite cement is common and can reach up 80% of the total rock fabric.

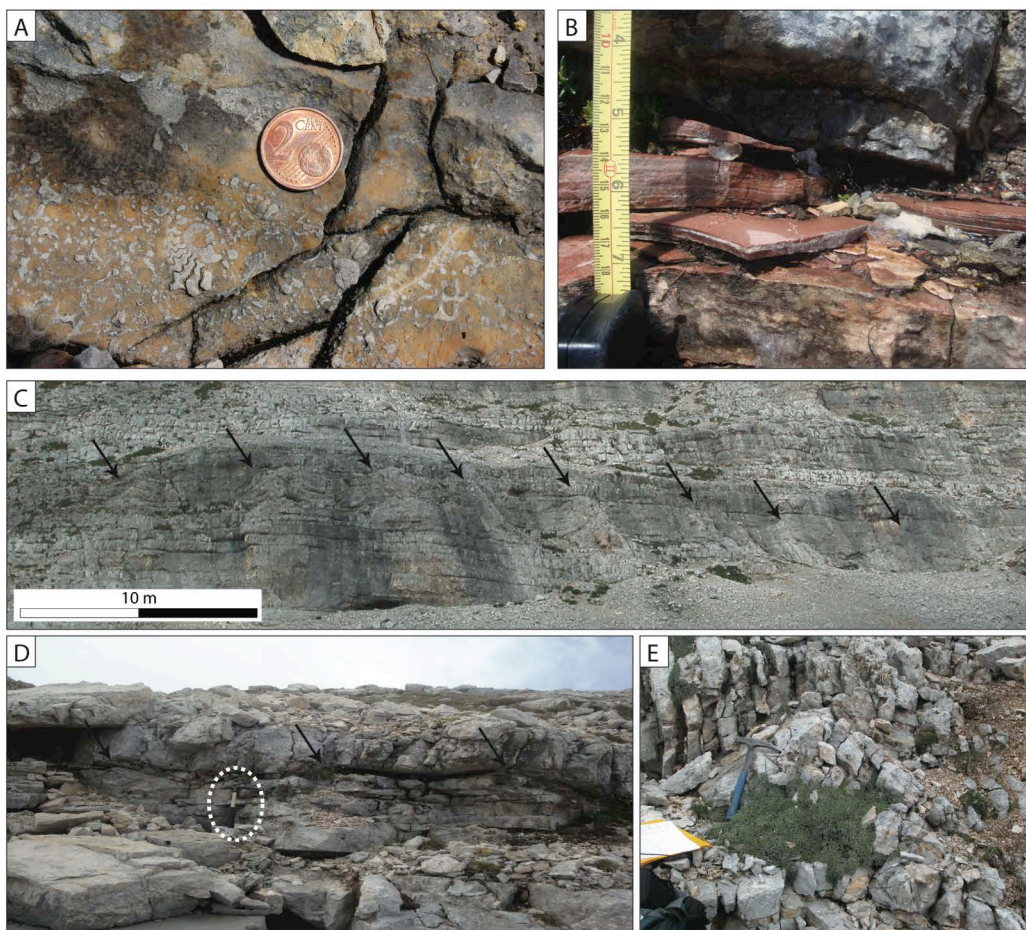
Two categories of tepee structures were observed in the study area and identified as juvenile and mature tepee structures (Assereto and Kendall, 1977). Both tepee types vary in terms of morphology and lateral continuity. Mature tepees are up to 1.5 m thick and form kilometer long horizons (Figure 4.7C). These structures mainly occur in the middle part of the MTF. Individual juvenile tepees are few decimeters thick and up to 1.5 m long (Figure 4.7E). Lateral association of juvenile tepee structures forms up to several tens of meters long horizons (Figure 4.7D).



Juvenile tepee structures were observed across the entire stratigraphic succession but are predominant within the LCF and at the base and top of the MTF.

#### *Interpretation*

Tepee structures are interpreted as formed within supratidal conditions associated with periodic and prolonged exposure conditions (Assereto and Kendall, 1977). The occurrence of dolomitic crusts, “terra rossa” clay surfaces, and subtidal to intertidal deposits within tepee structures indicate alternating emergence and immergence conditions. The thickness and lateral extension of tepee structures are related to the duration of exposure of the sea floor to depositional conditions favoring tepee development. Lithofacies 8 caps carbonate cycles and is classified as Type IV cycle top after Christ et al. (2012b).



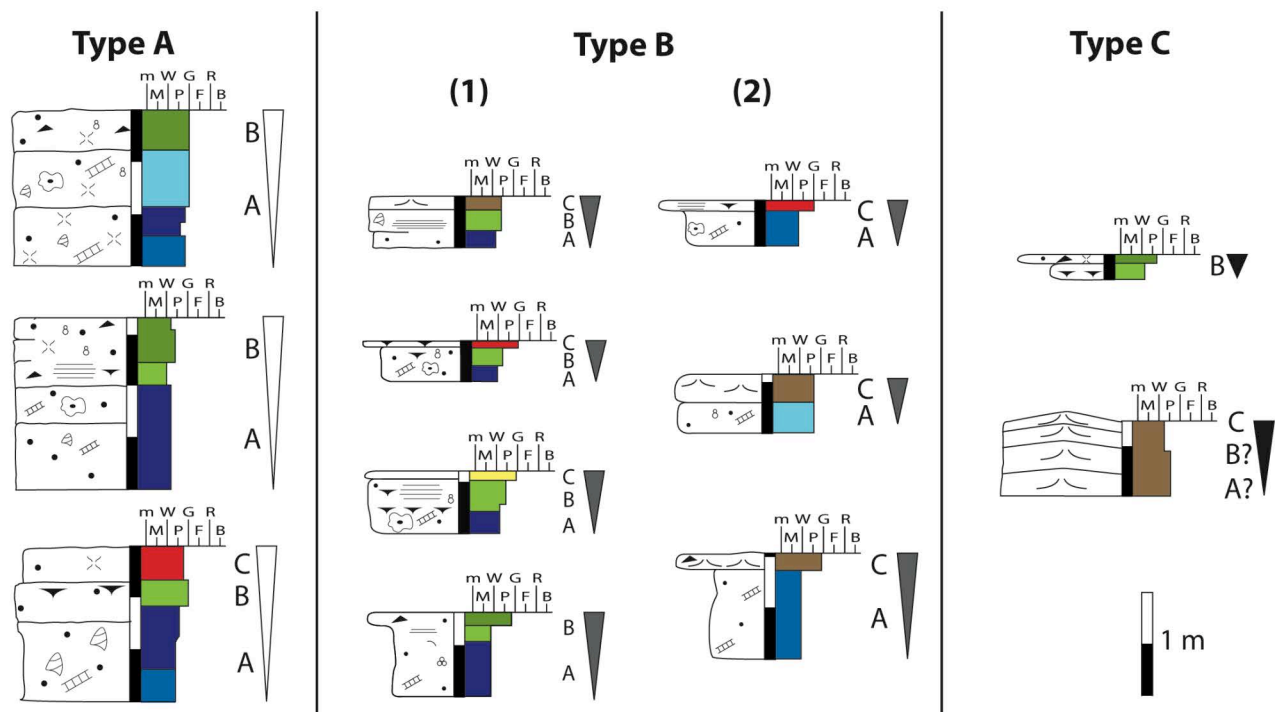
**Figure 4.7: Field pictures of inter- to supratidal features observed in the field. A. Dolomitic cap (Lithofacies 6) displaying an ammonite shell likely transport by storms events or high tides. Field picture A is located at 3.9 m in section L10. B. Thin “terra rossa” surface (Lithofacies 7) displaying horizontal laminations and fenestral fabrics and located at 12.6 m in section L5. C, D, and E. Field pictures showing two types of tepee structures (Lithofacies 8) observed in the study window. C. 2 m thick, mature tepee structures observed within several hundreds of meters long horizons and located at 16 m in section L6. D and E. Few decimeters thick, juvenile tepees observed either in several tens of meters long horizons (D) or isolated (E). Field pictures D and E are located at 22.5 m in section L13 and at 2.6 m in section L7, respectively. Please, refer to Appendix A2 for the location of field pictures.**

## 4.6. Vertical stacking pattern and lateral variability of Latemar carbonate cycles

### 4.6.1. Classification of carbonate cycles

Each of the 700 to 800 carbonate cycles comprises basal matrix-rich, subtidal-dominated lithofacies overlaid by fenestral wackestone to packstone and packstone to grainstone lithofacies interpreted as intertidal deposits. The cycle is capped by supratidal-related features such as dolomitic crust, “terra rossa” clay, and tepee structures (Goldhammer and Harris, 1989). The repetitive expression of cycles was schematized into a so-called “idealized” meter-scale carbonate cycle (Egenhoff et al., 1999).

The investigation reported here indicates significant deviations from this “idealized” cycle. Three types of cycles, Type A, Type B1-B2, and Type C cycles were identified, based on the expression of their thickness, shallowing-upward trend and lateral continuity.



**Figure 4.8:** Schematic summary of cycle types observed in the study area. Type A, B1-B2, and C cycles display significant variability of thickness and lithofacies stacking pattern, indicating changes of depositional conditions. A = subtidal, B = intertidal, and C = supratidal. For legend, please refer to Figure 4.4.

Type A cycles are the thickest (up to 1.5 m thick) type of cycle observed in the study area (Figure 4.8). The shallowing-upward trend is well expressed with a basal, subtidal lithofacies association overlaid by few decimeters thick intertidal deposits. Type A cycles are rarely capped by supratidal-related features. Thickness and lithofacies association indicates that Type A cycles recorded relatively high accommodation during the time of deposition.

Type B cycles are few decimeters thick and rarely reach 1 m (Figure 4.8). Considered as the most abundant type of cycle, it can be divided into Type B1 and Type B2 cycles. The shallowing-upward trend of Type B1 cycles is well expressed and displays smooth vertical transition from subtidal to intertidal and mostly to supratidal lithofacies (Figure 4.8). The occurrence of supratidal features comes along with a decrease of the cycle thickness. Contrarily, Type B2 cycles recorded abrupt vertical lithofacies changes (Figure 4.8). The shallowing-upward trend shows basal subtidal beds capped by supratidal features and intertidal deposits are absent. To conclude, Type B cycles are thinner and show shallower lithofacies association than Type A cycle, suggesting reduced accommodation available for sedimentation.

Type C cycles are the less common cycle type observed in the study area. These cycles are composed of 20 to 30 cm beds of intertidal lithofacies or up to 1.5 m thick tepee structures (Figure 4.8). The stacking pattern does not display a clear shallowing- or deepening-upward trend of lithofacies, resulting from either too gentle change of accommodation to induce change of depositional conditions or diagenetic overprinting linked to tepee growth, which makes observations difficult. Within tepee structures, thinning-upward trends of the beddings were assumed to reflect shallowing-upward trends.

#### ***4.6.2. Lateral variability of cycle types***

Three transects, A, B, and C (Figure 4.5) were investigated across the top part of the LCF and the MTF of Cima del Forcellone outcrop to document at high-resolution, spatial and temporal relationships between the three types of cycle (Figure 4.8). The transects were physically correlated by tracing five marker horizons in the field. The transect A spans from the top of the LCF to the lower part of the MTF. The middle and upper part of the MTF are covered by the transects B and C, respectively.

The transect A (Figure 4.9) is located toward the southwestern part of the study area and comprises the sections L1 to L5 (Figure 4.5). Spanning from the top of the LCF and the base of the MTF, these sections show a progressive upward increase of intertidal and supratidal features such as dolomitized grainstones, “terra rossa” surfaces, and tepee structures, culminating in marker horizon B (Figure 4.9). At the base of the transect, the section L4 mainly shows a stacking pattern of few decimeters thick, Type B1 cycles and in lesser amount Type B2 cycles capped by tepee structures. Thinning-upward bundles of two to three Type B cycles grade laterally to one single meter thick Type A cycle in the sections L1 and L2 over a distance of 130 m (Figure 4.9). Lateral transition between both types of cycle comes along with a 38.1% decrease of cycle numbers from the section L4 to L2. Toward the top part of the transect A (i.e. toward the middle part of the MTF), lateral variability of cycles is absent. The sections L4 and L5 display laterally continuous Type B1 cycles and few Type B2 cycles.



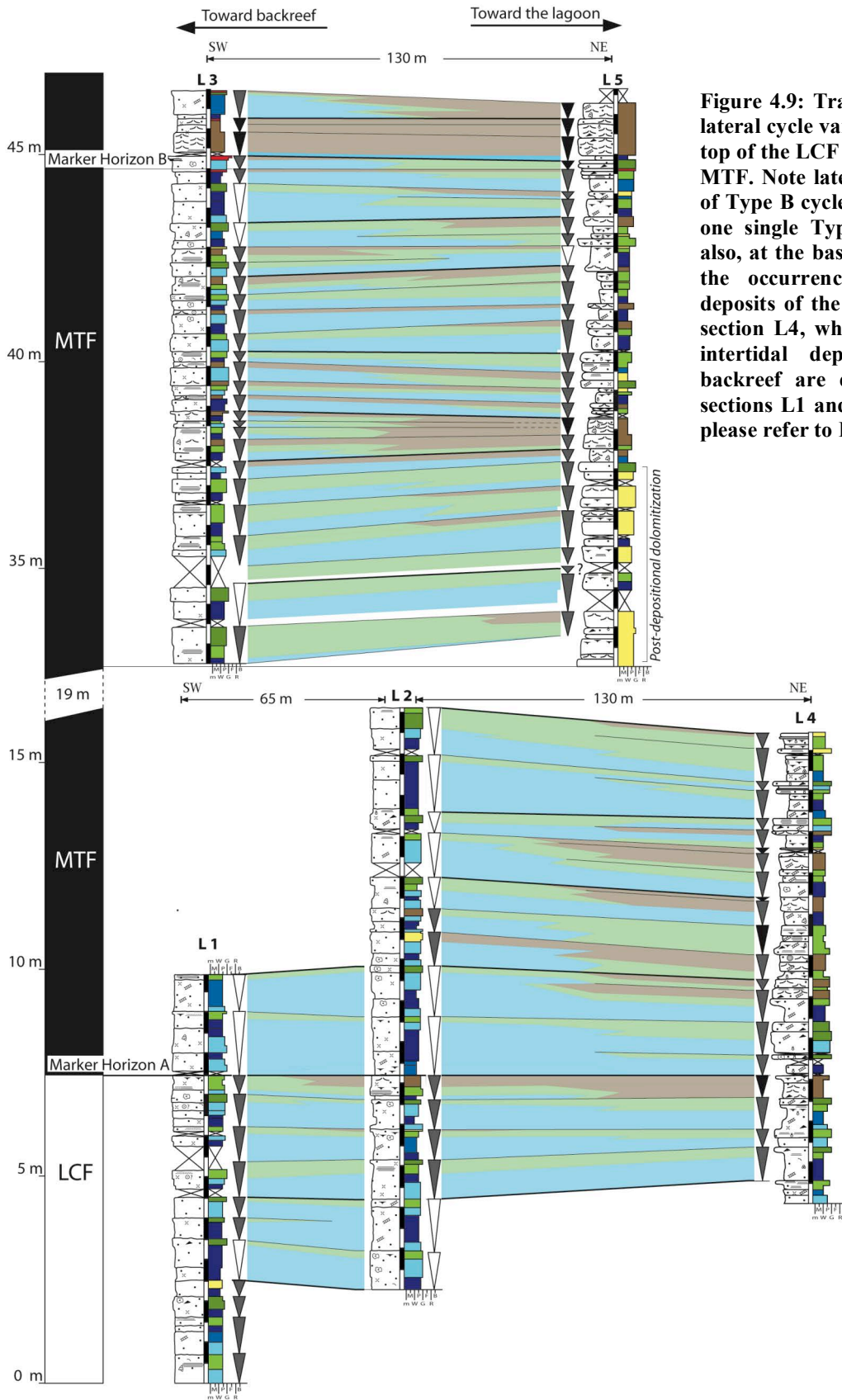
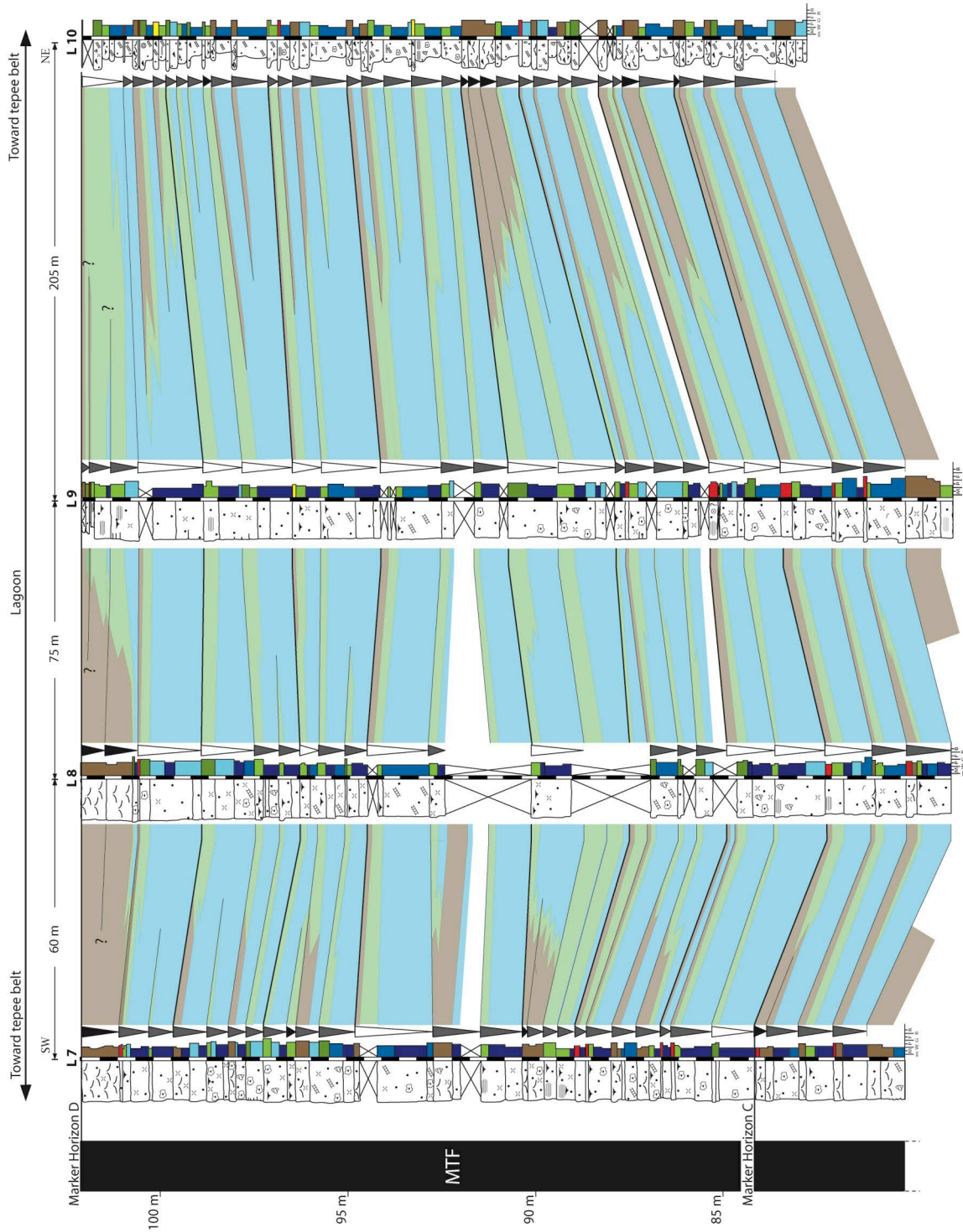


Figure 4.9: Transect A showing lateral cycle variability from the top of the LCF to the base of the MTF. Note lateral discontinuity of Type B cycles that grade into one single Type A cycle. Note also, at the base of the transect, the occurrence of supratidal deposits of the tepee belt in the section L4, whereas subtidal to intertidal deposits from the backreef are dominant in the sections L1 and L2. For legend, please refer to Figure 4.4.

The transect B (Figure 4.10) consists of the sections L7 to L10 (Figure 4.5) and is located within the middle part of the MTF. The transect displays similar characteristics in term of lateral cycle continuity and discontinuity than the base of the transect A. Thinning-upward bundles of two to three Type B cycles (Figure 4.8) in the sections L7 and L10 amalgamate into one single Type A cycle in the sections L8 and L9, leading to a 41.2% decrease of cycle number over a distance of 200 m. Furthermore, the transect B captures the lateral variability of the Type C cycles, which represent tepee structure (Figure 4.8). At the top part of the transect, mature tepee structures in the sections L7 and L8 grade to a thinning-upward bundle of three Type B1 cycles in the sections L9 and L10. At the middle part, mature tepee structures in the sections L7 and L10 change to one single Type A cycle in the sections L8 and L9. In the sections L7 and L10, the transect B shows the highest proportion of the Type B2 cycles (around 30%) in comparison to the other transects.

The transect C (Figure 4.11) located in the top part of the MTF, is composed of the sections L11 to L15 (Figure 4.5). The transect displays significant lateral continuity of the Type B cycles compared to the transects A and B. Only around 10% (locally 20%) increase of the cycle number were observed along a distance spanning from few tens of meters to 300 m. The Type A cycles grade laterally into bundles of two Type B1 cycles, which do not display a clear shallowing- or thinning-upward trend compared to the observations carried out within the transects A and B. At the middle part of the transect, the Type C cycles grade laterally into one to two Type B1 cycles.

To conclude, the transects A, B, and C show a significant lateral variability of the cyclic stacking pattern. The Type A cycles grade laterally to a thinning-upward bundle of two to three Type B cycles, leading to change of cycle numbers from 10% to 40% (locally 66%). In addition, the transects indicate that the Type C cycles grade laterally to either i) one Type A cycle, ii) one Type B cycle or iii) a thinning-upward bundle of two to three Type B cycles. Contrarily to previous studies (Goldhammer and Harris, 1989; Goldhammer et al., 1990; Egenhoff et al., 1999; Preto et al., 2001, 2004; Zühlke et al., 2003; Zühlke, 2004), observations reported here demonstrate that the carbonate cycles are not laterally continuous across the Latemar platform top. Amalgamation is observed as a common process and suggests that the Type B cycle recorded a higher order of relative sea level fluctuation compared to the Type A cycles. Hence, changes of the expression of the cyclicity record across the platform top should be considered during the establishment of a cyclostratigraphic framework.



**Figure 4.10:** Transect B displaying lateral cycle variability at the middle part of the MTF. Note lateral discontinuity of Type B cycles that grade into one single Type A cycle. The sections L7 and L10 capture the tepee belt to backmargin, whereas the sections L8 and L9 are located in the lagoon. Note that the transect B captures both, the southwestern (section L7) and northeastern (section L10) margin edge of the Latemar platform top. For legend, please refer to Figure 4.4.

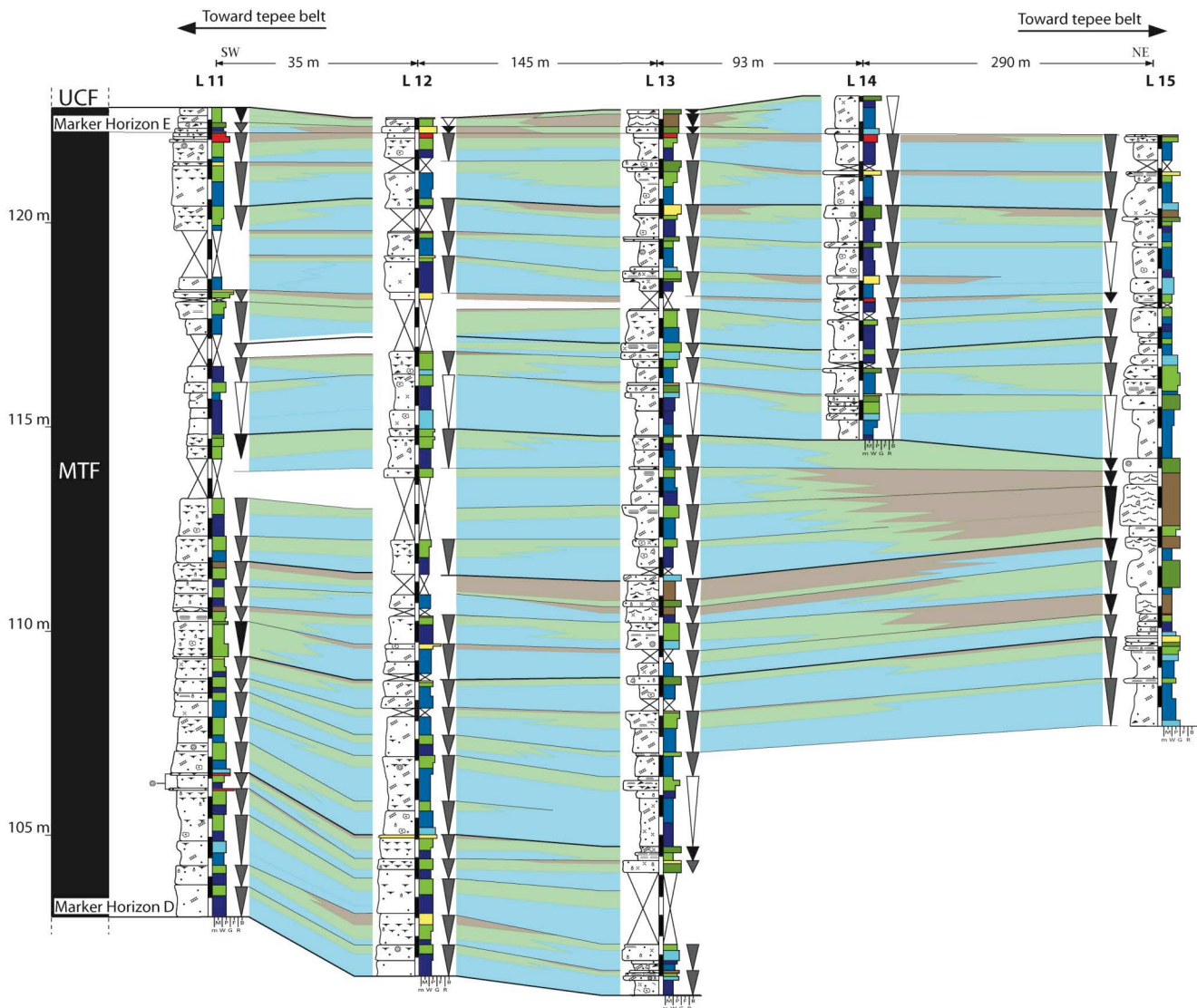


Figure 4.11: Transect C showing the lateral variability of cycles at the top part of the MTF. Lithofacies distribution indicates that the sections L11 and L15 are located close to the margin, whereas the sections L12, L13, and L14 tend to capture the lagoon. Note the increase of lateral lithofacies and cycle continuity compared to the transects A and B. For legend, please refer to Figure 4.4.



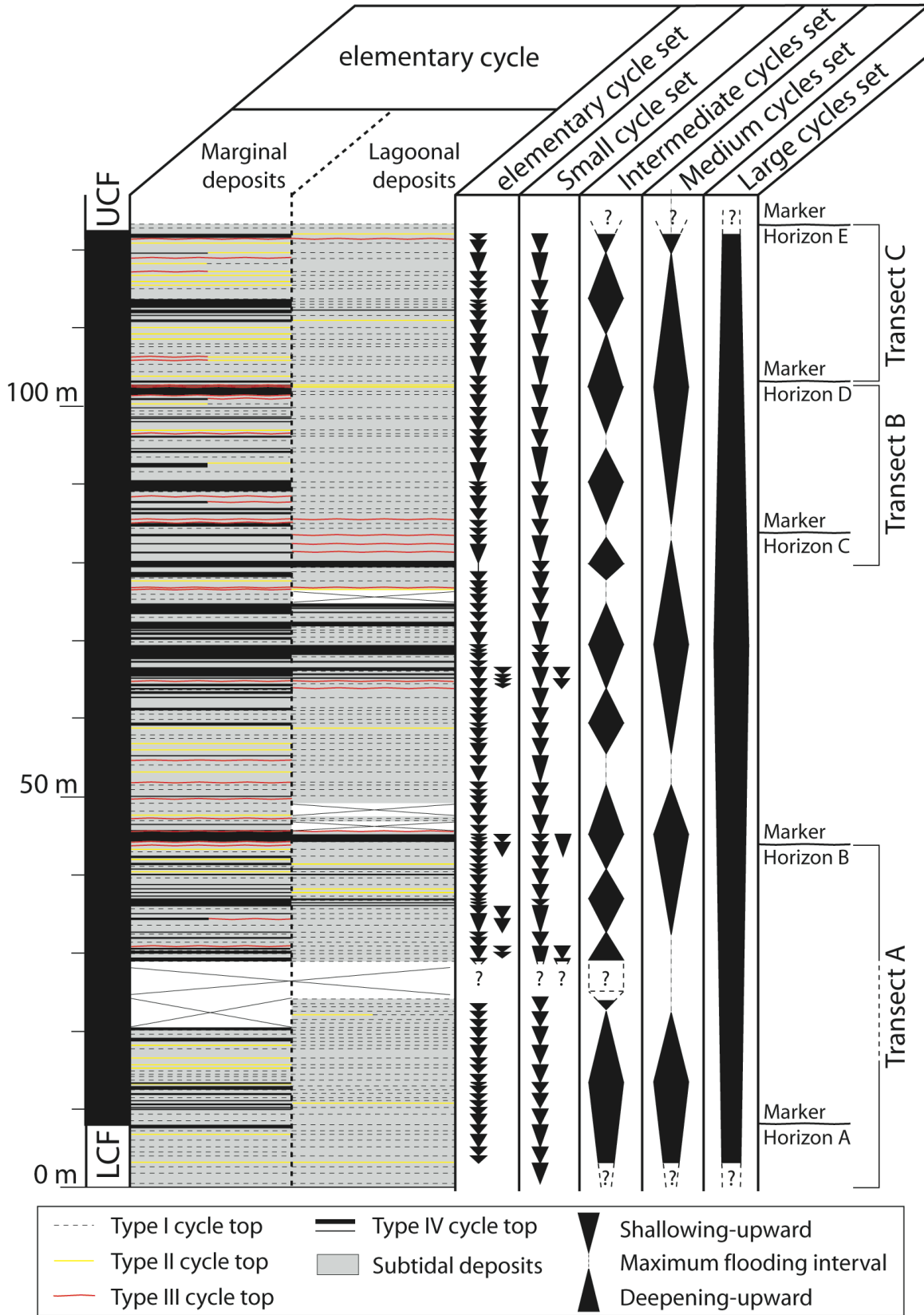
## 4.7. Hierarchical cyclicality of the Latemar platform top

The investigation of the spatial relationship between the Type A, Type B, and Type C cycles allowed for an interpretation of the hierarchical cyclicality in Cima del Forcellone. A composite section (Figure 4.12) was built from the sections L1, L2, L3, L7, and L11 (Figure 4.5) and comprises all lateral lithofacies variability observed in the study area.

Prior to introduce our results, it is necessary to review the existing nomenclature used to describe and interpret the cyclicality record in the Latemar platform top. Each decimeters to meter thick carbonate cycle was called shallowing-upward cycle (Hardie et al., 1986; Goldhammer and Harris, 1989; Goldhammer et al., 1990; Egenhoff et al., 1999; Mundil et al., 2003), microcycle (Zühlke et al., 2003; Zühlke, 2004), or sedimentary cycle (Preto et al., 2004) (Figure 4.1). Shallowing- and thinning-upward bundles of five cycles were recognized and referred to as megacycle, pentacycle (Goldhammer and Harris, 1989; Hinnov and Goldhammer, 1991), whereas the term macrocycle (Zühlke et al., 2003; Zühlke, 2004) was defined as a thinning-upward trend of two to six cycles.

The present study introduced a new and neutral nomenclature for each hierarchical cyclicality in order to avoid misunderstanding with previous works. The new nomenclature introduced from high to low order of cyclicality: elementary cycle, elementary cycle set, small cycle set, intermediate cycle set, medium cycle set, and large cycle set (Figure 4.12, Appendix A2). Elementary cycles correspond to the higher level of cyclicality observed with the Type B cycles, whereas elementary cycle sets, which represent a lower order of cyclicality, are referred to as Type A cycles. Consequently, each elementary cycle set is recognized by a shallowing- and thinning-upward bundle of two to three elementary cycles. The Type C cycles can be assigned to either elementary cycles or elementary cycle sets, depending of the ability to distinguish the cyclicality signal within tepee structures. Within the 115 m (+/- 2.5 m) thick MTF (4.5 m no cropping out), 208 elementary cycles and 92 to 97 elementary cycle sets were recognized with a thickness of 0.53 m and 1.14-1.20 m, respectively. At a larger scale, 47 to 50 small cycle sets were identified in the present study with an average thickness of 2.21-2.35 m. Small cycle sets are composed of a shallowing- and thinning-upward trend of four to five elementary cycles (Figure 4.12) and correspond to the definition of “megacycle” or “pentacycle” *sensu* Goldhammer and Harris (1989) and Goldhammer et al. (1990).

10 intermediate cycle sets were also recognized with an average thickness of 11.2-11.8 m. The basal part of these cycle sets is composed of a deepening-upward trend from supratidal-dominated deposits with tepee structures and “terra rossa” clay to subtidal and intertidal intervals. The deepening trend comes along with a thickness increase of cycle types. Intermediate cycle sets are capped by mature tepee structures, which are often laterally continuous across the study area. In addition, four, 28.1-29.4 m thick in average, medium cycle sets were also observed and show similar stacking pattern than intermediate cycle set. At the larger scale, two hemicycles, which controlled the transition between the LCF, the MTF, and the UCF, were also recognized.





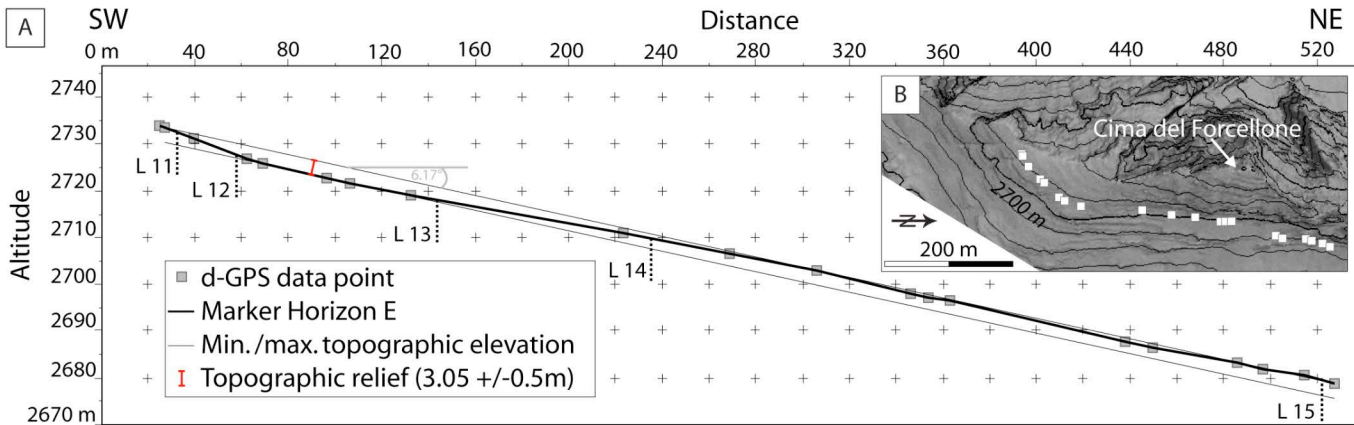
**Figure 4.12: Composite section of Cima del Forcellone from the top of the LCF to the top of the MTF, displaying the locations of marker horizons and transects. The composite section was created using the sections L1, L2, L3, L7, and L11. Each carbonate cycle is identified using the cycle tops classification of Christ et al. (2012b), in which intertidal deposits correspond to Type I cycle tops, dolomitized grainstone to Type II cycle tops, “terra rossa” clay to Type III cycle tops, and tepee structures to Type IV cycle tops. The lateral variability of cycle tops from marginal-dominated to lagoonal-dominated deposits is based on all data collected in the field. The MTF is 112.5 m to 117.5 m thick with 4.5 m of no-outcropping interval. Difference of the stratigraphic thickness is caused by changes of cycle thickness between the margin, the lagoon, and the backreef. 219 elementary cycles were observed from the top of the LCF to the MTF and the MTF is composed of 208 elementary cycles.**

## 4.8. Depositional profile and cyclicity

The cyclicity record displays a hierarchical stacking pattern of cycles and cycle sets and is characterized by significant lateral variability across the study area. A reconstruction of the palaeodepositional profile of the Latemar platform was performed in order to determine the relationship between the cyclicity record and the depositional conditions.

### 4.8.1 Margin to lagoon palaeotopographic relief

The palaeotopographic profile of the Latemar platform top played a major role in the establishment and evolution of the tepee belt (Egenhoff et al., 1999; Peterhänsel and Egenhoff, 2008). A DGPS mapping survey of the marker horizon E was carried out in order to quantify and characterize the platform top morphology. The marker horizon E that represents the MTF-UCF boundary highlights a palaeotopographic trough around the sections L12 and L13 surrounding by 3.05 m high (+/- 0.5 m) relief toward both sides of the study window (Figure 4.13). Furthermore, the DGPS mapping survey emphasizes an asymmetric morphology of the platform top. The southwestern margin part shows a steep and abrupt dipping profile between the sections L11 and L12 and a low-angle relief toward the northeastern part of the transect, between the sections L13 and L15. Facies variability along the marker horizon E does not exhibit clear evidences for a palaeobathymetric gradient apart from a slight thickness decrease of the “terra rossa” surface around the sections L12 and L13 (Figure 4.11). Nevertheless, the overall lithofacies distribution especially at the base of the transect C also suggests a palaeotopographic gradient from the sections L12 and L13 dominated by subtidal deposits to the sections L11 and L15 characterized by intertidal and supratidal features.



**Figure 4.13:** A. Graphic displaying DGPS data point (square) collected in the field during the mapping of the marker horizon E (black line). Sections L 11, L 12, L 13, L 14, and L 15 (dashed line) are also located. The mapping survey shows that the palaeotopographic gradient from the margin-to-lagoon depositional profile is around 3.05 m. B. Map view of the digital elevation model of Cima del Forcellone with the location of DGPS points (square).

#### 4.8.2. Cycle variability along the depositional profile

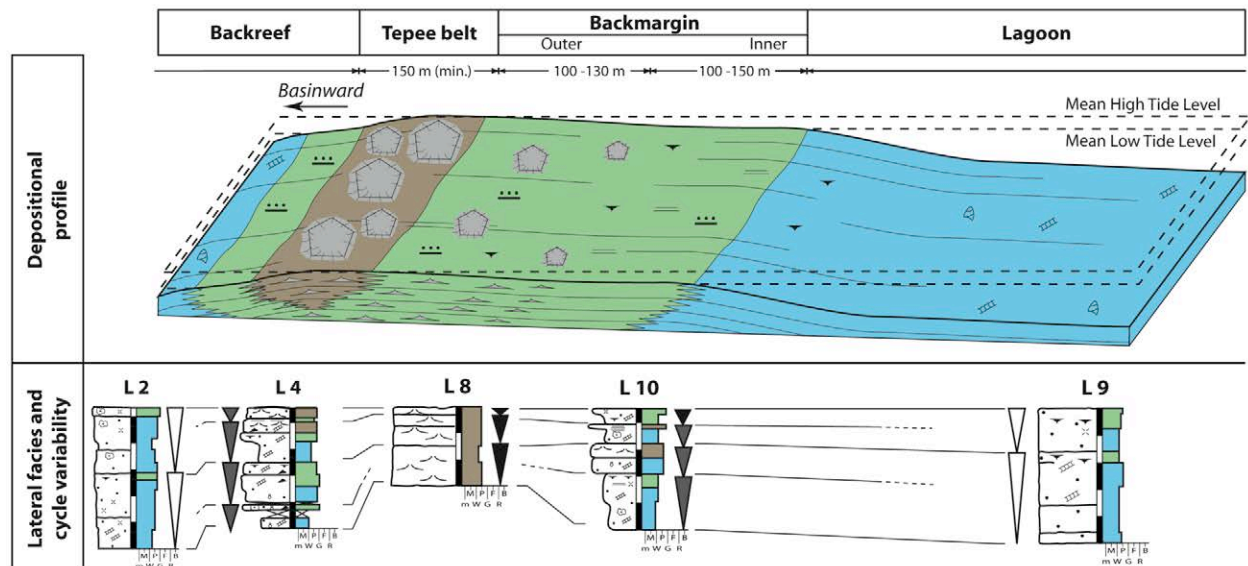
At the transition between the LCF and the MTF, tepee structures observed in the sections L4 and L5 grade laterally to subtidal and intertidal deposits in the sections L1, L2, and L3 (Figure 4.9). According to the location of the transect A (Figure 4.5), the palaeobathymetric deepening from supratidal to subtidal conditions corresponds to the transition between the palaeotopographically elevated tepee belt and the deeper backreef. The bathymetric gradient between both depositional environments comes along with a change of the cyclicity record. Bundle of two to three Type B cycles and in lesser amount Type C cycles, recorded in the tepee belt amalgamate into one single Type A cycle toward the backreef (Figure 4.14). Furthermore, the transition between the LCF and the MTF is associated with an overall relative sea level fall (Figure 4.12). During this period, the tepee structures in the sections L4 and L5 progressively extended toward the sections L2 and L3 up to the marker horizon B (Figure 4.9). The southwestward extension of the tepee structures is associated with an increase of lateral cycle continuity. Both observations suggest an attenuation of the bathymetric gradient across the transect A. Hence, the transect A captures the establishment of a tepee belt (section L4), which progressively overlap the backreef (sections L5 and L3) at the favor of a relative sea level fall.

At the middle part of the MTF, the sections L7 and L10, measured in both sides of the transect B (Figure 4.10), recorded numerous tepee structures, “terra rossa” surfaces, and intertidal deposits. The sections L8 and L9 display a subtidal-dominated lithofacies association (Lithofacies 1 and Lithofacies 2) capped by intertidal deposits and scarce supratidal features. In addition, the sections L8 and L9 show an increase of stratigraphic thickness compared to sections L7 and L10. Both observations indicate that the transect B captures the subtidal lagoon (sections L8 and L9) surrounded by the palaeotopographically elevated backmargin to tepee belt (sections L7 and L10). The palaeobathymetric gradient observed in both sides of the transect come along with the lateral variability of the cycle stacking pattern similar to the observations carried out in the transect A. Thinning-upward bundle of two to three

Type B and Type C cycles in the tepee belt to backmargin, tends to amalgamate lagoonward into one single Type A cycle (Figure 4.14). Furthermore, the tepee belt captured in the section L5 (Figure 4.9) is overlaid by lagoonal deposits in the section L8 (Figure 4.10), whereas the sections L4 and L7 recorded both the tepee belt (Figures 4.9, 4.10). Such stacking pattern of depositional environments indicates that the tepee belt shifted toward the backreef at the middle part of the MTF that corresponds to the maximum regressive phase of the large cycle set (Figure 4.12).

At the transition between the MTF and the UCF, the base of the sections L11 and L15 display respectively intertidal and supratidal deposits, whereas subtidal lithofacies are dominant in the sections L12 and L13 (Figure 4.11). The lithofacies variability is associated with thicker depositional package toward the sections L12 and L13. Hence, the sections L11 and L15 likely recorded the backmargin and the tepee belt and the sections L12 and L13 captured the lagoon. The transition from the tepee belt to the lagoon comes along with a subtle decrease of cycle numbers around 12% compared to 40% as reported from the transects A and B (Figures 9, 10). Upward, the top part of the transect C shows that lithofacies and cycle changes along the study area are less pronounced and tepee structures are rare to absent. Both observations point out the establishment of a laterally continuous lagoon at the favor of a relative sea level rise leading to the transition between the MTF and the UCF (Figure 4.12).

To conclude, the expression of the cyclicity record is highly dependent of the depositional environment considered. High-frequency relative sea level fluctuations were partially recorded within the lagoon and the backreef, whereas the backmargin and tepee belt were sensitive to each change of the relative sea level. The influence of autocyclic processes on the cyclicity record led to different stacking of carbonate cycles and cycle sets across the platform top (Figure 4.14).



**Figure 4.14:** Schematic view of the depositional profile of the Latemar platform top from the lagoon to backreef showing the lateral variability of small cycle sets, which correspond to the megacycle *sensu* Goldhammer and Harris (1989). The record of the Latemar cyclicity changes with respect to variations of bathymetry, leading to an increase of cycle number (up to 66% locally) from the deep lagoon and backreef to the palaeotopographically elevated tepee belt and backmargin. Note that i) Type A cycles recorded in the lagoon and backreef, correspond to two to three Type B cycles within the tepee belt and backmargin and ii) Type C cycles grade laterally to either Type A or Type B cycles. For legend, please refer to Figure 4.4.

## 4.9. Discussion

### 4.9.1. Controlling factors on lateral cycle variability

The megacycles or pentacycles *sensu* Goldhammer et al. (1990) (Figure 4.1) represent the shallowing-upward trend of five elementary cycles and correspond to small cycle sets in the present study. Condensed and amalgamated megacycles were also introduced by the same authors and represent the stacking pattern of two or three instead of five cycles. The difference of stacking pattern between megacycles was thought to represent unrecorded relative sea level oscillation referred as “missed beat”. The condensed megacycles developed during relative fall of sea level and recorded subaerial “missed beat”. At this period, whereas the tepee belt was exposed, the lagoon remained submerged, recording additional fluctuation of the relative sea level. Field observations reported here are in contradiction with the assumption of condensed cycles, which involves a decrease of the cycle number from the lagoon to the margin. Instead, the numbers of elementary cycles increase (up to 66% locally) from the lagoon to the tepee belt, indicating that the 3 m high margin recorded more high-frequency relative sea level fluctuations than the lagoon. The occurrence of subaerial “missed beats” *sensu* Goldhammer et al. (1990) and expressed by a carbonate cycle deposited in the lagoon that pinch out toward the tepee belt, is therefore unlikely to occur across the stratigraphic interval of the Latemar platform top. Nevertheless, laterally continuous, subaerial exposure surfaces (“terra rossa” clay and tepee structures) were described and interpreted as major exposure stages of the entire platform top (Goldhammer and Harris, 1989). The lack of time constraints makes it difficult to estimate the duration of each hiatus period (Christ et al., 2012b). Hence, subaerial “missed beats” *sensu* Goldhammer et al (1990) may have occurred and were recorded as continuous subaerial exposure surfaces, with a lack of pinch out of carbonate cycles from the lagoon to the tepee belt.

The second type of “missed beat” observed in amalgamated megacycle was assumed to result from periods of overall relative rising of sea level, when high-frequency sea level fluctuation failed to expose the sea floor (Goldhammer et al., 1990). The occurrence of these “missed beat” was thought to develop uniformly across the platform top. Amalgamated cycles is a common feature observed in the present study, leading to variations in the cycle number (Figure 4.14). However, the amalgamation process developed laterally along the lagoon-to-margin depositional profile. The marine flooding surfaces of elementary cycles disappear over a distance of few tens of meters (Figure 4.10) to 300 meters (Figure 4.11) and amalgamate into elementary cycle set. Contrarily elementary cycle sets and small cycle sets were observed to be laterally continuous. Amalgamation process seems to affect solely the expression and the record of elementary cycles. During each elementary cycle, the relative sea level fluctuation failed to expose the sea floor of the lagoon, whereas the margin was recorded subaerial stage. The repetition through time of a spatially-dependent cyclicality record led to changes of the expression of small cycle sets between the lagoon and the margin (Figure 4.14). The margin-to-lagoon palaeobathymetric gradient associated with tidal-amplitude (Kenter et al., 2004) relative sea level fluctuation are likely the two main factors causing unfilled accommodation in the lagoon. In addition, within the tepee margin, sediments were preferentially trapped within saucer-shaped polygonal tepee structures (Peterhänsel and Egenhoff, 2008), which likely facilitated the infilling of accommodation.

### ***4.9.2. Consequences on the Latemar Controversy***

In total, the present study reported a 115 m (+/- 2.5 m) thick MTF (4.5 m no cropping out) that consists of a stacking pattern of 208 elementary cycles, 92 to 97 elementary cycle sets, and 47 to 50 small cycle sets with an average thickness ranging of 0.53 m, 1.14-1.20 m, and 2.21-2.35 m, respectively. The number and thickness of the elementary cycles are in agreement with previous studies carried out in Cima del Forcellone (Bechstädt et al., 2003). The cyclostratigraphic interpretation reported here is supported by spectral analysis carried out on the MTF (Zühlke et al., 2003; Zühlke, 2004) (Table 4.2). Spectral analysis inferred two sub-Milankovitch and one Milankovitch forcing on the Latemar cyclicity with a period of 4.2 kyr, 15 kyr, and 19.3 kyr, respectively. The three cyclicity signals display similar stacking pattern and thickness compared to the elementary cycles, elementary cycle sets, and small cycle sets (Table 4.2). Hence, whereas elementary cycle and elementary cycle sets likely recorded sub-Milankovitch cyclicity, small cycle sets seem to be controlled by precession forcing. Furthermore, the amalgamation process leading to changes of the expression of the cyclicity record was previously interpreted as a result of 100 kyr eccentricity superimposed on 20 kyr precession forcing (Goldhammer and Harris, 1989; Goldhammer et al., 1990). The data reported here shows that the amalgamation process took place at a considerable shorter time period. Section correlations indicate that the flooding surfaces of the elementary cycles are laterally discontinuous along the platform top in contrast to those associated to the elementary cycle sets and small cycle set. The amalgamation process seems to occur exclusively at the sub-Milankovitch time scale.

At a larger scale, 10 intermediate cycle sets from 11.2-11.8 m thick were also recognized and consist of the stacking of 21 to 23 elementary cycles capped by tepee structures (Table 4.2). The occurrence of tepee structure every 10 m in average was previously mentioned in literature (Goldhammer and Harris, 1989; Goldhammer et al., 1990; Egenhoff et al., 1999). The cycle number and thickness of intermediate cycle sets are similar to the short eccentricity signal interpreted from spectral analysis and characterized by 13 m thick bundles of 23 to 25 elementary cycles in the MTF (Zühlke et al., 2003; Zühlke, 2004) (Table 4.2). Furthermore, the present study identified 30 m thick medium cycle sets, composed of 53 to 56 elementary cycles, whereas the transition between the LCF, MTF and UCF was defined by a 125 m thick (minimum value) large cycle set. Assuming that the intermediate cycle sets represent short eccentricity forcing, medium and large cycle sets should have recorded transient component of the eccentricity (Hinnov, 2000) and a lower order than long eccentricity forcing, respectively. The difficulty to interpret eccentricity forcing from the sedimentary record was also shown during previous spectral analysis (Zühlke et al., 2003; Zühlke, 2004). The superimposition of various amplitudes and frequencies in the stratigraphic record from sub-Milankovitch to Milankovitch forcing have likely caused modulations of the cyclicity signal (Hinnov, 2000; Preto et al., 2001, 2004).

The main difficulty faced during the establishment of the present cyclostratigraphic framework was the distinction between Type A and Type B cycles toward the LCF and the UCF (Figures 4.9, 4.11) and during relative sea level rise of the intermediate cycle sets (Figure 4.12). During periods of high accommodation, carbonate cycles tend to be thicker and Type B cycle reached up to one meter in thickness, displaying similar sedimentological features to those of Type A cycles. The increase of subsidence rate from 330 m to 450 m from the MTF to the UTF (Emmerich et al., 2005b) and the higher sedimentation rate during the LCF and the UCF compared to the MTF

(Zühlke et al., 2003) contributed to the thickening of cycle type. Type B cycles and Type A cycles recorded two different (likely sub-Milankovitch) cyclicity signals, which correspond to the elementary cycles and elementary cycle sets (Table 4.2). The identification of each cyclicity signal was solely feasible by the investigation of lateral cycle variability. Consequently, previous cyclostratigraphic studies carried out by using one single section, especially within cyclic units (LCF and UCF) may have led to errors during the interpretation of the cyclicity signal. The establishment of a reliable field-based cyclostratigraphic framework requires the investigation of a margin-to-lagoon transect in order to fully capture the hierarchical stacking pattern of carbonate cycles within the Latemar platform top.

**Table 4.2: Summary of the hierarchical cyclicity interpreted from the MTF of Cima del Forcellone and comparisons with previous spectral analysis (Zühlke et al., 2003; Zühlke, 2004). Note that both cyclostratigraphic interpretations display similar cycle stacking patterns.**

Nomenclature	Number of cycles and cycle sets	Thickness (m)	Ratio of cycle bundles		Controlling factors
			<i>Present study</i>	<i>Zühlke et al., 2003</i>	
Elementary cycle	208	0.53	1:1	1:1	<i>Zühlke et al., 2003 and present study</i> Sub-Milankovitch
Elementary cycle set	92-97	1.14-1.20	1:2 1:3	1:3.61	Sub-Milankovitch or Condensed precession
Small cycle set	47-50	2.21-2.35	1:4 1:5	1:4.92	Precession
Intermediate cycle set	10	11.2-11.8	1:21 1:23	1:23.95	Short eccentricity
Medium cycle set	4	28.1-29.4	1:53 1:56	1:105.65	Transient component of eccentricity
Large cycle set	1	125 (min. value)	1:236 (min. value)	1:105.65	Lower order than eccentricity

### 4.9.3. Platform top aggradation

The smooth transition of lithofacies and cycles between the margin and the lagoon as reported here, the absence of pinch out (Goldhammer et al., 1987; Goldhammer and Harris, 1989; Egenhoff et al., 1999) or tidal-flat progradation (Ginsburg, 1971; Pratt and James, 1986) features suggest an overall homogeneous and continuous accumulation of sediments such as the aggrading sheet model (Pratt et al., 1992) during the growth of the Latemar platform top. The present data distinguishes two phases during the aggradational stacking pattern. During periods of maximum sea level fall of intermediate cycle sets (Figure 4.12), the stacking pattern of few elementary cycles (Type B cycles) or elementary cycle sets (Type A cycles) in the interior platform grade marginward into a stack of Type C cycles, corresponding to tepee structures (Figure 4.9, around 37 m; Figure 4.10, around 90 m; Figure 4.11, around 113 m). The lateral variability of the cycle types comes along with a decrease of the stratigraphic thickness. Both



observations suggest the infilling of the lagoon trough during periods of tepee growth. The duration of infilling is variable but does not seem to exceed one precession period. The second phase took place during periods of relative sea level rise associated to intermediate cycle sets (Figure 4.12). During this period, the transect B (Figure 4.10; from 90 m to 100 m) and the transect C (Figure 4.11; around 105 m) show a thickening trend of the depositional package from the lagoon to the margin. This thickness change suggests a higher sedimentation rate toward the margin than toward the lagoon that would explain the preservation of a palaeotopographic relief in the margin during the entire evolution of the Latemar platform.

To conclude, the aggradational stacking pattern of the Latemar platform top seems to alternate between i) periods of preferential sediment accumulation within the margin and ii) periods of tepee growth in the margin that come along with the infilling of the lagoon. Whereas the first stage created palaeotopographic relief, the second stage tended to flatten the Latemar platform top.

## 4.10. Conclusion

The investigation of a 125 m thick and 800 m long backreef-to-lagoon transect located in Cima del Forcellone, emphasized significant lateral variability of the expression and number of carbonate cycles along the depositional profile. Findings reported here required the introduction of a cycle classification and the establishment of a new cyclostratigraphic framework of the Latemar platform top. The data set built on the collection of 15 sections with an inter-section ranging from 35 m to 235 m and correlated by using five marker horizons.

- Height lithofacies were recognized and reflect three depositional conditions i) subtidal deposits showing a semi-restricted to open marine biotic association ii) intertidal deposits with fenestral and laminar fabrics, and iii) intertidal to supratidal deposits displaying evidences of periodic, more or less prolonged subaerial exposure stages.
- Three types of cycle were identified, meter thick, subtidal-dominated Type A cycles deposited in the lagoon, which grade marginward into a thinning-upward bundle of two to three decimeters thick, peritidal-dominated Type B cycles in the backmargin. Type C cycles, which recorded mainly tepee structures, were observed in the tepee belt and pass laterally to either Type A or Type B cycles depending of the duration associated to the tepee growth. The lateral discontinuity of Type B cycle from the margin to the lagoon is a common feature in the platform top, leading to an increase of the cycle number (up to 40%).
- A new cyclostratigraphic nomenclature is introduced within the 115 m thick MTF (4.5 m no cropping out). From high to low order of cyclicity, 208 elementary cycles (0.53 m thick) correspond to Type B cycles, 92 to 97 elementary cycle sets (1.14-1.20 m thick) define Type A cycles, and 47 to 50 small cycle sets (2.21-2.35 m thick), which are comparable to the megacycles *sensu* Goldhammer et al., (1989). Ten intermediate cycle sets (11.2-11.8 m thick) bounded by continuous tepee horizons and four medium cycle sets (28.1-29.4 m thick) were also interpreted. The transition between the LCF, MTF, and UCF is controlled by large cycle sets. The establishment of the cyclostratigraphic framework shown here confirms previous model-independent spectral analysis.

- The expression of the small cycle sets was mainly recognized at the transition between the backmargin and the lagoon, where a clear stacking pattern of four to five elementary cycles can be observed. Lagoonward, small cycle sets grade into a thinning-upward of two elementary cycle sets. The irregularity of the expression of small cycle sets was mainly controlled by the palaeotopographic gradient from the tepee belt to the lagoon and the backreef.
- Section correlations carried along a backreef-to-lagoon transect indicate that the expression of the cyclicity record is highly dependent of the location of the study area in the depositional profile or along the stratigraphic record. The carbonate cycles are not identical between each other and can span different duration. The present study demonstrates that the investigation of lateral cycle variability is the unique method to fully identify and interpret the hierarchical cyclicity recorded in the stratigraphic succession of the Latemar platform top.



# 3-D modeling of the margin-to-lagoon depositional profile of the Latemar isolated platform (Middle Triassic, Dolomites)

### *Abstract*

Mechanisms controlling the growth of the Late Anisian-?Early Ladinian (Middle Triassic) isolated platform of Latemar and their impact on the depositional profile are still in debate, despite numerous studies carried out in the last 20 years. Most of these studies were based on the investigations of either margin-to-basin transects or on punctual, 1-D observations, whereas there was no detailed, field-based description of the lagoon-to-margin depositional profile and its evolution through time.

The present study documents and interprets the evolution of the lagoon-to-backreef depositional profile, using an approach, which combines facies analysis, cyclostratigraphy, and 3-D modeling. The study area is located in Cima del Forcellone and comprises the top part of the Lower Cyclic Facies (LCF) and the entire Middle Tepee Facies (MTF), which are described using 15 closely-spaced sedimentary sections across a 800 m long transect.

Field correlations and geological modeling of Cima del Forcellone demonstrates that the platform top recorded a complex lithologic and stratigraphic stacking pattern, which were not shown in previous studies. Four stratigraphic stages are recognized from the base to the top of the MTF, i) two basinward progradational phases, ii) an aggradational stacking pattern, and iii) a retrogradation of the tepee belt at transition between the MTF and UCF. A progradation-aggradation-retrogradation stacking pattern is typical of a lowstand to transgressive system tracts. In addition, the present study observes repetitive flooding of the tepee belt, indicating rhythmic variations between a rimmed and non-rimmed platform top.

The investigation of the lagoon-to-backreef depositional profile, combined with previous studies focused on the margin-to-slope transect, offers the opportunity to discuss the evolution of the Latemar platform in an integrated matter. Beyond tectonic, relative sea level fluctuation seems to have played a significant role during the platform growth by favoring sediment accumulation at the slope-to-margin transition.

## 5.1. Introduction

The stratigraphic architecture and facies heterogeneity of carbonate platforms and their evolution through time (Wilson, 1975; Tucker and Wright, 1990), are controlled by the interplay of numerous internal and external factors such as eustasy, tectonic, sea-water temperature, trophic conditions, sea water chemistry, type and size of grains (Kenter and Campbell, 1991; Osleger, 1991; Strasser et al., 1999; Wilkinson et al., 1999; Lehrmann and Goldhammer, 1999; Mutti and Hallock, 2003; Wilkinson and Drummond, 2004; Bosence, 2005; Wright and Burgess, 2005; Burgess, 2006; Strasser and Vadrine, 2009). The tectono-eustatic context in which a carbonate platform grows is well-known as a key factor conditioning its morphology and stacking pattern (Read, 1985; Kendall and Schlager, 1981; Handford and Loucks, 1993; Bosence, 2005).

Depositional mechanisms leading to the growth of the Latemar, a Triassic isolated platform outcropping in the Dolomites (northern Italy), have been debated since the early eighties (Bosellini, 1984; Goldhammer and Harris, 1989; Goldhammer et al., 1990; Zühlke et al., 2003; Emmerich et al., 2005a; Preto et al., 2011). Most of the studies were focused on the duration and the factors controlling the deposition of the ~700-800 decimeters to meter thick, shallowing-upward cycles observed across the platform top (Goldhammer and Harris, 1989; Goldhammer et al., 1990; Hinnov and Goldhammer, 1991; Brack and Rieber 1993; Brack et al., 1996; Preto et al., 2001; Mundil et al., 2003; Kent et al., 2004; Preto et al., 2004; Emmerich et al., 2005b; Zühlke, 2004; Meyers, 2008; Peterhänsel and Egenhoff, 2008). Most workers now agree for a sub-Milankovitch forcing model to explain the Latemar cyclicity. Few platform-scale studies investigated the mechanisms driving the architecture of the platform (Bosellini, 1984; Goldhammer and Harris, 1989; Harris, 1994; Egenhoff et al., 1999; Emmerich et al., 2005a; Preto et al., 2011). Whereas a majority of studies invoked relative sea level fluctuations (Bosellini, 1984; Goldhammer and Harris, 1989; Goldhammer et al., 1990; Egenhoff et al., 1999) as major factor controlling the platform evolution, recent works (Emmerich et al., 2005a; Preto et al., 2011) proposed a tectonically-driven model, based on the co-occurrence of local backstepping stages and synsedimentary faulting at the margin-to-slope transition. At the date, detailed, field-based descriptions of the lagoon-to-margin depositional profile and its evolution through time are scarce in literature.

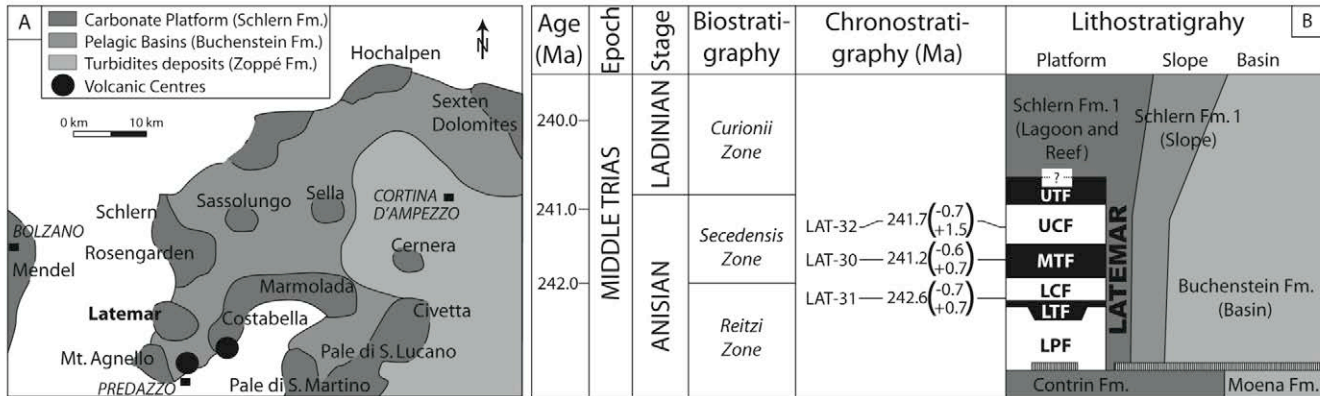
The present study documents and interprets the evolution of a lagoon-to-backreef depositional profile, through a multidisciplinary approach integrating facies analysis and stratigraphic architecture into a 3-D outcrop model. Using closely-spaced sedimentary sections, the 3-D outcrop model described cycle and facies distribution within two of the six lithostratigraphic units defined within the Latemar carbonate succession: the uppermost Lower Cyclic facies (LCF) and the Middle Tepee Facies (MTF). The modeling approach allowed for a quantitative investigation of the lateral and vertical variability of lithofacies and cycles along the lagoon-to-backreef depositional profile. The findings reported here were combined with previous studies focused on the backreef-to-slope transition (Harris, 1993, 1994; Emmerich et al., 2005a; Preto et al., 2011) in order to reconstruct the Late Anisian-?Early Ladinian Latemar platform evolution.

## **5.2. Geological and stratigraphic setting**

### ***5.2.1. The Latemar platform***

The Latemar platform is located in the Dolomites (northern Italy) and consists of a Middle Triassic shallow-water carbonate succession deposited in the northwestern margin of the Tethys Ocean (Figure 5.1A). During the Early to Late Anisian, a carbonate ramp (Contrin Formation; Masetti and Neri, 1980) developed along the margin of the Tethys Ocean and was fragmented into several graben and horst structures during a Late Anisian transpressive-transpressive tectonic event (Gaetani et al., 1981; Castellarin et al., 1988). Isolated carbonate platforms such as the Latemar (Schlern Formation; Gaetani et al., 1981) nucleated upon topographic highs, surrounded by sediment-starved basins filled by pelagic deposits (Buchenstein or Livinallongo Formations; Bosellini, 1984; Neri and Stefani,

1988) (Figure 5.1). During a Late Ladinian to Early Carnian magmato-tectonic event (Bosellini and Rossi, 1974; Viel, 1979; Doglioni, 1987), hundreds of meter thick volcano-clastic sediments (Wengen Group) coming from nearby volcanic centers (Figure 5.1A), were deposited within the basin and buried some carbonate platforms such as the Latemar (Bosellini, 1984; Bosellini et al., 1996).



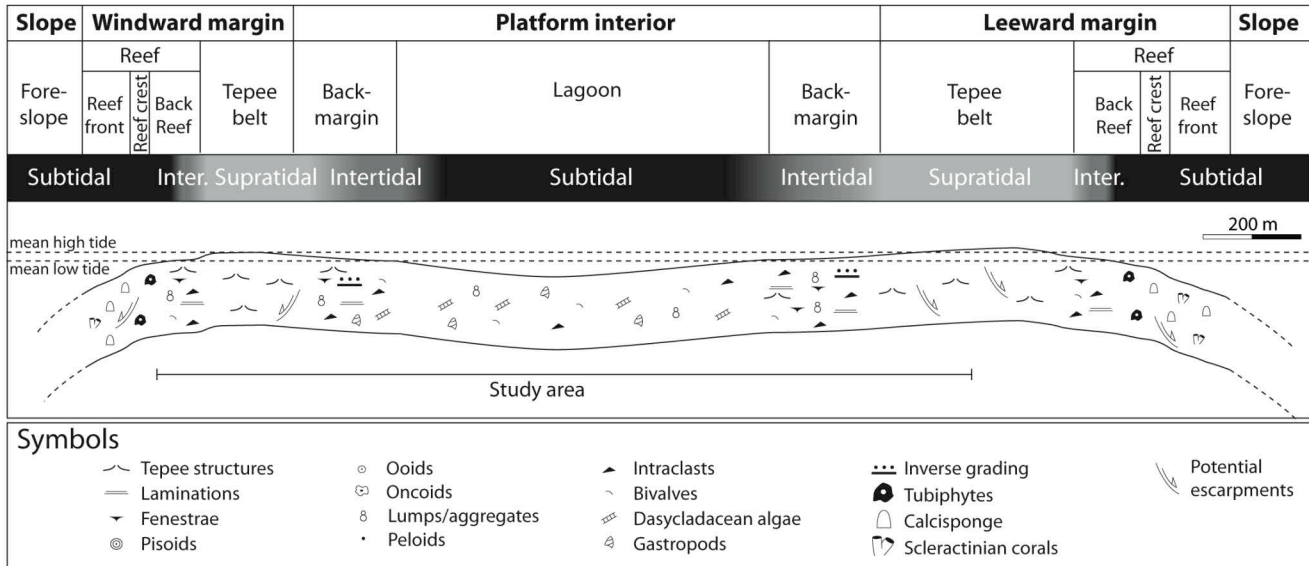
**Figure 5.1: A. Schematic palaeogeographic map of the Triassic carbonate platforms located in a passive continental margin at the northwest end of the Tethys Ocean during the Late Anisian to Early Ladinian (after De Zanche and Farabegoli, 1988; Emmerich et al., 2005a). B. Stratigraphic setting of the Latemar isolated platform comprising chronostratigraphic (Mundil et al., 2003), biostratigraphic (Brack and Rieber, 1993) and lithostratigraphic (Egenhoff et al., 1999) data. LPF = Lower Platform Facies, LTF = Lower Tepee Facies, LCF = Lower Cyclic Facies, MTF = Middle Tepee Facies, UCF = Upper Cyclic Facies, and UFT = Upper Tepee Facies. The present study focused on the top part of the LCF and the MTF.**

The Latemar isolated platform consists of a 800 m high submarine relief bordered by a 25-35° dipping slope. The depositional profile of the platform top comprises a subtidal lagoon, surrounded by a palaeotopographically elevated margin and backmargin settings with supratidal- to intertidal-dominated deposits (Figure 5.2). Toward the upper slope, the platform top is composed of a subtidal backreef that changes laterally into a reef with abundant microbial crusts (Harris, 1993; Emmerich et al., 2005a). The foreslope displays megabreccia deposits that pinch out basinward to rhythmic turbiditic sediments (Goldhammer and Harris, 1989; Harris, 1994). The foreslope also recorded localized rock falls, avalanches, and slump scars.

At present, the Latemar platform displays a 720 m thick stratigraphic interval of subtidal and peritidal carbonate deposits (Gaetani et al., 1981) (Figure 5.1B). The stratigraphic succession is composed of a rhythmic stacking pattern of ~700-800 decimeters to meter thick, shallowing-upward cycles (Goldhammer and Harris, 1989), thought to be controlled by sub-Milankovitch forcing (Zühlke et al., 2003). Six lithostratigraphic units were recognized: Lower Platform Facies (LPF), Lower Tepee Facies (LTF), Lower Cyclic Facies (LCF), Middle Tepee Facies (MTF), Upper Cyclic Facies (UCF), and Upper Tepee Facies (UFT) (Gaetani et al., 1981; Goldhammer and Harris, 1989; Egenhoff et al., 1999) (Figure 5.1B). At the base of the stratigraphic succession, the LPF and LTF were grouped into the Lower Edifice (Gaetani et al., 1981). The Lower Edifice consists of subtidal-dominated deposits with abundant submarine hardgrounds and rare subaerial exposure surfaces, representing the deepest depositional conditions of the stratigraphic interval. The overlying four lithostratigraphic units consist of a rhythmic succession of intertidal-



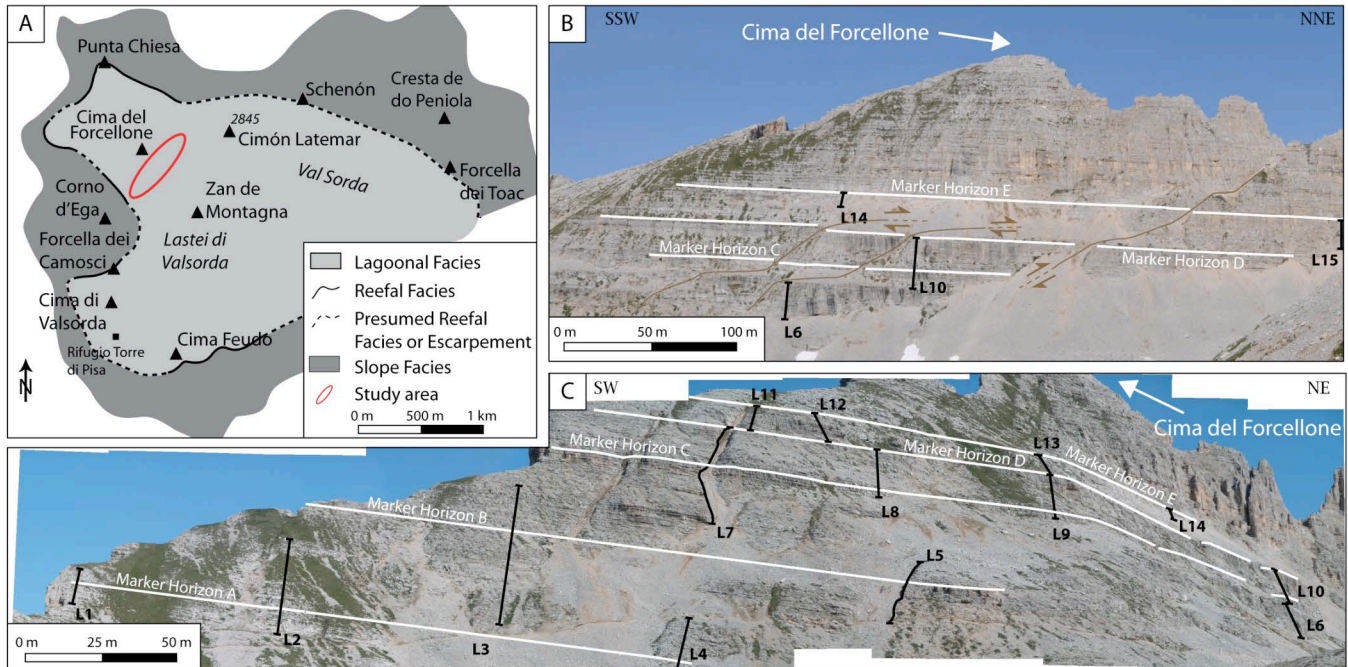
(LCF and UCF) and supratidal-dominated (MTF and UTF) intervals (Figure 5.1B). The rhythmic succession is thought to be driven by either 3<sup>rd</sup> order sea level fluctuations (1-10 m.y.) (Goldhammer et al., 1990; Egenhoff et al., 1999) or eccentricity forcing (Zühlke et al., 2003; Zühlke, 2004).



**Figure 5.2: Depositional profile of the Latemar platform top from the foreslope to the lagoon. Note the asymmetric morphology of the platform (Egenhoff et al., 1999; Emmerich et al., 2005a).**

### 5.2.2 The study area: *Cima del Forcellone*

The outcrop of Cima del Forcellone is located in the northwestern part of the platform, and has recorded a continuous depositional profile comprising the backreef, the tepee belt, the backmargin, and the lagoon (Figure 5.3). The present study investigates a 122.5 m thick stratigraphic interval spanning from the uppermost LCF to the boundary between the MTF and the UCF (Appendix A2). Cima del Forcellone outcrop offers the best configuration to document both lateral and vertical variability of lithofacies and cycles at the turning points in the stratigraphic succession between tepee-poor units (LCF and UCF) and tepee-rich units (MTF). The studied interval displays a hierarchically-ordered cyclicity record, which has been previously introduced and interpreted in Chapter 4 (Pages 86-89) (Appendix A2). To summarize, the MTF is composed of 208 elementary cycles, which constitute the genetic depositional packages of the stratigraphic succession (Figure 5.4). The bundle of two to three, shallowing-upward elementary cycles are grouped into elementary cycle sets, whereas small cycle set consists of a shallowing- and thinning-upward trend of four to five elementary cycles. At the larger scale, the stacking pattern of small cycle sets shows deepening- and shallowing-upward trends, which define intermediate, medium, and large cycle sets (Figure 5.4).



**Figure 5.3:** A. The Latemar isolated platform in map view with the location of the study area in Cima del Forcellone outcrop. B and C. Panorama of the SSW-NNE (B) and SW-NE (C) cliffs of Cima del Forcellone, showing the distribution of the sections (from L1 to L15; black), the marker horizons (white), and the post-depositional inverse faults (brown).

## 5.3. Methodology

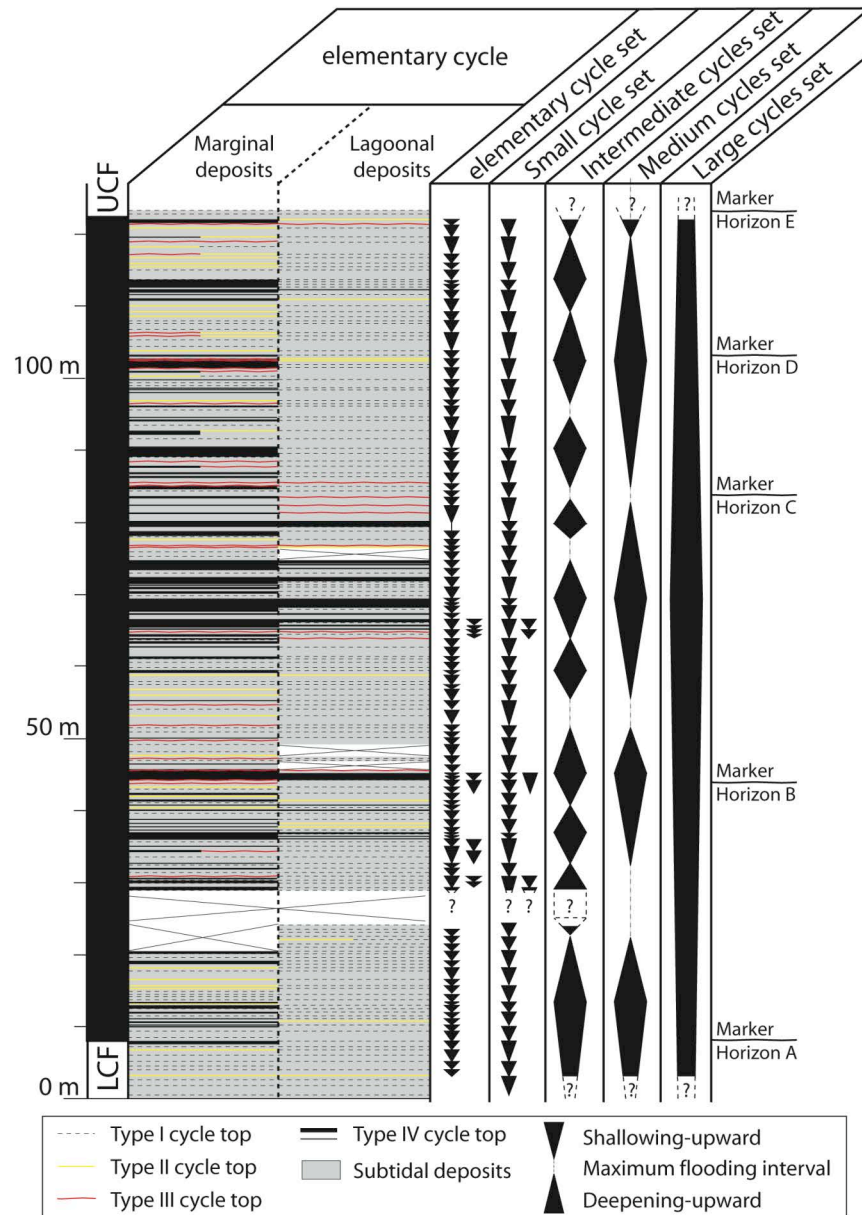
### 5.3.1. Field work

The data set comprises 15 stratigraphic sections covering a 800 m long transect, along the depositional profile of the platform top (Figure 5.3, Appendix A2). The inter-section spacing ranges between 35 m and 235 m. Each section was logged bed by bed, with samples taken with an average of 1 sample/20-30 cm. A total of 89 thin-sections were analyzed for facies analysis. The estimation of lithofacies proportion was extracted from the 3-D outcrop model.

### 5.3.2. GPS mapping

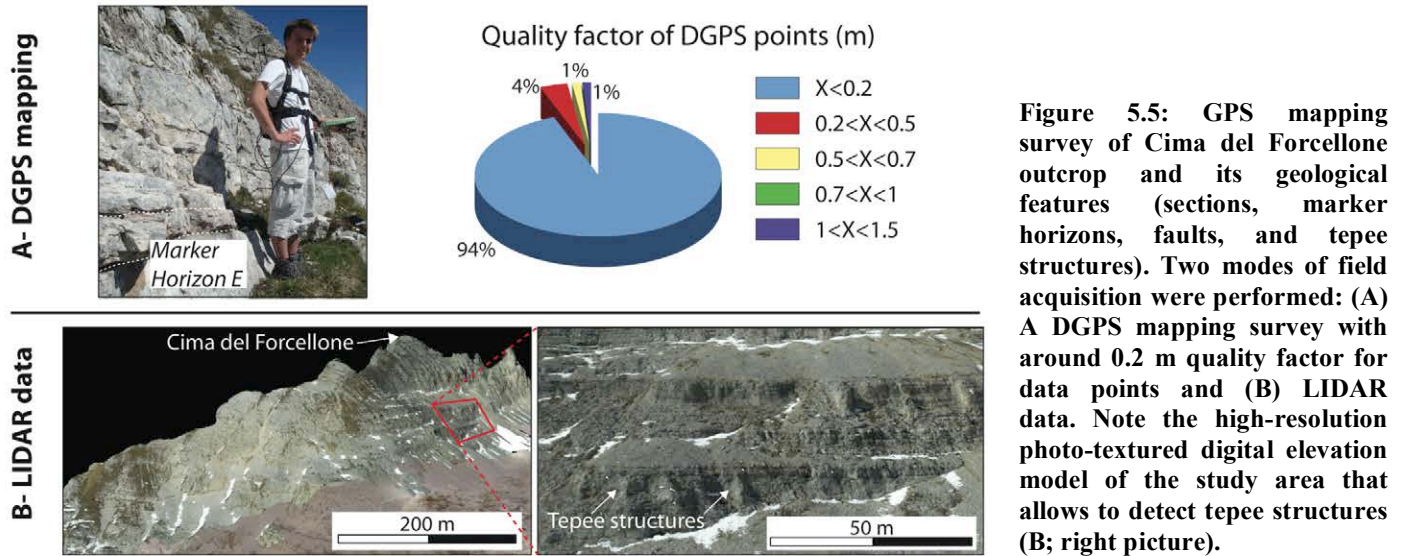
Five marker horizons were physically traced and mapped in the field for correlation and modeling purposes. The marker horizon A corresponds to the boundary between the LCF and MTF, the marker horizons B, C, and D are located within the MTF, whereas the marker horizon E represents the limit between the MTF and UCF (Figures 5.3, 5.4, Appendix A2). The mapping survey of surfaces and sections was performed using a DGPS system (Leica System 1200 Differential Global Positioning System) (Figure 5.5A). For details about the mapping methodology, please refer to Amour et al. (2012) (Chapter 2, page 11). Furthermore, helicopter-based LIDAR data were collected to obtain an accurate digital elevation model. LIDAR data was also used to provide additional GPS data points for inaccessible areas, by picking geological features on the photo-textured digital elevation model (Figure 5.5B).

LIDAR interpretations were performed using LIME, a visualization and interpretation software developed by Dr. Simon Buckley at the Centre for Integrated Petroleum Research in Bergen. Three major post-depositional inverse faults, observed in the northeastern part of the study area, were also mapped (Figure 5.3B). Georeferenced geological data were then integrated into a 3-D modeling package in order to build the outcrop model.



**Figure 5.4: Composite section of the uppermost LCF and the MTF showing the lateral variability of lithofacies and cycles from the margin to the lagoon. The composite section was built using the sections L1, L2, L3, L7, and L11 and displays six hierarchical orders of cyclicality (Appendix A2). Note the position of the marker horizons A to E. The type of cycle tops used to display the cyclic stacking pattern refers to the nomenclature of Christ et al. (2012b). Type I cycle tops represent intertidal deposits (dashed), Type II cycle tops identify dolomitic caps (yellow), Type III cycle tops represent “terra rossa” surfaces (red), and the tepee structures are shown by Type IV cycle tops (black). Note that the thickness of the black lines reflects the thickness of the tepee structures.**





### 5.3.3. Constrains on facies modeling

The evaluation of geobody dimensions (major and minor directions of elongation) using semi-variogram analysis (Gringarten and Deutsch, 2001) is crucial for stochastic facies simulation. However, the distribution of geological dataset and the exposure conditions of Cima del Forcellone outcrop (Figure 5.3) allow only for a 2-D, NE-SW investigation of the geobody dimensions parallel to the depositional profile. Consequently, only the minor direction of sedimentary bodies was captured, assuming that their major direction is oriented perpendicular to the depositional profile. Major directions of elongation were arbitrary assumed as covering two times the distance of the minor direction for modeling purposes.

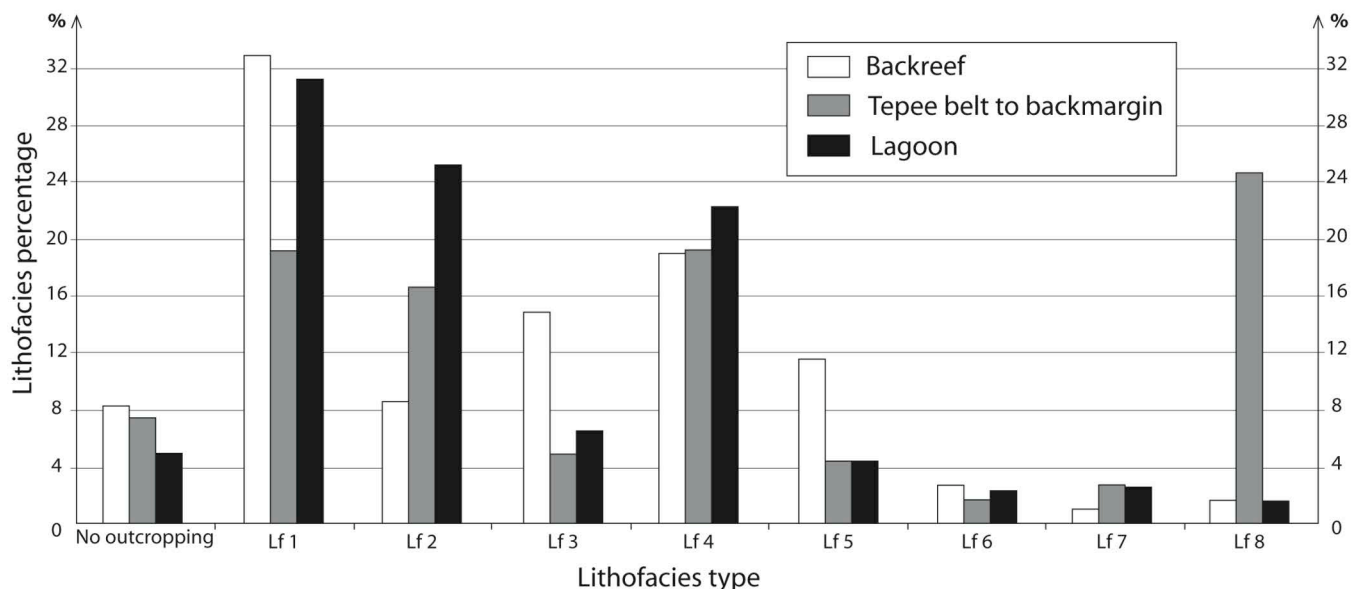
Geological modeling of shallow-water carbonate rocks requires the implementation of various modeling techniques (Falivene et al., 2006a, 2007; Amour et al., 2012; Amour et al., in press), in order to properly simulate the spatial complexity of carbonate bodies (Wilkinson et al., 1997; Burgess, 2008). Hence, the facies association corresponding to the backreef, tepee belt, backmargin, and lagoon depositional domains were modeled using the TGSim algorithm because of its capability to simulate trend between depositional domains. Each lithofacies type is characterized by its own morphology and dimension (Table 5.2, Appendix A3). In addition, the lithofacies distribution lacks clear geological trends along the depositional profile of the platform (Chapter 4, Figures 4.8, 4.9, 4.10, 4.11). Such type of lithofacies arrangement similar to a mosaic distribution (Burgess, 2008) can be properly simulated using the SISim algorithm. For more details about the modeling approach, please refer to Amour et al. (in press) (Chapter 3, pages 53-55). The scale-dependent modeling approach allows for the simulation of spatially independent lithofacies bodies, while distal-proximal geological trends between depositional domains are integrated into the 3-D model.

## 5.4. Lithofacies and facies association

Eight lithofacies types were recognized (Table 5.1) and grouped into three depositional domains the lagoon, the tepee belt to backmargin, and the backreef. Whereas the backreef and lagoon are dominated by subtidal lithofacies association (Lithofacies 1, 2, and 3), the tepee belt to backmargin is characterized by intertidal to supratidal deposits (Lithofacies 4, 5, 6, 7, and 8), showing laminations, fenestral fabrics, caliche crusts, and tepee structures (Table 5.1, Figure 5.6).

### 5.4.1. The lagoon

Peloidal and bioclastic wackestone-packstones (Lithofacies 1 and Lithofacies 2) represent around 55% in abundance of the lagoon, whereas peloidal intraclastic packstone-grainstones to bindstones (Lithofacies 3) are rare to present (6.5% in abundance) (Figure 5.6). The predominance of mud-supported Lithofacies 1 and Lithofacies 2 and the scarcity of packstone-grainstones Lithofacies 3, suggests that the lagoon was mainly characterized by subtidal, low-energy depositional conditions within the photic zone, favoring the abundance of dasycladacean algae. Intertidal depositional conditions are also observed, as shown by the occurrence of peloidal packstone to grainstones with fenestrae and microbially-encrusted intraclastic grainstones (27% in abundance). The abundance of intertidal-related features decreases toward the central part of the lagoon. Intertidal- to supratidal-related features such as dolostone, “terra rossa” surface, and tepee structures are rare (below 6% in abundance).



**Figure 5.6: Lithofacies proportion within the backreef, the tepee belt to backmargin, and the lagoon. Note the abundance of subtidal lithofacies (Lithofacies 1 to 3) within the lagoon and the backreef, whereas the tepee belt to backmargin is characterized by abundant tepee structures (Lithofacies 8). Note also the abundance of Lithofacies 3 within the backreef compared to the lagoon. Lf = Lithofacies.**

### 5.4.2. The backmargin to tepee belt

The backmargin to tepee margin represents the palaeotopographically elevated area of the platform top, surrounding the deeper lagoon. The palaeobathymetric gradient is evidenced by abundant intertidal- and supratidal-related features (55% in abundance). Intertidal sediments mainly deposited within the backmargin display tidal-related laminations and fenestral fabrics (Lithofacies 4) and microbially-incrusted intraclastic grainstones (Lithofacies 5), associated with pendant and meniscus cements (Table 5.1, Figure 5.6). Toward the tepee belt, evidences of exposure conditions, such as “terra rossa” surfaces and juvenile and mature tepee structures are abundant (28% in abundance). The juvenile tepee structures are few tens of meters to 100 m long and around 0.6 m thick (Table 5.2, Appendix A3). Mature tepees are laterally continuous over several hundreds of meters and up to 1.7 meter thick (Table 5.2, Appendix A3).

**Table 5.1: Classification of lithofacies types and their depositional conditions. Lf = Lithofacies, W = Wackestone, P = Packstone, G = Grainstone, F = Floatstone, R = Rudstone, B = Boundstone.**

Lf code	Lf types	Skeletal/non-skeletal components	Sedimentological features	Depositional conditions
Lf 1	Peloidal W to P	Few dasycladecean algae, foraminifera, bivalves Peloids, micritic intraclasts		Subtidal
f2	Bioclastic P to F	Dasycladecean algae, gastropods few foraminifera, echinoderms Peloids, micritic intraclasts, oncoids		Subtidal
Lf 3	Intraclastic P-G to B	Dasycladacean algae, gastropods, foraminifera, echinoderms, bivalves, <i>in situ</i> cyanobacteria Peloids, micritic intraclasts, aggregate grains, oncoids, lumps	Localized inverse grading, localized clotted fabrics	Subtidal
Lf 4	Peloidal P to G	Dasycladacean algae, bivalves, gastropods, foraminifera, echinoderms, cyanobacteria Peloids, micritic intraclasts, oncoids	Laminations, fenestral fabrics, inverse gradings, microbial encrustations	Intertidal
Lf 5	Intraclastic G	Dasycladacean algae, gastropods, foraminifera, echinoderms, bivalves, cyanobacteria, bryozoans Peloids, micritic intraclasts, aggregate grains, oncoids, lumps, pisoids	Laminations, fenestral fabrics, inverse gradings	Intertidal
Lf 6	Dolostone	Mainly texture-replacive with visible dasycladacean algae, gastropods, foraminifera, echinoderms, bivalves, cyanobacteria Peloids, intraclasts, aggregate grains	Laminations, fenestral fabrics	Intertidal to supratidal
Lf 7	Terra Rossa F to R	Dasycladacean algae, gastropods Intraclasts, oncoids, pisoids, aggregate grains, lumps, clastic sediments, and breccia	Fenestral fabrics, caliches	Supratidal
Lf 8	Tepee	See components of all others lithofacies, up to 80% of cement	Tepee structures Caliches, laminations, fenestral fabric, inverse grading	Supratidal



### 5.4.3. *The backreef*

Similar to the lagoon, the backreef consists of an association of Lithofacies 1, Lithofacies 2, and Lithofacies 3, and scarce supratidal-related features (below 6% in abundance), reflecting a palaeotopographically deeper position compared to the tepee belt to backmargin (Figure 5.6). Nevertheless, variations of the lithofacies proportion between the backreef and the lagoon, suggest specific conditions of sedimentation controlling each depositional domain. Peloidal intraclastic packstone-grainstones to bindstones (Lithofacies 3) represent 15% in abundance in the backreef, whereas only 6.5% is observed in the lagoon. Lithofacies 3 shows a relatively high biotic diversity made of dasycladacean algae, gastropods, foraminifera, bivalves, and echinoderms if compared to Lithofacies 1 and Lithofacies 2 (Table 5.1). In addition, the abundance of intraclasts and the texture of the Lithofacies 3, suggest a relatively high energy environment. Higher energy depositional conditions in the backreef compared to the lagoon are also indicated by the abundance of intraclastic grainstones (Lithofacies 5) (Figure 5.6). This line of evidences suggests overall higher energy and more open-marine conditions within the backreef than in the lagoon.

**Table 5.2. Vertical and NE-SW dimensions of the facies associations and lithofacies types. Note that Lithofacies 6 and Lithofacies 7 were modeled deterministically by drawing on the 3-D cellular model due to their too thin thickness. Lf = Lithofacies.**

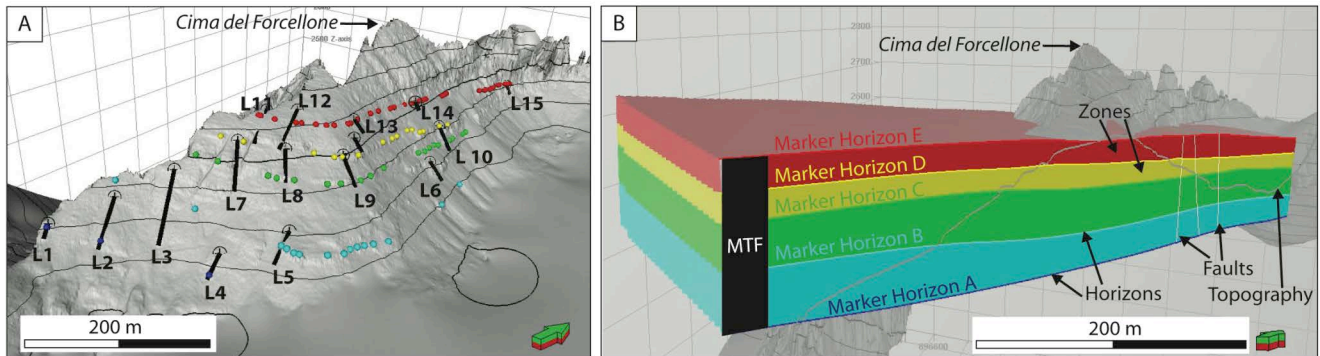
Lf and facies association	NE-SW dimensions (average value in m)	Thickness (average value in m)
Lf 1	141.1	0.5
Lf 2	125.4	0.7
Lf 3	54.8	0.3
Lf 4	139.6	0.3
Lf 5	65.2	0.4
Lf 6	No value	0.2
Lf 7	No value	0.2
Lf 8	101 to 297.9	0.6 to 1.7
Backreef	198	26.5
Tepee belt to backmargin	358.8	38.6
Lagoon	248.4	46.6

## 5.5. Scale-dependent geological modeling

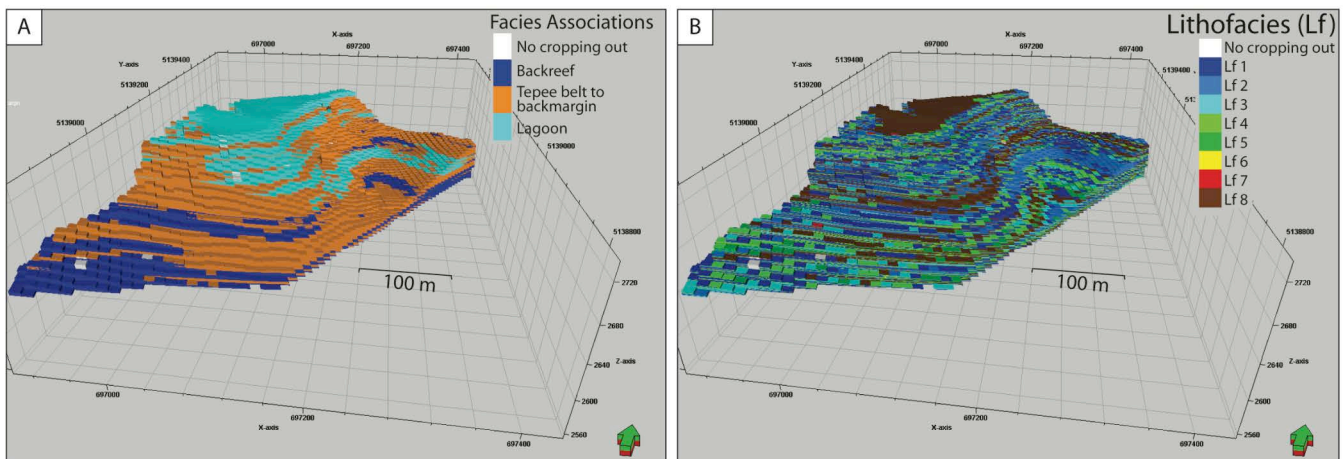
### 5.5.1. *Skeleton framework of the 3-D model*

Prior to stochastic simulation, cell dimensions that compose the geocellular model need to be determined and based on i) the size of the smallest modeled geological feature and ii) the shortest distance between the sections. Semi-variogram analysis (Table 5.2, Appendix A3) highlights that Lithofacies 3 is the smallest lithofacies with about 55 m of lateral extension, whereas the shortest distance between the sections is 30 m between the sections L11 and L12 (Figure 5.3C). Consequently, 10 x 10 m (X, Y) plan-view dimensions of the cells were chosen. 0.1 to 0.2 m thick “terra rossa” surfaces (Lithofacies 7) determined the vertical dimensions of the cells (Table 5.2). Hence, 3D cells dimensions are 10 x 10 x 0.1 m (X, Y, Z).

A total of 202 DGPS and LIDAR data points were used to georeference the marker horizons, the faults, and the sections (Figure 5.7). Additional control points were added to the GPS dataset due to the 2-D exposure conditions of the study area that do not allow a 3-D capture of the bed dipping. Additional data points were constrained by stratigraphic thicknesses, fault offsets, and the overall dipping trend of the beds measured in the field. The marker horizons were modeled using a 10 m grid node spacing.



**Figure 5.7:** A. Data input of the 15 sections (L1 to L15), the digital elevation model, and GPS data points of the marker horizons A (dark blue), B (light blue), C (green), D (yellow), and E (red) into the PETREL™ modeling software. B. Building of the 3-D skeleton framework (zone and horizons) of Cima del Forcellone outcrop. Three post-depositional inverse faults were recognized in the field and modeled (white line).

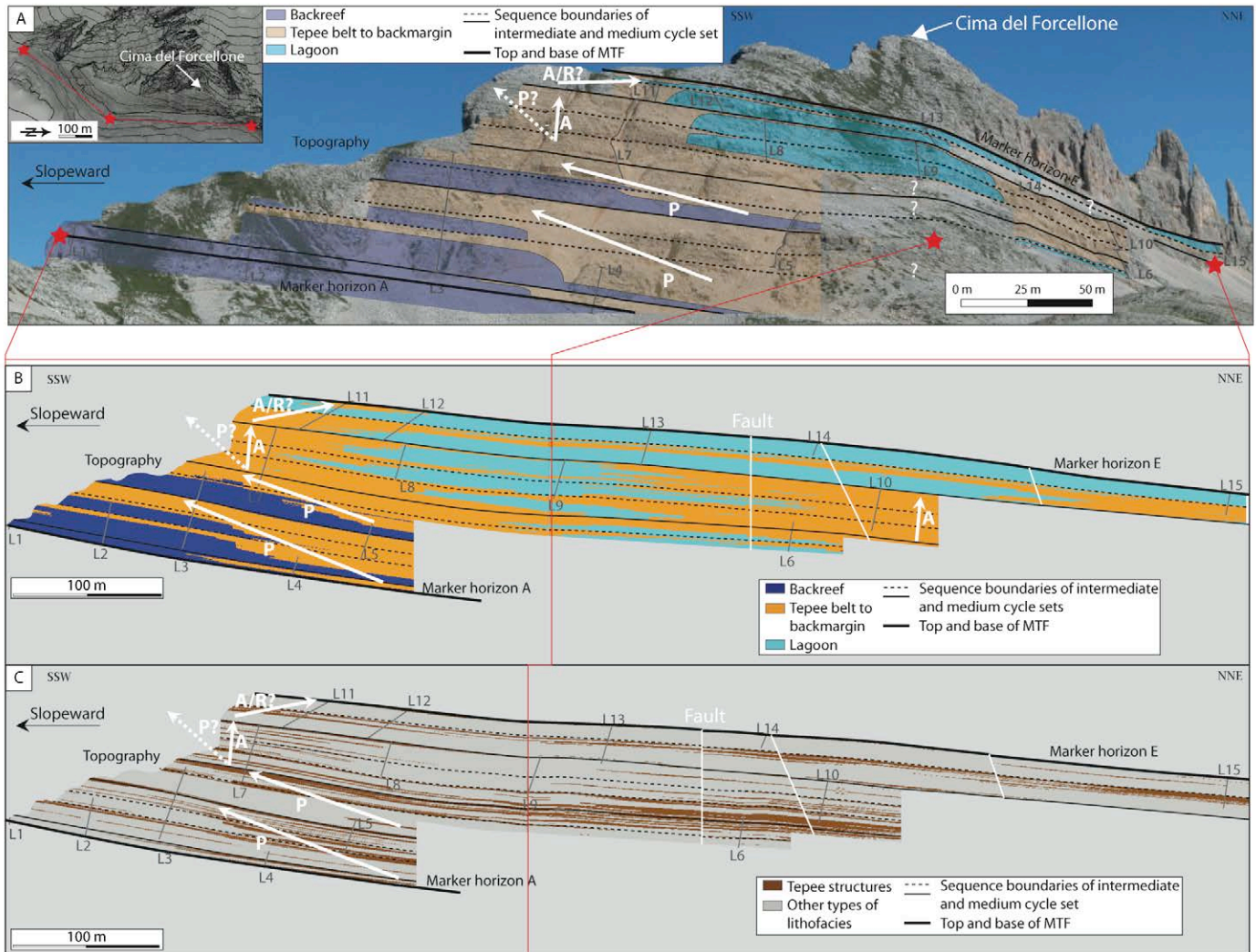


**Figure 5.8:** 3-D view of the scale-dependent outcrop model of Cima del Forcellone displaying the distribution of the facies associations (A) and the lithofacies types (B).

### 5.5.2. Evolution of the margin-to-lagoon depositional profile

The scale-dependent geological model (Figure 5.8) of Cima del Forcellone outcrop, which is validated by field observations (Figure 5.9A) allowed for the recognition of four stages during the evolution of the Latemar platform top. Whereas the two first stages display a progradational stacking pattern, the third and fourth stages are mainly aggradational to retrogradational, respectively (Figure 5.9A).

At the base of the MTF, the first stage corresponds to the first complete medium cycle set, which is composed of three intermediate cycle sets (Figure 5.4). The first stage is captured by the top part of the sections L2 and L4 and by the base of the sections L3 and L5 (Figure 5.9A). The tepee belt is located in the sections L4 and L5 and shows intervals dominated by tepee structures (Figure 5.9C).



**Figure 5.9:** A and B. SSW-NNE transect of Cima del Forcellone showing the distribution of the backreef, the tepee belt to backmargin, and the lagoon based on field observations (A) and on the 3-D outcrop model (B). A map view (A) of the digital elevation model of Cima del Forcellone (upper left) shows the location of the transect (red). The transect is delimited by the marker horizons A at the base and the marker horizon E at the top and shows the location of the sections from L1 to L15 (grey) and sequence boundaries (black). C. SW-NE transect of the 3-D outcrop model showing exclusively the distribution tepee structures. Note that the platform top evolution displays four stages from the base to the top of the interval: two phases of progradation and a third phase recording an aggradational stacking pattern, with a late retrogradation during the fourth stage. Note also the absence of tepee structures at the base of medium cycle sets. A = aggradation; P = progradation; R = retrogradation.

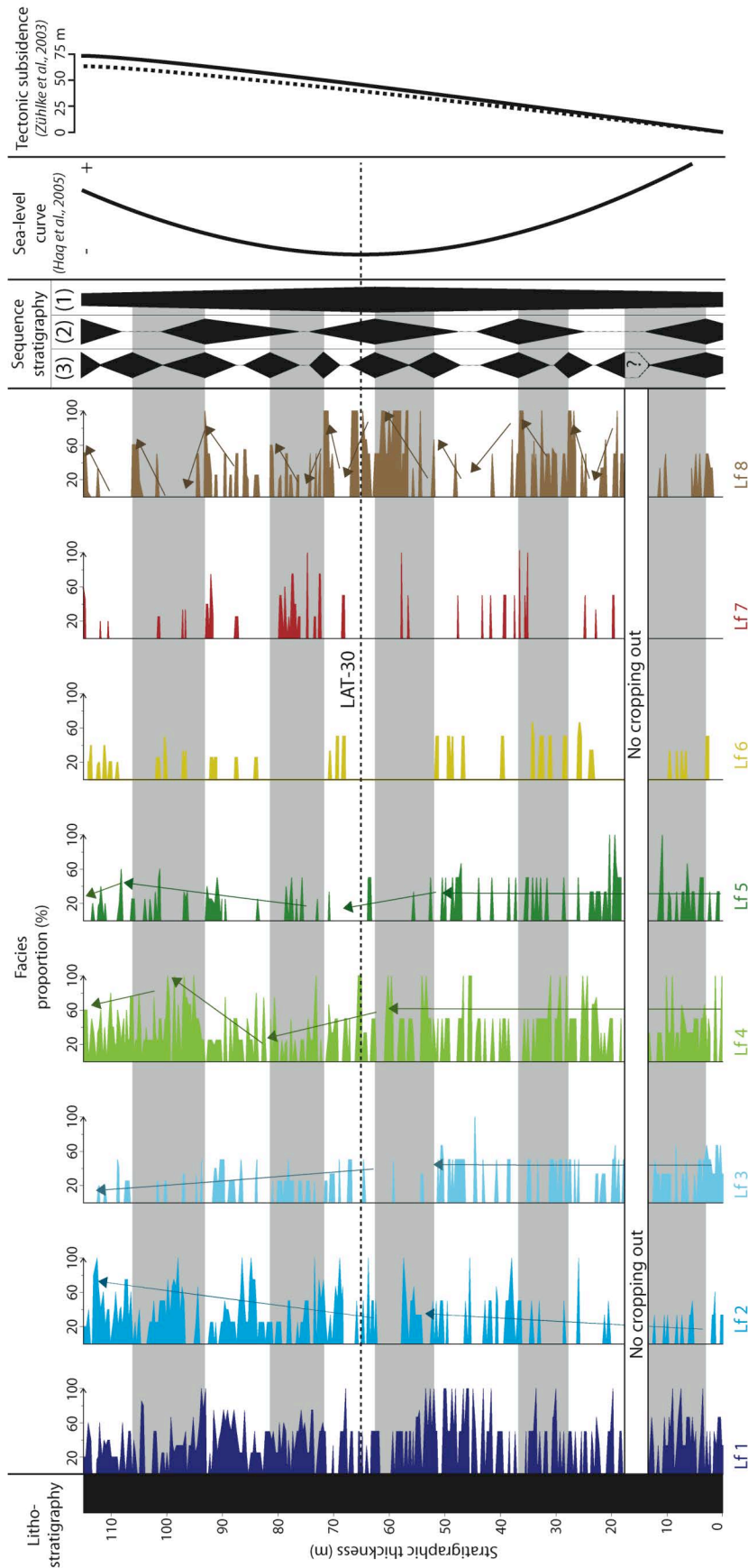
Toward the southwestern backreef (sections L2 and L3), supratidal-related features are scarcer and grade into a subtidal-dominated backreef (Figures 5.9A, 5.9B). At the basal part of the interval, the depositional profile of the platform top is characterized by the absence of a tepee belt and a backmargin. Upwards, a tepee belt (Figures 5.9A, 5.9B) developed as shown by the occurrence tepee structures, which progressively overlaid the subtidal backreef deposits toward southwest (Figure 5.9C). Furthermore, the basinward progradation of the tepee belt and backmargin is not continuous through time. (Figures 5.9A, 5.9B). The base of the two first intermediate cycle sets is characterized by the scarcity or absence of tepee structures, which became progressively abundant toward the top of the cycle set (Figures 5.9, 5.10). The absence of tepee structures at the base of intermediate cycle sets indicates repetitive, partial or complete flooding of the tepee belt.

The second stage, which is recorded by the second medium cycle set, is captured by the top part of sections L3 and L5 and the base of section L7. The second stage displays similar lateral and vertical features compared to the first stage. An overall progradational stacking pattern of the tepee belt and backmargin was also observed (Figures 5.9A, 5.9B). The second stage is composed of two intermediate cycle sets. Each intermediate cycle set is characterized by a basal lack or scarcity of tepee structures, which increase upward and prograde (Figure 5.10). Consequently, the two first stages, located at the base of the MTF, showed periodic flooding intervals of the tepee belt associated to the stacking pattern of intermediate and medium cycle sets.

At the middle of the MTF, the third stage is recorded by the third medium cycle set, which is composed of three intermediate cycle sets (Figures 5.10). The third stage of the platform top evolution is described with the sections L8, L9, and L10 and the top part of the sections L7 and L6 (Figure 5.9A). The lagoonal facies associations located in the sections L8 and L9 (Figures 5.9A, 5.9B), grade laterally toward both sides of the transect into the backmargin and tepee belt, as shown by the abundance of tepee structures in the sections L6, L7, and L10 (Figures 5.9B, 5.9C). The presence of thicker and laterally more continuous tepee structures in the northeastern area (sections L6 and L10), compared to the southwestern margin (section L7) (Figure 5.9C), suggests a more elevated palaeotopography toward the northeastern margin. During the third stage, the occurrence of tepee structures through the entire interval (Figure 5.9C) indicates that the tepee belt was never entirely submerged. The three intermediate cycle sets show successive aggradational phases of the depositional profile.

Toward the top part of the MTF, the fourth stage of the MTF stratigraphic succession is composed of the last medium cycle set, which consists of two intermediate cycle sets (Figure 5.4). The section L11 and the lower part of the section L15, capture the backmargin to tepee belt in both the sides of the transect, whereas the sections L12, L13, L14, and the top part of L15, display lagoonal facies association (Figure 5.9A). Within the tepee belt to backmargin, the section L11 is dominated by intertidal facies association, in contrast with the underlying section L7 that shows tepee structures (Figure 5.9C). Predominance of intertidal lithofacies (Figure 5.10) is also observed in the section L15 that partially captured the evolution of the northwestern margin of the platform. Vertical transition from a supratidal- (sections L7 and L10) to intertidal-dominated margin (sections L11 and L15) indicates partial flooding of the tepee belt (Figure 5.4). Upward, the flooding event persisted during the second intermediate cycle set, as shown by the abundance of lagoonal deposits (Figures 5.9A, 5.10). At the top part of the interval, mature tepee structures were only observed in the section L13.





**Figure 5.10: Vertical variation of lithofacies proportion through the 3-D outcrop model and showing the rhythmic occurrence of tepee structures controlled by intermediate and medium cycle set cyclicity. Decrease of the proportion of intertidal lithofacies (Lithofacies 4 and 5) in the middle part of the MTF, is caused by the abundance of tepee structures that disturb the primary sedimentary record. Note i) the relative variation of proportion of Lithofacies 3 compared to Lithofacies 2, from base to top of the MTF (and ii) frequent intertidal deposits (Lithofacies 4) at the uppermost MTF. The sequence stratigraphy interpretation shows intermediate (3), medium (2), and large (1) cycle set. The sea level curve (Haq et al., 2005) and tectonic subsidence (Zühlike et al., 2003) were correlated to the MTF using volcanic layer LAT-30 dated at 241.2Ma (+0.7/-0.6) (Mundil et al., 2003). Lf = Lithofacies.**

## 5.6. Discussion

### 5.6.1. *Depositional profile of the platform top*

The reconstruction of the Latemar depositional profile was previously based on kilometer long correlations between stratigraphic intervals located close to the platform margin such as Cimón del Latemar, Cima di Valsorda, and Forcella dei Camosci outcrops and intervals located within the platform interior such as the northern part of Cima del Forcellone outcrop (Figure 5.3A). The latter correlations showed abundant tepee structures along the margin that grade lagoonward to subtidal deposits (Goldhammer et al., 1987; Egenhoff et al., 1999; Zühlke et al., 2004; Peterhänsel and Egenhoff, 2008). The Latemar platform top was then interpreted as a lagoon surrounded by a palaeotopographically elevated tepee belt. The latter depositional profile has been questioned by a previous study (Preto et al., 2010) that indicated the absence of a tepee belt at the immediate backside of the reef belt, in various localities such as Forcella dei Toac (LPF), Cima Feudo (LPF to lowermost LCF), and Corno d'Ega (upper LCF) (Figure 5.3A). The present study documents for the first time, the lateral variability of lithofacies using few tens of meters long section correlations in order to investigate potential changes of the Latemar depositional profile through time. Section correlations (Figures 5.9A) indicate that the tepee margin was repetitively overlaid by subtidal deposits indicating periodic floodings of the platform margin. These flooding events are located at the base of intermediate and medium cycle sets (Figures 5.9A, 5.10). Hence, the margin-to-lagoon depositional profile was not static through time and alternates between a rimmed to a non-rimmed platform according to relative sea level fluctuations.

A comparison with previous chronostratigraphic studies (Zühlke et al., 2003; Zühlke, 2004) is required in order to infer controlling factors on intermediate and medium cycle sets. Spectral analysis was applied to a 460 m thick interval spanning from the LCF to UTF to identify and interpret the cyclicity signal. Time calibration was constrained by considering all previous chronostratigraphic information such as cyclostratigraphic (Hardie et al., 1986; Goldhammer and Harris, 1989; Goldhammer et al., 1990), biostratigraphic (Brack and Rieber 1993; De Zanche et al., 1995; Brack et al., 1996), magnetostratigraphic (Kent et al., 2004) data and radiometric dating layers (Mundil et al., 1996, 2003) available in literature. Zühlke et al. (2003) indicated that the short and long eccentricity forcing were recorded by cycle bundles of 23-25 and 64-147 elementary cycles, respectively. Short eccentricity signal are similar in term of thickness and cycle number to the stacking pattern of intermediate cycle sets, which represents bundles of 21-23 elementary cycles (Chapter 4, Table 4.2). In addition, medium cycle sets composed of bundles of 53-56 elementary cycles may represent a modulation between short and long eccentricity forcing (Chapter 4, Table 4.2) (Hinnov, 2000; Preto et al., 2001, 2004). To conclude, data shown here suggests that the rhythmic succession between a rimmed and a non-rimmed platform top was controlled by eccentricity forcing. In addition, the scarcity of tepee structures in the uppermost part of the LCF (Figure 5.9A) suggests that the tepee margin was absent during periods of high accommodation creation such as the Lower Edifice, LCF, and UCF (Gaetani et al., 1981; Goldhammer and Harris, 1989; Egenhoff et al., 1999).



### ***5.6.2. Stratigraphic architecture of the platform top***

The Latemar isolated platform is interpreted as an aggrading platform associated with either a late progradation (Goldhammer and Harris, 1989; Preto et al., 2011) or a late retrogradation phase (Emmerich et al., 2005a). An overall aggrading stacking pattern cannot be confirmed by the present data. The investigation of a margin-to-lagoon depositional profile documents progradational, aggradational, and retrogradational trends of the margin during the evolution of the platform. The MTF displays a progradation-aggradation-retrogradation stacking pattern, which is characteristic of a lowstand to transgressive system tract, likely controlled by eccentricity forcing (see above). Previous studies defining tepee-rich units (MTF and UTF) as periods of relative sea level fall are in agreement with this interpretation (Goldhammer and Harris, 1989; Goldhammer et al., 1990; Egenhoff et al., 1999). Furthermore, the areal extent of the tepee margin was thought to vary in time according to relative sea level change (Egenhoff et al., 1999; Peterhänsel and Egenhoff, 2008). During periods of relative falling of sea level, a large portion of the platform top was exposed to subaerial conditions that led to the development of tepee structures within the lagoon and the backreef. The present study showed that the variability of the areal extent of tepee structures comes along with basinward and lagoonward shifting of the margin (Figure 5A). The stratigraphic architecture of the Latemar platform top does not display a purely aggradational stacking pattern. Successive progradational, aggradational, and retrogradational phases of the depositional profile can be observed and are likely controlled by eccentricity-driven sea level fluctuation.

### ***5.6.3. Evolution of the Latemar isolated platform***

The investigation of the impact of margin progradation and retrogradation on the evolution and architecture of the platform requires an integrated analysis of the lagoon-to-basin depositional profile. In this purpose, a recall of the sedimentary features observed in the slope is needed. Upper slope deposits display clast-supported breccia and megabreccia, which grade to turbiditic grainstones toward the toe of the slope (Harris, 1994). The main feature of the slope is the occurrence of hundreds of meters long slump scars, which record major collapses of the margin (Emmerich et al., 2005a; Preto et al., 2011). The hundreds of meter long dimensions of the margin failures, observed in different locations in time and space (Lastei di Valsorda, Cima Feudo, Corno d'Ega, Forcella dei Camosci, and Cresta de do Peniola) (Figure 5.3A) instigated previous studies to infer tectonic as the main controlling factor on the architecture of the platform (Emmerich et al., 2005a; Preto et al., 2011). In addition to local collapses, synsedimentary faults were assumed to take place in the western part of the platform and to control the margin-to-slope transition during the platform growth (Preto et al., 2011). Synsedimentary tectonic activity was associated to a Late Anisian N-S extensional regime (Preto et al., 2011) and to episodic volcanic eruptions recorded by volcanoclastic layers (Mundil et al., 1996; Brack et al., 1996; Mundil et al., 2003) (Figure 5.11).

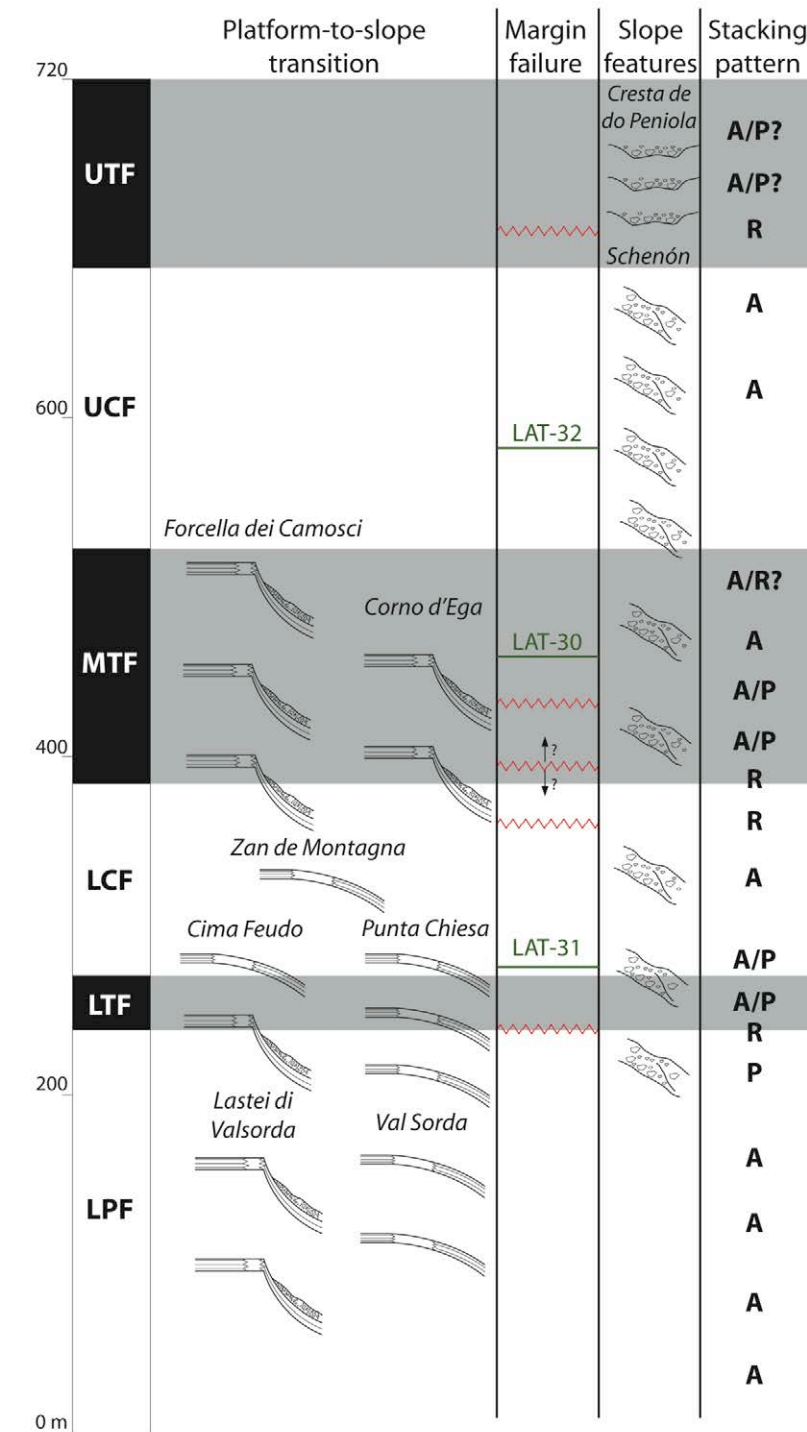


Figure 5.11: Compilation of the major geological features at the transition between the platform top and the slope based on the present data and previous studies (Harris, 1993, 1994; Emmerich et al., 2005a; Preto et al., 2011). Note that the margin failures occur either at the transition between cyclic and tepee units or within tepee units, which correspond to periods of relative sea level falls. Ash layers LAT-30, LAT-31, and LAT-32 are located in the figure.

Platform-to-slope transition	Slope features	Stacking pattern
Continuous margin	Channel	A: Aggradation
Steeply cliffed margin	Subparallel cliniform	P: Progradation
		R: Retrogradation

The compilation of the timing of each margin failure as well as the morphology of the platform top to slope transition (Figure 5.11) indicate that gravitary instabilities occurred either at the transition between tepee-poor (LPF, LCF, and UCF) and tepee-rich (LTF, MTF, UTF) units or at the base of tepee-rich units, whereas cyclic units remained unaffected. Consequently, gravitary instabilities at the slope-to-margin transition were contemporaneous to platform top progradations associated to relative sea level falls (Figure 5.9). The data shown here does not rule out tectonic as the main factors triggering margin collapses. However, the temporal relationship between platform top progradation and gravitary instability suggests that relative sea level fluctuation played a major role during the evolution of the platform. During lowstand stages, the margin was exposed to subaerial conditions. The high rate of carbonate sedimentation, from 300m/Ma (Zühlke et al., 2003) to 750m/Ma (Emmerich et al., 2005b) then shifted toward the reef belt, which does not show any emersion feature (Harris, 1993; Emmerich et al., 2005a) and toward the upper slope (Goldhammer and Harris, 1989; Harris, 1994). The sediment accumulation at the margin-to-slope transition, associated to a 100 m slopeward progradation of the margin (Figure 5.9A), likely contributed to gravitary instability and margin failures. The present study shows that the timing of gravitary collapses of the margin corresponds to periods of relative sea level fall. Beyond tectonic, relative sea level fluctuation seems to have played a significant role during the evolution of the Latemar isolated platform by favoring sediment surcharge at the slope-to-margin transition.

## 5.7. Conclusion

Field analysis combined with the geological modeling of a backreef-to-lagoon transect in Cima del Forcellone, allowed for a quantitative investigation of the platform top depositional profile and its evolution through time and space. The present study demonstrated that the platform top recorded a complex lithologic and stratigraphic stacking pattern, which need to be considered during the interpretation of the Latemar platform growth.

- The platform top consists of a lagoon, a tepee belt to backmargin and a backreef. The lagoon shows mud-dominated lithofacies associated with a low biotic diversity. Contrarily, the backreef is characterized by relatively high energy and more open marine depositional conditions as shown by the occurrence of dasycladacean algae, gastropods, foraminifera, bivalves, and echinoderm. The backmargin to tepee margin is composed of abundant intertidal- and supratidal-related features (55% in abundance). Juvenile tepee structures are few tens of meters to 100 m long and 0.6 m thick, whereas mature tepees are laterally continuous over several hundreds of meters and up to 1.7 m thick.
- A reexamination of the Latemar depositional model introduced by Egenhoff et al. (1999) was carried out here. The tepee belt was not observed continuous across the study window and was periodically flooded. The present study suggests eccentricity-driven changes of the depositional profile from a rimmed to non-rimmed platform top.
- The stacking pattern of the platform top does not show a purely aggradational trend. Four stratigraphic stages were recognized from the base to the top of the MTF, i) two basinward progradations, ii) an

aggradation, and iii) an aggradation to retrogradation of the margin. A progradational, aggradational, and retrogradational trend is characteristic of a lowstand to transgressive system tract.

- Margin collapses, reported in literature, occurred during periods of relative sea level fall and were contemporaneous to margin progradation shown in the present study. The temporal relationship between slope instability and platform top progradation indicates that, beyond tectonic, eustatism may have played a significant role during the evolution of the platform by favoring sediment surcharge within the 35° dipping slope-to-margin transition.



# Chapter 6

---

## Discussion

### 6.1. Intrinsic properties of carbonate systems

#### *6.1.1. Morphological profile and depositional environment*

A depositional environment can be defined by a combination of physical, chemical, and biological processes leading to the accumulation of an association of lithofacies types genetically linked by similar depositional conditions. The morphology of the carbonate system plays a major role on the ability to predict the type and distribution of environments along a depositional profile as well as their biotic associations present (Wilson, 1975; Read, 1985). Three morphological profiles of carbonate platform can be recognized: rimmed carbonate shelf, carbonate ramp, and unattached platform. The two last profiles correspond to the Bajocian ramp in Morocco (Chapters 2 and 3) and the Latemar isolated platform in Italy (Chapters 4 and 5), respectively. The present study investigated both study areas because they represent two end members of the spectrum of platform morphologies. In one setting, the proximal-distal depositional profile of the carbonate ramp consists of a few kilometers long, grain-supported inner ramp, mud-supported proximal middle ramp, and alternating mudstone-marls toward the distal middle ramp to outer ramp. In the other setting, the proximal to distal depositional profile of the Latemar isolated platform is composed of a few hundreds of meter long lagoon, margin, and backreef environment. The growth of a low-angle ramp or steep-flanked unattached platform defines the (palaeo-)topographic profile that affect current/wave pattern and subdivides the depositional profile into different environments (shoreline, lagoon, barrier, slope, deep ramp, basin) with more or less independent palaeoecological conditions. Quantitative investigations of ancient and modern carbonate systems on carbonate ramps (Wagner and van der Togt, 1973; Borkhataria et al. 2005; Barnaby and Ward 2007; Qi et al., 2007; Aigner et al., 2007; Palermo et al., 2010) and steep-flanked platforms (McNeill et al., 2004; Rankey et al., 2004; Verwer et al., 2009; Harris, 2010) indicate that depositional environments tend to form linear belt subparallel to the margin and laterally extending from few hundreds of meters to tens of kilometers long (Wright and Burgess, 2005).

Concepts of sequence stratigraphy applied to the stacking pattern of carbonate deposits enable prediction on landward and basinward migration of the depositional profile according to change of accommodation in order to reconstruct the basin evolution (Handford and Loucks, 1993). Nevertheless, the morphological type of a carbonate platform and its associated depositional profile is not invariant through time. Relative sea level fluctuation and regional tectonic can lead to change of platform morphology and consequently limit the ability to predict the distribution of depositional environments along the carbonate system (Kendall and Schlager, 1981; Bosence, 2005). Both studied areas the Bajocian carbonate ramp in Morocco (Chapters 2 and 3) and the Triassic isolated platform in Italy (Chapters 4 and 5) are two examples of the influence of both factors. In Morocco, an Early Toarcian crustal extension event (Laville et al., 2004) led to the dislocation of the southern shelf margin of the central High Atlas rift basin into numerous ramp systems. Each ramp was bounded by syndepositional ridges, which represented the crests



of tilted blocks. In the Dolomites, a late Anisian relative sea level rise drowned small isolated highs, whereas others buildups such as the Latemar or Marmolada were able to match sea level leading to the growth of a 800 m high topographic relief surrounded by sediment-starved basins (Bosellini, 1984). The deposition profile of carbonate system adapts to changes in accommodation and tectonics by evolving from one morphological profile to another. Such evolution implies a reorganization of the distribution of depositional environments accordingly. In addition, the temporal changes in global climate and ocean circulation, impacting the types (photozoan and heterozoan) and ability for the biotic community to produce and accumulate carbonate sediments, play a role on the capability for carbonate systems to respond and adapt to such changes in relative sea level and tectonic regime (Mutti and Hallock, 2003; Pomar and Kendall, 2007).

Carbonate systems evolve by i) adapting their depositional profile and ii) reorganizing their depositional environments according to variations in accommodation and palaeoecological conditions. The dynamic growth of carbonate platforms through time led to the reconsideration of the static morphological classification introduced by Wilson (1975) and Read (1985). Sequence stratigraphy models, which integrate the evolution of facies distribution through time, were established for the ramp, the rimmed shelf, and the unattached platform (Handford and Loucks, 1993). Each model summarizes the depositional and erosional responses of carbonate systems to each stage of relative sea level oscillation (lowstand, transgressive, and highstand system tracts) for both arid and humid climatic conditions.

Furthermore, Bosence (2005) questioned the pertinence of a morphological classification of carbonate platform and erected the tectonic and basinal settings as a first-order criterion to classify carbonate systems. This study schematizes the spatial and temporal relationship between the three morphological profiles of platforms according to the geodynamic context such as rifting, passive margin, mature ocean, intracratonic, fore-arc, and back-arc settings. Nevertheless, the establishment of carbonate depositional models (Handford and Loucks, 1993; Bosence, 2005) is based on defining rules and discriminate factors controlling the temporal and spatial evolution from one morphological type of platform to another. Fundamentally, the characterization of carbonate systems at a given period of time still relies on the original morphological classification introduced by Wilson (1975) and Read (1985). The identification of a rimmed carbonate shelf, a carbonate ramp, or an unattached platform involves a predictable and gradational distribution trend of depositional environments along a proximal-to-distal transect. The distribution of depositional environments remains stable during a certain period of time, during which the depositional profile shifts landward and basinward according to change of accommodation (Figure 6.1).

### ***6.1.2. Lithofacies mosaic and depositional sequence***

A depositional environment consists of an association of lithofacies, which records similar depositional conditions. The spatial arrangement of lithofacies along the surface of sedimentation displays a certain degree of disorder, which can be referred as a “mosaic” distribution (Wilkinson and Drummond, 2004; Wright and Burgess, 2005). A lithofacies mosaic is defined by Wilkinson et al. (1997) as a planar arrangement of spatially independent lithofacies types lacking a clear trend between each other and taking place within a depositional environment. All lithofacies types are characterized by their own morphology and dimension and their spatial distribution is

undistinguishable from random. Such mosaic-like distribution was observed within both study areas the Bajocian carbonate ramp (Chapter 3) and the Triassic isolated platform (Chapters 4, 5) as well as within a large number of Phanerozoic and Proterozoic carbonate successions (Wilkinson et al., 1997, 1999; Burgess, 2008; Strasser and Védérine, 2009) and modern analogues (Wilkinson et al., 1999, Wilkinson and Drummond 2004). Hence, the ability to predict the distribution and association of lithofacies types along a depositional profile tends to be a more complex task than at the depositional environment scale.

At first glance the stacking pattern of a lithofacies mosaic seems to be incompatible with the use of sequence stratigraphy, which involves a certain level of predictability (shallowing- and deepening-upward trend) through the stratigraphic succession. The scale at which both concepts refer needs to be considered in order to emphasize their coexistence in the sedimentary record. On one hand, the observation of a lithofacies mosaic is based on the investigation of spatial lithofacies-to-lithofacies relationship. Wilkinson et al. (1999), Wilkinson and Drummond (2004), and Burgess (2008) showed that the vertical and horizontal transition from one lithofacies to another is unpredictable. In other words, the latter studies emphasized the inability to predict the horizontal and vertical (i.e. the timing) location at which one lithofacies terminates and another starts. As stated by Wilkinson and Drummond (2004), *“if a small insect were to walk vertically up through a typical sedimentary succession, each step along the vertical transect would embody some random continuous probability of passing out of one lithofacies into another”*. On the other hand, sequence stratigraphy studies the stacking pattern of numerous lithofacies types in order to identify deepening- and/or shallowing-upward trends in the sedimentary record. The recognition of vertical trends, which display repetitive and hierarchical stratigraphic arrangements, implies that the superimposition pattern of lithofacies is predictable (Lehrmann and Goldhammer, 1999; Strasser et al., 1999). Hence, the investigation of a mosaic distribution focuses on the transition from one lithofacies to another, whereas sequence stratigraphic analysis interprets the stacking pattern of several lithofacies. The inability to predict when a lithofacies terminates through the sedimentary record, as introduced by the concept of mosaic distribution, does not involve a lack of overall deepening- and/or shallowing-upward trend in stacked carbonate lithofacies. Both concepts the mosaic distribution and the sequence stratigraphy can then coexist in the stratigraphic record. Accordingly, a sequence stratigraphy framework was established within both study areas: the Jurassic carbonate ramp (Chapter 3) and the Triassic isolated platform (Chapter 4) despite the observation of a mosaic-like distribution of lithofacies. Within the Bajocian carbonate ramp, a nested hierarchy of depositional sequences from large-scale, to medium-scale, and to small-scale depositional sequences was recognized. Each depositional sequence exhibits a thin deepening-upward trend at its base followed by a thick shallowing-upward trend marked at the top by a marine hardground. The studied stratigraphic interval of the Latemar isolated platform displays a hierarchical cyclostratigraphic record spanning from elementary cycles, to elementary cycle sets, to small cycle sets, to intermediate cycle sets, to medium cycle sets, and to large cycle sets (Appendix A3).

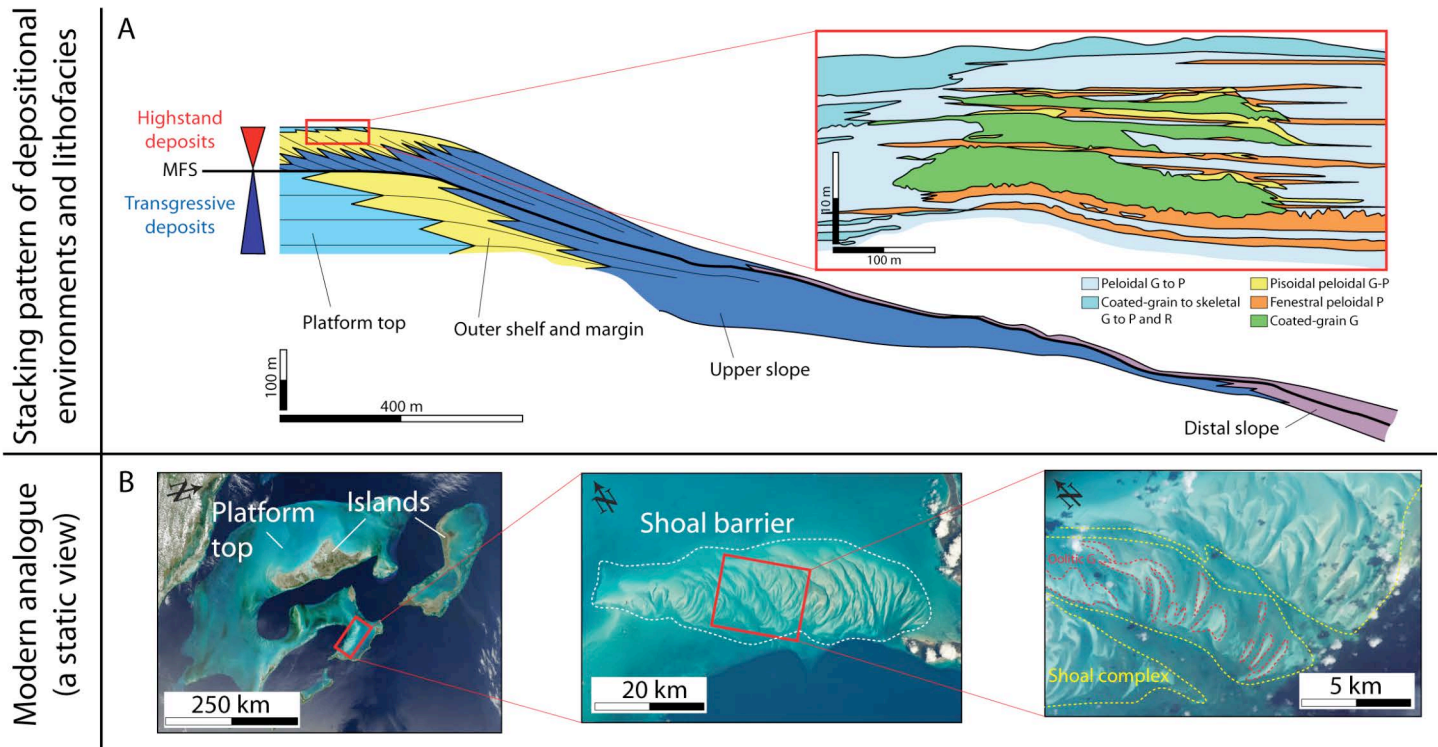
Inferring controlling factors on the development of a lithofacies mosaic is of primary importance. The deposition of a lithofacies type much as a depositional environment is controlled by the interaction between physical, chemical, and biological processes affecting the carbonate factory. However, the deposition of lithofacies shows a higher sensitivity than depositional environment to subtle changes of palaeoecological conditions as illustrated for example

by the study of the Kimmeridgian carbonate ramp in Spain (Bádenas and Aurell, 2010). Within the inner ramp, the shoals complexes are alternatively dominated by peloids, ooids, and ooids-oncoids from one high-frequency depositional sequence to another, whereas the overall distribution of depositional environments along the ramp remains stable. In this peculiar case, it was suggested that change of hydrodynamic conditions was the main factor driving this alternation. Within a depositional environment, the highly variable types and proportions of lithofacies observed from one depositional sequence to another is well known (e.g. Strasser et al., 1999; Qi et al., 2007; Verwer et al., 2009; Palermo et al., 2010) and is at the heart of studies that had introduced the notion of mosaic distribution (Wilkinson and Drummond, 2004).

The unpredictability aspect of lithofacies distribution in the sedimentary record is thought to reflect the predominant influence of internal factors (autocyclic model) compared to external factors (allogenic model) on carbonate precipitation and transport during time of deposition (Read, 1995; Wilkinson et al., 1997, 1999). According to the present study, the deposition of lithofacies within the Bajocian carbonate ramp (Chapter 3) was likely controlled by hydrodynamic level, storm events, tidal parameters, and differential fluvial input, whereas the palaeotopographic gradient and unfilled accommodation seem to play a major role during the growth of the Latemar isolated platform (Chapter 4). Overall, tidal-flat progradation, unfilled accommodation, turbidity, nutrient availability, topographic profile, lag-depth effect as well as variation in current/wind direction and velocity, storm frequency, and clastic input are interpreted as the main internal factors influencing the deposition of shallow-water carbonate lithofacies (Ginsburg, 1971; Hardie and Shinn, 1986; Pratt and James, 1986; Read, 1995; Drummond and Wilkinson, 1993; Wilkinson et al., 1997, 1999). The latter depositional factors are assumed to drown the periodic external signal induced by accommodation change and thus to lead to a chaotic vertical and horizontal lithofacies distribution. However, the interpretation of an autocyclic or allogenic forcing on carbonate deposition solely based on the degree of ordering within a stacked lithofacies succession can be questioned. Forward modelling of shallow-water carbonates indicates that autocyclic-controlled depositional systems can generate ordered lithofacies stacking (Burgess, 2006; Burgess and Pollitt, 2012; Burgess et al., 2012). Furthermore, high-amplitude, high-frequency relative sea level oscillations and high rate of carbonate production relative to rate of accommodation creation can lead to a disorder in the stacked lithofacies succession. The latter studies indicate that a lithofacies mosaic does not systematically reflect the influence of autocyclic factors and can also result from the interplaying between relative sea level oscillation and sedimentation rate. Hence, the interpretation of controlling factors on the deposition of lithofacies requires a full knowledge about the palaeoecological conditions at time of deposition, which are hardly accessible from outcrop studies (Wright and Burgess, 2005; Pomar and Kendall, 2007). The quantitative investigation of modern carbonate systems (Rankey, 2002, 2004; Rankey et al., 2006; Harris et al., 2010) and forward modeling studies (Burgess and Pollitt, 2012) are adequate tools and need to be further promoted to document and emphasize linkages between lithofacies distribution observed in the sedimentary record and palaeoecological conditions taking place at time of deposition.

The above discussion highlights that the intrinsic properties of modern and ancient shallow-water carbonate systems exhibit at least two hierarchies of geological heterogeneity the depositional environment and lithofacies. Both stratigraphic levels exhibit specific spatial patterns in term of distribution and association of carbonate bodies

(Figure 6.1). Depositional environments tend to display a gradational and linear arrangement along a proximal-distal depositional profile, whereas lithofacies types lack clear trends between each other leading to a mosaic-like arrangement. The spatial patterns of each hierarchical scale need to be properly captured during the modeling process in order to ensure the quality of the final 3-D geological model.



**Figure 6.1:** Examples of ancient and modern carbonate systems showing the morphology, distribution, and association of carbonate bodies from large to small scale. **A.** Djebel Bou Dahar, a Jurassic isolated platform located in the High Atlas mountain range (Verwer et al., 2008, 2009; Merino-Tomé et al., 2012). Note the landward and basinward shifting of the depositional profile according to accommodation change, whereas lithofacies types display a more complex distribution at the small scale. **B.** The Eleuthera Island part of the Great Bahamas Bank. Satellite images downloaded from [www.nasa.gov](http://www.nasa.gov). Note the nested arrangement of shoal bodies from large to small scale (B). P = packstone, G = grainstone, R = rudstone, MFS = maximum flooding surface.

## 6.2. 3-D modeling of shallow-water carbonate systems

### 6.2.1. *A compromise between deterministic and stochastic approaches*

Numerous variogram-based simulation techniques are applied in literature and are common practice in industry to model ancient carbonate deposits (Aigner et al., 2007; Falivene et al., 2007; Koehrer et al., 2010). A brief overview of the operating modes and limitations of variogram-based techniques (Chapter 2) is introduced here prior to discuss the capabilities of a scale-dependent modeling approach. The pioneering works were launched on developing Indicator Kriging (IK) and Sequential Indicator Simulation (SISim) algorithms (Journel, 1983; Deutsch and Journel, 1992). The operating mode of both algorithms displays a similar methodological approach (Appendix A4). Each lithofacies type is transformed into an indicator variable, which defines its probability of occurrence. Several 3-D probability models, one for each lithofacies, are then estimated by kriging (Appendix A4) and compared between each other in order to assign a lithofacies type to each grid cell and thus build the 3-D geological model. The key aspect of IK and SISim relies on the simulation of each lithofacies type independently. On the one hand, the latter operating mode allows populating each lithofacies type across the study area according to its specific dimension and preferential orientation. On the other hand, any spatial relationship between lithofacies (e.g. proximal-distal trend, specific lithofacies association) interpreted from data analysis can be inserted to constrain the stochastic simulation. The use of IK and SISim leads to the building of a patchy lithofacies distribution in a planar view (Chapter 2).

The drawbacks of IK and SISim instigate the development of novel algorithms, which enable the consideration of geological concepts and knowledge during simulation in order to better constrain the distribution of lithofacies in the 3-D model. Truncated Gaussian Simulation (TGSim) (Matheron et al., 1987; Galli et al., 1994) and Truncated Plurigaussian Simulation (PGS) (Le Loc'h and Galli, 1997) are designed to reproduce geological trends between lithofacies such as a proximal-distal trend or specific lithofacies associations. In this purpose, all lithofacies types are transformed into one single continuous Gaussian function (Appendix A4) following a specific ordered sequence (e.g. from Lf 1, to Lf 2, to Lf 3, and to Lf 4). The ordered sequence reflects the depositional model of the carbonate system interpreted from data analysis. A threshold is defined at the transition between each lithofacies type leading to the truncation of the continuous Gaussian field into several domains. All lithofacies types are then modeled together under the form of a continuous Gaussian variable. The simulation of one single variable (i.e. the Gaussian variable) involves the use of a single variogram to determine the dimensions of all lithofacies types modeled. The simulated Gaussian variable is finally transformed back into lithofacies types according to the ordered sequence in order to build the facies model (Appendix A4). TGSim enables the defining of an ordering transition between lithofacies types with respect to a given direction. Nevertheless, the latter lithofacies order is invariant. TGSim does not allow the transition between lithofacies types, which do not respect the pre-defined ordering trend. Following the example above, Lf 3 can grade laterally to Lf 2 or Lf 4 but not to Lf 1. The stiffness of TGSim to capture multiple facies transitions makes it difficult to honor a mosaic-like distribution (Chapter 2; Appendix 4). PGS is an extension of TGSim in which two or more continuous Gaussian functions are simulated simultaneously (Le Loc'h and Galli, 1997). Each continuous Gaussian function characterizes an ordered sequence associated with a specific

morphological constraint (semi-variogram). The use of several Gaussian fields permits the consideration of numerous geological trends between lithofacies instead of solely one as for TGSim. Hence, the PGS method provides more flexibility in honoring high variability of facies transition occurring along the depositional profile (Armstrong et al., 2011). Whilst critical testing is lacking in literature, two major limitations characterize PGS and consist of its inability to i) apply facies transition with respect to a given direction unlike TGSim and ii) assign a variogram to each lithofacies type (Mariethoz et al., 2009).

Comparisons between algorithms emphasize two critical issues that geoscientists face in the process of facies modeling either in subsurface or outcrop studies. Firstly, each stochastic algorithm presented here has unique capabilities and limitations according to its operating mode (Chapter 2). TGSim and PGS promote the simulation of a pre-defined depositional model interpreted from data analysis, whereas IK and SISim value the distribution and dimension of each lithofacies given by the data input. The selection of one algorithm compared to another involves a specific operating mode to populate lithofacies, which is not capable to match all intrinsic properties of carbonate systems across the entire modeled area (Chapter 2) (Journel et al., 1998; Falivene et al., 2006a; Falivene et al., 2007; Bastante et al., 2008; Mariethoz et al., 2009). Secondly, the improvement of variogram-based stochastic simulations from IK and SISim to TGSim and to PGS is driven by the need to find a compromise between both parameters i) the integration of geological concepts and ii) the computing flexibility required to honor complex lithofacies distribution during the simulation (Chapter 2) (Falivene et al., 2007). In other words, a reliable stochastic simulation should simultaneously capture the deterministic and stochastic characters of ancient carbonate systems, which result from the predictable proximal-distal trend of a depositional profile and from the mosaic-like distribution of lithofacies, respectively (Figure 6.1). A scale-dependent modeling approach, as introduced in the present study (Chapters 3, 5), also tries to enhance geological modeling by considering the dualism (deterministic and stochastic) of the sedimentary record. However, this approach relies on the implementation of several stochastic algorithms instead of the improvement of a single algorithm. At a large scale, the depositional environments are modeled using TGSim to portray the proximal-distal trend along the depositional profile. Each depositional environment is then filled by its unique association of lithofacies. Individual lithofacies were modeled using SISim because of its tendency to produce spatially independent lithofacies elements (Figure 6.2). Consequently, the modeling methodology takes into account the characteristics of each scale of observation by adjusting the relative strengths of stochastic and deterministic methods during simulation.

### ***6.2.2. A nested arrangement of carbonate bodies***

The brief summary of variogram-based algorithms available in literature highlights attention paid to realistically model the spatial relationships between lithofacies and their dimensions, especially in a plan view. The selection of the adequate algorithm is based on the depositional model of lithofacies interpreted from the geological data. The assumption of a spatially independent lithofacies mosaic can be modeled using SISim or IK, whereas observations of more or less complex but recurrent trends require TGSim and PGS. Then, the adequate simulation tool reconstructs the stratigraphic architecture and geological heterogeneity of the basin in the third dimension based on the vertical variation of lithofacies proportion. The quality of a 3-D geological model built by solely considering



quantitative data acquires from one scale of heterogeneity, in this case the lithofacies scale, can be questioned. Ancient and modern carbonate systems consist of at least two hierarchies of heterogeneity the depositional environment and lithofacies (Figure 6.1). Capturing both scales and their intrinsic properties into a 3-D geological model is of primary importance for reservoir characterization and simulation (Harris, 2010). Firstly, the analysis of the distribution and dimensions of depositional environments such as shoals complex within an inner ramp affords access to the reservoir size and continuity. The large-scale perspective enables the evaluation of the economical potential of a reservoir. Secondly, the quantitative investigation of lithofacies distribution, morphology, and association documents the internal heterogeneity of a reservoir in order to predict fluid flow pattern and improve oil and gas recovery. Because of the stratigraphic hierarchy of carbonate deposits, the geological modeling solely performed at the lithofacies scale implies that the simulation of individual lithofacies bodies are able to reproduce the morphometric parameters of their associated depositional environments.

Both study areas, the Bajocian carbonate ramp (Chapter 3) and the Triassic isolated platform (Chapter 5) offer the opportunity to quantitatively compare the morphologic parameters of depositional environments and lithofacies types. The kilometers long shoal complex in the inner ramp consists of inter-connected, 350 m long, 190 m width, and 5 m thick shoal bodies with a preferential orientation of elongation of 125°N. At the lithofacies scale, the shoal complex is composed of i) 200 m long, 140 m wide, and 2 m oolitic grainstones with a 114°N orientation, ii) 260 m long, 145 m wide, and 3.1 m thick peloidal grainstones with an orientation of 97°N, and iii) 210 m long, 190 m wide, and 1 m thick rudstone bodies, which exhibit a nearly isotropic morphology. Within the Triassic isolated platform, the backreef, margin, and lagoon environments are ranging from 200 to 350 m long and from 25 to 45 m thick, whereas the dimensions of the eight lithofacies span from 55 m long and 0.3 m thick (Intraclastic packstone-grainstone to bindstone) to 300 m long and 1.7 m thick (tepee structures). Both study areas indicate that each lithofacies type has a specific dimension and preferential orientation and is encompassed into a depositional environment, which in turn is characterized by its own morphometric parameters.

Furthermore, numerous databases were developed in order to compile the morphometric patterns of carbonate deposits across the Phanerozoic time (Kenter and Harris, 2005, 2006; Rankey and Reeder, 2011). Databases apply the concept of stratigraphic hierarchies and are divided into at least three scales of observation from the morphological type of the platform, to the depositional environment, and to the lithofacies. Each scale comes along with its own dimensions, orientations, and distribution, which are not directly linked between each other (Figure 6.1) (Jung and Aigner, 2012a). The acquirement of quantitative data on individual lithofacies does not provide any further information about the morphometric parameters of depositional environments. Hence, populating the distribution of individual lithofacies across the modeled area is unlikely to reproduce the specific shape and size of their associated depositional environments. By using a scale-dependent modeling approach, the individual simulation of the depositional environments and lithofacies enables to respect their specific spatial patterns within the final 3-D model.

### ***6.2.3. Scale-dependent modeling approach***

The present study establishes a nested simulation approach in order to properly capture i) the stacking pattern of depositional sequences and ii) the distribution, association, and morphometric parameters of both the depositional environments and the lithofacies types (Figures 6.1, 6.2). The individual simulation of each hierarchical level of carbonate deposits has two main advantages in comparison to previous modeling studies, which solely build a lithofacies model. Firstly, the implementation of several stochastic algorithms enables to take advantage of each algorithm's abilities, while its drawbacks can be offset by the use of other simulation tools (Chapters 2, 3) (Deutsch and Wang, 1996; Deutsch and Tran, 2002; Patterson et al., 2006). For example, a purely stochastic algorithm like SISim, which was used to simulate mosaic-like lithofacies patterns, should not be used to model the entire study window. If the simulation methodology had applied only the SISim algorithm, the ordered transitions between depositional environments across the depositional profile would not have been captured, and the final model would have included significant errors in terms of geobody placement and association (Chapters 2, 3; Appendix 4). In addition, TGSim can only use a single variogram for all lithofacies, which is clearly an oversimplification of the geological reality and its operating mode produces a poor approximation of the observed lithofacies mosaic (Chapters 2, 3; Appendix 4). The implementation of several stochastic simulations provides then essential computing flexibility to accommodate the deterministic as well as stochastic characters of the sedimentary record. Secondly, the individual simulation of each hierarchical level enables to simultaneously respect the morphometric parameters of both the depositional environments and the lithofacies types. Hence, the present simulation approach relies on an effort to reproduce the unique sedimentary characteristics of each stratigraphic level in term geometry, association, and distribution (Figure 6.2). This method can be applied to most of the Proterozoic and Phanerozoic carbonate successions (Figure 6.1) (Wilkinson et al., 1997, 1999; Wilkinson and Drummond, 2004; Wright and Burgess, 2005; Burgess, 2008; Strasser and Védérine, 2009).

The present modeling strategy favors a Gaussian simulation at a large scale, whereas an algorithm using an indicator-based approach such as SISim is promoted at the smaller scale (Appendix A4). A Gaussian simulation, which enables the defining of trends between environments is essential to integrate the depositional model interpreted from data analysis into the 3-D final model. Consequently, algorithms such as TGSim and PGS are considered suitable simulation tools at this scale (Matheron et al., 1987; Le Loc'h and Galli, 1997). The major drawback of TGSim is the inability to assign a specific dimension and morphology to each environment modeled (Appendix 4). The use of two or more semi-variograms with PGS tends to overcome the latter drawback and can represent an enhancement at this scale of modeling. At the smallest scale, indicator-based algorithms such as SISim and IK provide the essential computing flexibility to honor the variability of lithofacies dimension, morphology, and association observed in carbonate systems (Aigner et al., 2007; Qi et al., 2007; Burgess, 2008; Verwer et al., 2009; Palermo et al., 2010; Koehrer et al., 2010). This computing flexibility relies on the modeling of each lithofacies type individually (Chapter 3; Appendix A4). Nevertheless, the observation of recurrent lithofacies transitions in the data set may involve the need to apply a transition probability between lithofacies during simulation. A variant of SISim so called Transition Probability Geostatistical Simulation (T-PROGS) was developed in order to consider facies transition probabilities (Carle and Fogg, 1996). In addition to the probability of occurrence of a lithofacies such as

Lf 1 defined from SISim (Appendix 4), this method estimates another probability of occurrence of Lf 1 (i.e. the transition probability) conditioned by the presence of another lithofacies at a neighboring location. Hence, T-PROGS is capable of providing to the modeler a certain degree of control on the distribution and association of lithofacies unlike SISim. T-PROGS, which was successfully applied to clastic sediments (Weissmann et al., 1999; Weissmann et al., 2002), has not been yet applied to carbonate deposits despite its potential to enhance simulation (Dell'Arciprete et al., 2012).

A scale-dependent approach implies the establishment of a methodology to implement each simulation algorithm and to merge their resulting realizations into a single 3-D geological model (Deutsch and Wang, 1996; Deutsch and Tran, 2002; Falivene et al., 2006b; Zappa et al., 2006). The present study simulates each hierarchical scale separately. The modeling of depositional environments does not take into account quantitative data obtained from the lithofacies analysis. Similarly, the modeling of lithofacies types does not consider data from the interpretation of depositional environments. The large-scale model solely provides the stratigraphic framework in which smaller-scale sedimentary features such as lithofacies are populated (Chapters 3, 5). The main issue resulting from this modeling approach relies on the degrees of reliability to simulate the transitional zone between depositional environments, which turns out to be controlled by lithofacies-to-lithofacies interfingering (Figure 6.1A) (Sech et al., 2009). The latter transitional zones, built during the simulation of depositional environments, should be then refined during lithofacies modeling. The initial challenge encountered for the simulation of lithofacies interfingering relies on the location and 3-D morphology of the transitional zone between data points (McDonald and Aasen, 1994; Falivene et al., 2009). In the present study, the transitional zone is already located during the modeling of the depositional environments and can be manually mapped in order to obtain a 3-D volume. Then, the 3-D volume can be used as a conditioning data during the lithofacies modeling, in which the depositional environment does not constrain the lithofacies distribution. This method will enable the refining of interfingering patterns and thus can lead to the enhancement of the final 3-D geological model.

To conclude, ancient and modern carbonate systems exhibit a nested arrangement of stratigraphic hierarchies, which display specific spatial patterns in term of dimension, morphology, and association of carbonate bodies (Figure 6.1). A scale-dependent modeling strategy relies on an effort to reproduce the unique sedimentary features of each stratigraphic level and thus enhances the quality of stochastic models. The present study applies a surface-based modeling to build the sequence stratigraphic framework of the studied area. Then, a Gaussian-based simulation approach is favored at the depositional environment scale in order to integrate into the 3-D model geological concepts and knowledge interpreted from data analysis, whereas at the smallest scale the variability of lithofacies dimension and association requires an indicator-based approach (Figure 6.2). This new perspective on modeling strategy involves i) the development of Gaussian-based algorithms, which better simulate various sizes and shapes of carbonate bodies such as PGS and ii) the improvement of indicator-based simulations to constrain lithofacies transitions such as T-PROGS.

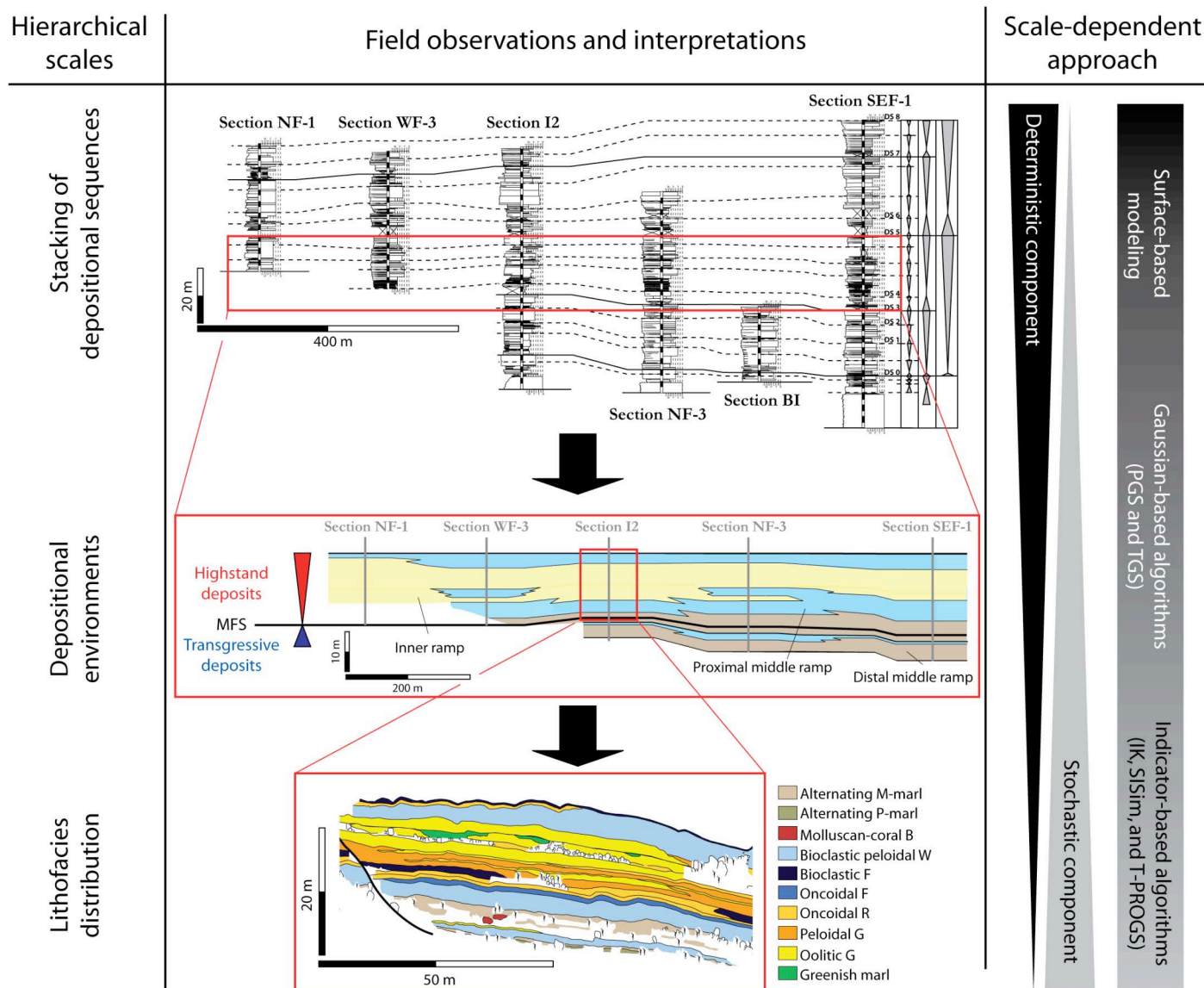


Figure 6.2: Summary of the hierarchical arrangement of shallow-water carbonate patterns and their associated modeling approaches based on the Jurassic ramp case study. Note the increasing geological complexity from large to small scale implying the adjustment of the relative strengths of stochastic and deterministic methods from surface-based, to Gaussian-based, and to indicator-based simulations. M = mudstone, W = wackestone, P = packstone, G = grainstone, F = floatstone, R = rudstone, B = boundstone, MFS = maximum flooding surface, PGS = truncated plurigaussian simulation, TGS = truncated gaussian simulation, IK = indicator kriging, SISim = sequential indicator simulation, T-PROGS = transition probability geostatistical simulation.



## Chapter 7

---

# Conclusion

The present study focused on outcrop modeling is located at the interface between two fields of expertise, Sedimentology and Computing Geoscience. Link between both fields of expertise, which is lacking in the literature, is yet of primary interest to establish a reliable and coherent workflow guiding outcrop and sub-surface modeling case studies. Consequently, the present study is based on a close relationship between the comprehension of the depositional model of ancient shallow-water carbonate systems and the improvement of facies modeling strategy. Two shallow-water carbonate outcrops were investigated to quantitatively analyze the facies distribution, morphology, and association and to interpret their controlling factors along the depositional profile. In parallel, an evaluation of the capabilities and drawbacks of commonly used simulation techniques were performed in order to properly model field observations.

The building of a realistic 3-D geological model requires the full understanding of the operating mode of each simulation tool used during the simulation. Three commonly used algorithms Truncated Gaussian Simulation (TGSim), Sequential Indicator Simulation (SIS) and Indicator Kriging (IK) were tested on a 320 m long, 190 m wide, and 30 m thick, isolated outcrop (Chapter 2). The configuration of the outcrop offers the opportunity to distinguish the impact of each algorithm on the facies distribution, by comparing visually and quantitatively field data and models. The results showed that: • the IK algorithm oversimplifies the facies distribution by modeling the most abundant lithofacies, whereas the other lithofacies are not taken into account during simulation; • the operating mode of the TGSim produces lower quality models compared to SISim during the modeling of complex geological geometries; • the SISim algorithm is confident to model spatial-independent lithofacies arrangement, whereas the TGSim algorithm is adequate to simulate lithofacies displaying linear and order trend between carbonate bodies. Carried out for the first time on carbonate rocks, the testing reveals that the operating mode of each algorithm involves inherent assumptions on the geometry and spatial arrangement of geological bodies that need to be modeled. Prior to the modeling exercise, a visual and quantitative analysis of the geological heterogeneity observed in the sedimentary record is of primary importance in order to select and apply the adequate modeling technique. The evaluation of stochastic tools has also demonstrated the inability for one single algorithm to simulate the entire geological complexity observed within ancient shallow-water carbonate systems. The operating mode of each algorithm involves capabilities as well as drawbacks, which were not capable to match field observations across the entire modeled area.

Two shallow-water carbonate systems were investigated and modeled a low-angle, Jurassic carbonate ramp in Morocco and a steeply flanked, Triassic isolated platform in the Dolomites (Italy). The selection of two opposed morphologies allow for a complete overview of the geological heterogeneity observed in shallow-water carbonate settings. Both study areas highlight similar stacking pattern and lateral variability of carbonate rocks that: • at the lithofacies scale (x 0.1km), field observations and statistical analysis show a mosaic-like distribution, which consists of the distribution of spatially-independent lithofacies bodies across the depositional profile of the ramp (Chapter 3) and the platform (Chapters 4 and 5); • at the basin scale (x 1km), depositional environment reflecting similar



depositional conditions, tends to display a more ordered distribution between i) the inner, middle, and outer ramp within the Jurassic ramp and ii) the backreef, tepee belt, and lagoon in the Triassic isolated platform. Based on the later results and literature, the occurrence of two types of geological heterogeneity, from the bedding scale to the basin scale, is a common features observed in the sedimentary record of carbonate rocks, independently of the geological time and the morphology of the platform. The reconstruction of the depositional profile of both case studies associated with the interpretation and the correlation of depositional sequences between sections allow for the identification of factors controlling each type of geological heterogeneity (Chapters 3 and 4): • at the basin scale, variation of accommodation influences the deposition and the linear distribution of depositional environments in both study areas; • at the bedding scale, the lithofacies mosaic reflects the superimposition of accommodation changes associated with internal factors such as palaeotopographic variation, unfilled accommodation, hydrodynamic level, storm frequency and runoff.

The scale-dependent heterogeneity of carbonate rocks observed in both study areas (Chapters 3 and 4) associated with the evaluation of algorithms (Chapter 2), emphasized that the use of one single simulation technique is unlikely to correctly capture the complexity of ancient shallow-water carbonate systems. Contrarily, the modeling of carbonate outcrop requires the combination of different simulation approach (Chapters 3 and 5). A new workflow is then proposed and combines the use of TGSim to portray the ordered trends observed between depositional environments, whereas at the finest scale, individual lithofacies were modeled using SISim because of its tendency to produce spatially independent lithofacies elements. A scale-dependent modeling approach takes advantage of each simulation technique's abilities, while its drawbacks can be offset by the use of other simulation tools. This new perspective on modeling strategies will i) provide the essential flexibility to capture the natural patterns and variability of carbonate bodies and ii) lead to better integration of the geological heterogeneity in a 3-D model. The selection of multiple simulation techniques based on detailed facies characterization and their implementations into one single modeling workflow should be a common procedure when building outcrop or subsurface models of carbonate rocks. Therefore, further efforts should be devoted to i) the development of algorithms designed to capture the distribution of either lithofacies or depositional environments and ii) the methods to combine several simulation techniques into a modeling workflow.

# References

---

- Adams, E.W., Grotzinger, J.P., Watters, W.A., Schröder, S., McCornick, D.S., and Al-Siyabi, H.A.** (2005) Digital characterization of thrombolite-stromatolite reef distribution in a carbonate ramp system (terminal Proterozoic, Nama Group, Namibia). *AAPG Bull.*, 89, 1293-1318.
- Agada, S., Chen, F., Geiger, S., Toigulova, G., Agar, S.M., Benson, G., Shekhar, R., Hehmeyer, O., Amour, F., Mutti, M., Christ, N., and Immenhauser, A.** (In review) Deciphering the fundamental controls of flow in carbonates using numerical well-testing, production optimisation, and 3D high-resolution outcrop analogues for fractured carbonate reservoirs. *Soc. Petrol. Geosc.*
- Aigner, T., Braun, S., Palermo, D., and Blendinger, W.** (2007) 3-D geological modelling of a carbonate shoal complex: reservoir analog study using outcrop analogs. *First Break*, 25, 65-72.
- Ait Addi, A.** (1998) Nouvelles données sédimentologiques et géodynamiques sur les facies de l'Aalénien-Bajocien inférieur du Haut Atlas marocain (Nord d'Errachidia). *CR Acad. Sci. Paris*, 326, 193-200.
- Ait Addi, A.** (2006) The dogger reef horizons of the Moroccan Central High Atlas: New data on their development. *J. Afr. Earth Sci.*, 45, 162-172.
- Amour, F., Mutti, M., Christ, N., Immenhauser, A., Benson, G. S., Agar, S.M., Tomás, S., and Kabiri, L.** (in press) Outcrop analogue for an oolitic carbonate ramp reservoir: a scale-dependent geological modeling approach based on stratigraphic hierarchy. *AAPG Bull.*
- Amour, F., Mutti, M., Christ, N., Immenhauser, A., Agar, S. M., Benson, G. S., Tomás, S., Always, R., and Kabiri, L.** (2012) Capturing and modeling metre-scale spatial facies heterogeneity in a Jurassic ramp setting (Central High Atlas, Morocco). *Sedimentology*, 59, 1158-1189.
- Armstrong, M., Galli, A., Beucher, H., Le Loc'h, G., Renard, D., Doligez, B., Eschard, R., and Geffroy, F.** (2011) Plurigaussian Simulations in Geosciences. Springer-Verlag, Berlin, 176 pp.
- Assereto, R.L.A.M. and St.C. Kendall C.G.** (1977) Nature, origin and classification of peritidal tepee structures and related breccias. *Sedimentology*, 24, 153-210.
- Aurell, M. and Bádenas, B.** (2004) Facies and depositional sequence evolution controlled by high-frequency sea-level changes in a shallow-water carbonate ramp (late Kimmeridgian, NE Spain). *Geol. Mag.*, 141, 717-733.
- Bádenas, B. and Aurell, M.** (2010) Facies models of a shallow-water carbonate ramp based on distribution of non-skeletal grains (Kimmeridgian, Spain). *Facies*, 56, 89-110.
- Bailey, T.R., Rosenthala, Y., McArthurb, J.M., van de Schootbruggea, B., and Thirlwallc, M.F.** (2003) Paleooceanographic changes of the Late Pliensbachian–Early Toarcian interval: a possible link to the genesis of an Oceanic Anoxic Event. *Earth Planet. Sci. Lett.*, 212, 307-320.
- Barnaby, R. J. and Ward, W. B.** (2007) Outcrop analog for mixed siliciclastic–carbonate ramp reservoir - stratigraphic hierarchy, facies architecture, and geologic heterogeneity: Grayburg Formation, Permian basin, U.S.A. *Jrnl. Sed. Res.*, 77, 34-58.
- Bassoulet, J. P., Poisson, A., Elmi, S., Cecca, F., Bellion, Y., Guiraud, R., Le Nindre, Y. M., and Manivit, J.** (1993) Middle Toarcian palaeoenvironments. In *Atlas Tethys Palaeoenvironmental maps* (Eds. J. Dercourt, L.E. Ricou, and B. Vrielynck), Gauthier-Villars, Paris, 63-80.
- Bastante, F.G., Ordóñez, C., Taboada, J., and Matías, J.M.** (2008) Comparison of indicator kriging, conditional indicator simulation and multiple-point statistics used to model slate deposits. *Eng. Geol.*, 98, 50-59.
- Beauchamp, W., Allmendinger, R.W., and Barazangi, M.** (1996) Inversion tectonics and the evolution of the High Atlas Mountains, Morocco, based on a geological-geophysical transect. *Tectonics*, 18, 163-184.
- Bechstädt, T., Brack, P., Preto, N., Rieber, H., and Zühlke, R.** (2003) Fieldtrip to Latemar: Guidebook, Triassic Geochronology and Cyclostratigraphy – A Field Symposium, St. Christina/Val Gardena, Italy, Sept. 11-13, 72 pp.
- Bertotti, G., Picotti, V., Bernoulli, D., and Castellarin, A.** (1993) From rifting to drifting: tectonic evolution in the South-Alpine upper crust from the Triassic to the Early Cretaceous. *Sed. Geol.*, 86, 53-76.
- Blendinger, W., Brack, P., Norborg, A.K., and Wulff-Pedersen, E.** (2004) Three-dimensional modelling of an isolated carbonate buildup (Triassic, Dolomites, Italy). *Sedimentology*, 51, 297-314.
- Blomeier, J.P.G. and Reijmer, J.J.G.** (1999) Drowning of a Lower Jurassic Carbonate Platform: Jbel Bou Dahar, High Atlas, Morocco. *Facies*, 41, 81-110.
- Boisvert, J.B., Pyrcz, M.J., and Deutsch, C.V.** (2010) Multiple Point Metrics to Assess Categorical Variable Models. *Nat. Resour. Res.*, 19, 165-175.
- Borgomano, J.R.F., Fournier, F., Viseur, S., and Rijkels, L.** (2008) Stratigraphic well correlations for 3-D static modeling of carbonate reservoirs. *AAPG Bull.*, 92, 789-824.
- Borkhataria, R., Aigner, T., Pöppelreiter, M.C., and Pipping, J.C.P.** (2005) Characterization of epeiric “layer-cake” carbonate reservoirs: Upper Muschelkalk (Middle Triassic), The Netherlands. *J. Petrol. Geol.*, 28, 15-42.

- Bosellini, A. and Rossi, D.** (1974) Triassic carbonate build-ups of the Dolomites, northern Italy. In *Reefs in Time and space* (Ed. L.F. Laporte), SEPM Spec. Publ., 18, 209-233.
- Bosellini, A.** (1984) Progradation geometries of carbonate platform: example from the Triassic of the Dolomites, Northern Italy. *Sedimentology*, 31, 1-24.
- Bosellini, A. and Stefani, M.** (1991) The Rosengarten: a platform-to-basin carbonate section (Middle Triassic, Dolomites, Italy). *Dolomieu conf. on Carbonate Platforms, Guidebook Excursion*, 1-24.
- Bosellini, A., Neri, C., and Stefani, M.** (1996) Geometrie deposizionali e stratigrafia fisica a grande scala di piattaforme carbonatiche triassiche. 78<sup>a</sup> riunione estive. *Guidebook, Soc. Geol. Ital., San Cassiano*, 36 pp.
- Bosence, D.** (2005) A genetic classification of carbonate platforms based on their basinal and tectonic settings in the Cenozoic. *Sed. Geol.*, 175, 49-72.
- Brack, P. and Rieber, H.** (1993) Toward a better definition of the Anisian/Ladinian boundary: new biostratigraphic data and correlations of boundary sections from the Southern Alps. *Eco. Geol. Helv.*, 86, 415-527.
- Brack, P., Mundil, R., Oberli, F., Meier, M., and Rieber, H.** (1996) Biostratigraphic and radiometric age data question the Milankovitch characteristics of the Latear cycles (Southern Alps, Italy). *Geology*, 24, 371-375.
- Brandner, R., Flügel, E., and Senowbari-Daryan, B.** (1991) Microfacies of carbonate slope boulders; indicator of the source area (Middle Triassic; Mähknecht Cliff, western Dolomites). *Facies*, 25, 279-296.
- Bryant, I.D. and Flint, S.S.** (Eds.) (1993) *The geological modeling of hydrocarbon reservoirs and outcrop analogs.* IAS Spec. Publ. 15, Blackwell Publishing Ltd., London, 269 pp.
- Burchette, T. P., and Wright, V. P.** (1992) Carbonate ramp depositional systems. *Sed. Geol.*, 79, 3-57.
- Burgess, P.M.** (2006) The signal and the noise: forward modeling of allocyclic and autocyclic processes influencing peritidal carbonate stacking patterns. *Jrnl. Sed. Res.*, 76, 962-977.
- Burgess, P.M.** (2008) The nature of shallow-water carbonate lithofacies distributions. *Geology*, 36, 235-238.
- Burgess, P.M. and Pollitt, D.A.** (2012) The origins of shallow-water carbonate lithofacies thickness distributions: one-dimensional forward modelling of relative sea-level and production rate control. *Sedimentology*, 59, 57-80.
- Burkhalter, R.M.** (1995) Ooidal ironstones and ferruginous microbialites: origin and relation to sequence stratigraphy (Aalenian and Bajocian, Swiss Jura mountains). *Sedimentology*, 42, 57-74.
- Caers, J. and Zhang, T.** (2004) Multiple-point geostatistics: a quantitative vehicle for integration geologic analogs into multiple reservoir models. In *Integration of Outcrop and Modern Analogs in Reservoir Modeling* (Eds. M. Grammer, P.M. Harris, and G.P. Eberli), AAPG Mem, 80, 383-394.
- Carballo, J.D., Land, L.S., and Miser, D.E.** (1987) Holocene dolomitization of supratidal sediments by active tidal pumping, Sugarloaf Key, Florida. *Jrnl. Sed. Petrol.*, 57, 153-165.
- Carle, S.F. and Fogg, G.E.** (1996) Transition probability-based indicator geostatistics. *Math. Geol.*, 28, 453-477
- Castellarin, A., Lucchini, F., Rossi, P.L., Selli, L., and Simboli, G.** (1988) The Middle Triassic magmatic-tectonic arc development in the Southern Alps. *Tectonophysics*, 146, 79-89.
- Choubert, G. and Faure-Muret, A.** (1962) Evolution du domaine atlasique marocain depuis les temps paléozoïques. In *Livre à la mémoire du Professeur Paul Fallot* (Ed. M. Durand-Delga), Soc. Geol. Fr., 1, 447-527.
- Christ N., Immenhauser A., Amour F., Mutti M., Susan M. Agar S. M., Always R., and Kabiri, L.** (2012a) Characterization and interpretation of discontinuity surfaces in a Jurassic ramp setting (High Atlas, Morocco). *Sedimentology*, 59, 249-290.
- Christ N., Immenhauser A., Amour F., Mutti M., Preston, R., Whitaker, F.F., Peterhänsel, A., Egenhoff, S.O., Dunn, P., and Agar, S.M.** (2012b) Triassic Latemar cycle tops – Subaerial exposure of platform carbonates under tropical arid climate. *Sed. Geol.*, 265, 1-29.
- Coburn, T. C., Yarus, J. M., and Chambers, R. L.,** (2006) Geostatistics and stochastic modeling: Bridging into the 21st century. In *Stochastic modeling and geostatistics: Principles, methods, and case studies, volume II* (Eds. T. C. Coburn, J. M. Yarus, and R. L. Chambers), AAPG Comp. Appl. Geol., 5, 3-9.
- Crevello, P.** (1992) Field Trip Excursion: Jurassic Carbonate facies, Sequence Stratigraphy, and Rift Tectonics of the High Atlas Mountains, Morocco. *Soc. Sed. Geol. and IAS Res. conf.*, 99 pp.
- De Zanche, V. and Farabegoli, E.** (1988) Anisian paleogeographic evolution in the Central-Western Southern Alps. *Mem. Sci. Geol.*, 40, 399-411.
- De Zanche, V., Gianolla, P., Manfrin, S., Mietto, P., and Roghi, G.** (1995) A Middle Triassic back-stepping carbonate platform in the Dolomites (Italy): sequence stratigraphy and biochronostratigraphy. *Mem. Sci. Geol.*, 47, 135-155.
- Dell'Arciprete, D., Bersezio, R., Felletti, F., Giudici, M., Comunian, A., and Renard, P.** (2012) Comparison of three geostatistical methods for hydrofacies simulation: a test on alluvial sediments. *Hydro. Jrnl.*, 20, 299-311.

- Dercourt, J., Gaetani, M., Vrielynck, B., Barrier, E., Biju Duval, B., Brunet, M.F., Cadet, J.P., Crasquin, S., and Sandulescu, M.** (Eds.) (2000) Atlas Peri-Tethys, Palaeogeographical Maps, CCGM/CGMW, Paris, 24 maps and explanatory notes.
- Deutsch, C.V. and Wang, L.** (1996) Hierarchical object-based modelling of fluvial reservoirs. *J. Math. Geol.*, 28, 857–880.
- Deutsch, C.V. and Tran, T.T.** (2002) FLUVISIM: a program for object-based stochastic modeling of fluvial depositional systems. *Comp. Geosc.*, 28, 525-535.
- Deutsch, C.V. and Journel, A.G.** (Eds) (1992) Geostatistical Software Library and User's Guide. Oxford University press, New York, p. 340.
- Dewey, J.F., Helman, M.I., Turco, E., Huton, D.H.W., and Knott, S. D.** (1989) Kinematics of the western Mediterranean. In *Alpine Tectonics* (Eds. M.P. Coward, D. Dietrich, and R.G. Park), *Geol. Soc. London Spec. Publ.*, 45, 265-283.
- Dogliani, C.** (1987) Tectonics of the Dolomites. *Jrnl. Struct. Geol.*, 9, 181-193.
- Drummond, C.N. and Wilkinson, B.H.** (1993) Carbonate cycle stacking patterns and hierarchies of orbitally forced eustatic sea level changes. *Jrnl. Sed. Petrol.*, 63, 369-377.
- Du Dresnay, R.** (1979) Sédiments jurassiques du domaine des chaînes atlasique du Maroc. Symposium "La sédimentation du Jurassique ouest-européenne. *Assoc. Séd. Fr. Publ. Spéc.*, 1, 345-365.
- Dunham, R. J.** (1962) Classification of carbonate rocks according to their depositional texture. In *Classification of Carbonate Rocks—a symposium* (Ed. W.E. Ham), *AAPG Mem.*, 1, 108-121.
- Dunn, P.A.** (1991) Cyclic Stratigraphy and Early Diagenesis: an example from the Triassic Latemar Platform, Northern Italy. PhD Thesis, The Johns Hopkins University, Baltimore, 836 pp.
- Durlet, C., Almeras, Y., Chellai, E. H., Elmi, S., Le Callonnec, L., Lezin, C., and Neige, P.** (2001) Anatomy of a Jurassic carbonate ramp: a continuous outcrop transect across the southern margin of the High Atlas (Morocco). *Géol. Méditerranéenne*, 28, 57-61.
- Eaton, T.T.** (2006) On the importance of geological heterogeneity for flow simulation. *Sed. Geol.*, 184, 187-201.
- Eberli, G.P., Harris, P.M., and Grammer, G.M.** (2008) Implication of Unfilled Accommodation Space in Carbonate Depositional Systems for Cyclo-Stratigraphy. *AAPG Conf.*, San Antonio, Texas, April 20-23.
- Egenhoff, S.O., Peterhänsel, A., Bechstädt, T., Zühlke, R., and Grötsch, J.** (1999) facies architecture of an isolated carbonate platform: tracing the cycles of the Latemar (Middle Triassic, northern Italy). *Sedimentology*, 46, 893-912.
- Ellouz, N., Patriat, M., Gaulier, J-M., Bouatmani, R., and Sabounji, S.** (2003) From rifting to Alpine inversion: Mesozoic and Cenozoic subsidence history of some Moroccan basins. *Sed. Geol.*, 156, 185-212.
- Embry, A. F. and Klovan, J. E.** (1971) A Late Devonian reef tract on northeastern Banks Island, N.W.T.. *Bull. Can. Petrol. Geol.*, 19, 730-781.
- Emmerich, A., Zamperelli, V., Bechstädt, T., and Zühlke, R.** (2005a) The reefal margin and slope of a Middle Triassic carbonate platform: the Latemar (Dolomites, Italy). *Facies*, 50, 573-614.
- Emmerich, A., Glasmacher, U.A., Bauer, F., Bechstädt, T., and Zühlke, R.** (2005b) Meso-/Cenozoic basin and carbonate platform development in the SW-Dolomites unraveled by basin modelling and apatite FT analysis: Rosengarden and Latemar (Northern Italy). *Sed. Geol.*, 175, 415-438.
- Fabuel-Pérez, I.** (2008) 3D Reservoir Modeling of Upper Triassic Continental Mixed Systems: Integration of Digital Outcrop Models (DOMs) and High Resolution Sedimentology. The Oukaimeden Sandstone Formation, Central High Atlas, Morocco. PhD Thesis, University of Manchester, Manchester, 275 pp.
- Falivene, O., Arbués, P., Gardiner, A., Pickup, G., Muñoz, J.A., and Cabrera, L.** (2006a) Best practice stochastic facies modeling from a channel-fill turbidite sandstone analog (the Quarry outcrop, Eocene Ainsa basin, northeast Spain. *AAPG Bull.*, 90, 1003-1029.
- Falivene, O., Arbués, P., Howell, J., Muñoz, J.A., Fernández, O. and Marzo, N.** (2006b) Hierarchical geocellular facies modeling of a turbidite reservoir analogue from the Eocene of the Ainsa basin, NE Spain. *Mar. Petrol. Geol.*, 23, 679-701.
- Falivene, O., Cabrera, L., Muñoz, J. A., Arbués, P., Fernández, O., and Sáez, A.** (2007) Statistical grid-based facies reconstruction and modelling for sedimentary bodies. Alluvial-palustrine and turbiditic examples. *Geol. Acta*, v. 5, p. 199-230.
- Falivene, O., Cabello, P., Arbues, P., Munoz, J.A., and Cabrera, L.** (2009) A geostatistical algorithm to reproduce lateral gradual facies transitions: Description and implementation. *Comp. Geosc.*, 35, 1642-1651.
- Flügel, E.** (2004) *Microfacies of carbonate rocks. Analysis, Interpretation and Application.* Springer-Verlag, Berlin, 976 pp.

- Gaetani, M., Fois, E., Jadoul, F., and Nicora, A.** (1981) Nature and evolution of Middle Triassic carbonate build-ups in the Dolomites (Italy). *Mar. Geol.*, 44, 25-57.
- Galli, A., Beucher, H., Le Loc'h, G., Doligez, B., and Group, H.** (1994) The pros and cons of the truncated gaussian method. In *Geostatistical Simulations* (Eds. M. Armstrong, and P.A. Dowd). Kluwer Acad., Dordrecht, 217-233.
- Germann, K., Schwarz, T., and Wipki, M.** (1994) Mineral deposit formation in Phanerozoic sedimentary basins of north-east Africa: the contribution of weathering. *Geol. Rundsch.*, 83, 787-798.
- Ginsburg, R.N.** (1971) Landward movement of carbonate mud: a new model for regressive cycles in carbonate. (Abstract) *AAPG Bull.*, 55, 340.
- Gischler, E. and Lomando, A. J.** (1999) Recent sedimentary facies of isolated carbonate platforms, belize-Yucatan system, Central America. *Jrnl. Sed. Res.*, 69, 747-763.
- Goldhammer, R.K., Dunn, P.A., and Hardie, L.A.** (1987) High-frequency glacio-eustatic oscillations with Milankovitch characteristics recorded in northern Italy. *Am. Jrnl. Sci.*, 297, 853-893.
- Goldhammer, R.K. and Harris, M.P.** (1989) Eustatic controls on the stratigraphic and geometry of the Latemar buildup (Middle Triassic), the Dolomites of northern Italy. In *Controls on Carbonate Platform and Basin Development* (Eds. P.D. Crevello, J.L. Wilson, J.F. Sarg, and J.F. Read), *SEPM Spec. Publ.*, 44, 323-338.
- Goldhammer, R.K., Dunn, P.A., and Hardie, L.A.** (1990) Depositional cycles, composite sea-level changes, cycle stacking patterns, and the hierarchy of stratigraphic forcing. *Geol. Soc. Am. Bull.*, 102, 535-562.
- Gómez-Hermández, J. and Srivastava, R.M.** (1990) ISIM 3D: an ANSI-C three-dimensional and multiple indicator conditional simulation program. *Comput. Geosci.*, 16, 355-410.
- Goovaerts, P.** (1999) Impact of the simulation algorithm, magnitude of ergodic fluctuations and number of realizations on the spaces of uncertainty of flow properties. *Stoch. Environ. Res. Risk Assess.* 13, 161-182.
- Gotway, C. A. and Rutherford, B. M.** (1994) Stochastic simulation for imaging spatial uncertainty: Comparison and evaluation of available algorithms. In *Geostatistical Simulation*, (Eds. M. Armstrong and P. A. Dowd), Kluwer Acad., Dordrecht, 1-22.
- Gradstein, F. M., Ogg, J. G., and Smith, A. G.** (2004) *A geologic Time Scale 2004*. Cambridge, Cambridge University Press, 589 p.
- Grammer, G.M., Harris, P.M., and Eberli, G.P.** (2004) Integration of outcrop and modern analogs in reservoir modeling: Overview with examples from the Bahamas. In *Integration of outcrop and modern analogs in reservoir modeling* (Eds. G.M. Grammer, P.M. Harris, and G.P. Eberli), *AAPG Mem.*, 80, 1-22.
- Gringarten, E. and Deutsch, C.V.** (2001) *Teacher's Aide Variogram Interpretation and Modeling*. *Math. Geol.*, 33, 507-534.
- Hadri, M.** (1993) *Un modèle de plate-forme carbonatée au Lias-Gogger dans le Haut-Atlas Central au nord-ouest de Goulmina*. PhD Thesis, University Paris 11, Paris, 285 pp.
- Hallam, A.** (1993) Jurassic climates as inferred from the sedimentary and fossil record. *Phil. Trans. Roy. Soc. London*, 341, 287-296.
- Handford, C.R. and Loucks, R.G.** (1993) Carbonate depositional sequences and systems tracts – responses of carbonate platforms to relative sea-level changes. In *Carbonate sequence stratigraphy; recent developments and applications* (Eds. R.G. Loucks and J.F. Sarg), *AAPG Mem.*, 57, 3-42.
- Hardie, L.A. and Shinn, E.A.** (1986) Carbonate depositional environment. *Colorado School of Mines, Quarterly*, 81, 74 p.
- Hardie, L.A., Bosellini, A., and Goldhammer, R.K.** (1986) Repeated subaerial exposure of subtidal carbonate platforms, Triassic northern Italy: evidence for high-frequency sea-level oscillation on a 10<sup>4</sup> year scale. *Paleoceanography*, 1, 447-457.
- Harris, L.A.** (1986) Stratigraphic Models for carbonate tidal-flat deposition. In *Carbonate Depositional Environment, part 3: Tidal Flats* (Eds. L.A. Hardie and E.A. Shinn), *Colorado School of Mines, Quarterly*, 81, 59-73.
- Harris, M.T.** (1993) reef fabrics, biotic crusts and syndepositional cements of the Latemar reef margin (Middle Triassic), Northern Italy. *Sedimentology*, 40, 383-401.
- Harris, M.T.** (1994) The foreslope and toe-of-slope of the middle Triassic Latemar buildup (Dolomites, northern Italy). *Jrnl. Sed. Res.*, B64, 132-145.
- Harris, P.M.M.** (2010) Delineating and quantifying depositional facies patterns in carbonate reservoirs: Insight from modern analogs. *AAPG Bull.*, 94, 61-86.
- Hillgärtner, H. and Strasser, A.** (2003) Quantification of high-frequency sea-level fluctuations in shallow-water carbonates: an example from the Berriasian - Valanginian (French Jura): *Pal. Pal. Pal.*, 200, 43-63.

- Hinnov, L.A. and Goldhammer, R.K.** (1991) Spectral analysis of the Middle Triassic Latemar Limestone. *Jrnl Sed. Res.*, 61, 1173-1193.
- Hinnov, L.A.** (2000) New perspectives on orbitally forced stratigraphy. *Annu. Rev. Earth Plant. Sci.*, 28, 419-475.
- Hu, L. Y. and Le Ravalec-Dupin, M.** (2004) Elements for an Integrated Geostatistical Modeling of Heterogeneous Reservoirs. *Rev. Inst. Fr. Pétrol.*, 59, 141-155.
- Immenhauser, A., Hillgärtner, H., Sattler, U., Berttoti, G., Schoepfer, P., Homewood, P., Vahrenkamp, V., Steuber, T., Masse, J-P., Droste, H., Tall-van Koppen, J., van der Kooij, B., van Bentum, E., Verwer, K., Hoogerduijn Strating, E., Swinkels, W., Peters, J., Immenhauser-Potthast, I., and Al Maskery, S.A.J** (2004) Barremian-lower Aptian Qishn Formation, Haushi-Huqf area, Oman: a new outcrop analogue for the Kharaib/Shu'aiba reservoirs. *GeoArabia*, 9, 153-194.
- Immenhauser, A.** (2009) Estimating palaeo-water depth from the physical rock record. *Earth Sci. Rev.*, 96, 107-139.
- Jacobshagen, V., Brede, R., Hauptmann, M., Heinitz, W., and Zylka, R.** (1988) Structure and post-Palaeozoic evolution of the central High Atlas. In *The Atlas System of Morocco* (Ed. V. Jacobshagen), *Lect. Notes Earth Sci.*, 15, 245-271.
- Jenkyns, H.C.** (1988) The Early Toarcian (Jurassic) Anoxic Event: stratigraphic, sedimentary and geochemical evidence. *Am. Jrnl. Sci.*, 288, 101-151.
- Jenny, J., Le Marrec, A., and Monbaron, M.** (1981) Les empreintes de pas de dinosauriens dans le Jurassique Moyen du Haut Atlas Central (Maroc): Nouveaux gisements et précisions stratigraphiques. *Géobios*, 14, 427-431.
- Johnson A. L. A., Liquorish, M. N., and Sha, J.** (2007) Variation in growth-rate and form of a Bathonian (Middle Jurassic) oyster in England, and its environmental implications. *Palaeontology*, 50, 1155-1173.
- Jones, R.R., Mccaffrey, K.J.W., Imber, J., Wightman, R., Smith, S.A.F., Holdsworth, R.E., Clegg, P., De Paola, N., Healy, D., and Wilson, R.W.** (2008) Calibration and validation of reservoir models: the importance of high resolution, quantitative outcrop analogues. *Geol. Soc. Spec. Publ.*, 309, 87-98.
- Jones, R.R., McCaffrey, K.J. W., Clegg, P., Wilson, R.W., Holliman, N.S., Holdsworth, R.E., Imber, J., and Waggott, S.** (2009) Integration of regional to outcrop digital data: 3-D visualization of scale-dependent geological models. *Comput. Geosci.*, 35, 4-18.
- Journel, A.G., Gunderso, R., Gringarten, E., and Yao, T.** (1998) Stochastic modeling of a fluvial reservoir: a comparative review of algorithms. *J. Petrol. Sci. Eng.*, 21, 95-121.
- Journel, A.G. and Deutsch, C.V.** (1993) Entropy and Spatial Disorder. *Math. Geol.*, 25, 329-355.
- Journel, A.G.** (1983) Nonparametric Estimation of spatial Distributions. *Math. Geol.*, 15, 445-468.
- Jung, A. and Aigner, T.** (2012a) Carbonate geobodies: hierarchical classification and database – a new workflow for 3D reservoir modeling. *Jrnl. Petrol. Geol.*, 35, 49-65.
- Jung, A., Aigner, T., Palermo, D., Nardon, S., and Pontiggia, M.** (2012b) A new workflow for carbonate reservoir modelling based on MPS: shoal bodies in outcrop analogues (Triassic, SW Germany). In *Advances in Carbonate Exploration and Reservoir Analysis* (Eds. J. Garland, J.E. Neilson, S.E. Laubach and K.J. Whidden), *Geol. Soc.y, London, Sp. Publ.*, 370, 277-293.
- Kaoukaya, A., Laadila, M., Fedan, B., and Saadi, Z.** (2001) La plate-forme carbonatée liasique au NE d'Errachidia (Haut Atlas oriental, Maroc) : modèle d'organisation des dépôts margino-littoraux. *Bull. Inst. Sci. Rabat*, 23, 27-38.
- Kendall, St.C.C.G. and Schlager, W.** (1981) Carbonates and relative changes in sea level. In *Carbonate Platforms of the Passive-Type Continental Margins, Present and Past* (Eds. M.B. Cita and W.B.F. Ryan), *Elvesier Scientific Co., Amsterdam*, 181-212.
- Kent, D.V., Muttoni, G., and Brack, P.** (2004) Magnetostratigraphic confirmation of a much faster tempo for sea-level change for the Middle Triassic Latemar platform carbonates. *Earth Planet. Sci. lett.*, 228, 369-377.
- Kenter, J. and Campbell, A.E.** (1991) Sedimentation on a Lower Jurassic carbonate platform flank: geometry, sediment fabric and related depositional structures (Djebel Bou Dahar, High Atlas, Morocco). *Sed. Geol.*, 72, 1-34
- Kenter, J.A.M. and Harris, P.M.** (2006) Web-based Outcrop Digital Analog Database (WODAD): Archiving Carbonate Platform Margins. *AAPG Int. Conf., Australia, Nov. 5-8.*
- Kenter, J.A.M. and Harris, P.M.** (2005) Web-based Outcrop Digital Analog Database (WODAD): A Public Relational Database Archiving Carbonate Platform Margins in the Geological Record. *EGU Conf., Austria, Vienna, April 25-29.*
- Kenter, J., Harris, M., and Pierre, A.** (2008) Digital Outcrop Models of Carbonate Platform and Ramp systems: Analogs for Reservoir Characterization and Modeling. *AAPG Conf., South Africa, Abstract.*



- Kerans, C., Lucia, F.J., and Senger, R.W.** (1994) Integrated Characterization of Carbonate Ramp Reservoir using Permian San Andres Formation Outcrop Analogs. AAPG Bull., 78, 181-216.
- Kjonsvik, D., Doyle, J., Jacobsen, T., and Jones, A.** (1994) The effect of sedimentary heterogeneities on production from shallow marine reservoir – What really matters? Eur. Petrol. Conf. London, 25-27.
- Klappa, C.F.** (1980) Brecciation textures and tepee structures in Quaternary calcrete (caliche) profiles from eastern Spain: the plant factor in their formation. Geol. Jnl., 15, 81-89.
- Koehrer, B.S., Heymann, C., Prousa, F., and Aigner, T.** (2010) Multi-scale facies and reservoir quality variations within a dolomite body – Outcrop analog study from the Middle Triassic, SW German Basin. Mar. Petrol. Geol., 27, 386-411.
- Kostic, B. and Aigner, T.** (2004) Sedimentary and poroperm anatomy of shoal-water carbonates (Muschelkalk, South-German Basin): an outcrop-analogue study of inter-well spacing scale. Facies, 50, 113-131.
- Le Loc'h, G. and Galli, A.** (1997) Truncated plurigaussian method: theoretical and practical point of view. In Geostatistics Wollongong '96 (Eds.. E. Baafi and N.A. Schofield), Kluwer Acad., Dordrecht, 1, 211–222.
- Lachkar, N., Guiraud, M., El Harfi, A., Dommergues, J-L., Dera, G., and Durllet, C.** (2009) Early Jurassic normal faulting in a carbonate extensional basin: characterization of tectonically driven platform drowning (High Atlas rift, Morocco). Jnl. Geol. Soc., 166, 413-430.
- Lathuilière, B.** (2000a) Coraux constructeurs du Bajocien Inférieur de France. 1ère Partie. Geobios, 33, 51-72.
- Lathuilière, B.** (2000b) Coraux constructeurs du Bajocien Inférieur de France. 2ème Partie. Geobios, 33, 153-181.
- Laville, E., Pique, A., Amrhar, M., and Charroud, M.** (2004) A restatement of the Mesozoic Atlasic Rifting (Morocco), J. Afr. Earth Sci., 38, 145-153.
- Lehrmann, D.J. and Godlhammer, R.K.** (1999) Secular variation in parasequence and facies stacking patterns of platform carbonates: a guide to application of stacking patterns analysis in strata of diverse ages and settings. In Advances in Carbonate Sequence Stratigraphy: Applications to Reservoirs, Outcrop, and Models. (Eds.. P. M. Harris, A. H. Saller, and J. A. Simo), Soc. Sed. Geol. Spec. Publ. 63, 187-225.
- Løseth, T., Rivenaes, J.C., Thurmond, J.B., and Martinsen, O.J.** (2004) The value of digital outcrop data in reservoir modeling. AAPG conf., USA, Abstract.
- Mancinelli, A. and Ferrandes, D.** (2001) Mesozoic cyanobacteria and calcareous? Algae of the Apennine platform (Latium and Abruzzi, Italy). Geobios, 34, 533-546.
- Manspeizer, W., Puffer, J.H., and Cousminer, H.L.** (1978) Separation of Morocco and eastern North America: a Triassic-Liassic stratigraphic record. Geol. Soc. Am. Bull, 89, 901-920.
- Mariethoz, G., Renard, P., Cornaton, F. and Jaquet, O.** (2009) Truncated Plurigaussian Simulations to Characterize Aquifer Heterogeneity. Ground Water, 47, 13–24.
- Masetti, D. and Neri, C.** (1980) L'Anisico della Val di Fasa (Dolomiti Occidentali) sedimentologia e paleogeografia. Annali dell'Università di Ferrara, 7, 1-19.
- Matheron, G., Beucher, H., de Fouquet, C., Galli, A., and Ravenne, C.** (1987) Conditional Simulation of the Geometry of Fluvio-Deltaic Reservoirs. Soc. Petrol.Eng. conf., Dallas, USA, 591-599.
- McCaffrey, K.J.W., Jones, R.R., Holdsworth, R.E., Wilson, R.W., Clegg, P., Imber, J., Holliman, N., and Trinks, I.** (2005) Unlocking the spatial dimension: digital technologies and the future of geoscience fieldwork. Jnl. Geol. Soc. London, 162, 927-938.
- McDonald, A.C. and Aasen, J.O.** (1994) A prototype procedure for stochastic modeling of facies tract distribution in shoreface reservoirs. In Stochastic Modeling and Geostatistics (Eds.. J.M. Yarus and R.L. Chambers), AAPG Comp. Appl. Geol., Tulsa, 91–108.
- McNeill, D.F., Eberli, G.P., Harris, P.M., and Cruz, F.E.G.** (2004) Field guide to carbonate sediments along the Exuma bank margin, and a virtual fieldtrip to the Exuma Island chain, Bahamas. University of Miami Comparative Sedimentology Laboratory, Miami, Florida , Sedimenta CD Series 2, 237 p.
- Mehdi, M., Neuweiler, F., and Wilmsen, M.** (2003) Les formations du Lias inférieur du Haut Atlas central de Rich (Maroc) : précisions lithostratigraphiques et étapes de l'évolution du bassin. Bull. Soc. Geol. Fr., 174, 227-242.
- Merino-Tomé, O.A., Della Porta, G., Kenter, J.A.M., Verwer, K., Playton, T., van Lanen, X., Adams, E.W., Harris, M.T., Corrochano, D., Lilly, R., Canto-Toimil, N., Navarro-Molina, V., Bahamonde, J.R., and Pierre, A.** (2007) Development, evolution and drowning of a high rising Jurassic carbonate platform in a rift basin: the Djebel Bou Dahar (High Atlas, Morocco). 13<sup>th</sup> Bathurst Meeting of carbonate Sedimentologists, Norwich, UK, (abstract).
- Merino-Tomé, O., Della Porta, G., Kenter, J.A.M., Verwer, K., Harris, P.M., Adams, E.W., Playton, T., and Corrochano, D.** (2012) Sequence development in an isolated carbonate platform (Lower Jurassic, Djebel Bou Dahar, High Atlas, Morocco): influence of tectonics, eustacy and carbonate production. Sedimentology, 59, 118-155.

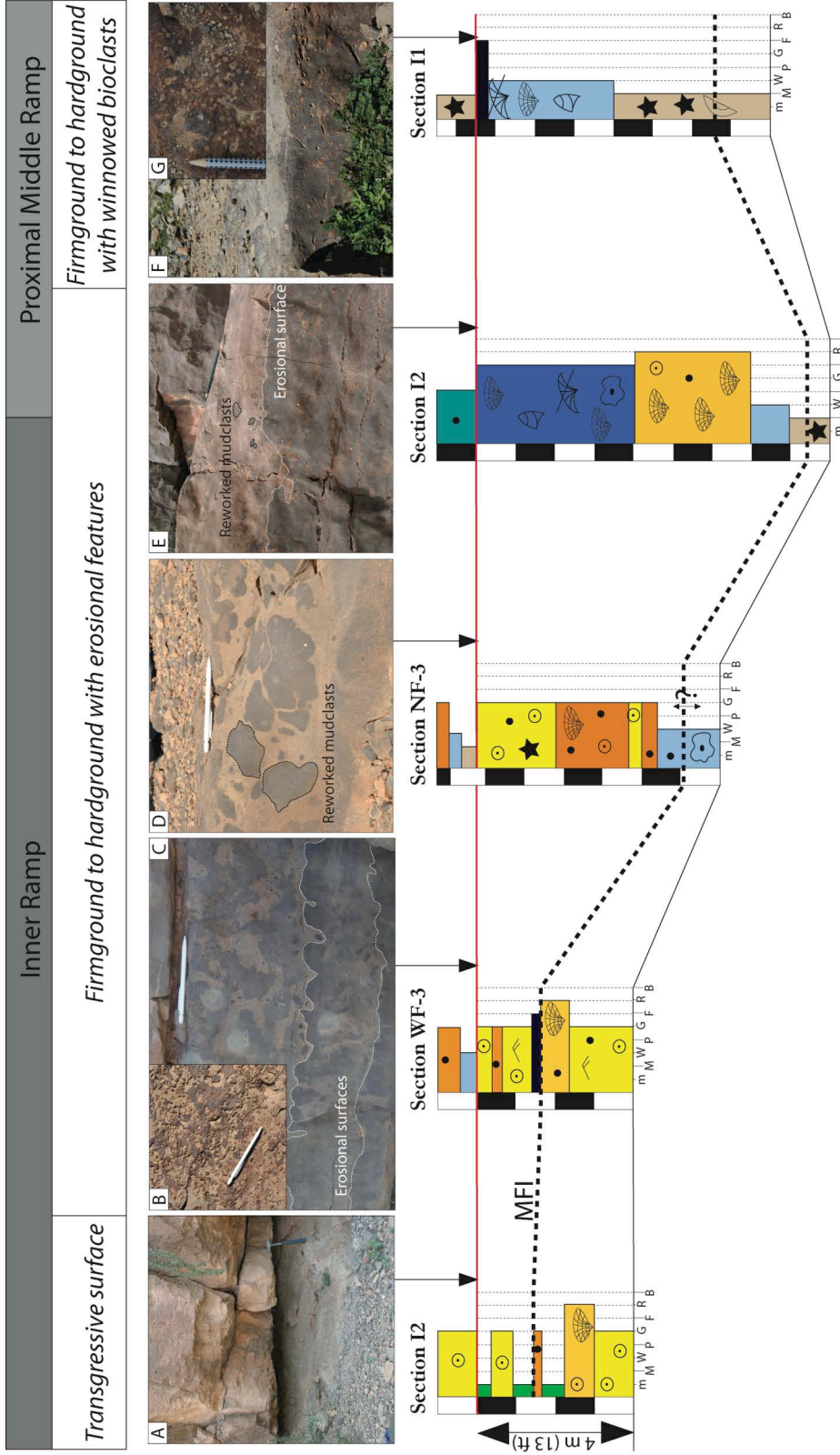
- Meyers, S.R.** (2008) Resolving Milankovitch controversies: the Triassic Latemar Limestone and the Eocene Green River Formation. *Geology*, 36, 319-322.
- Mikes, D. and Geel, C.R.** (2006) Standard facies models to incorporate all heterogeneity levels in a reservoir model. *Mar. Petrol. Geol.*, 23, 943-959.
- Milhi, A., Ettaki, M., Chellaï, E.H., and Hadri, M.** (2002) Les formations lithostratigraphiques jurassiques du Haut-Atlas central (Maroc): corrélations et reconstructions paléogéographiques. *Rev. Paléobiol.*, 21, 241-256.
- Monbaron, M.** (1979) Nouvelles recherches sur les gisements de Dinosaures du synclinal de Taguelft (Atlas de Beni Mellal); discussion sur leur position stratigraphique. *Min. Géol. Energie Rabat*, 46, 57-61.
- Moore, G.T., Hayashida, D.N., Ross, C.A., and Jacobson, J.R.** (1992) Paleoclimate of the Kimmeridgian/Tithonian (Late Jurassic) world: I. Results using a general circulation model. *Palaeogeogr. Palaeoclimatol. Palaeoecol.*, 93, 113-150.
- Mundil, R., Brack, P., Meier, M., Rieber, H., and Oberli, F.** (1996) High resolution U-Pb dating of Middle Triassic volcanoclastics; time-scale calibration and verification of tuning parameters for carbonate sedimentation. *Earth Planet. Sci. Lett.*, 141, 137-151.
- Mundil, R., Zühlke, R., Bechstädt, T., Peterhänsel, A., Egenhoff, S.O., Oberli, F., Meier, M., Brack, P., and Rieber, H.** (2003) Cyclicities in Triassic platform carbonates: synchronizing radio-isotopic and orbital clocks. *Terra Nova*, 15, 81-87.
- Mutti, M.** (1994) Association of tepees and paleokarst in the Ladinian Calcare Rosso (Southern Alps, Italy). *Sedimentology*, 41, 621-641.
- Mutti, M. and Hallock, P.** (2003) Carbonate systems along nutrient and temperature gradients: some sedimentological and geochemical constraints. *Int. J. Earth Sci.*, 92, 465-475.
- Miall, A.D. and Tyler, N.** (Eds.) (1991) The three-dimensional facies architecture of terrigenous clastic sediments and its implication for hydrocarbon discovery and recovery. *SEPM Concepts Sed. Paleont.*, 3, 309 pp.
- Neri, C. and Stefani, M.** (1988) Sintesi cronostratigrafia e sequenziale dell'evoluzione permiana superiore e triassica delle Dolomiti. *Mem. Soc. Geol. It.*, 53, 417-463.
- Osleger, D.** (1991) Subtidal carbonate cycles: Implications for allocyclic vs. autocyclic controls. *Geology*, 19, 917-920.
- Palermo, D., Aigner, T., Nardon, N., and Blendinger, W.** (2010) Three-dimensional facies modeling of carbonate sand bodies: Outcrop analog study in an epicontinental basin (Triassic, southwest Germany). *AAPG Bull.*, 94, 475-512.
- Patterson, P.E., Jones, T.A., Donovan, A.D., Ottmann, J.D., and Donofrio, C.J.** (2006) Hierarchical description and geologic modeling of a braided-stream depositional system. In *Stochastic modeling and geostatistics: Principles, methods, and case studies, volume II* (Eds. T.C. Coburn, J.M. Yarus, and R.L. Chambers), AAPG Comp. Appl. Geol., Tulsa, 5, 221-236.
- Peterhänsel, A. and Egenhoff, S.O.** (2008) Lateral variabilities of cycle stacking patterns in the Latemar, Triassic, Italian Dolomites. *SEPM Spec. Publ.*, 89, 217-229.
- Phelps, R.M., Kerans, C., Scott, S.Z., Janson, X., and Bellian, J.A.** (2008) Three-dimensional modelling and sequence stratigraphy of a carbonate ramp-to-shelf transition, Permian Upper San Andres Formation. *Sedimentology*, 55, 1777-1813.
- Pierre, A., Durlet, C., Razin, P., and Chellai, E.H.** (2010) Spatial and temporal distribution of ooids along a Jurassic carbonate ramp: Amellago transect, High Atlas, Morocco. *Geol. Soc. London Spec. Publ.*, 329, 65-88.
- Pierre, A.** (2006) Un exemple de référence pour les systèmes de rampes oolitiques. Un affleurement continu de 37 km (falaises jurassiques d'Amellago, haut Atlas, Maroc), PhD Thesis, University of Bourgogne, Dijon, 213 pp.
- Poisson, A., Hadri, M., Milhi, A., Julien, M., and Andrieux, J.** (1998) The central High-Atlas (Morocco). Litho- and chrono-stratigraphic correlations during Jurassic times between Tinjdad and Tounfite. Origin of subsidence. *Mém. Mus. Hist. Nat.*, 179, 237-256.
- Pomar, L. and St.C. Kendall, C.G.** (2007) Architecture of carbonate platforms: a response to hydrodynamics and evolving ecology. In: *Controls on carbonate platform and reef development* (Eds. J. Lukasik and A. Simo), *SEPM Spec. Publ.*, Tulsa, 89, 187-216.
- Pöppelreiter, M.C., Balzarini, M.A., Hansen, B., and Nelson, R.** (2008) Realizing complex carbonate facies, diagenetic and fracture properties with standard reservoir modeling software, *Geol. Soc. London Spec. Publ.*, 309, 39-49.
- Pratt, B.R. and James, N.P.** (1986) The St George Group (Lower Ordovician) of western Newfoundland: tidal flat island model for carbonate sedimentation in shallow epeiric seas. *Sedimentology*, 33, 313-343.
- Pratt, B.R., James, N.P., and Cowan, C.A.** (1992) Peritidal carbonate. In *Facies Models, Response to Sea Level Change* (Eds. R.G. Walker and N.P. James), *Geol. Assoc. Can.*, 303-322.

- Preto, N., Hinnov, L.A., Hardie, L.A., and De Zanche, V.** (2001) Middle Triassic orbital signature recorded in the shallow-marine Latemar carbonate buildup (Dolomites, Italy). *Geology*, 29, 1123-1126.
- Preto, N., Hinnov, L.A., De Zanche, V., Mietto, P., and Hardie, L.A.** (2004) The Milankovitch interpretation of the Latemar platform cycles (Dolomites, Italy): implications for geochronology, biostratigraphy and Middle Triassic carbonate accumulation. In *Cyclostratigraphy: Approaches and Case Histories* (Eds. B. D'Argenio, A.G. Fischer, I. Premoli Silva, H. Weissert, Ferreri, V.), *SEPM Spec. Publ.*, 81, 167-182.
- Preto, N., Franceschi, M., Gattolin, G., Massironi, M., Riva, A., Gramigna, P., Bertoldi, L., and Nardon, S.** (2011) The Latemar: A Middle Triassic polygonal fault-block platform controlled by synsedimentary tectonics. *Sed. Geol.*, 234, 1-18.
- Pringle, J.K., Howell, J.A., Hodgetts, D., Westerman, A.R., and Hodgson, D.M.** (2006) Virtual outcrop models of petroleum reservoir analogues: a review of the current state-of-art. *First break*, 24, 33-42.
- Qi, L., Carr, T.R. and Goldstein, R.H.** (2007) Geostatistical three-dimensional modeling of oolite shoals, St. Louis Limestone, southwest Kansas. *AAPG Bull.*, 91, 69-96.
- Rankey, E.C.** (2002) Spatial patterns of sediment accumulation on a Holocene carbonate tidal flat, Northwest Andros Island, Bahamas. *J. Sed. Res.*, 72, 591-601.
- Rankey, E.C.** (2004) On the interpretation of shallow shelf carbonate facies and habitats: How much does water depth matter?. *Jrnl. Sed. Res.*, 74, 2-6.
- Rankey, E.C. and Reeder, S.L.** (2011) Holocene Oolitic Marine Sand Complexes of the Bahamas. *Jrnl. Sed. Res.*, 81, 97-117.
- Read, J.F.** (1985) Carbonate platform facies models. *AAPG Bull.*, 69, 1-21.
- Read, J.F., Kerans, C., Weber, L.J., Sarg, J.F., and Wright, F.M.** (1995) Milankovitch sea-level changes, cycles and reservoirs on carbonate platforms in greenhouse and icehouse worlds. *Soc. Sediment. Geol. Short Course* 35.
- Sadki, D.** (1992) Les variations de facies et les discontinuités de sédimentation dans le Lias – Dogger du Haut-Atlas central (Maroc): chronologie, caractérisation, corrélation. *Soc. Geol. Fr.*, 163, 179-186.
- Sadler, P.M.** (1981) Sediment accumulation rates and the completeness of stratigraphic sections. *Jrnl. Geol.*, 89, 569-584.
- Schlager, W.** (2005) Carbonate Sedimentology and Sequence Stratigraphy. *SEPM Concepts in Sedimentology and Paleontology*, 8, 200 p.
- Sech, R.P., Jackson, M.D., and Hampson, G.J.** (2009) Three-dimensional modeling of a shoreface-shelf parasequence reservoir analog: Part 1. Surface-based modeling to capture high-resolution facies architecture. *AAPG Bull.*, 93, 1155-1181.
- Shekhar, R., Sahni, I., Benson, G.S., Agar, S.M., Amour, F., Tomás, S., Christ, N., Alway, R., Mutti, M., Immenhauser, A., and Kabiri, L.** (Subm.) Modelling and simulation of the Amellago “Island” outcrop study area, High Atlas Mountain, Morocco. *Petrol. Geosc.*
- Shinn, E.** (1983) Birdseyes, fenestrae, shrinkage pores, and loferites: a reevaluation. *Jrnl. Sed. Res.*, 53, 619-628.
- Stanley, R.G.** (1981) Middle Jurassic shoaling of the central High Atlas sea near Rich, Morocco. *Jrnl. Sed. Petrol.*, 51, 895-907.
- Strasser, A.** (1986) Ooids in Purbeck limestones (lowermost Cretaceous) of the Swiss and French Jura. *Sedimentology*, 33, 711-727.
- Strasser, A., Pittet, B., Hillgärtner, H., and Pasquier, J-B.** (1999) Depositional sequences in shallow carbonate-dominated sedimentary systems: concepts for a high-resolution analysis. *Sed. Geol.*, 128, 201-221.
- Strasser, A., Hillgärtner, H., Hug, W., and Pittet, B.** (2000) Third-order depositional sequences reflecting Milankovitch cyclicity. *Terra Nova*, 12, 303-12.
- Strasser, A. and Védrine, S.** (2009) Controls on facies mosaics of carbonate platforms: a case study from the Oxfordian of the Swiss Jura. In *Perspectives in Carbonate Geology* (Eds. P. Swart, G., Eberli, J. McKenzie, I. Jarvis, and T. Stevens), *IAS Spec. publ.*, 41, 199–213.
- Studer, M. and Du Dresnay, R.** (1980) Déformations synsédimentaires en compression pendant le Lias supérieur et le Dogger, au Tizi n'Irhil (Haut Atlas central de Midelt, Maroc). *Bull. Soc. Géol. Fr.*, 22, 391-397.
- Tebbutt, G.E., Conley, C.D., and Boyd, D.W.** (1965) Lithogenesis of a distinctive carbonate rock fabric. *Rocky Mountain Geology*, 4, 1-13.
- Tolosana-delgado, R., Pawlowsky-Glahn, V., and Egozcue, J-J.** (2008) Indicator Kriging without Order Relation Violations. *Math. Geosci.*, 40, 327-347.
- Tomás, S., Zitzmann, M., Homann, M., Rumpf, M., Amour, F., Benisek, M., Marcano, G., Mutti, M., and Betzler, C.** (2010) From ramp to platform: building a 3D model of depositional geometries and facies architectures in transitional carbonates in the Miocene, northern Sardinia. *Facies*, 56, 195-210.
- Tucker, M.E. and Wright, V.P.** (1990) Carbonate sedimentology. Blackwell Publishing Ltd., London, 482 pp.

- Verwer, K., Kenter, J.A.M., Maathuis, B., and Della Porta, G.** (2004) Stratal patterns and lithofacies of an intact seismic-scale Carboniferous carbonate platform (Asturias, northwestern Spain): a virtual outcrop model. In Geological prior information: informing science and engineering (Eds. A. Curtis and R. Wood), Geol. Soc. London Spec. Publ., 239, 29-41.
- Verwer, K., Adams, E.W., and Kenter, J.A.M.** (2007) Digital outcrop models: technology and applications. First Break, 79, 57-63.
- Verwer, K., Merino-Tomé, O., Kenter, J.A.M., Della Porta, G., Adams, E., and Harris, P.M.** (2008) High-Resolution Spatial Models of a High Rising Carbonate Platform Slope (Early Jurassic, Djebel Bou Dahar, High Atlas, Morocco). AAPG Conf., Texas, April 20-23.
- Verwer, K., Merino-tomé, O., Kenter, J.A.M., and Della Porta, G.** (2009) Evolution of a high-relief carbonate platform slope using 3D digital outcrop models: Lower Jurassic Djebel Bou Dahar, High Atlas, Morocco, Jnl. Sed. Res., 79, 416-439.
- Viel, G.** (1979) Lithostratigrafia ladinica: una revisione. Ricostruzione paleogeografia e paleostrutturale dell'area dolomitica-cadorina (Alpi Meridionali). I and II Parte. Riv. Ital. Paleontol., 85, 88-125 and 297-352.
- Wagner, C.W. and Van Der Togt, C.** (1973) Holocene sediment types and their distribution in the southern Persian Gulf. In The Persian Gulf (Ed. B.H. Purser), Springer-Verlag, New York, 123-155.
- Warne, J.E.** (1988) Jurassic carbonate facies of the Central and Eastern High Atlas rift, Morocco. In The Atlas System of Morocco (Ed. V. Jacobshagen), Lect. Notes Earth Sci., Heidelberg, 15, 169-200.
- Weissmann, G.S., Carle, S.F., and Fogg, G.E.** (1999) Three-dimensional hydrofacies modeling based on soil surveys and transition probability geostatistics. Water Resour. Res., 35, 1761-1770.
- Weissmann, G.S., Zhang, Y., Labolle, E.M., and Fogg, G.E.** (2002) Dispersion of groundwater age in an alluvial aquifer system. Water Resour. Res., 38, 1198-1211.
- Whitaker, F.F., Felce, G.P., Benson, G., Amour, F., Mutti, M., and Smart P.L.** (Subm.) Simulating fluid flow through forward sediment model stratigraphies: insights into climatic control of reservoir quality in isolated carbonate platforms. Petrol. Geosc.
- White, C.D., Novakovic, D., Dutton, S.P., and Willis, B.J.** (2003) A geostatistical Model for Calcite Concretions in Sandstone. Math. Geol., 35, 549-575.
- Wilkinson, B.H., Drummond, C.N., Rothman, E.D., and Diedrich, N.W.** (1997) Stratal order in peritidal carbonate sequences. Jnl. Sed. Res., 67, 1068-1082.
- Wilkinson, B.H., Drummond, C.N., Diedrich, N.W., and Rothman, E.D.** (1999) Poisson processes of carbonate accumulation on Paleozoic and Holocene platforms. Jnl. Sed. Res., 69, 338-350.
- Wilkinson, B. H. and Drummond, C. N.** (2004) Facies mosaic across the Persian Gulf and around Antigua-Stochastic and deterministic products of shallow-water sediment accumulation. Jnl. Sed. Res., 74, 513-526.
- Willis, B.J. and White, C.D.** (2000) Quantitative outcrop data for flow simulation. Jnl. Sed. Res., 70, 788-802.
- Wilmsen, M. and Neuweiler, F.** (2008) Biosedimentology of the Early Jurassic post-extinction carbonate depositional system, central High Atlas rift basin, Morocco. Sedimentology, 55, 773-807.
- Wilmsen, M., Fürsich, F.T., Seyed-Emami, K., Majidifard, M.R., and Zamani-Pedram, M.** (2010) facies analysis of a large-scale Jurassic shelf-lagoon: the Kamar-e-Mehdi Formation of east-central Iran. Facies, 56, 59-87.
- Wilson, E.N.** (1975) Carbonate facies in geologic history. Springer Verlag, New York, 471pp.
- Wilson, E.N., Hardie, L.A., and Phillips, O.M.** (1990) Dolomitization front geometry, fluid flow patterns, and the origin of massive dolomite: the Triassic Latemar buildup, Northern Italy. Am. Jnl. Sci., 290, 741-796.
- Wright, V.P. and Burgess, P.M.** (2005) The carbonate factory continuum, facies mosaics and microfacies: an appraisal of some of the key concepts underpinning carbonate Sedimentology. Facies, 51, 17-23.
- Young, T.P.** (1989) Phanerozoic ironstones: an introduction and review. In Phanerozoic Ironstones (Eds.. T.P. Young and W.E.G. Taylor), Geol. Soc. London Spec. Publ., 46, ix-xxv.
- Zappa, G., Bersezio, R., Felletti, F., and Giudici, M.** (2006) Modeling heterogeneity of gravel-sand, braided stream, alluvial aquifers at the facies scale. Jnl. Hydrol., 325, 134-153.
- Zheng, S.Y., Legrand, V.M., and Corbett, P.W.M.** (2007) Geological model evaluation through well test simulation: a case study from the Wytch farm oilfield, southern England. J. Petrol. Geol., 30, 41-58.
- Ziegler, P.** (1994) Evolution of Peri-Tethyan basins as a mirror of Tethys dynamics. In Peri-Tethyan Platforms (Ed. F. Roure), Technip, Paris, p. 3-8.
- Zühlke, R., Bechstädt, T., and Mundil, R.** (2003) Sub-Milankovitch and Milankovitch forcing on a model Mesozoic carbonate platform – the Latemar (Middle Triassic, Italy). Terra Nova, 15, 69-80.

**Zühlke, R.** (2004) Integrated cyclostratigraphy of a model Mesozoic carbonate platform – Latemar (Middle Triassic, Italy). *Cyclostratigraphy: Approaches and Case Histories* (Eds. B. D'Argenio, A.G. Fischer, I. Premoli Silva, H. Weissert, and V. Ferreri), *SEPM Spec. Publ.*, 81, 183-212.

# Appendix

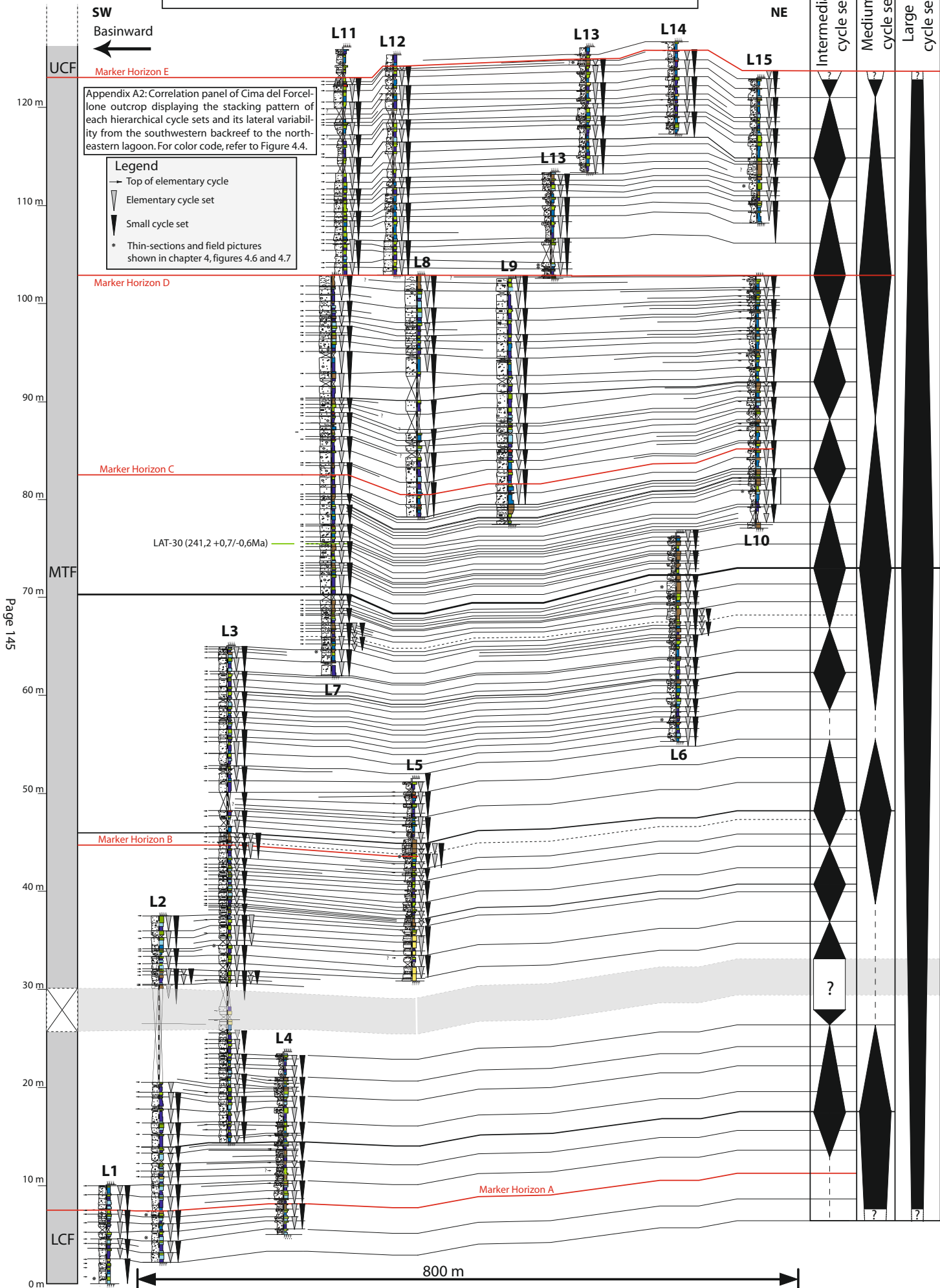


**Appendix A1: Interpretation of the lateral variability of small-scale sequences from the inner to proximal middle ramp. Note the changes on the expression of sequence boundaries with the occurrence of erosional features caused by wave action toward the more proximal and shallower part of the carbonate ramp. Refer to Figure 3.4 for color code and symbols. MFI = Maximum flooding interval.**

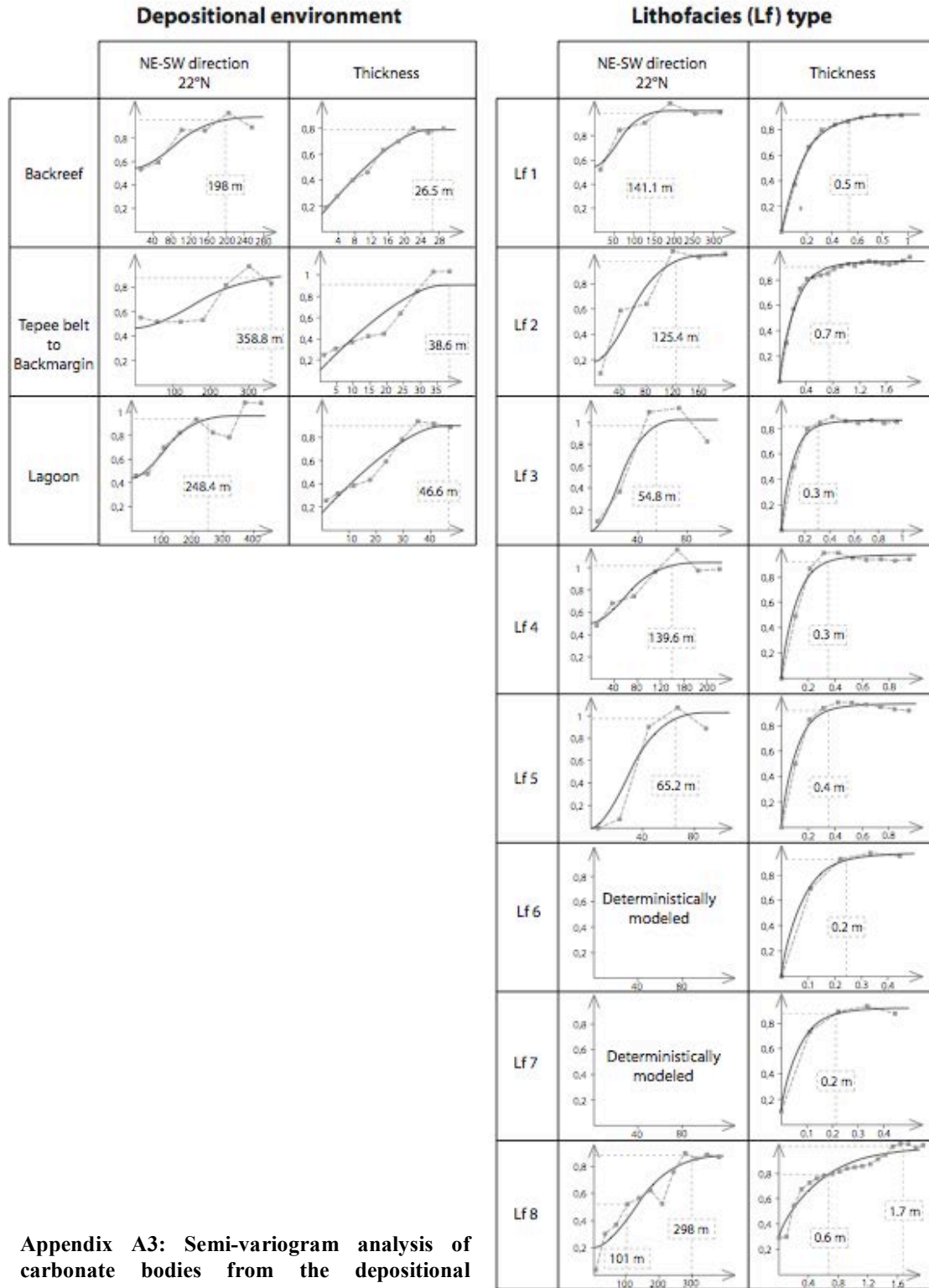




# Log correlation across Cima del Forcellone outcrop







Appendix A3: Semi-variogram analysis of carbonate bodies from the depositional environments (left) to lithofacies types (right).

## Appendix A4: Mathematical concepts applied during stochastic simulation

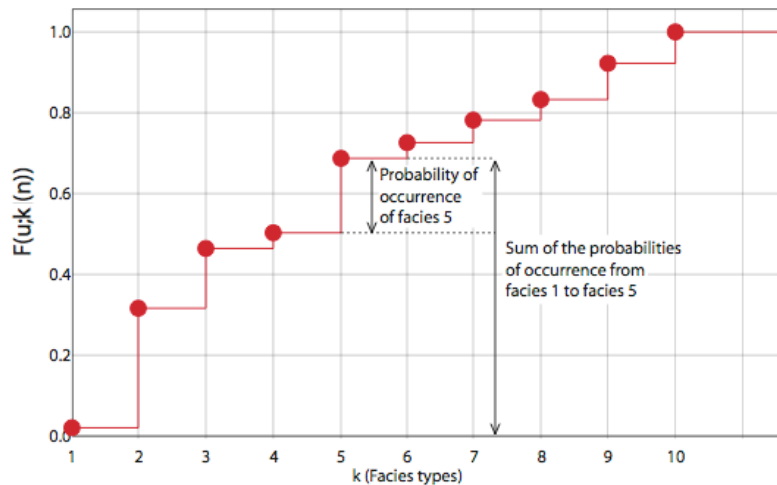
Appendix A4 provides an overview of the mathematical concepts underlying each of the three algorithms: Truncated Gaussian Simulation (TGSim), Sequential Indicator Simulation (SISim), and Indicator Kriging (IK). In opposition to deterministic method, stochastic modeling aims to predict the distribution of facies between two data points, by assigning a probability of occurrence to each facies across the modeled area. Such method is essential to build a 3-D geological model, which is mainly based on 1-D dataset such as stratigraphic sections, whereas the spatial distribution of facies between sections is unknown.

The mathematical approach used to estimate the probability of occurrence of each facies is based on the theory of random variable. Let a set of  $K$  random numbers be given and defined as a categorical random variable. A categorical (or discrete) random variable  $Z(\mathbf{u})$  does not have one single value  $z(\mathbf{u})$  at a location  $\mathbf{u}$  but a set of  $K$  possible values ( $z_1, z_2, z_3, \dots, z_K$ ), each with an associated probability of occurrence. The conditioning cumulative distribution function (CCDF) (Figure A4.1) estimates and assigns a probability to each value of  $z(\mathbf{u})$ . The CCDF of a categorical random variable  $Z(\mathbf{u})$  is denoted:

*Equation 1*

$$F(u; k|n) = \text{Prob}\{Z(u) = k|n\}$$

where,  $k$  represents the  $K$  values,  $k=1, 2, 3, \dots, K$ , that a categorical random variable can take and  $(n)$  the conditioning information available in the neighborhood of location  $\mathbf{u}$ .



**Figure A4.1: Example of conditioning cumulative distribution function (red) of a categorical random variable such as facies types at a location  $\mathbf{u}$  ( $K=10$ ). Each probability value of the ten facies types (dots) is successively added to reach 100%.**

By analogy with geological modeling, K facies types or categories can be considered as a categorical random variable  $Z(\mathbf{u})$ . The occurrence of one facies type at a location  $\mathbf{u}$  is unknown but an expected probability of occurrence can be assigned by calculating the CCDF (Equation 1; Figure A4.1). The estimation of a facies probability is conditioned by data input such as facies distribution, proportion, and dimensions (semi-variogram analysis) calculated prior to simulation from the digitalized stratigraphic sections. Each of the three algorithms, which aim to estimate the probability values of each facies, differs in the assumption made to deal with facies categories and to compute the CCDF.

#### ***A4.1. Indicator Kriging (IK):***

The essence of IK applied to categorical random variables  $Z(\mathbf{u})$  is based on a binomial coding of each categories (i.e. each facies types) into a binary random variable (0 or 1 values). This new random variable is called an indicator random variable  $I(\mathbf{u}; k)$  and defined as:

*Equation 2*

$$I(\mathbf{u}; k) = \begin{cases} 1, & \text{if } Z(\mathbf{u}) \in k \\ 0, & \text{otherwise} \end{cases}$$

In Equation 2,  $k$  represents the IK cutoff at which  $Z(\mathbf{u})$  is categorized as 1 or 0. In the case of facies modeling, the cutoff represents a facies type. The indicator variable  $I(\mathbf{u}; k)$  at the location  $\mathbf{u}$  is set to 1 if a facies  $F_1$  is present [ $Z(\mathbf{u}) \in F_1$ ] and to 0 when the facies  $F_1$  is absent. There are as many indicator variables created as the number of facies types. Then, ordinary kriging interpolates independently each new indicator variable  $I(\mathbf{u}; k)$  in order to estimate the probability value that facies  $F_1$  is present at location  $\mathbf{u}$ , i.e.  $i(\mathbf{u}; k) = I$ . The probability estimation is conditioned by the  $n$  known neighboring data values  $i(\mathbf{u}_\alpha; k)$ ,  $\alpha = 1, 2, \dots, n$ , at location  $\mathbf{u}_\alpha$ . The ordinary kriging estimator  $i_{OK}^*(\mathbf{u}; k)$ , which represents the mathematical rule for calculating the CCDF and sub-consequently the probability value that  $i(\mathbf{u}; k) = I$  (Equation 2), is defined by:

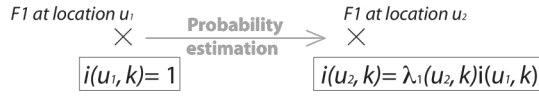
*Equation 3*

$$i_{OK}^*(\mathbf{u}; k) = \text{Prob}^* \left\{ I(\mathbf{u}; k) = 1 \mid (n) \right\} = \sum_{\alpha=1}^n \lambda_{\alpha}^{OK}(\mathbf{u}; k) \cdot i(\mathbf{u}_\alpha; k)$$

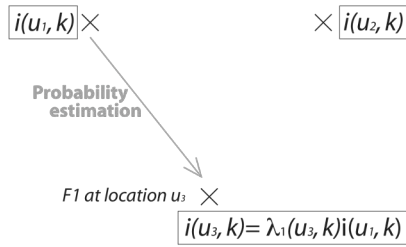
In Equation 3,  $(n)$  represents the conditioning information available in the neighborhood of location  $\mathbf{u}$ .  $\lambda_{\alpha}^{OK}(\mathbf{u}; k)$  are the  $n$  weights assigned to the  $n$  known indicator variables  $i(\mathbf{u}_\alpha; k)$  at location  $\mathbf{u}_\alpha$  and situated at a neighboring location of  $\mathbf{u}$  (Figure A4.2). The weighting values  $\lambda_{\alpha}^{OK}(\mathbf{u}; k)$ , which are constrained to sum to 1, are determined to minimize the error variance between the variance of the indicator variable  $I(\mathbf{u}; k)$  measured by the indicator semi-variogram and the variance given as input data by the semi-variogram. The goal of ordinary kriging is to determine

the appropriated kriging weights  $\lambda_\alpha$  by requiring a minimal error variance between the modeled and experimental variance, denoted  $\text{Var}[i_{OK}^*(u;k) - i(u;k)]$ .

**Step 1**



**Step 2**



**Figure A4.2: Schematic explanation of the probability estimation of a facies F1 using IK. Let one single known neighboring data  $i(u_1;k)$  be given at location  $u_1$ . The probability of occurrence of facies F1 equals to 1 by assuming that location  $u_1$  is situated in a digitalized section. The probability of facies F1 to be present at location  $u_2$  is estimated based on the single known data at location  $u_1$ . In step 2, the probability of facies F1 to be present at location  $u_3$  is also estimated using the single known data at location  $u_1$ . The process is then repeated until a facies probability is assigned to every location  $u$  of the study area.**

**Key aspects of IK:**

IK is building independently 3D probabilistic models for each facies type. Then, probabilistic models are compared to each other and the facies type showing the higher probability of occurrence at a location  $u$  is assigned to the cell. If one grid cell contains two or more facies types with a similar probability value, the more abundant facies type in the study area is favored. Consequently, IK tends to overestimate facies types with the highest global proportion, whereas facies types with low global proportion are absent. The latter drawback was observed during the evaluation of the stochastic algorithms performed in chapter 2.

**A4.2. Sequential Indicator Simulation (SISim):**

The sequential procedure of SISim can be summarized as follows:

(1) SISim applies the same binomial coding than IK (Equation 2) in order to define an indicator variable  $I(u; k)$  for K facies types,  $k=1, 2, \dots, K$ . Hence, K probability values  $p_k(u_1|(n))$  are generated at location  $u_1$  with ordinary kriging (Equation 3) and based on the conditioning data  $(n)$ .

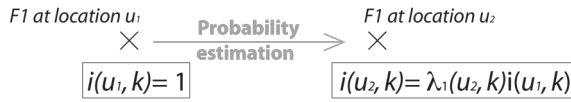
(2) Instead of assigning the most probable facies type to location  $u_1$  like IK, a CCDF-type function with a probability interval  $[0,1]$  is built by adding the probabilities of occurrence of each facies type  $p_k(u_1|(n))$ . The CCDF-type function is then composed of K probability intervals corresponding to the K facies types.

(3) A random number  $p$  uniformly distributed in  $[0,1]$  along the CCDF-type function is drawn. The interval in which  $p$  falls determines the facies type assigned to location  $u_1$ . The arbitrary ordering defined to add the

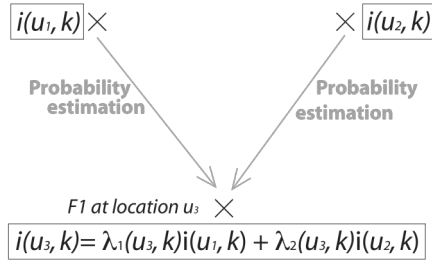
probability values  $p_k(u_1|(n))$  does not affect the assignment of a facies type at location  $u_1$  thanks to the uniform distribution of the random number  $p$ .

(4) Prior to simulate the  $K$  probability values  $p_k(u_2|(n))$  at a next location  $u_2$ , the facies type attributed to location  $u_1$  is considered as an additional conditioning datum for all subsequent probability estimations (Figure A4.3).

### Step 1



### Step 2



**Figure A4.3: Schematic explanation of the probability estimation of a facies F1 by using SISim.** Let one single known neighboring data be given at location  $u_1$  as stated in Figure A4.2 (i.e. the probability of occurrence of facies F1 equals to 1 at location  $u_1$ ). The probability of facies F1 at location  $u_2$  is estimated based on the single known data at location  $u_1$ . In step 2, there are now two known neighboring data at the locations  $u_1$  and  $u_2$ . The probability of facies F1 at location  $u_3$  is then estimated using the known data at both locations  $u_1$  and  $u_2$ . The sequential procedure (Equation 4) is repeated until a facies probability is assigned to every location  $u$  of the study area.

The sequential procedure from (1) to (4) is repeated until all location  $u$  within the study area are simulated. At the end of each sequence, the conditioning data  $(n)$  is updated to  $(n+1)$ . Considering the estimation of  $N$  unknown values of a binary random variable  $I(u;k)$  (e.g.  $N$  unknown probability values of facies F1) at  $N$  locations, the sequential simulation is defined by:

Equation 4

- Step 1:  $\text{Prob} \{I(u_1;k) = 1|(n)\}$
- Step 2:  $\text{Prob} \{I(u_2;k) = 1|(n+1)\}$
- Step 3:  $\text{Prob} \{I(u_3;k) = 1|(n+2)\}$
- ⋮
- Step N:  $\text{Prob} \{I(u_N;k) = 1|(n+N-1)\}$



**Key aspects of SISim:**

The strength of SISim results from the building of a CCDF-type function, which considers simultaneously all available probability values prior to assign a specific facies type at location  $\mathbf{u}$ . In comparison, IK simply assigns the facies type with the higher probability value. SISim represents an improvement of IK in order to better integrate extreme values such as facies types with low global proportion into the final 3-D model.

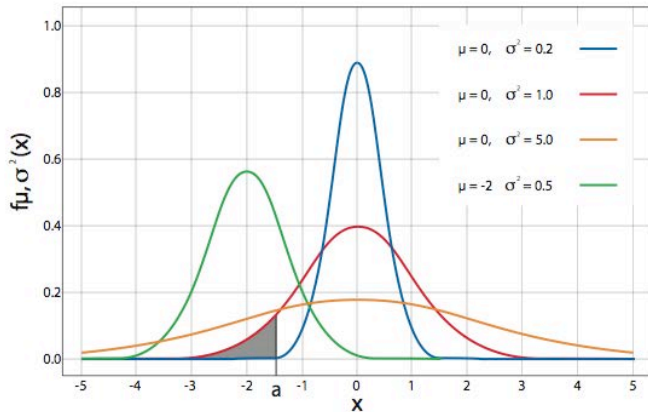
**A4.3. Truncated Gaussian Simulation (TGSim):**

TGSim does not simulate facies types directly. The algorithm transforms a categorical random variable such as facies type to a continuous random variable  $Y(\mathbf{u})$  assuming a standard Gaussian distribution. Prior to explain the methodology associated to TGSim, a recall of the definition of a Gaussian random variable is required. A continuous random variable  $Y(\mathbf{u})$  has a Gaussian distribution (Figure A4.4) if its probability density function (PDF)  $f(x)$ , which estimates the probability that one value  $x$  occurs at location  $\mathbf{u}$ , is defined as:

Equation 5

$$f(x) = \frac{1}{\sigma\sqrt{2\pi}} e^{-\frac{1}{2}\left(\frac{x-\mu}{\sigma}\right)^2}$$

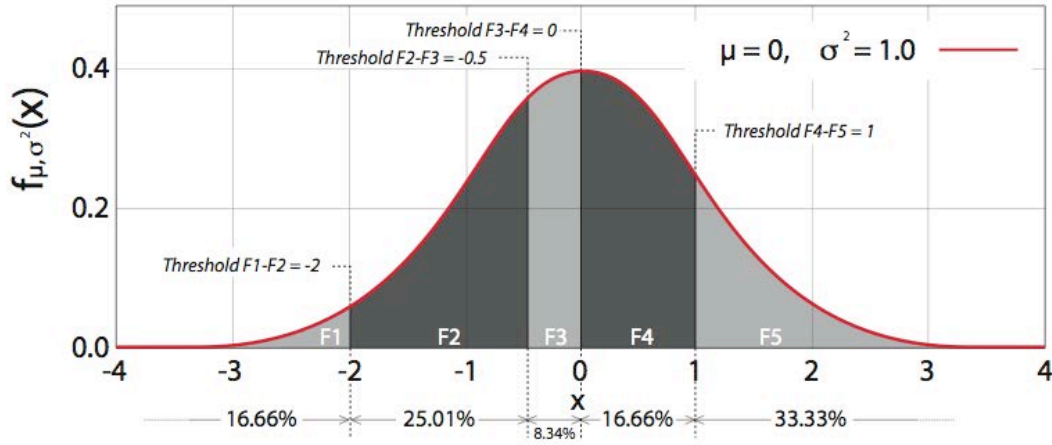
In Equation 5, the parameter  $\mu$  is the mean or expectation of the distribution and is defined by the sum of each number that composed the Gaussian random variable, weighted by its probability. In addition, the parameter  $\sigma$  is the standard deviation and therefore  $\sigma^2$  is the variance. The estimation of the CCDF at location  $\mathbf{u}$  is then reduced to the estimation of these two parameters since the CCDF is calculated by integrating the PDF from  $-\infty$  to  $x$ .



**Figure A4.4: Four examples of the probability density function (PDF) of a Gaussian random variable according to the mean  $\mu$  and the variance  $\sigma^2$  values. For the standard normal distribution (red), the probability that  $x$  is less than  $a$  equals the area under the normal curve bounded by  $a$  and minus infinity (grey area).**

Three major steps can be identified during TGSim. Firstly, a categorical random variable such as facies type is transformed into a standard Gaussian random variable  $Y(\mathbf{u})$ . The latter transformation is based on the notion of truncation of the Gaussian field by  $N-1$  thresholds  $t_i, i=1, 2, 3, \dots, N-1$  for  $N$  possible facies types  $F_i$  (Figure A4.5). A 1 by 1 relationship is applied between the estimation of the threshold values  $t_i$  along the Gaussian distribution and

the proportion of the N facies types within the modeled area. The example illustrated in Figure A4.5 considers five facies types (N=5).



**Figure A4.5: Example of truncation of a standard ( $\mu=0$ ,  $\sigma^2=1$ ) Gaussian random function  $Y(u)$  (red) by five facies types F1, F2, F3, F4, and F5 (N=5). In the modeled area, the facies proportion is 16.66% for F1, 25.01% for F2, 8.34% for F3, 16.66% for F4, and 33.33% for F5. The values of each threshold that enable the truncation of the Gaussian curve are estimated from the facies proportion. Note the ordering of the facies (from F1, to F2, to F3, to F4, and to F5), which determines the simulated facies distribution.**

Secondly, the estimation of the CCDF at location  $\mathbf{u}_o$  under a standard Gaussian random function  $Y(\mathbf{u})$  requires the estimation of the mean or conditional expectation (Equation 6) and the variance (Equation 7) using the simple kriging estimator  $Y_{SK}^*(u_o)$ . Simple kriging is similar to ordinary kriging and solely differs from the assumption that the weighting values  $\lambda_\alpha(u; k)$  are not summed to 1.

Equation 6

$$E\left\{Y(u_o) \mid y(u_\alpha) = y_\alpha, \alpha = 1, \dots, n\right\} \equiv Y_{SK}^*(u_o) = m(u_o) + \sum_{\alpha=1}^n \lambda_\alpha [y_\alpha - m(u_\alpha)]$$

where  $m(\mathbf{u})=E\{Y(\mathbf{u})\}$  is the expected value of the normal Gaussian random variable  $Y(\mathbf{u})$ . Note that the  $n$  conditioning data  $y_\alpha$ ,  $\alpha=1, 2, \dots, n$ , include the data input and the previously simulated values as for SISim (Equation 4).

Equation 7

$$\text{Var}\left\{Y(u_o) \mid y(u_\alpha) = y_\alpha, \alpha = 1, \dots, n\right\} = C(u_o, u_o) - \sum_{\alpha=1}^n \lambda_\alpha C(u_o, u_\alpha)$$

where  $C(u_o, u_\alpha)$  represents the covariance of the Gaussian random variable  $Y(u)$  between the locations  $u_o$  and  $u_\alpha$ .

Thirdly, the standard Gaussian random variable  $Y(u)$  is transformed back into the categorical variable (i.e. facies type) according to the truncation rule previously applied to the Gaussian field (Figure A4.5). Considering an indicator variable  $I_{F_i}(u; k)$  for each facies  $F_i$  (Equation 2), the  $i^{\text{th}}$  facies type  $F_i$  is defined by:

*Equation 8*

$$I_{F_i}(u; k) = 1 \Leftrightarrow t_{i-1} \leq Y(u) < t_i$$

### **Key aspects of TGSim:**

The distinctive feature of TGSim is its capability to model an ordered facies distribution. The truncation of a simulated Gaussian field enables the defining of a trend between facies types. In figure A4.5, the ordered sequence is from F1 to F5. Sub-consequently, the stochastic simulation will build a facies distribution, in which for example F1 is only in contact with F2 and in which F4 grades solely to either F3 or F5. The facies ordering is invariant and TGSim does not simulate a transition between two facies, which do not respect the pre-defined ordering trend; for example a transition from F2 to F4. Furthermore, contrarily to IK and SISim that assign one semi-variogram to each facies type, the simulation of one single Gaussian random function involves the use of one single semi-variogram to characterize facies geometries. Then, the simulation of several facies displaying specific morphological patterns cannot be fully captured with TGSim. The latter drawbacks were observed during the evaluation of the stochastic algorithms performed in chapter 2.